Design and development of antimicrobial and biocompatible model implant surfaces: Bio-interfacial interactions

A thesis submitted

In Fulfilments of the Requirements

for the degree of

DOCTOR OF PHILOSOPHY

by

Aman Bhardwaj

176106117

Under the supervision of

Prof. Lalit Mohan Pandey

Department of Biosciences and Bioengineering

Indian Institute of Technology Guwahati

Guwahati 781039, Assam, India

30 January 2025

TH-3560_176106117

Dedicated
to
My Family

भारतीय प्रौद्योगिकी संस्थान गुवाहाटी • Indian Institute of Technology Guwahati •

DECLARATION

I, hereby declare that the research carried out in the thesis entitled "***Design and development of antimicrobial and biocompatible model implant surfaces: Bio-interfacial interactions***", submitted by me to the *Indian Institute of Technology Guwahati*, for the award of the Doctor of Philosophy, is a bonafide work carried out by me under the supervision of Dr. Lalit M. Pandey. The content of this thesis, in whole or in parts, has not been submitted to any other University or Institute for the award of any degree or diploma. I also wish to state that nothing in this report amounts to plagiarism to the best of my knowledge and understanding.

Aman Bhardwaj

Aman Bhardwaj
Department of Biosciences and Bioengineering,
Indian Institute of Technology Guwahati,
Guwahati - 781039, Assam, India

Date: 30 January 2025

CERTIFICATE

This is to certify that the thesis entitled "***Design and development of antimicrobial and biocompatible model implant surfaces: Bio-interfacial interactions***", submitted by **AMAN BHARDWAJ (176106117)**, a Ph.D. student in the *Department of Biosciences and Bioengineering*, *Indian Institute of Technology Guwahati*, for the award of the degree of Doctor of Philosophy, is a record of an original research work carried out by her under my supervision and guidance. The thesis has fulfilled all requirements as per the Institute's regulations and, in my opinion, has reached the standard needed for submission. The results embodied in this thesis have not been submitted to any other University or Institute to award any degree or diploma.

Supervisor
Prof. Lalit M. Pandey
Department of Biosciences and Bioengineering,
Indian Institute of Technology Guwahati,
Guwahati - 781039, Assam, India

Date: 30 January 2025

ACKNOWLEDGEMENT

First and foremost, I would like to thank **Prof. Lalit Mohan Pandey,** my PhD supervisor, for his unwavering guidance and support during my PhD journey. While a good guide will instruct you to obey the rules and work accordingly, a better guide will point you in the right direction and let you choose your path, fostering a scientific mindset and attitude while adhering to research ethics. I will always be indebted and grateful to him for instilling the right scientific temperament and ethics in me.

I would also like to express my heartfelt appreciation to my committee members, **Prof. Selvaraju Narayanasamy, Prof. Amit Kumar, and Prof. Senthilkumar Sivaprakasam** (DC Chairperson), for their insightful feedback, valuable suggestions, constructive criticisms, and instrumental role in guiding me to achieve this significant milestone.

I am sincerely thankful to the **Department of Biosciences and Bioengineering (BSBE), Indian Institute of Technology Guwahati,** for allowing me to be part of this Institute. I am grateful to the faculty members and staff of BSBE for their assistance and support. Additionally, I am grateful to the **Central Instrument Facility (CIF), IIT Guwahati,** for allowing me to conduct my experiments using their advanced instruments.

I like to express my gratitude to my seniors and labmates, **Dr. Abshar Hasan, Dr. Rasmi Ranjan Behera, Dr. Poulami Datta, Dr. Rahul Verma, Dr. Aquib Jawed, Dr. Laipubam Gayatri, Dr. Pagidi Madhukar, Rushikesh Fopase, Vivek Yadav, Anurag Mishra, Chinmaya Panda, Mehak, Shalini Prajapati, Shilpa Nandi, Onkar Chowkekar, Smrity Sonbhadra, Jayaprabhakaran M., Jaya Bharti Singh, Sushmita Mishra, Mohit Kumar, Shreya R., Debasmita Seal, and Akshay Kumar.**

I am also thankful to my seniors and friends**, Dr. Apurba Das, Dr. Angshu Dutta, Dr. Yogendra Pratap Singh, Dr. Pratap Chandra, Dr. Venkat Naira, Dr. Mahesh R., Yashwanth P. R., Jitendra Singh, Shweta Deswal, Dr. Ratan Kumar, Dr. Mayur Ketan**

Mukherjee, Dr. Kishore Banik, Dr. Bhuvan Dixit, Dr. Senjuti Halder, Dr. Poulomi Dey, Arindom Neog, Dr. Bibhas Bhunia, Dr. Renu Sharma, Dr. Vianni Chopra, Dr. Manisha Sharma, Dr. Vishakha Jain.

I sincerely thank my teachers, **Dr. Antar Virk, Dr. Neetu Sharma, Ms. Shweta Kanwar, Ms. Meenakshi Sharma, and Ms. Vandana Sharma.**

I am also highly grateful to **the National Institute for Materials Science (NIMS), Japan, for allowing me to research at their esteemed Institute under the NIMS-ICGP program. I extend my gratitude to Dr. Akiko YAMAMOTO, Dr. Masanori KIKUCHI, Dr. Toru YOSHITOMI, MORIGUCHI San, TSUDA San, KIKUTA San, VAN San, Dr. Aaditya Manjanath, Adrija Das, and YUKA San.**

Additionally, I extend my greatest appreciation to my beloved **parents, brother, grandparents, and family members** for their unflinching support and faith in me. I am also thankful for my constant motivation and support, my brother **Achal Bhardwaj; Dr. Rajkumari Mazumdar, and Master Riokun** for their unwavering support and guidance.

I am also grateful to my friends and acquaintances, whom I have not mentioned, for their tremendous help and support, directly or indirectly, in my PhD journey.

Lastly, I am highly grateful to GOD for guiding me through the ups and downs of my PhD journey.

With heartfelt appreciation,
Aman Bhardwaj

Abstract:

A modern sedentary lifestyle and an aging population have weakened the immune response to various diseases and increased bone brittleness. So, bone damage has increased many folds, leading to augmentation of the damaged parts with biomaterial-based implantation. The cost of biomedical implants is increasing with time, and inversely, the success rate of the implants is decreasing. Implants, particularly orthopedic implants, lack blood vessels on the surfaces, making the immunological agents to eradicate bacterial contamination at the implant surface impossible. This necessitates heavy antibiotics administration to prevent bacterial contamination and, thus, sepsis at the site. This might lead to the development of antibiotic-resistant bacterial strains and other side effects. Biomaterials suffer stress shielding, micromotion, biofouling, lesser biocompatibility, and surface leaching compared to natural bone. Surface phenomena govern implant interactions with the physiological microenvironment; thus, tuning the surface properties using various chemical and physical modification strategies can enhance the overall implant properties.

In this work, silane-based Self Assembled Monolayers (SAMs) with various chain lengths and terminal moieties were fabricated on the model implant surfaces (silica, titanium, and Ti6Al4V) to enhance the biocompatibility, modulate the protein adsorption behaviour with antimicrobial surface coatings. The entire thesis has been divided into four sections. In the first section, silane SAMs were fabricated on the model implant surfaces (silica and titanium alloy) with variable SAMs lengths and diverse terminal groups such as amine-, octyl-, hybrid-, carboxyl-, hexadecyl- and octadecyl- on the surfaces. Surface properties insights were investigated by altering surface hydrophilicity and the surface energy. The change in the peak area of the various functional groups (elucidated by FTIR) on the SAMs surface also explored surface behaviour. Surface parameters were correlated with the thickness of the SAMs functionalities, giving valuable insights regarding surface tunability. The second section

explored the surface behaviour regarding the nature of protein adsorption (protein-biomaterial). Change in the protein secondary structure due to the formation of the contact points with the surfaces were investigated to tune the protein adsorption behaviour as the nature of the protein adsorbing on the surface determines the implant fate. In the initial studies, Bovine Serum Albumin (BSA) was explored as the model protein for the adsorption studies on silane-modified surfaces.

Fetal Bovine Serum (FBS), a cocktail of various physiological proteins, was also explored for the adsorption behaviour on the functionalized surfaces along with other blood proteins (collagen and fibrinogen). The degree and the nature of the conformational changes determined the efficacy of the said fabrications in the physiological microenvironment. The following section dealt with the cell adhesion behaviour of the osteoblast cell line (MG63) with the functionalized materials (cell-biomaterial interactions). Various cell adhesion parameters (surface coverage, average cell area, and circularity index) were quantified to get a deeper and broader insight into cell adhesion behaviour. Moreover, the cell adhesion studies were clubbed with the protein pre-adsorption (FBS, Collagen, fibrinogen, and BSA) to investigate the behaviour in simulated physiological conditions and to explore the potential of the various proteins for surface coating applications.

The last section of the thesis dealt with the fabrication of antimicrobial and anti-biofilm coatings on the silane SAMs functionalized surfaces. Biogenic AgNPs were explored as the antibiofilm coatings against *Pseudomonas aeruginosa*. Also, chitosan (natural biopolymer) was utilized as the antimicrobial agent and drug-loading vehicle for ampicillin against the clinically relevant bacterial strains (*Escherichia coli* and *Staphylococcus aureus*) on functionalized surfaces. The thesis aimed to investigate surface tunability using various silanes to modulate protein adsorption behaviour and enhance cell adhesion nature with antimicrobial coating fabrication.

Contents

Indian Institute of Technology Guwahati

Indian Institute of Technology Guwahati

List of Figures

Indian Institute of Technology Guwahati

Indian Institute of Technology Guwahati

List of Tables

TH-3560_176106117

Abbreviation

AFM	Atomic force microscopy
APTMS	3-Aminopropyl trimethoxysilane
AgNPs	Silver nanoparticles
BCA	Bicinchoninic acid
BSA	Bovine serum albumin
DMEM	Dulbecco’s modified Eagle’s medium
EDX	X-ray spectroscopy (EDX)
ECM	Extracellular matrix
FBS	Fetal bovine serum
FESEM	Field emission scanning electron microscopy
FN	Fibronectin
FTIR-ATR	Fourier transform infrared-attenuated total reflection
HAI	Hospital-acquired infections
HREELS	High-resolution electron energy loss spectroscopy
ITC	Isothermal titration calorimetry
MIC	Minimum inhibition concentrations
MPTS	3-mercaptopropyl trimethoxysilane
OTS	Octadecyltrichlorosilane
PBS	Phosphate buffer saline
PDMS	Polydimethylsiloxane
PEG	Polyethylene glycol
PEO	Polyethylene oxide
PLGA	Polylactic-co-glycolic acid
PMEMA	Poly-2-methoxyethyl methacrylate
PMPC	Poly-2-methacryloyloxyethyl phosphorylcholine
PU	Polyurethane
PVP	Polyvinyl pyrrolidone
PFS	Polytetrafluoroethylene
QCM	Quartz crystal microbalance

SAMs	Self-assembled monolayers
SPR	Surface plasmon resonance
TEOS	Triethoxy(octyl)silane
WCA	Water contact angle
WEDM	Wire-electro discharge machining
XPS	X-ray photoelectron spectroscopy

Chapter 1

Introduction

This chapter focuses on the overall theme of the thesis and the research objectives, along with the brief layout of all the thesis chapters.

1.1 Overview

Research related to biomaterials undergoing extensive scrutiny to fabricate the ideal implant materials with the least immunological response, better biocompatibility with anti-biofouling, and antimicrobial features [1-4]. Implant features are dominated mainly by the surface, so tuning the surface properties of the model surfaces using various modification techniques can be utilized, namely chemical and physical modification strategies. Chemical modification strategy based on Self Assembled Monolayers (SAMs) with terminal functional groups can be varied, or its nature can be varied (hydrophobic/ hydrophilic nature) [3, 4], and charge gradient or varied silanes can also be simultaneously incorporated into the surfaces. Fabrication strategies can be utilized alone or in combination with polymer or nanoparticle incorporation via covalent attachment, cross-linking, encapsulation, or entrapment strategies [5, 6]. This study uses a silanization approach for surface tunability, forming self-assembled monolayers with surface flexibility. The main focus of this research was to address the issues related to the success rate of the implants introduced into the body of the affected individuals by tuning the surface properties with desired features. Many factors contribute to success, including implants and the physiological environment.

As far as the implants are concerned, the surface properties contribute to the success and not the bulk. So, implant success is a surface phenomenon, not a bulk phenomenon [7]. The cost of an implant is also a serious issue. The cost of implant manufacture is very high compared to the success rate of the administered implant. Cost and demand for implants are increasing day by day due to the increased occurrence of accidents and diseased conditions in people due to a growing elderly population requiring implant administration. At the same time, implant failure is increasing due to implant rejection [8]. Implant rejection is a major concern as it adds an extra financial burden on the patient, and also implant replacement is not feasible every time. The physical, chemical, and biological nature of the implant surface contributes to the implant success. Our approach was to study and manipulate the properties of the model implant surfaces according to the properties of the implantation site. Incision at the implant site leads to a race between various proteins present in the vicinity among themselves and with various microbes that infiltrate the incised site [9].

Protein molecules with the smallest size and highest diffusivity rate will attach easily to the surface. Various proteins will adsorb and desorb from the surface until stable adsorption occurs. This phenomenon is known as the Vroman effect. Protein transfer occurs to form an adsorbed protein layer onto the surface. Moreover, surface properties were tuned to enhance the biocompatibility and cell adhesion parameters of the bone cells, along with the fabrication of the antimicrobial coatings on the surface using chitosan as both the antimicrobial and drug loading vehicle.

1.2 Objectives

To address the knowledge gap as explored in detail in Chapter 2 and to provide deeper insights into the design and development of the antimicrobial and biocompatible coatings on the model implant surfaces, the following thesis objectives were framed:

1. Surface modification and characterization of metallic implant surfaces
2. Bio-interfacial study of protein adsorption and cellular interactions with functionalized model implant surfaces mediated by adsorbed proteins (in-vitro study).
3. Design of antimicrobial coatings on functionalized model implant surfaces without compromising with biocompatibility

1.3 Thesis outline

The following seven thesis chapters were formed based on the above three objectives; the chapter-wise thesis outline is as follows:

Chapter 2

This chapter focuses on the literature review on the designing and developing antimicrobial and biocompatible model implant surfaces and addresses the related knowledge gap. This chapter reviews the latest developments related to biomaterials, followed by various strategies focussed on eradicating the non-specific protein adsorption on the implant surfaces. Strategies for enhancing the biocompatibility and fabricating various antimicrobial coatings have been discussed in detail.

Chapter 3

This chapter includes the surface modification of the titanium alloy surfaces using the silanization-based surface modification approach. Silane molecules with varied terminal moieties, such as octyl, amine, carboxyl, hybrid, mixed, hexadecyl, and octadecyl, were functionalized on the acid and UV-activated surfaces. These self-assembled monolayers (SAMs) of the various silane molecules were characterized after modification using the Contact Angle goniometer, Fourier Infrared Transform Spectroscopy (FTIR), and ellipsometer spectroscopy. Change in the surface energy and hydrophobicity, along with the change in the peak area of various functional groups, was quantified to get an insight into the silanization and surface tunability of various model implant surfaces.

Chapter 4

This chapter focuses on the protein adsorption studies (BSA, FBS, Col-I, and FN) on the silane-functionalized Ti6Al4V surfaces. BSA and FBS adsorption studies were performed on the AO-, AC-, HO-, and HC series surfaces, followed by the carboxyl SAMs surfaces with varied acidified $KMnO_4$ and incubation time. Moreover, mixed$_{(16\text{-}8)}$ and carboxyl$_{(16\text{-}8)}$ SAMs were investigated for BSA adsorption insights, along with hexadecyl SAMs for protein adsorption (BSA, Col-I, and FN) investigation.

Chapter 5

This chapter focuses on cell adhesion studies using MG63 cell lines on various silane-functionalized titanium surfaces. The first section explores the cell adhesion behavior of the MG63 cell line on the AO-, AC-, HO-, and HC- series Ti6Al4V surfaces. The following section dealt with the effects of the FBS pre-adsorption on the Octyl and Bare Ti6Al4V surfaces to enhance the cell-material interactions. The third section discussed the longer Hexadecyl SAMs and their cellular interactions with and without pre-adsorption of proteins (BSA, Col-I, and FN).

Chapter 6

This chapter focuses on fabricating various antimicrobial coatings for biomedical applications. In the first section, benign silver nanoparticles were fabricated and coated on the amine SAMs-modified silica surfaces and explored for their antimicrobial and anti-biofilm properties. The second section explored natural biopolymer chitosan. The second section explored natural biopolymer chitosan as an antimicrobial agent and drug-loading vehicle.

Chapter 7

This chapter focussed on the overall research conclusion of the thesis along with the future ideas related to the fabrication of biocompatible and antimicrobial coatings on functionalized titanium surfaces.

Chapter 2

Literature Review

This chapter focuses on the literature review on the designing and developing antimicrobial and biocompatible model implant surfaces and addresses the related knowledge gap. This chapter reviews the latest developments related to biomaterials, followed by various strategies focussed on eradicating the non-specific protein adsorption on the implant surfaces. Strategies for enhancing the biocompatibility and fabricating various antimicrobial coatings have been discussed in detail.

2.1 Introduction

Biomaterials are synthetic or nature-derived materials that aid in the normal functioning of a diseased or lost body part for enhancing longevity and normal well-being either directly/indirectly [1]. Some applications of biomaterials include orthopaedics, dental implants, soft/hard bone implants, blood vessels, artificial heart valves, stents, pacemakers, and hip or knee replacement [1-8]. Besides implant material, biomaterials find applications in other biomedical engineering fields, such as surgical instruments, artificial organs, blood storage bags, drug delivery, and tissue engineering [9-12]. At the biomaterial interface in the physiological microenvironment, protein-surface interactions, protein-protein interactions, inflammatory reactions, and many other dynamic interactions simultaneously occur [13]. For effectiveness, biomaterials need to be integrated with the surrounding tissues/bones without intervening fibrous tissue material [14]. This can be achieved by tuning the bio-interfacial interactions using the surface engineering approaches.

It has been observed that the success of the implant is determined by the surface properties and not by the bulk properties. All the issues related to titanium and alloys can be addressed easily by modulating the surface properties. Biomaterials interact with the physiological microenvironment by the adsorbed protein on the surface. So, enhancing the protein adsorption capability of the surfaces will lead to better osseointegration. Protein adsorption behaviour of the titanium surfaces can be easily tuned by using techniques such as physical (plasma spraying, electron beam sputtering, hydrothermal treatment, ion beam sputtering, surface roughness tuning) [15, 16], chemical (sol-gel method, electrochemical etching, anodization, silanization, apatite coating, electrochemical oxidation, doping of other elements) [17-21], biological (surface protein grafting, bioactive molecule grafting) [22] modifications, respectively. Modification can tune the surface morphology, roughness, chemical composition, and surface chemistry. Modulating the surface morphology may lead to tuning biochemical signals related to cell adhesion and increasing the surface area, leading to better bone-implant mechanical interlocking. There has been extensive work carried out to overcome the disadvantages of titanium and alloy implants [23, 24]. Various generations of biomaterials used for biomedical applications are shown in **Fig. 2.1**.

Indian Institute of Technology Guwahati

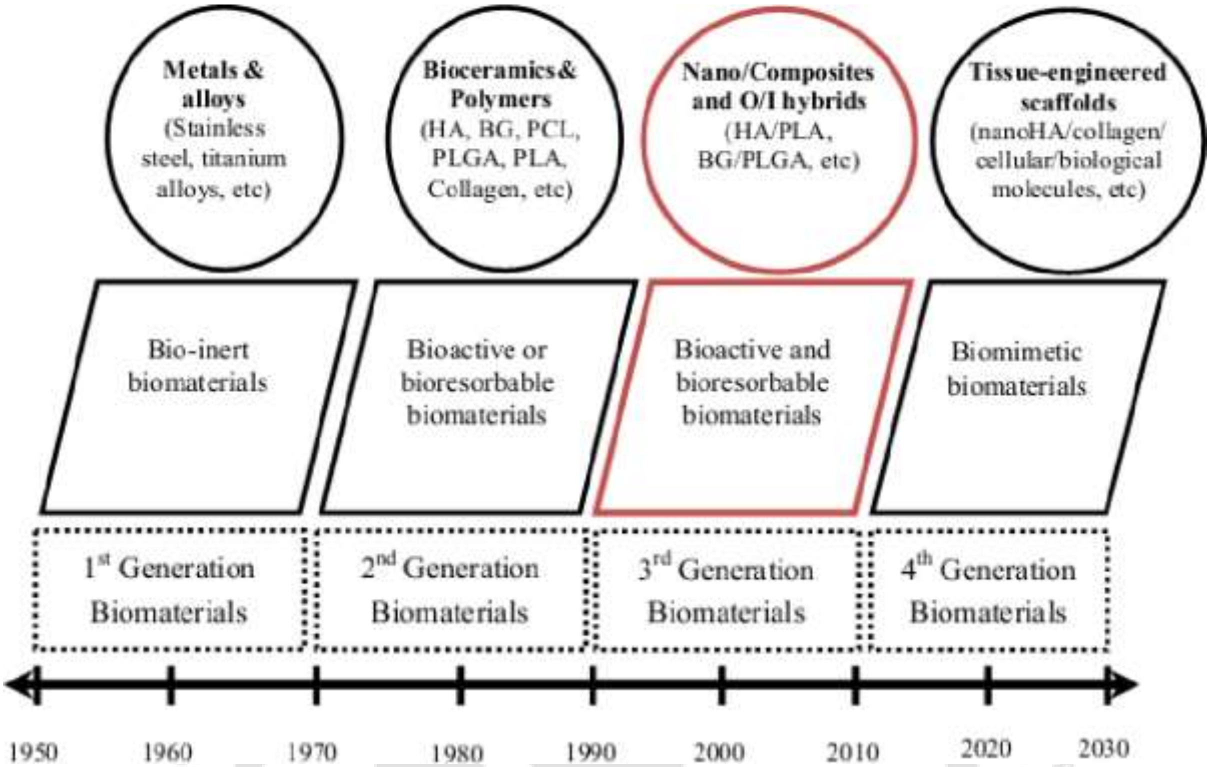

Figure 2.1: Generations of biomaterials comprising bioinert, bioactive, bioactive resorbable, and biomimetic materials

Patients with implants having weak immunity due to aging and other medical complications suffer from various infections, particularly implant-associated infections, which lower the success rate and life expectancy of the implants. Failure of the implant implies the need to replace it with a new one, increasing the cost of healthcare [7]. Patients are given high doses of antibiotics to prevent and treat these infections, which increases the likelihood of developing multi-drug resistant pathogenic strains. Antimicrobial features can be added to implant surfaces to avoid the need for antibiotic therapy [7]. Various physical and chemical modification techniques can directly alter implant surfaces to provide antibacterial properties [8-11]. To preserve the other inherent properties of the implant materials, additional biomaterials with antimicrobial properties may be coated onto the implant surfaces [12].

This chapter reviews the various strategies to enhance the surface properties of various biomaterials, eradicating non-specific protein adsorption to the surfaces and fabricating various biocompatible antimicrobial coatings on the surface.

2.2 Biomaterials

In this section, biomaterials have been discussed, with implant development as the prime focus. **Table 2.1** summarizes the various biomaterials utilized for biomedical applications. This section intends to introduce the various biomaterials in a simplified manner.

2.2.1 Metallic biomaterials

Various metals and their alloys have been explored for biomedical applications based on mechanical, chemical, and surface properties. 316L stainless steel exhibits mechanical and electrochemical properties such as better corrosion resistance, work hardening, and formability [25, 26]. Stainless steel with Young's modulus of 210 GPa is utilized to develop orthopaedic and dental implants [27]. CoCrMo alloys' application dental material was initially started in the late nineties and is now used as an orthopaedic implant material. These alloys are widely used for the augmentation, replacement, and repair of damaged bones. For example, CoCrMo wrought grade alloys are frequently used to manufacture the knee and hip joints [28]. However, recent concerns regarding corrosion and the generation of toxic wear debris limited their utilization [29]. It has been observed that corrosion is also mediated by the inflammatory agents that are attracted to the implant site [29].

Table 2.1: Biomedical applications of the various biomaterials

Biomaterial		**Application**	**Reference**
Type	Name		
Metal	316L	Orthopedic implants	[26]
	CoCr	Hip/knee joints	[28]
	CoCrMo	Orthopaedic implants	[29]
	AZ31	Degradable bone implants	[30]
	Ti6Al4V	Orthopedic/dental implants	[31]
Polymer	PVC	catheters	[32]
	UHMWPE	Acetabular cup	[33]
	Polypropylene	Sutures	[34]
	PMMA	Ocular lenses	[35]
	Polyurethanes	Implant coating	[36]
	Polycaprolactone	Tissue engineering	[37]

	Polylactic acid	Orthopaedic regenerative medicine	[38]
	PEKK	Bone tissue engineering	[39]
	Polyester	Cardiac tissue engineering	[40]
Ceramics	HAP	Bioactivity enhancement	[41]
	Calcium phosphate	Bioactivity/Tribological features enhancement	[42]
	Bioceramic	Bone healing	[43]
	Ceravital	Middle ear surgery	[44]
Composites	Chitosan/TiO_2	Wound dressing/skin regeneration	[45]
	HAP/β glucan	Bone substitute	[46]
	PMMA/silica	Corrosion resistant coating	[47]
	Alumina/zirconia	Dental implant	[48]
	Zn/HAP	Orthopaedic applications	[49]

PVC: polyvinyl chloride; UHMWPE: ultra-high molecular weight polyethylene; PMMA: polymethylmethacrylate; PEKK: polyetherketone ketone; HAP: hydroxyapatite;

The lower rigidity of titanium alloys compared to CoCr alloys and stainless steel makes them suitable for implant development, particularly for orthopaedic and dental implants [50, 51]. Titanium and alloys display good biocompatibility, corrosion resistance, and lower elastic modulus [52]. Passive TiO_2 layer present on the surface of Ti6Al4V imparts corrosion resistance [53]. β phase titanium alloys are the most promising candidates for implant development due to good biocompatibility and superior mechanical properties [54]. Titanium alloys occur in the β phase at a higher temperature, and β phase stabilizers are used to obtain the β phase at a lower temperature [50].

The addition of Mo to titanium imparts low elasticity with superior strength for implant development and is a most efficient β phase stabilizer [27]. However, Mo addition has ductility and density issues that alloying Zr and Nb can address to Ti-Mo-based binary alloy to form Ti6Mo4Nb4Zr, which resulted in Young’s modulus of 32.3 Gpa [27]. Nb addition improves the hot workability and mechanical performance, while strength is increased by Zr addition [27]. β alloy, such as Ti-(3-18)Mn, is a low-cost and biocompatible alloy with high tensile strength and performance comparable to widely utilized Ti6Al4V alloys [51].

However, Ti6Al4V suffers from poor wear resistance, stress shielding, and micromotion at the implant site, which causes the detachment of the debris. Cyclic load-bearing areas such as plates and screws lead to the generation of debris [1]. This leads to the release of metal leachate in the vicinity. The release of aluminum and vanadium from the Ti6Al4V is toxic to the human body. Al release results in neurotoxic effects in the body [51]. Vanadium ions at a concentration of >23 μM become toxic to the physiological microenvironment [53]. The released metal leachates interact with surrounding tissues, which causes the immunological response and failure of the implant [55]. Toxicity issues of Al and V led to the exploration of other non-toxic β-phase stabilizers such as tantalum (Ta), zirconium (Zr), and niobium (Nb). Ti13Nb13Zr, Ti-Mo, Ti12Mo6Zr2Fe, and Ti29Nb13Ta4.6Zr are some of the recently developed biomaterials to address the leaching issues of the titanium alloys [25]. However, the higher cost of Ta and Nb steered the examination of low-cost candidates such as manganese [25, 51].

Further, a mismatch in Young's modulus of cortical bone (10-30 GPa) and the metallic implant such as Ti6Al4V (110 GPa) causes a stress shielding effect leading to bone resorption [51]. This causes weak interfacial interactions between the implant and host bone, bone atrophy, and premature rejection of the implants [54]. Developing alloys with Young's modulus closer to the bone might address the stress shielding issue. Recently, binary and ternary titanium alloys were developed with desirable Young's modulus, such as Ti35Nb4Sn (43 GPa), Ti15Mo (78 GPa), and Ti15Mo5Zr3Al (80 GPa) [51]. Nontoxic β stabilizers-based binary (Ti-Mo, Ti-Nb) and ternary (Ti-Mo-Nb and Ti-Ta-Nb) alloys provide the low modulus (~80 GPa) suitable for implants with low-stress shielding effect [54]. Alloying Mo, Zr, and Nb with Ti resulted in Ti8Mo4Nb2Zr with Young's modulus of 35 GPa comparable to that of cortical bone, making it a suitable implant for development [50].

Besides, Ti6Al4V suffers from fretting wear and poor tribological features. Metal ions released from the surface may infiltrate the intercellular spaces or penetrate the cellular structures, leading to metallosis [56]. This challenge is addressed by applying surface modification strategies such as shot peening, water jet peening, case hardening, low plasticity burnishing, plasma nitriding, and LASER peening [57, 58]. The tribological behaviour of Ti alloys can be addressed by reinforcing them with B_4C particles by a hot pressing method [55]. An anodization-based surface modification strategy can be used to block cellular infiltration. This process involves forming a thin oxide layer onto the outermost surface whose properties depend on the production method, time of oxidation, electrolyte, and electric parameters used for the process [56]. Plasma nitriding also improves wear resistance, preventing inflammation at the site [58]. Various other surface modification techniques like thermal oxidation, etching, sputtering, silanization, surface roughening, and surface coatings are reported to improve the integration of the implant surface with the host tissues [42, 59-62].

To mimic the natural ECM in the metallic biomaterials, various porous metallic biomaterials are developed using Selective LASER Melting (SLM) to improve the biological properties of the metallic biomaterials [52, 63]. Porous metallic biomaterials mimic the natural bones' mechanical and topological properties, making them a suitable candidate for orthopaedic applications [64]. Porous titanium alloys were developed with non-toxic elements to transfer stress from the implant to the host bone [52]. The porous structure enhances the electrochemical and mechanical properties of the implants [52]. Ti-(Ta, Nb)-Fe alloys-based development of porous Ti with reduced processing can be a promising biomaterial for orthopaedic applications [65].

The promising biodegradable ability of Mg alloys enabled the design of implants with better stiffness and mechanical strength [66]. Implants fabricated using magnesium and biodegradable alloys possess mechanical properties comparable to natural bone and high biocompatibility and strength/weight ratio. Magnesium ions in the magnesium-based implants stimulate new bone formation and osteogenesis [30]. However, these biodegradable Mg alloys suffer from drawbacks, such as a faster degradation rate due to the elevated pH of the surrounding microenvironment and the formation of the hydroxide as the degradation product, causing the release of hydrogen from the site leading to irritation to the surrounding tissues. These challenges have compromised the long-term biocompatibility of the Mg alloys. Degradation of the alloys depends on the alloying material, grain size, and metal purity [66]. The presence of chloride ions in the physiological microenvironment elevates the corrosion rate of AZ31 Mg alloys. Various strategies like anodization, sputtering, electroplating, thermal spraying, micro-arc oxidation, and organic coatings enhance the corrosion resistance of magnesium and alloys [30, 67]. The corrosion resistance of magnesium-based biomaterials can also be improved by alloying with zinc or calcium, but the low solubility of other metals in magnesium limits this approach [67]. In this direction, alloying magnesium to form binary (Mg-Ca) and ternary (Mg-Zn-Ca) alloys resulted in enhanced corrosion resistance [68, 69].

2.2.2 Polymeric biomaterials

Both natural and synthetic polymers are utilized as biomaterials for the fabrication of implants. Chitosan is a natural biocompatible and osteoconductive polymer that was explored for wound healing applications [70]. Natural hydrophilic polymer, i.e., gelatin, is a derivative of collagen protein. Thus, along with biocompatibility, gelatin exhibits a tunable degradation rate in the physiological environment [71]. These polymeric biomaterials, such as collagen, polyamide, gelatin, polyester, and chitosan, also suffer from low physical and mechanical properties compared to natural bones [72]. Polymeric biomaterials exhibit many advantages compared to other biomaterials, such as Young's modulus, similar to the human bone, and radio-transparency [73]. However, they also have a few drawbacks, such as inadequate bone integration and unregulated degradation rates [74].

Many synthetic polymers are utilized for application in bone tissue engineering, like poly (lactic acid) (PLA), poly(caprolactone) (PCL), poly(glycolic acid) (PGA) and copolymers due to better mechanical strength, biocompatibility, and bioresorbability [75]. In the standard design of the artificial hip joint, an acetabular cup is lined with a polymer liner, usually ultra-high molecular weight polyethylene (UHMWPE)[58]. Polyetheretherketone (PEEK) and polyetherketoneketone (PEKK) are the members of the high-temperature thermoplastic polyaryletherketone (PAEK) polymers. PEKK is a promising candidate for fabricating implants with stiffness and density comparable to natural bone, good biocompatibility, and ease of patient-specific implant fabrication using the 3D LASER sintering technique [39]. However, these PAEK family polymers suffer from poor osseointegration at the bone-implant interface due to the formation of the fibrous tissue layers on the implant surface `[39].

Polyurethane (PUs) is the widely utilized synthetic polymer for biomedical applications due to its mechanical, biological, and physicochemical properties and tunability. Biodegradable PUs films can be fabricated using PCL triol and poly(ethylene glycol) (PEG) as the soft segment and glycerol and hexamethylene diisocyanate (HDI) as the hard segment [72]. PU polymers display better versatility and mechanical properties due to the presence of both hard and soft segments. The soft segment usually comprises polycarbonate polyols, polyether or polyester, and elastomeric features to the PU polymer backbone. Hard segments arise due to a reaction between diamine/diol chain extender and diisocyanate and are responsible for the mechanical strength due to urethane linkage mediated hydrogen bonds, as shown in **Fig. 2.2 [72]**. PUs can be easily tuned by varying the hard to soft segment ratio, molecular weight, and chemical composition [72]. PUs are affectively processed into fibrous scaffolds and films [10].

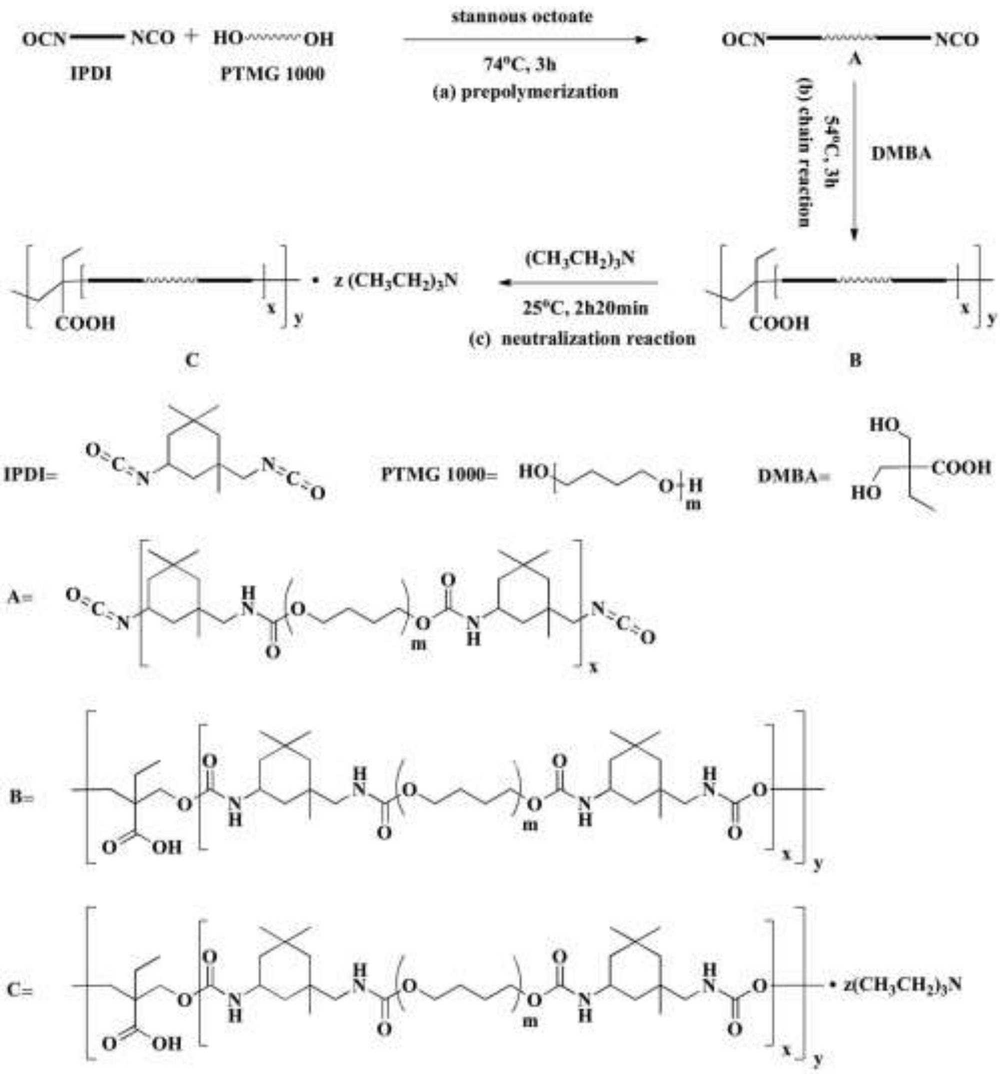

Figure 2.2: Schematic showing the polyurethane synthesis via bulk polymerization of polytetramethylene ether glycol (PTMG 1000), isophorone diisocyanate (IPDI), and 2,2-bis(hydroxymethyl) butyric acid (DMBA) species (Adapted with permission from Acta biomaterials 59 (2017): 45-57).

PCL is a biocompatible hydrolysable hydrophobic polymer with a slower degradation rate in the physiological microenvironment, high tensile strength, and releases non-toxic products on degradation [71, 72]. PCL has a low melting point (55-60 °C) and offers good blend capability with other additives, enabling the fabrication of scaffolds with a specific shape. However, PCL lacks bioactivity, which can be addressed by blending it with bioactive materials like ceramics [75]. In contrast, PEG is a hydrophilic polymer soluble in organic solvents and water, non-antigenic, soluble in organic solvents and water, non-antigenic and non-immunogenic, and releases non-toxic degradation molecules [72]. PEG is widely reported to resist non-specific adsorption via its strong hydration layer and steric repulsion [73]. However, the poor stability of PEG in physiological environments limits its practical *in-vivo* biomedical applications.

Aliphatic polyester family member PLA contains ester groups, making them vulnerable to hydrolytic degradation in the physiological microenvironment. This degradation leads to a decrease in the molecular weight due to ester bond cleavage in the polymeric chain and secretion of the lactic acid in the tissue vicinity, converted to carbon dioxide and water via the citric acid cycle [66]. The degradation of polyester polymers releases acidic products that cause tissue necrosis and enhance the immunological response at the site [76]. The degradation of polyesters is complex and depends on the size, shape, molecular weight, crystallinity, chirality, and processing conditions [74]. Biodegradable polymers like PLA and PGA hold promise in dental and orthopaedic implants for bone replacement [74]. Bioresorbable polymers exhibit an uncontrolled dissolution rate in the microenvironment, which increases due to a decrease in the pH because of inflammatory agents at the site. Bio-resorption might cause fibrous capsule formation and inflammation, leading to implant failure [74]. These drawbacks of the bioresorbable polymers can be addressed by incorporating carbon nanotubes or ceramic materials, which decreases the degradation rate in the physiological environment [66].

2.2.3 Ceramic biomaterials

Ceramic biomaterials are composed of metallic/non-metallic elements and are classified based on physiological microenvironment behaviour. Ceramics are classified as bioinert, biodegradable/bioresorbable, and bioactive ceramics [77-80]. The main constituent of the natural bone matrix is nano-hydroxyapatite (nano-HAP) [$(Ca_{10}(PO_4)_6(OH)_2)$], which is applied extensively for fabricating biomimicking biomaterials for implant-related applications. HAP is also used as a bone substitute as it resembles the nanocrystals in the natural bone [75]. The morphology, crystallinity, size, and surface properties of the nano-HAP can be easily tailored for the desired applications [75]. The stronger bond formation capability of bioglass bioceramics makes it ideal for bone grafting applications because of its similarity with the inorganic component of the natural bone [70]. Bioactive glass interacts with the body fluids and creates an alkaline environment due to salting out of bioactive glass [74]. Bioglass was observed to precipitate the calcium phosphates in the physiological solutions [70], forming an apatite layer on the surface. Bio-ceramics based surface coatings are known to enhance the bioactivity of titanium and alloys [1]. Ceramics such as Al_2O_3/Si_3N_4 are combined with metallic biomaterials to enhance the wear resistance of the artificial hip joints [58]. Ceramics are also widely utilized to fabricate orbital and dental implants [48, 81-85]. However, ceramics suffer from surface cracking under stress conditions, leading to implant failure [55].

2.2.4 Composite biomaterials

Composite biomaterials are composed of two or more biomaterials to fabricate an implant material with desired/hybrid features [86]. This enables the design of biomaterials with combined features originating from the constituents of composites. In turn, this addresses the limitations of individual materials to quite an extent. The composites offer improved mechanical properties, wear resistance, degradation behavior, and multifunctionality. Various composites are used for load-bearing, dental and orthopaedic implants along with drug delivery applications [49, 87-89].

The incorporation of hard ceramic particles with metals results in metal matrix composites (MMCs), which improves the wear-resistant and load-bearing properties of the composite; for example, the addition of boron carbide to titanium results in MMCs [55]. Cifuentes *et al.* investigated the degradation behaviour of the fabricated biodegradable composites with magnesium microparticles (10 wt%) reinforced polylactic acid (PLA) matrix. Mg reinforcement regulated the degradation behaviour of the PLA/Mg composites, and the shape of the microparticles controlled the degradation rate of the composite, as shown in **Fig. 2.3 [66]**. Manavitehrani *et al.* fabricated a composite of poly(propylene carbonate) and starch to eradicate the risk of harmful product leaching in the tissue vicinity. The fabricated composite properties were tuned by varying the concentration of the starch in the composite, as the compression strength varied depending on the starch content (0.2-33.9 MPa) [76].

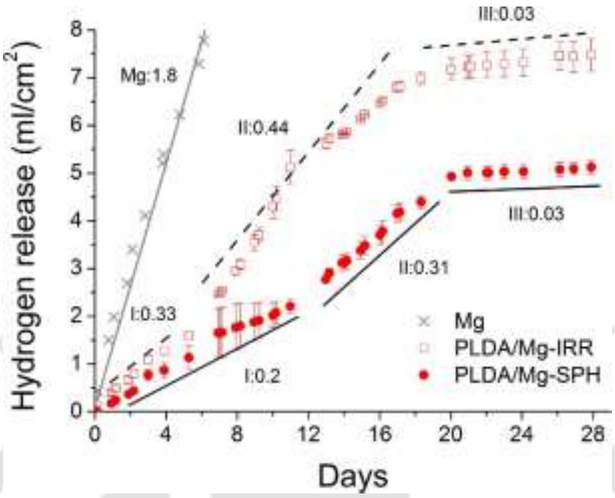

Figure 2.3: Degradation behaviour of the Mg/PLA composites as a function of the hydrogen release after immersion in PBS for a span of time where IRR means irregularly shaped and SPH refers to spherical particle composite (Adapted with permission from Acta biomaterialia 32 (2016): 348-357).

Tuning the degradation rate of the composites is a pre-requisite for the development of composite biomaterials [66]. The main disadvantages of conventional bioresorbable material are the lack of bioactivity, low mechanical properties, and uncontrolled degradation of the material in the physiological environment [90, 91]. Healing of the bone can be met only when the degradation of the biomaterial and bone healing rate are in synchrony with each other. Further understanding of the degradation kinetics, especially the underlying mechanisms such as corrosion behaviour and matrix hydrolysis, led to tuning the composite properties for better bone healing [66, 92]. The incorporation of metallic biomaterial with bio-resorbable polymers (poly (α-hydroxy acid)) to form composites enhanced the degradation behaviour [66]. Besides, polymer properties can be enhanced by incorporating the polymeric matrix with bioactive ceramic fillers such as HAP and tricalcium phosphates. Bioactive ceramic fillers form a calcium phosphate layer that interacts with the body fluids and improves interaction with the body fluids, improving bone-bonding ability. PLA properties can be tuned by the addition of the bioactive mineral to form the organic-inorganic composites. Bioactive ceramic fillers decreased the degradation rate and neutralized the released lactic acid [74]. A composite of bioglass/chitosan has been utilized as injectable bone substituent material due to better biological properties [70].

Nowadays, scaffolds with tunable properties based on hybrid composites are developed and contain synthetic and natural polymers. Natural polymers such as gelatin, chitosan, and collagen simulate the natural physiological micro-structures, thus stimulating the attachment, proliferation, and differentiation of the cells. Synthetic polymers aid the mechanical properties of the composites [93]. These nanofibrous scaffolds can be fabricated using techniques such as dry spinning, wet spinning, electrospinning, phase separation, and self-assembly [71]. Hart *et al.* utilized a 3D printing technique to fabricate the composite based on the self-assembled supramolecular polymeric network impregnated with silica nanoparticles that were non-toxic towards the chondrogenic cell line [94]. Ke *et al.* fabricated a guided bone regeneration membrane via electrospinning based on the PCL-gelatin hybrid nanofibers using genipin as the crosslinker. Acetic acid was used to make a homogeneous membrane by resolving the phase separation of PCL and gelatin. Nanofibrous membranes mimicked the natural ECM with high surface area and porosity, resulting in better cellular interactions. Surface properties were easily modified by varying the ratio of PCL to gelatin. Electrospun PCL/gelatin [71].

The nanocomposite (CCNWs-AgNPs) of silver nanoparticles (AgNPs) decorated on carboxylated CNWs (CCNWs) exhibited dual functions of improved mechanical strength and induced antimicrobial activity [95]. In another study, a composite film of chitosan (CS) and polyvinylpyrrolidone (PVP) with incorporated cellulose nanowhiskers (CNWs) was explored for drug delivery application [96]. The integration of CNWs enhanced the thermal and mechanical properties of films. The prepared composite films also resulted in high biocompatibility with excellent antibacterial activities.

2.2.5 Biomaterials for implant fabrication

The implant site undergoes inflammation and migration, and subsequent proliferation of the immunological mediators occurs at the site. The immunological response is quite complex at the implantation site. Post implantation, the interactions of immune cells with the implant surfaces initiate the immunological cascade that ultimately determines the fate of the implant material. The integration and long-term implant survival depend on the immune system's initial response to the implant surface [29, 97]. Innate immune response agents, namely platelets, neutrophils, and macrophages, migrate to the implant site and attract other immune cells by releasing cytokines and chemokines. This leads to phagocytosis of the damaged cells/tissues. Macrophages are the critical mediator of the initial immune response and inflammation at the site, along with normal tissue homeostasis maintenance [97]. The prolonged immune response may damage the proximal healthy tissues due to chronic immune response [98]. Moreover, collagen network formation and angiogenesis also occur as a part of the healing process. Loading of the inflammatory agents causes the generation of the Reactive oxygen species (ROS) that impairs the proper wound healing [99].

Cell response to the implant is determined by surface properties such as wettability, surface topography, and chemistry. Implant surface interactions with the physiological surroundings further get complicated due to the calcium, phosphate, and chloride ions in the microenvironment [66]. A study on the effect of surface roughness and wettability of implant material concluded that increased hydrophilicity and surface roughness resulted in synergism with increased osseointegration and reduced healing times, thus increasing the success rate [97]. Thus, osteogenic differentiation is promoted by surface modification strategies, which enhance the wettability and surface roughness. Keeping the complex interfacial phenomenon at the implant surface, various features crucial for implant fabrication are discussed in this section.

2.2.6 Features of ideal biomaterials

The biomaterial selection for implant fabrication depends on the volume, size, and shape of the affected site and the patient-related ailments for an ideal bone substitute material. Biocompatibility, better osseointegration, and favourable biomechanics are among the main features of an ideal biomaterial [39]. Biocompatibility of the implant material determines the success of the material dependent on the implant-tissue/bone interlocking, lack of micromotion, biofouling, and bacterial invasion at the implant site [57, 100, 101]. A few general criteria are listed below.

a) As proteins mediate cell-surface interactions, mimicking the ECM proteins might enhance bone regeneration at a fast pace. ECM, a complex dynamic structure with various proteins (fibrin, collagen, and elastin), hormones, signaling molecules, growth factors, and glycosaminoglycans, becomes challenging to mimic easily [93]. Instead of mimicking the natural ECM, it can be incorporated in biomaterials like an amalgamation of the ECM in synthetic polymers to prepare a scaffold [93]. Surfaces pre-adsorbed with adhesive proteins like fibronectin and collagen exhibit better cell adhesion and spreading [102, 103].

b) Surface microstructure, chemistry, topography, and surface energy of the biomaterials determine the response of the fabricated implant material for response in the biological microenvironment [26]. Nano/microscale surface roughness improves osteoblast adhesion, proliferation, and spreading, along with the deposition of calcium-containing minerals and alkaline phosphatase production [26]. Implant surface and biomacromolecule interactions are also modulated by the grain size and crystal structure of the implant materials [26].

c) Reconstruction and reorganisation of functional tissues are required to recover the damaged bone tissue [75]. Faster growth of cells and tissue on the damaged site is one of the prerequisites for developing the implant materials [104]. The development of biomaterial with surface properties comparable to the diseased/damaged site's tissues/bone amplifies the healing process. In this direction, selecting a biomaterial for implant fabrication with no stress shielding prevents bone degradation/resorption at the site due to osteoclast activity [100].

d) Bone-implant direct interactions occur only in the case of an implant without fibrous tissue growth at the site. Direct interaction leads to the spreading, growth, and differentiation of the osteoblasts on the implant surface, thus assuring and eliminating the biofouling agents from the site.

e) The application of antimicrobial agents on the implant surface eliminates the pathogenic contamination at the site, thus contributing to the success of the implant [105].

2.2.7 Applications

Biomaterials with desirable features are used for a varied number of applications in the biomedical field. This section discusses the applications of different biomaterials in orthopaedic implants and tissue engineering.

2.2.7.1 Orthopaedic implants:

The advancements in surface engineering have enabled us to tune the physical, chemical, surface, and biological properties of implant biomaterials. Bock *et al.* modified the properties of silicon carbide ceramic for orthopaedic implant application. Silicon carbide is unique as it possesses higher fracture toughness, strength, scratch resistance, biocompatibility, and resistance to bacterial adhesion. Changes in the surface composition and properties of silicon carbide were investigated to vary the chemical, thermal, and mechanical treatments. Thermal treatment in air/N_2 reduced the contact angle to 9 ±1°, compared to etched in hydrofluoric acid (HF) (60 ± 13°) and control sample (66 ± 12°). Surface roughness enhanced for the HF etched surface (341 nm) compared to control (336 nm) and decreased for air/N_2 thermal treated surfaces (287-296 nm) [106]. Yazdi *et al.* investigated the effect of the biodegradable magnesium-based ternary alloy (Mg-Zn-Ca) on the adipose-derived behaviour of mesenchymal stem cells (ASCs) for orthopaedic applications. Alloying Mg with Zn and Ca improved the corrosion resistance of alloys compared to pure Mg. The viability and proliferation of the ASCs enhanced with no observed toxic effects of the Zn, Ca, and Mg [107]. To enhance the tissue growth at the implant site, Chakraborty *et al.* utilized a pulsed electro-deposition method for the coating of HAP and calcium hydrogen phosphate on the SS316 surface at different current densities from the diluted calcium phosphate solution [104]. In a study, biphasic calcium phosphate (BCP) film was deposited on bare as well as textured Ti6Al4V specimens by radio frequency (RF) sputtering [108]. The texturing resulted in the enhanced wettability of Ti6Al4V because of increased surface roughness from 94 nm to 1.84 μm. The water contact angle decreased from 89° to 71°. BCP-deposited textured surfaces resulted in better adhesion and proliferation of osteoblast cells compared to bare Ti6Al4V and BCP-deposited bare-Ti6Al4V surfaces. This indicated improved cellular behaviour with increased roughness of surfaces with the same surface chemistry and clear from **Fig. 2.4 [108]**. In another study, BCP and titania (TiO_2) composite films were deposited on Ti-6Al-4V substrates by RF magnetron sputtering[109]. The wettability and bonding strength of composite films were improved with increased TiO_2 contents. Cell adhesion and proliferation significantly improved on coated Ti6Al4V compared to the uncoated surface. In a separate investigation, Pradhan *et al*. investigated the effect of (TiO_2) and Niobium oxide (Nb_2O_5) on the biocompatibility enhancement of Ti6Al4V alloys for orthopaedic implants. The effect of the crystallinity on the surface bioactivity was evaluated by varying the heating temperature. Nb_2O_5 (525 °C) and TiO_2 (500 °C) showed CaP precipitation in the simulated body fluid, which is used as an indicator of bioactivity. Additionally, cell viabilities on both surfaces were above 100 % [110].

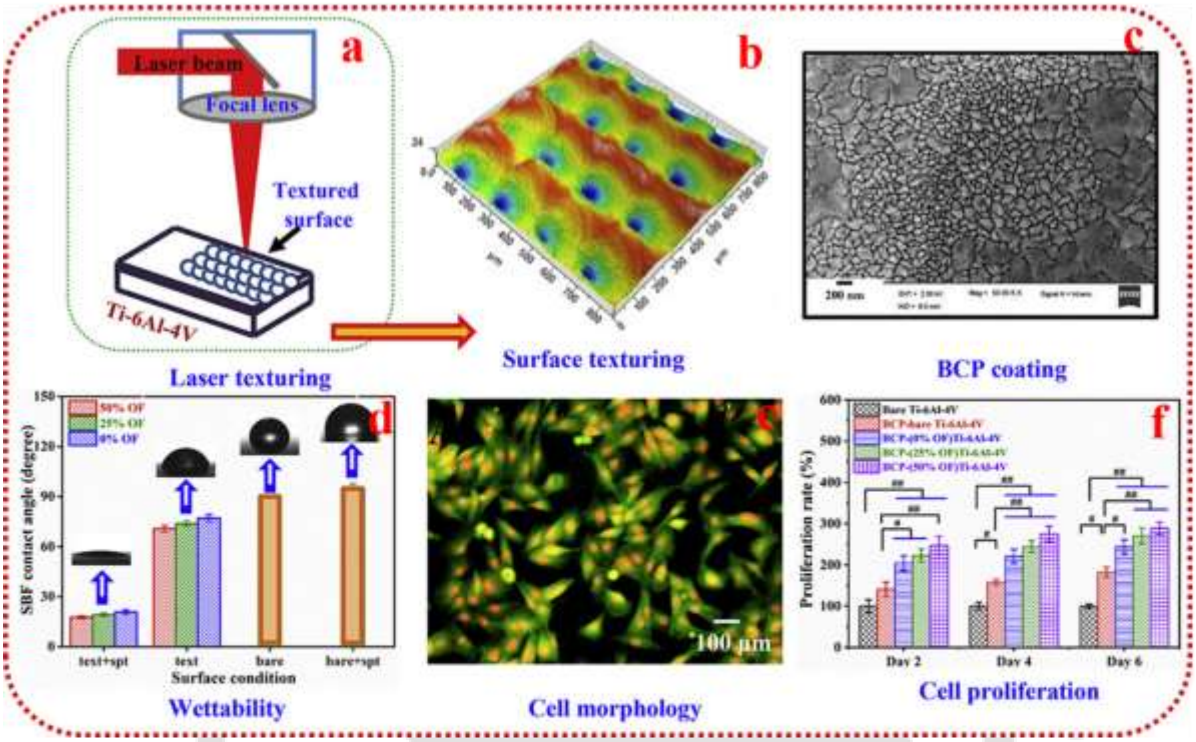

Figure 2.4: Schematic showing the deposition of the calcium phosphate film on the LASER textured surface;(b-c) surface texturing as analyzed using a 2D profilometer and SEM; (d) contact angle measurement performed to determine the surface wettability; (e-f) cell adhesion and proliferation studies (Adapted with permission from Journal of Alloys and Compounds 842 (2020): 155683).

2.2.7.2 Tissue Engineering:

Usually, bone reconstruction is preferred using autogenous bone, but it involves increased operative procedures along with the morbidity of the donor. To address this issue, 3D scaffolds have been prepared for tissue engineering applications. Scaffolds with 3D configuration can be fabricated using electrospinning, phase separation, tomography mediated deposition, and extrusion [75]. Scaffold architecture regulates the cellular behaviour of attachment, migration, proliferation, and differentiation [75].

Adamzyk *et al.* fabricated biocompatible 3D polyetherketoneketone (PEKK) scaffolds. It was observed that human MSCs were successfully differentiated into different cell lineages, such as adipogenic, osteogenic, and chondrogenic, under suitable stimulations. The fabricated scaffold was conducive to human and ovine MSCs, i.e., supporting attachment, growth, and differentiation required for tissue engineering applications [39]. Goncalves *et al.* fabricated a 3D scaffold-based on PCL and starch incorporated with iron oxide magnetic nanoparticles (MNPs) for tissue engineering applications. The effect of MNPs on the tenogenic differentiation capability of the adipose stem cells was investigated, and magnetic driven stimulation was found to influence the stem cell response [111]. The hierarchical structure of the aligned fibers was responsible for the functionality and mechanical properties of the tendon [111]. In a separate study, Gao *et al.* fabricated a novel mussel-inspired nano-HAP using polydopamine as the template and was electrospun with PCL to form a nanofibrous scaffold for bone regeneration applications [75]. This scaffold enhanced the adhesion, proliferation, and spreading of the human mesenchymal stem cells (hMSCs) along with the enhancement of osteogenesis in the hMSCs [75]. In another investigation, Cheng *et al.* fabricated a blood vessel mimicking scaffold of PCL and poly(lactide-co-glycolide) (PLGA) with a multilayered tubular structure. It contained an outer shrinkable PLGA layer and an inner expandable PCL layer for artificial blood vessels. These fabricated scaffolds retained their size/shape during the degradation over months due to the expansion of the inner PCL layer and shrinkage of the outer PLGA layer. Inward shrinkage and outward expansion of the PCL-PLGA components attain equilibrium for layer packaging, resulting in multilayered tube formation, as illustrated in **Fig. 2.5 [112]**.

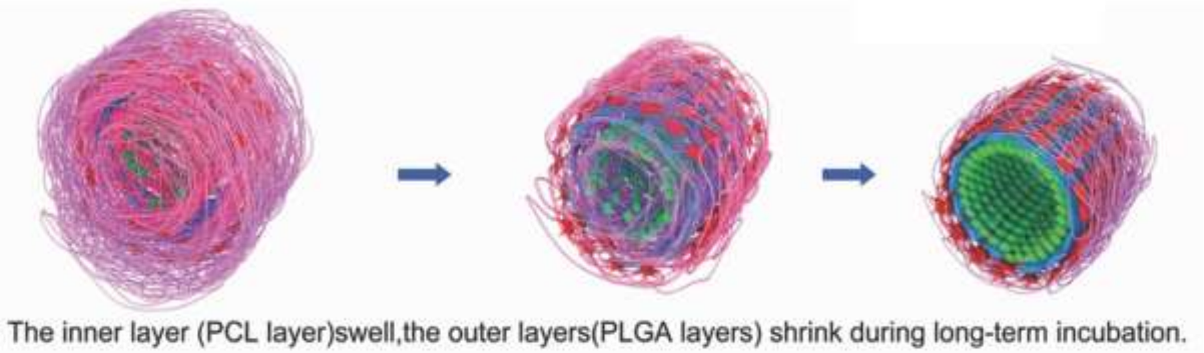

Figure 2.5: Schematic showing the swelling behaviour of the cell-laden multilayered PCL-PLGA tubes, long-term culture results in the shrinking of the outer PLGA layer and swelling of the inner PCL layer (Adapted with permission from Advanced Materials 29.28 (2017): 1700171).

Conventional soft tissue replacement has many drawbacks, including lack of mechanical integrity, fibrous capsular contraction, and resilience. Tissue regeneration can be stimulated using resorbable scaffolds. Further, the optimal degradation rate is a crucial asset for scaffold fabrication as a higher degradation rate minimises the foreign body interactions with the immunological agents. In contrast, a slower degradation rate allows cell infiltration and growth with mechanical support [10]. In a study, Da *et al.* fabricated a 3D scaffold using small intestinal submucosa (SIS) containing bioactive ECM with PU for soft tissue engineering. SIS is an acellular matrix with an intact natural composition that enhances tissue regeneration and differentiation [93]. Geesala *et al.* fabricated a porous scaffold of PEG-PUs with an interpenetrating polymer network for tissue repair enhancement and cell delivery. These fabricated scaffolds prevented the cellular oxidative stress at the injured sites and were highly cytocompatible, thermostable with better porosity, and undergo biodegradation at an acidic pH of 5.8 [99]. In another study, Xu *et al.* fabricated a bioactive/biodegradable scaffold based on reduction sensitive elastomeric PUs to control the scaffold degradation rate according to an application. An antioxidant such as glutathione was incorporated in the scaffold for initialising and controlling the scaffold degradation rate, which was dependent on the disulfide amount in the PUs backbone [10].

In a study, Buyuksungur *et al.* fabricated PCL scaffolds based on fused deposition modeling. They modified them with poly(propylene fumarate) and nano-HAP to control the porosity, mechanical strength, osteoconductivity, and surface wettability [113]. These scaffolds were implanted in rabbits' femurs with and without seeding with rabbit Bone Marrow Stem Cells (BMSC). BMSC seeded scaffolds exhibited improved tissue regeneration after 4 and 8 weeks [113].

2.3 Protein-Biomaterial Interactions

Proteins are composed of amino acid chains. The general structure of amino acid comprises central alpha carbon attached to the amino group, carboxyl group, R group, and hydrogen atoms. At physiological pH, carboxyl and amino groups are charged, and amino acids in a zwitterion form have equal positively and negatively charged groups. Depending on the ionization pH of the side groups, amino acids have a characteristic isoelectric point (pH) at which they exist in zwitterion form (neutral charge). Proteins result from the condensation of water molecules, while amino acids are converted to amino acid residues in the primary protein chain. The primary structure of proteins can assume 20^n combinations. However, proteins assume only certain favourably conformation that can be determined using the Ramachandran plot. Usually, hydrophobic amino acids reside inside the core of the proteins and hydrophilic groups on the surface, thus stabilizing the overall structure, but the reverse occurs in nature. A slight change in the primary structure of a protein can also have severe impacts depending on the change. For example, the substitution of valine for glutamic acid in hemoglobin results in a disease called sickle cell anemia with an altered haemoglobin molecule called Hemoglobin S. This altered form results in blood clogging and restricting blood supply to tissues [114].

Proteins do not exist as a long-extended chain under a physiological environment, but amino acids interact, resulting in the bending, folding, and coiling of the chain to attain a 3D conformation. Secondary structure refers to intrachain interactions of amino acids resulting in a distinctive 3D conformation. Peptide bonds between adjoining amino acid residues have a partial double bond character, so they are rotationally constrained. Bending and coiling occur mainly due to hydrogen bonding between carbonyl groups of one amino acid residue with an amine of another. Secondary structures that are possible are alpha helix, beta sheets, beta turns, and random coils. Each amino acid residue in the alpha helix forms hydrogen bonds with the fourth amino acid residue above and below. Hydrogen bonds are parallel to the axis. Helices may be right-handed or left-handed, but right-handed helices are more stable. In beta sheets/strands, polypeptides exit in an extended chain conformation. Beta sheets are also stabilized by hydrogen bonding between two or more beta strands. In parallel, beta-sheet chains run in the same direction, and in antiparallel structures, chains run in opposite directions. Side chains lie above and below the planes of the beta-sheet, having the appearance of pleated sheets [115].

Tertiary structure is governed by distant section interactions among amino acid residues; mainly interaction of side groups governs the tertiary interactions. Four types of interactions can occur between side groups of amino acid residues, namely covalent disulfide, ionic, hydrogen, and hydrophobic interactions. Disulfide interactions occur between cysteine and methionine residues. Ionic interactions among positively charged and negatively charged amino acids. Hydrogen interactions between polar amino acid residues. Hydrophobic interactions among non-polar amino acids are driven by water hating nature of non-polar amino acid residues [116]. It involves interactions between individual polypeptide chains in a multi-subunit protein. The same interactions are involved in stabilizing the quaternary structure as in the tertiary structure. Multi-subunits may or may not be identical, and the signal subunit is called a monomer, the double is called a dimer, the three is called a trimer, and so on [116].

2.3.1 Importance of conformation

Correct conformation is required for optimum functioning of the protein. Change in conformation or denaturation may result in a permanent change in protein structure, leaving it unsuitable for functioning [117]. Denaturation of protein may occur due to changes in pH, ionic strength, and temperature, which destabilizes the normal conformation of the protein chain [118]. pH can alter the ionization state of the side groups of amino acid residues. Similarly, the introduction of biomaterial in the body may alter the normal conformation of the proteins present due to the binding of proteins onto the implant surface [119].

2.3.1.1 Collagen:

It is the most abundant protein in higher vertebrates, comprising around 25% of total body proteins. Collagen provides a structural framework involving the skin, extracellular matrix, skeleton, and blood vessels. Type I collagen is most abundant in the body, including bone, ligaments, tendons, skin, and others, with about nineteen types of collagen found in the body. The primary structure of collagen involves the motif of Gly-Pro-Hyp-X-Y, where X and Y may be any amino acids, and Hyp is hydroxyproline. Glycine comprises about one-third of the residues, proline about 13%, and hydroxyproline 10%. Collagen exists in a triple helical structure with three alpha chains wrapped around to form the right-handed procollagen superhelix. The presence of glycine helps the triple helical structure to wrap tightly [120].

2.3.1.2 Elastin:

It is an important component of skin, ligaments, and skin, in which elasticity is required. Elastin is rich in proline and glycine; unlike collagen, proline is not hydroxylated. Hydrophobic amino acids comprise about 50% and alternating segments of hydrophobic amino acids rich in lysine and alanine. Elastin is secreted by cells in the form of tropoelastin that assemble into filaments, fibrils, and sheets of fibers having an unordered coiled structure [121].

2.3.1.3 Fibronectin:

It is the main component of the extracellular matrix (ECM) and plays a crucial role in organizing the ECM and helping cells to attach to it. It comprises two, joined by two disulfide bonds near the carboxyl termini. Fibronectin comprises segments of 40-90 amino acids long and comprises beta sheets and strands. It has a modular structure composed of three types of structures, type I, II, and III, which are serially repeated with linker peptides between these segments. Fibronectin contains domains that have an affinity for different molecules, such as collagen, heparin, and cell surface receptors. It typically contains the RGD motifs that bind to cell surface receptors, resulting in cell adhesion [122].

2.3.1.4 Fibrinogen:

It has a complex structure and is a large plasma protein that helps clot blood. Fibrinogen typically comprises two identical subunits, consisting of three different polypeptide subunits denoted by A-alpha, B-beta, and gamma. Calcium ions are essential for the normal functioning of fibrinogens, which interact with protein via high-binding and low-binding sites. Fibrinogen also contains two RGD motifs for binding with the cells. Cells involved in tissue repair and blood clotting bind to the fibrinogen. Fibronectin can also bind to fibrinogen via enzyme catalysed reaction. Fibrinogen also contains sites for proteolytic cleavage, whose products play a crucial role in inflammation and clotting [123, 124].

2.3.2 Protein surface interactions

The protein surface plays a crucial role in determining the success of the implant by causing desired favourable interactions between the tissue-implant interface. Adhered proteins may regenerate the immune response via complement activation, blood clotting, and bacterial and cell adhesion that might result in bio-fouling. The nature and type of proteins adhering to the implant surface may influence biomaterial surface properties and dissolution. Protein, as well as biomaterial surface properties, influence interfacial properties and behaviour, which need to be taken into consideration for designing successful implants [125].

2.3.2.1 Protein properties:

The primary structure of protein influences the protein-surface interactions. The larger the protein, the more strongly it will bind to the surface due to more contact points between the protein and implant surface, but this is not always the case. For example, albumin (67 kDa) forms about 77 contact points with a silica surface, and fibrinogen (340 kDa) forms nearly 703 contacts points with the implant surface, while haemoglobin (65 kDa) forms greater contact points compared to much larger fibrinogen [126]. Polar amino acids are usually present on the surface of the proteins that interact with the surface and make contact points. Protein adsorption is driven by charged species present on the surface, but it is not the sole determinant [127]. Proteins show enhanced surface activity near its isoelectric point. Proteins do not interact with the surface in isolation [128]. Adsorption of proteins to the surface causes alterations in the protein structure and unfolding that enhances adsorption strength. The higher the protein unfolding rate, the faster the adsorption, and more contact points will be made between the protein and the surface. Intramolecular/disulfide bonds among the protein subunits affect the adsorption. The amphipathic nature of proteins also affects adsorption. Usually, hydrophilic groups are present on the exterior of protein. Some proteins contain hydrophobic groups on the exterior that interact more strongly due to the contribution of hydrophobic interactions [129, 130].

2.3.2.2 Surface properties:

Electrical, geometrical, and chemical properties contribute to surface properties. Implant surfaces having a protrusion, pores, or grooves have more surface area exposed for protein adsorption, varying the topographical features of the implant surface may cause variable protein adsorption. The surface contains various functional groups that might influence protein adsorption. Passivated surfaces expose oxygen ions for interactions with proteins on metallic surfaces. A wide range of functional groups such as carbonyl, aromatic, carboxyl, amine, and octyl on the polymeric surfaces have different affinities for biomolecules with hydrophobic surface binding more protein due to hydrophobic interactions [131-133].

At the microscopic level, the implant surface might not be homogeneous, with various domains or patches of different functionality. For example, titanium implants contain two different phases, alpha and beta phases, that behave differently, as well as the grain boundaries. Different domains have different functional groups so that, an affinity may vary from domain to domain for proteins. Apart from the functional groups present on the surface, electrolyte solution or body fluids may affect the surface potential of the implants, resulting in adsorption of counterions on the surface and, thus, protein adsorption affected [133].

2.3.2.3 Conformational changes:

Proteins are flexible, having coils, bends, or folds to assume a particular conformation that might be affected by a change in pH, ionic strength, or temperature. Conformation of the protein alters on adsorption to the implant surface. Two mechanisms have been proposed for conformational changes occurring during protein-implant interactions: time-dependent molecular spreading and change in bulk solution concentrations. In time-dependent molecular spreading, exterior surface amino acids may interact with the surface and form minimal contact points. With the passage of time, protein unfolding occurs, resulting in exposure of hydrophobic amino acids and an increase in contact points. A time-dependent increase in contact points occurs. In a change in bulk concentration mechanism, minimal contact points form when the solution concentration is high, and contact points increase as the solution concentration is lowered as the large surface area is available for protein adsorption [134, 135].

2.3.2.4 Adsorption:

Adsorption involves adhering molecules, such as biomolecules, onto the surface of the implant. Protein-surface interactions result in a 1000 times higher concentration of the protein at the surface compared to the bulk. Accumulation of proteins at the surface plays a crucial role in determining the success of the implant. Adsorption depends on the availability of the proteins for adsorption as well as molecular size, concentration, velocity and adhesion strength that determines the arrival of protein molecules on the surface. Biomolecules arrive at the surface by diffusion, thermal convection, and coupled transport involving convection, diffusion, and flow. Moreover, they adsorb on the surface in different orientations depending on the space availability due to the heterogeneity of both proteins as well as the surface to minimize repulsive interactions of previously bound proteins [129, 136-138].

2.3.2.5 Multicomponent solutions:

Various bloodstream proteins compete for interaction on the implant surface when introducing an implant into the body. Smaller and fast-moving proteins will adhere to the surface until a pseudo-steady state is reached. Various factors contribute to the type of proteins adsorbing onto the surface, such as size, conformation, surface charge, and concentration. Initially, adsorbed proteins will be replaced with bulky and tightly adsorbed proteins. At the interface, there will be dynamic competition between various proteins present in the solution for adsorption onto the implant surface. With the passage of time, these proteins will also be replaced with other proteins having a higher affinity for the surface but with a slower arrival rate due to large size and low concentrations until permanent protein adsorption occurs. New proteins can only adsorb to the surface after detachment of adsorbed proteins. This dynamic series of adsorption and replacement processes until permanent protein adsorption occurs is termed the Vroman effect [139-141].

2.3.2.6 Desorption:

Desorption is just the reverse of the adsorption; adsorbed biomolecules detach from the surface and return to the bulk. Desorption requires all the contact points to be broken simultaneously. Desorption of protein is an irreversible process naturally due to the requirement for the simultaneous dissociation of all interactions. Proteins adsorbed can only be replaced by other proteins from the surface. Changes in interfacial environments, such as lowered pH, use of detergents, and increased ionic strength, may result in desorption [142, 143].

2.4 Protein adsorption enhancement strategies

Titanium and alloys can be modified to enhance protein adsorption using various techniques. Protein adsorption can be enhanced by increasing the surface roughness and charge density

[144] and eradicating the passive oxide layer, leading to enhanced bioactivity. The formation of silane SAMs and other chemical moieties alters the surface chemistry favouring better adsorption [102, 145]. Various surface coatings have been discussed throughout this section to highlight the interactions with various serum and ECM proteins. Protein adsorption onto various tuned surfaces.

2.4.1 Surface modification

To enhance the desirable implant properties, surface treatment can be carried out. The primary purpose of surface treatment is to modify the outermost layer of an implant by some functional groups to improve its surface properties, wettability, cell adhesion, osseointegration, biocompatibility, and other properties. Surface modification is required to tune the surface to influence the protein and cellular response, as mentioned in **Table 2.2**. Surface modification can be carried out to enhance the success rate and biocompatibility of the implant surface and reduce the side effects generated by the implant surfaces, such as leachates or debris, into the physiological environment, leading to the formation of the fibrous capsules at the site. Various modification strategies have been reported in the scientific literature, such as physical, chemical, and biological modifications [146-153].

The physical approach deals with manipulating the physical properties such as surface roughness parameters, surface energy, hydrophobicity, and porosity of the surface. This route includes methodologies such as laser cladding, pulsed laser deposition, plasma treatment, corona discharge, oxygen plasma, electron beam treatment, and UV or gamma irradiation [154-156]. The biological route has also been mentioned in great detail in the scientific literature, which includes biomacromolecules such as nucleic acids, protein, carbohydrates, or even enzymes, cells, or part thereof, for the physical adsorption on the surface via non-covalent interactions [149, 152]. Other means of tuning the surface properties suffer from certain disadvantages, such as poor stability and non-uniform modification generation of wastes for the modification, which is the case with physical modification. Both physical and biological methods suffer from drawbacks, which are addressed by chemical modification methods to an extent. Chemical methods involve modifying the surface functional groups or aiding further fabrication to enhance the stability, biocompatibility, and other features of the implant surface. These chemical modifications can be carried out by different approaches, such as layer-by-layer fabrication and self-assembled monolayer formation. Various chemicals have been utilised for chemical modification, such as thiols, silanes, siloxanes, thiourea, and polymers. Titanium (Ti) and its alloys are utilised for various biomedical applications such as dental, orthopaedic, or other implants. For the success and long-term survival of the implant, various factors play a key factor, such as the formation of the seal between peri-implant and soft tissues [157], osseointegration to assure the biocompatibility [158], corrosion resistance [159], cell adhesion and proliferation promotion, hydroxyapatite nucleation in case of bone-implant along with other factors [159]. Other chemical modifications can also be utilised for tuning the surface properties, such as the incorporation of inorganic calcium polyphosphates or combining physical modification with chemical modification [146, 160].

Table 1.2: Modification techniques for titanium

Method	Modification	Features	Objective	Ref.
Physical	Plasma treatment	Corrosion-resistant surface	Enhancing electrochemical features of pure Ti for dental implants	[161]
		Oxide layer formation	Enhancement and exploration of the effect of the plasma treatment on the biocompatibility of the surface	[162]
		Polymer deposition	Regulation of the surface chemistry, roughness, polymer release, and stability	[163]
	3D printing	Titanium microspheres	Construction of the 3D surface topography for studying the biocompatibility on MC3T3-E1 cell line	[164]
		Micro/nanostructured, HAP coating	Investigation of protein adsorption enhancement to determine the osseointegration properties	[165]
	Sputtering	BCP coating on titanium surface	Investigating the bioactivity and protein adsorption behaviour of BCP sputtered surfaces.	[42]
	Electrochemical anodization	TiO_2 nanotubes	To accelerate the bone integration process and investigate protein adsorption behaviour	[166]
			To screen the nanotubes dimensions optimal for the protein adsorption and cellular response among the nanotubes gradient generated	[167]
			Investigation of biocompatibility of the fabricated surface via protein adsorption and pre-osteoblast cell studies	[168]
		Silicate surface coating	To maintain the constant surface energy for long-term storage using silicate coating	[169]
	Hydrothermal treatment	HAP/carbonated HAP coating	In-vitro studies were carried out to investigate the effect of carbonated HAP on the bio-functionality of the material.	[170]
		Fe incorporated micro/nano hierarchy	To get insights into the effect of the Fe-fabricated surface on protein adsorption and biocompatibility	[171]
		Si-doped micro/nano topography	Investigation of the Si incorporated structure on the biocompatibility	[172]
		TiO_2 coating	To assess the role of the surface properties of the TiO_2 anatase on protein adsorption	[173]
	UV treatment	Hydrophilic surface	Modulation of the surface to enhance the surface properties	[174]

	Micro arc oxidation		Cu incorporated nano/micro topographical surface	To monitor the release of the Cu from the surface in terms of bio-activity	[175]
	LASER treatment		Micro-textured surface	To investigate the initial osseointegration in terms of protein adsorption	[176]
				Role of LASER sintered surfaces in osteogenic differentiation and protein adsorption	[177]
				To explore the bacterial resistance of LASER textured surfaces along with cytotoxicity and protein adsorption	[105]
	Electrospinning		Collagen-PCL-collagen coating	Electrospun polymer matrix for enhancing the surface mechanical properties	[178]
	Electrodeposition		Phospholipid coating	Enhancement of blood compatibility features	[179]
Chemical	Silanization		Chitosan/(HAP) biocomposite	To enhance the suitability for biomedical applications	[180]
			Silane moieties for titanium modification	Investigating the effect of silane moieties on protein adsorption and fibroblast adhesion	[181]
			Attachment of streptavidin to biotinylated surface	Inhibition of the non-specific protein adsorption to the surface	[182]
	Immobilization	Dip coating	Covalent immobilization of PMPC coatings	Fabrication of anti-fouling surface coatings	[183]
	Crosslinking		pH-controlled metal-phenolic network fabrication	To investigate the modulation of the bioactive metal ions from the surface along with protein adsorption studies	[184]
	Attachment		DLDH^{RGD} attachment	Fabrication of bioactive coating to enhance implant-cell interactions	[185]
	Acid/alkali treatment		Sodium bicarbonate treated surface	Investigation of the surface wettability on the protein adsorption	[186]
	Siloxane functionalization		Siloxane-gelatin coated titanium	To assess the adsorption behaviour of plasma proteins	[187]

BCP: biphasic calcium phosphate; PMPC: poly(2-methacryloyloxyethyl phosphorylcholine); DLDH: dihydrolipoamide dehydrogenase;

2.4.2 Physical modification of titanium and alloys

This section deals with the effect of the various nano/micro-scale surface fabrication on the wettability, surface charge, surface energy, and bioactivity of the surface. Pore size, biomimetic bone features incorporation, and modulation of the surface elements will also be discussed in relation to their effect on protein adsorption. Various modification strategies have been depicted in **Fig. 2.6**. Physical treatment on the titanium surface may lead to the tuning of the surface properties.

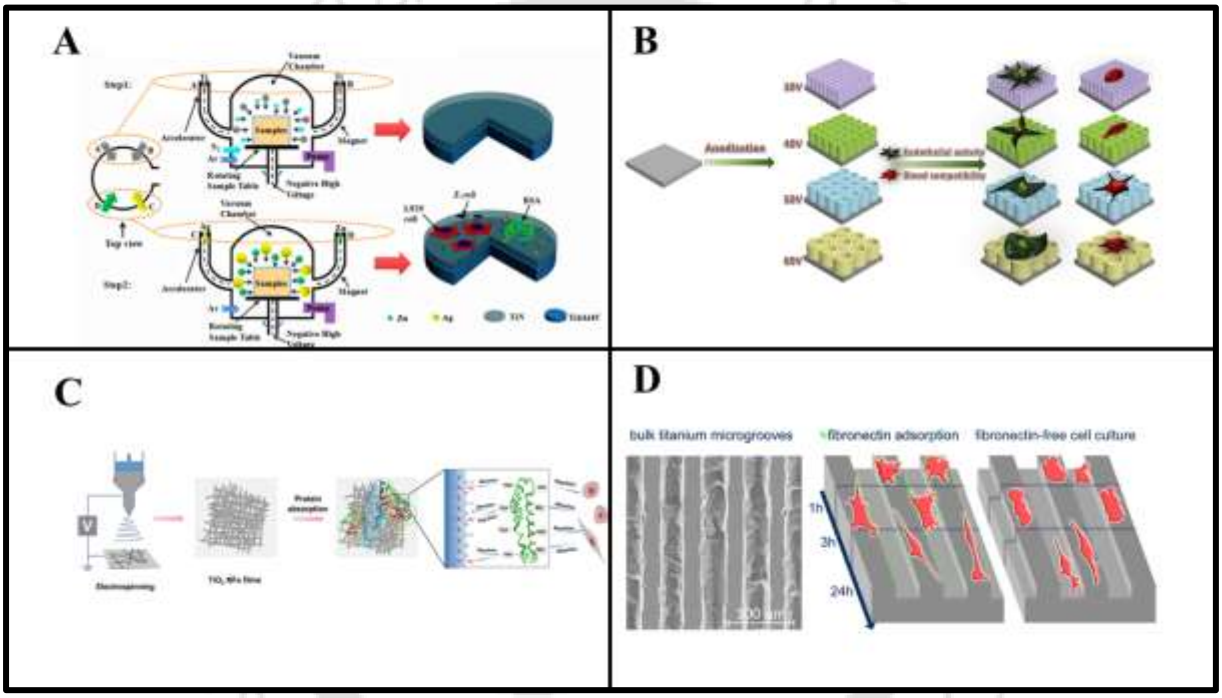

Figure 2.6: Various physical modification methods, (A) plasma treatment, (B) anodization, (C) electrospinning and (D) lithography (Adapted with permission from ACS Biomaterials Science & Engineering 5.7 (2019): 3303-3310; Colloids and Surfaces B: Biointerfaces 184 (2019): 110521; Colloids and Surfaces B: Biointerfaces 185 (2020): 110604; ACS Applied Bio Materials 2.3 (2019): 1066-1077).

2.4.2.1 Crystallinity and surface topography modulation:

Surface geometry and porosity have a prominent effect on the adsorption behaviour of proteins. Along with nano-scale topography, the pore size of the surface also affects protein adsorption. Stefano et al. utilized Diffuse reflectance infrared Fourier transform spectroscopy (DRIFT) to determine the effect of pore size (8 and 17 nm) and drying time on the horse heart myoglobin adsorption onto the mesoporous TiO_2 [188]. Changan et al. fabricated mesoporous TiO_2 with varied geometric structures and investigated the effect of ionic strength and geometry on protein adsorption behaviour. Controlled calcination temperatures (300, 500, 600, and 700 °C) were used to fabricate the mesoporous TiO_2 from the precursor hydrated titanate [189].

The crystallinity of the titanium also affects the protein adsorption trend. Keeping this in mind, Dan et al. devised a novel method for the creation of nano-scale anatase onto micro-arc-oxidized (MAO) titanium surface using a microwave-assisted hydrothermal process (MW). Calcium and phosphorous ions were doped on the surface using calcium hydroxide and ammonium dihydrogen phosphate. In this study, protein adsorption was linked to the surface potential and nanoscale surface patterns [190]. Other crystal phases of titanium may also be effective apart from anatase. So, Marcela et al. investigated the effect of variable crystalline titanium nanotubes array on adhesion and proliferation of adipose-derived stem cells by carrying out electrochemical anodization at room temperature for 6 hr at 60V. Variations in the surface topography (nanotube arrays) enhanced the surface properties compared to the blank Ti. The best result at 630 °C was observed due to the fact that it contained both anatase and rutile crystal phases in the structure [191].

The optimized pore size of the biomimetic nanotubes ~~is~~ crucial for protein adsorption in correct orientation and conformation. So, Zhihao et al. synthesized TiO_2 nanotube arrays in-situ using anodic oxidation on the titanium surfaces with varying diameters (30-90 nm) and further annealed shown in **Fig. 2.7**. Titanium nanotubes anodized at 30V followed by annealing showed the highest BSA adsorption (~604 $\mu g/cm^2$) and least fibrinogen adsorption (~64 $\mu g/cm^2$)[192]. Behera et al. fabricated a functionalized HAP coating from fish scales onto Ti6Al4V alloy via the LASER cladding method. Pure HAP and functionally graded TiO_2-HAP material (FGM) were cladded onto the Ti6Al4V alloy surface [193].

Indian Institute of Technology Guwahati

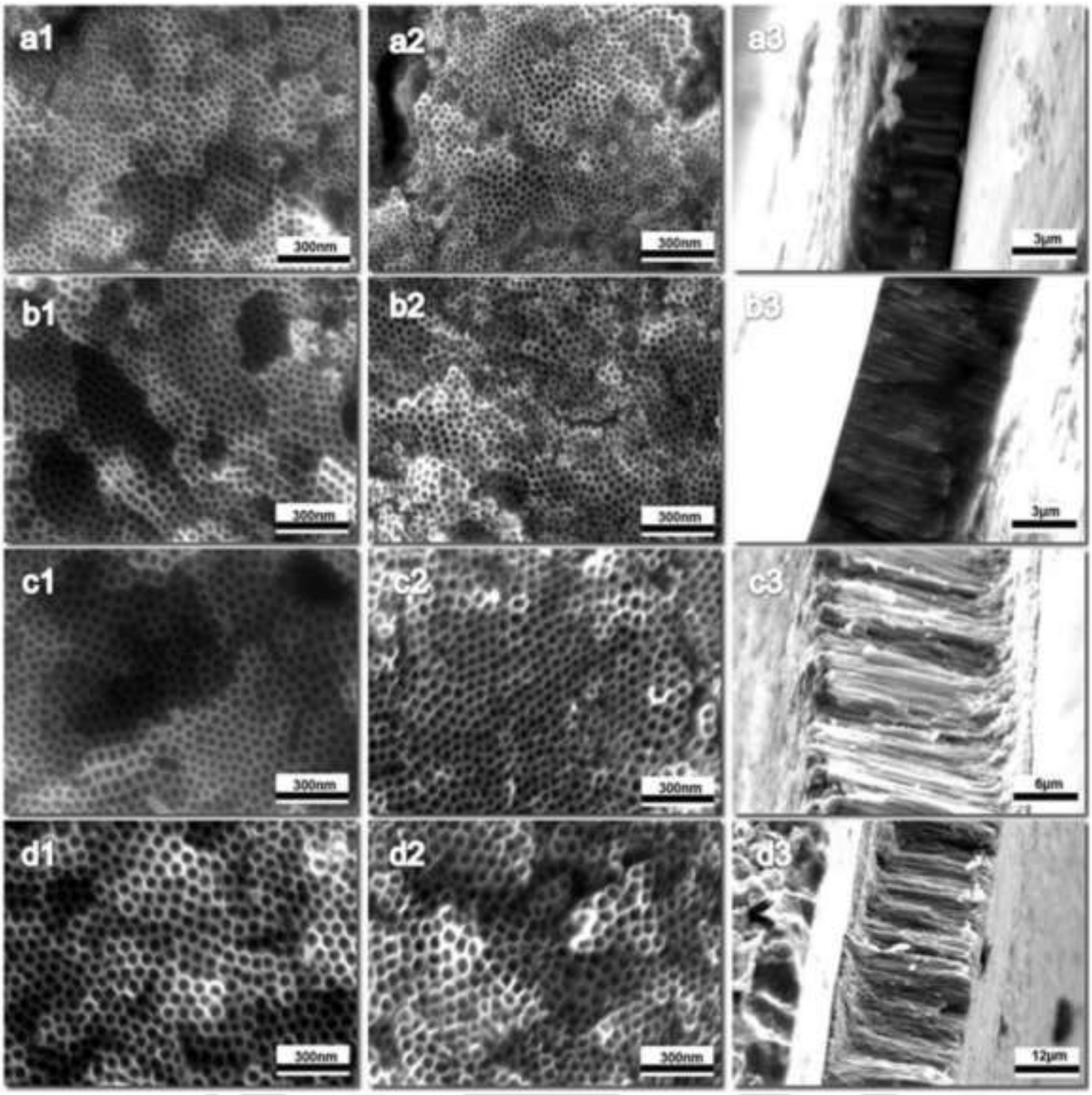

Figure 2.7: SEM images showing nanotube fabrication on titanium surface (Adapted with permission from Colloids and Surfaces B: Biointerfaces 184 (2019): 110521).

2.4.2.2 Metal/metal oxide incorporation:

Titanium suffers from poor wear resistance that may lead to the leaching of toxic aluminum and vanadium ions in the microenvironment. Doping titanium with suitable metal may impart wear resistance. Xiangyu et al. have used this strategy to investigate the effect of nanostructured Zr and ZrO_2 layers alloyed Ti6Al4V on protein adsorption and osteoblast cell behaviour. It was observed that the higher the roughness and more complex the surface microstructure, the better the protein adsorption [194]. The tribological property of titanium and alloy is a great concern that has been addressed. Majumdar et al. carried out boron addition to β type Ti-13Zr-13Nb (TZN) alloy to form Ti-13Zr-13Nb-0.5B (TZNB) and studied the protein adsorption behaviour, cell morphology, and proliferation [195]. Claudia et al. fabricated both hydrophilic and hydrophobic surfaces for the protein adsorption study, and fibrinogen adsorption was qualitatively determined by using fluorescently labeled protein [196]. Vanadium leachate from the titanium surface causes toxicity, so Li et al. deposited the surface of Ti6Al4V with titanium nitride to eradicate the toxic effect of vanadium present in the alloy using the sputtering technique [197]. The formation of TiO_2 nanotube layers in situ can also modulate the surface properties. A study by Xuejiao et al. addressed the lack of osseointegration between implant-tissues arising due to the biological inertness of the implant surface [198].

2.4.3 Physical treatment

Various physical treatments affect the adsorption behaviour of the protein on the surface. Sung et al. evaluated the effect of UV and non-thermal atmospheric pressure plasma (NTP) treatment on the bioactivity of the surfaces. Formation of the nano-structures while storage and reduced hydrocarbon contamination resulted in better protein adsorption[199]. UV functionalization may affect the hydrophilicity of the surface, making it more hydrophilic. Caroline et al. investigated the effect of UV photo-functionalization on the activity of pure titanium discs [200]. Fuminori et al. also investigated the activity of photo-functionalized (UV-treated) titanium surfaces [201]. Miryam et al. used sand-blasted and acid-etched Ti surfaces for the adsorption of histatin 5, alpha-amylase, and cystatin S for the reduction of colonization oral bacterial species. Surface roughness and wettability were modulated to enhance the efficacy. Adsorption studies were carried out for 2 hours on the salivary protein [202]. Variation in surface wettability may result in varied protein adsorption behaviour. Andrea et al. utilized a micro-rough Ti surface and enhanced the hydrophilicity by thermal treatment. Sand-blasted and acid-etched samples showed the highest BSA (~14.1 µg/ml) and human fibronectin adsorption (~13.9 µg/ml) due to changes in the surface chemistry upon treatment [203].

2.4.4 Electrospinning/3D printing/lithography

Chao et al. fabricated a nanoporous structure on Titanium (Ti) surface using the acid-alkali treatment in an autoclave at 80 °C for 24 hours, followed by drying at 70 °C for 2 hours and sintering at 450 °C for 2 hours to form an anatase film onto the surface. Surface topography, along with surface roughness, had an impact on the protein adsorption trend of BSA [204]. Nano/microscale topography affects the wettability/surface energy, which changes the protein adsorption and cell adhesion behaviour of the surface. Astrid et al. investigated the effect of the micro-grooved titanium surface on the protein adsorption and cell adhesion behaviour with 27-35 µm wide and 15-19 µm deep micro-grooves. The adsorption phenomenon observed on the edges of micro-grooves occurred due to electrostatic interactions on the edges of the ridge, as shown in **Fig. 2.8 [205]**.

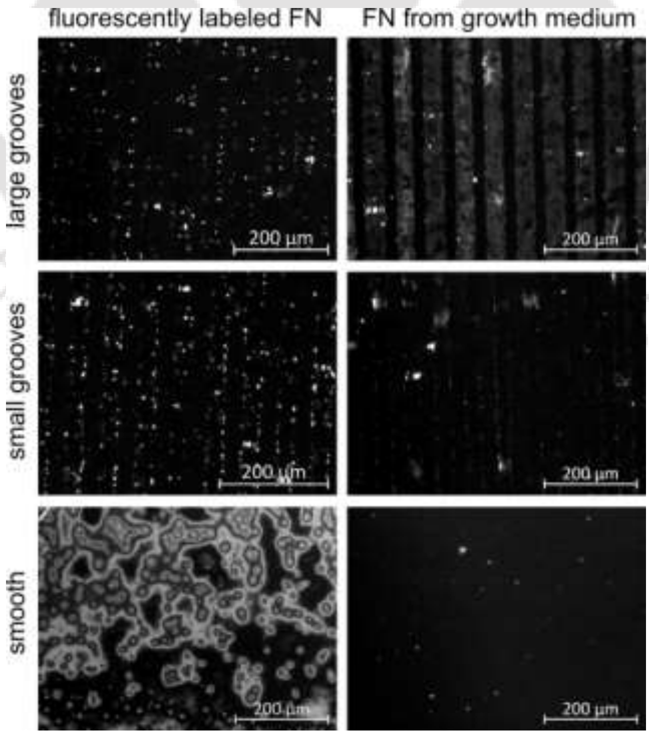

Figure 2.8: Fibronectin adsorption on the micro-grooved surface (Adapted with permission from ACS Applied Bio Materials 2.3 (2019): 1066-1077).

Zhao et al. electrospun structures of TiO_2 nanofibers (NFs) such as anatase, anatase with beads, anatase-rutile and rutile nanofibers onto pure titanium at 18kV potential showed that protein conformation and adsorption pattern were dependent on the structure of the nanofibers[206]. The creation of a 3D scaffold might mimic the normal physiological surroundings, leading to better protein adsorption. So, Nicole et al. utilized the commercially available Hive interbody fusion scaffolds based on Ti6Al4V. 3D printing technique known as Direct metal LASER sintering was used for the synthesis [207]. 3D-printed scaffolds provide higher modulation capability. So, Jia et al. utilized 3D printing with metallic powder to make a fully porous 3D titanium scaffold onto which nano-silver encapsulated micro/nano-structured titanate layers were grown via hydrothermal treatment. Electron beam melting (EBM) was used to selectively melt the Ti6Al4V powder to fabricate the porous hexagonal structures with interconnected networks [208].

Indian Institute of Technology Guwahati

2.4.5 Chemical modification of titanium and alloys

This section deals with the incorporation of various elements into the surface of various metals and alloys. All these issues have been addressed in detail. **Fig. 2.9** summarizes the various chemical modification strategies.

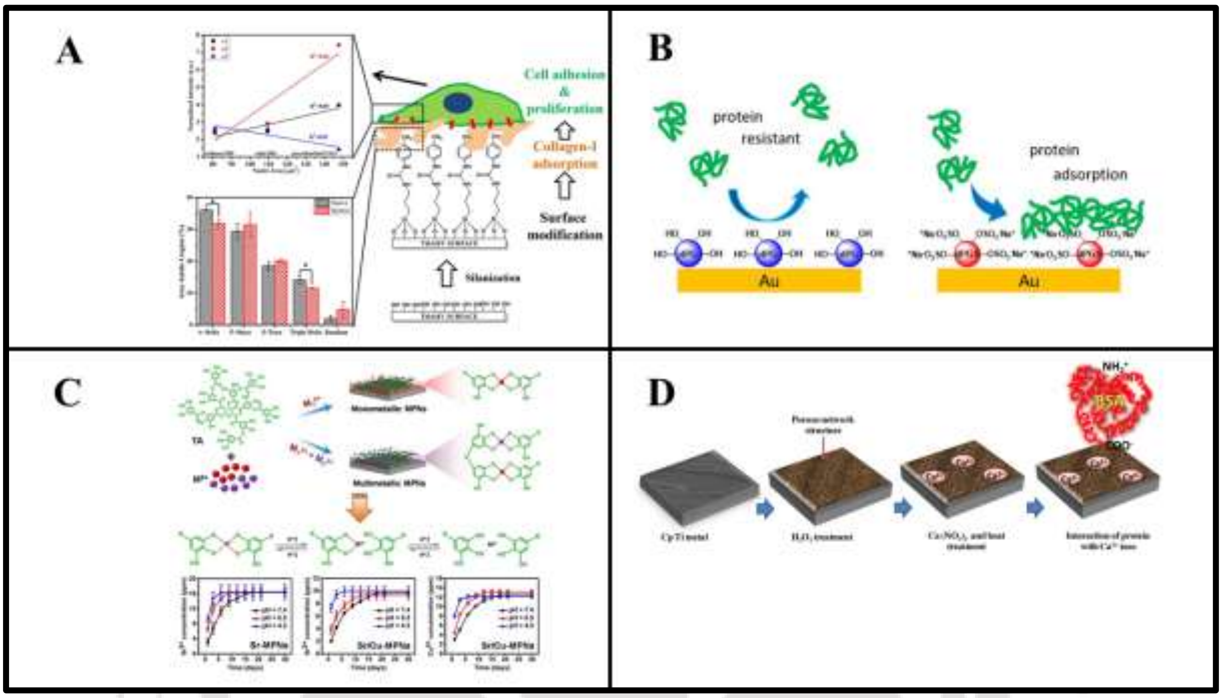

Figure 2.9: Various chemical modification methods, (A) silanization, (B) functionalized SAMs, (C) crosslinking, and (D) adsorption on the chemically treated surface (Adapted with permission from Applied Surface Science 505 (2020): 144611; Langmuir 34.35 (2018): 10302-10308; Applied Surface Science 511 (2020): 145569; Colloids and Surfaces B: Biointerfaces 143 (2016): 213-223).

2.4.5.1 Metal/metal oxide incorporation:

The bioinert TiO_2 layer on titanium and alloys need to be addressed as it inhibits the favourable interactions of the implants with the physiological microenvironment. Nan et al. addressed this issue using phosphorylated Ti coatings with nano/micro hierarchical structures[209]. This strategy would be more effective in mimicking the bone structure with the incorporation of various nano-scale morphologies to provide a 3D surface for effective protein adsorption. So, the fabrication of micro/nano-scaled hierarchical hybrids containing Ti oxide and Ti phosphate to synthesize different samples with varied morphologies can be utilized, as clear from **Fig. 2.10 [210]**.

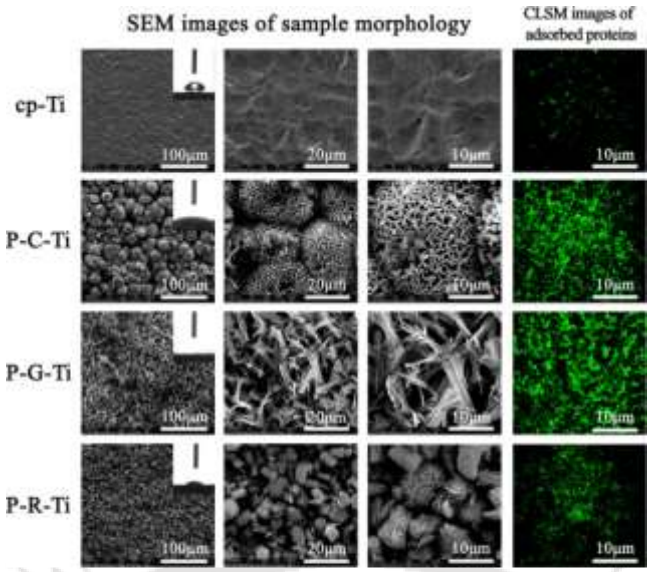

Figure 2.10: *Surface morphology of fabricated surfaces* (Adapted with permission from ACS Nano 12.8 (2018): 7883-7891).

In another study, Park et al. modified the titanium surfaces via micro-, nano-, or hybrid micro/nanoscale topography and carried out a comparative analysis on protein adsorption. High-density nano-rods aided by micro perturbations on mn-Ti surfaces favoured the highest adsorption of fibrinogen and fibronectin [211]. Incorporation of readily available metal and metal oxides onto the surface might address the disadvantages connected with titanium. Esaitamil et al. generated hydrogen titanate by modification of the pure titanium surface with hydrogen peroxide, which further underwent heat treatment, leading to the incorporation of the magnesium, calcium, and strontium ions. Ca incorporation showed the highest BSA adsorption because it has calcium-binding sites in its imidazole rings [212]. Strontium is known to stimulate the osteoblast maturation and inhibition of osteoclast formation. Strontium incorporation can be a potential solution for enhancing the biocompatibility of the implant surfaces. In a study, Romero et al. coated the silica-hybrid sol-gel network doped with various concentrations of strontium chloride onto titanium surfaces [213]. These studies dealt with the incorporation of strontium in the surface. Surface charge of the surface is also a vital asset for protein adsorption. Keigo et al. investigated the role of the electrical charge on the titanium surface on protein adsorption [214].

2.4.5.2 Titanium nanotubes/nanoparticles fabrication:

Nanoparticles also actively interact with proteins. Keeping in mind the ease of NPs synthesis, they might help know the protein behaviour in a broader scenario. In this direction, Izaac et al. studied the interaction of titanium oxide nanoparticles (TiO_2 NPs) with proteins, especially adsorption studies using ATR-FTIR and two-dimensional correlation spectroscopy (MW2D), as shown in **Fig. 2.11**. Temperature-induced structural changes observed for TiO_2 NPs-proteins were dependent on the initial interaction of proteins with the nanoparticle surface [215]. In the physiological microenvironment, phosphate ions co-adsorb onto the surface of NPs/implants along with various proteins. Zhenzhu et al. quantified the interactions of the TiO_2 NPs with BSA at different pH conditions, viz. 7.4, 4.5, and 2 to stimulate the pH of the blood, lungs, and stomach, respectively [216]. Protein adsorption varies from surface to surface, so investigation of protein adsorption on different surfaces might give an in-depth insight about the adsorption. Helena et al. investigated the adsorption behaviour of BSA, fibronectin, and collagen-I sequentially and in a mixture onto various implant surfaces [217].

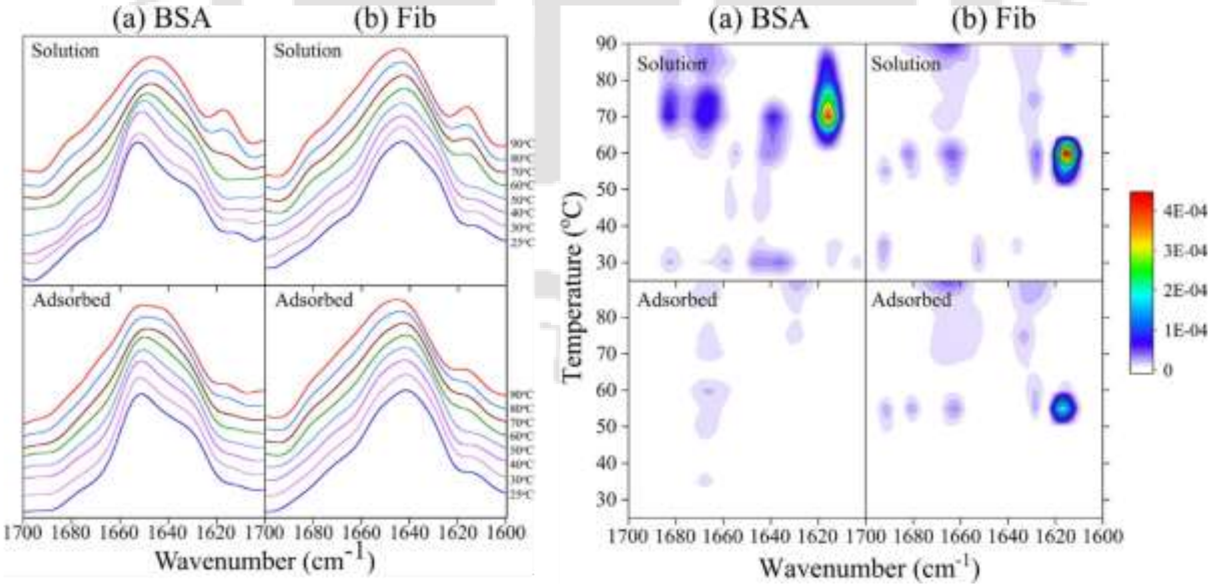

Figure 2.11: FTIR spectra and 2D correlation map (Adapted with permission from Polyhedron 171 (2019): 147-154).

2.4.5.3 Anti-fouling fabrication:

Non-specific protein adsorption is not suitable for the fate of the titanium and alloy-based implants. Non-specific adsorption attracts the inflammatory and coagulation cascade proteins, leading to biofouling. To address this, in-situ nanotubes can be easily fabricated with anti-fouling agents. To carry it forward, Roberta et al. studied the interaction of blood plasma proteins with superhemophobic titania nanotubes. Surface nanotube (NT) formation was carried out using an anodization process followed by modification with two different silane moieties, (heptadecafluoro-1,1,2,2-tetrahydrodecyl) trichlorosilane [FL] and 2-(methoxy(polyethyleneoxy) propyl)trimethoxysilane [-PEG] [218]. Apart from the nanotube-based approach, various biomimetic agents were utilized. In a study by Stobener et al., dendritic polyglycerol sulfate (dPGS) with thiotic acid functionality was coupled on the surface of gold chips and used as the low-fouling agent [219]. Fabrication of responsive anti-fouling coating is a desirable feature to be incorporated. Chun et al. fabricated a zwitterionic catecholic assembly of anti-fouling sulfobetaine and photocleavable o-nitrophenyl moiety to generate sulfobetaine nitrodopamine (mussel inspired) on TiO_2 substrate. The fabrication strategy showed lesser protein adsorption, exhibiting excellent anti-fouling properties, and showed a potential to be used as a biocompatible surface coating [220].

Self-assembly mediated fabrication is one of the most convenient ways for uniform layer formation throughout the surface. So Miku et al. fabricated SAMs onto titanium alloy using poly (ethylene glycol) methacrylate phosphate (Phosmer PE) onto which carboxymethyl betaine (zwitterionic monomer) [CMB] was copolymerized via methacryloyl group as a linker [221]. Combining the anti-fouling feature with other anti-bacterial or cell adhesive properties might enhance the fabrication efficacy. Li et al. utilized a combined fabrication approach based on an electrochemical process to synthesize the composite of TiO_2-SiO_2-polydopamine onto Ti6Al4V with polydopamine as the crosslinking agent, as shown in **Fig. 2.12 [222]**. In the same direction of fabrication, Mireia et al. utilized a trifunctional anti-fouling coating of polyethylene glycol (PEG) using electrodeposition followed by binding of the dual-functional platform containing RGD and LF1-11peptide (lactoferrin peptide) with bactericidal and cell-adhesive properties, respectively onto the titanium surface. Less protein adsorption implies that protein-mediated adhesion of the bacteria to the surface is inhibited, thus blocking bacterial interactions to the surface [223].

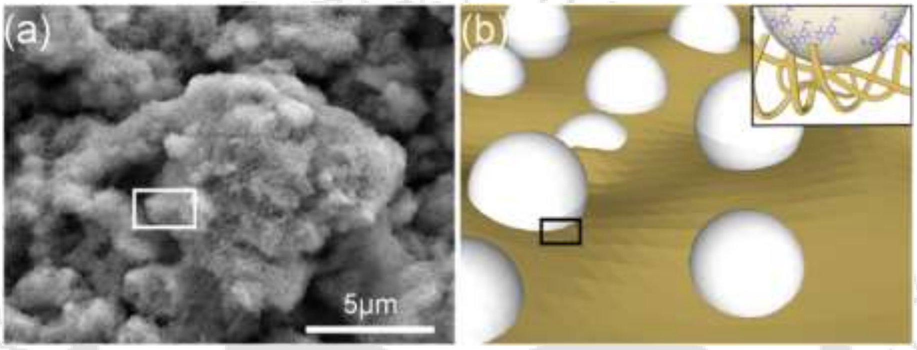

Figure 2.12: Morphology and computer-aided diagram of the composite material (Adapted with permission from Materials Science and Engineering: C 76 (2017): 1041-1047).

2.4.5.4 Surface modification:

Chirality/orientation of the adsorbed protein/amino acid is a requisite for effective activity and osseointegration. Yonghong et al. incorporated selenocysteine in various chirality on the TiO_2 surface for the protein adsorption studies. Layers of dopamine were coated on the silicon wafers with TiO_2 deposition via the immersion method for linking the selenocysteine in different chirality on the surface [224]. Varying hydrophilicity may vary the protein adsorption behaviour of the surface. Keeping this into consideration, Fabre et al. carried-out a protein adsorption investigation on a titanium surface using bisphosphonate with terminal chemical moieties [225]. Samarah et al. synthesized composite coating onto Ti6Al4V using poly (methyl methacrylate) [PMMA] covalently linked to silica via 3-(trimethoxysilyl)propyl methacrylate. Radical polymerization of methyl methacrylate using the sol-gel method was used for the synthesis and enhanced the bioactivity of the modified surfaces [47].

Felgueiras et al. investigated the role of chemically grafted poly(sodium styrene sulfonate) onto Ti6Al4V. Adsorption studies of albumin, FBS, collagen type-I, and fibronectin were carried out to understand the biomaterial interactions [226]. The surface property is easily modulated using various silane-based moieties for the generation of the SAMs. Using silane chemistry, Abshar et al. investigated the effect of surface properties of the titanium surface on the behaviour of collagen-I adsorption [103].

Proteins interact more strongly and specifically with some peptide-based sequences. Combining this approach with HAP alone or in combination might enhance the outcome of many folds. Keeping this in mind, Gabriela et al. succeeded in the formation of biomimetic hydroxyapatite coating onto titanium surfaces (Ti6Al4V) using peptide linkers (EEEEEEEE and KKLPDA) in various combinations to adsorb peptides on the combined titanium-HAP surface [227]. HAP is an excellent bone substituent material. So, Sai et al. utilized the spray-coated HAP on a pure titanium surface to investigate the effect on the protein adsorption and surface property [228]. A HAP-based approach with other strategies is also fruitful. So, Marjan et al. fabricated a meso-macroporous nano-HAP coating onto Ti6Al4V alloy at different calcination temperatures (350, 500, and 650 °C) using a non-ionic template of a di-block copolymer (C12E10) by dip-coating and sol-gel method along with TiO_2 intermediate layer to enhance the bonding strength [229].

2.5 Enhancement of biocompatibility

Reconstructive implants require osseointegration with surrounding cells and tissues [230], without toxic leachate from the implant surface. The success of an implant is determined by tissue-level events such as blood clotting, surface fouling, and bone resorption, which are derived from molecular and cellular interactions with the implant-tissue interface [231]. The environment inside the body is electrically, mechanically, and chemically active, and at the interface, many dynamic biological events occur due to alteration of the normal physiology around the implant [232]. The implant surface (metallic, polymeric, or ceramic) contains various surface ions arising due to functional groups present on the implant surface, the incorporation of the biological ions, and the formation of a surface oxide layer [233].

For the success of the implant, inflammatory response and biocompatibility need to be determined. For this, cytotoxicity and cell adhesion studies can be performed. Mammalian cell adhesion is carried out by the surface receptors specific against the extracellular matrix (ECM) proteins (**Fig. 2.13**). Cell adhesion molecules fall in the transmembrane protein family and comprise three major classes. Cell-cell adhesion molecules that comprise Calcium-dependent (cadherins) and calcium-independent (CAMs). Cell-substrate interacting molecules comprise integrins that have a receptor for binding to collagen, fibronectin, laminin, and others. It becomes of utmost importance to tune various surface properties of the implant to enhance the biocompatibility of the surfaces.

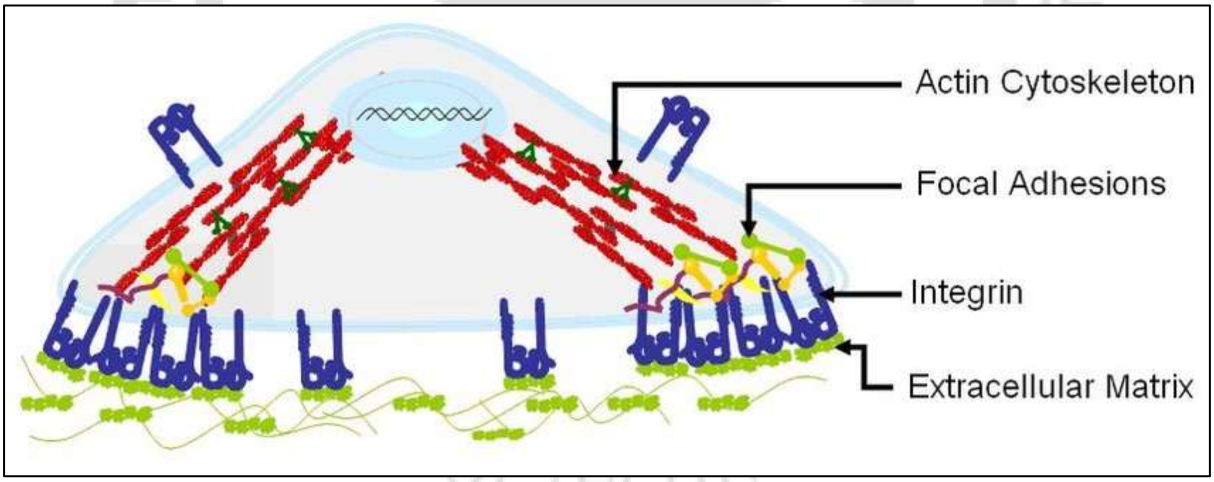

Figure 2.13: Various proteins involved in cell adhesion (Adapted with permission from Methods in cell biology 83 (2007): 329-346).

Stainless steel alloy 316L is currently being utilised for applications related to peripheral and coronary vessel stents. To improve the cell viability of the biomaterial, Foerster et al. have functionalized the surface with amine-SAMs to further carry out the immobilisation of the recombinant fragment of an antibody. This biofabrication was carried out to enhance the human endothelial progenitor cell attachment (HucPE55.1) [234]. Gallardo et al. determined gene expression in the Sarcoma osteogenic (SaOS-2) osteoblast and Human primary foreskin fibroblasts (HFF) cell line on the anhydride functionalized titanium surface. Osteoblastic cell differentiation was induced in the cell lines grown on the fabricated surfaces [235]. To enhance the osseointegration of the titanium implants, Gomes et al. have utilised a two-step fabrication strategy in which the sol-gel method was utilised for the formation of two types of hybrid surfaces onto titanium. Two hybrids include methyltrimethoxysilane (MTMS) and 3-glycidoxy propyl-trimethoxysilane (1:1 ratio) and another MTMS and tetraethylorthosilicate (7:3 ratio) [158].

Bhavya et al. have utilised the nano-patterned silicon surface for studying the cell adhesion of Human adipose-derived stem cells (hADSCs) for determining the influence of surface topography on cellular behaviour. Cell differentiation behaviour, particularly chondrogenic, osteogenic, and adipogenic differentiation, was carried out by focusing on collagen II and aggrecan, collagen I and osteocalcin, and perilipin and GLUT4, respectively [236]. Muller et al. have coupled inorganic calcium polyphosphate onto the surface via APTMS linker. This compound is morphogenetically active and upregulated the expression level of two biomarkers, namely carbonic anhydrase and alkaline phosphatase in osteoblasts. Amine silanes were crosslinked via etching of Ti surfaces [160]. Nano-topography via titanium dioxide nanotubes was coupled with GPTMS silane modification to enhance the biocompatibility of the surface by enhancing osteoblast adhesion and proliferation. This dual strategy acted synergistically to tune the desired surface properties [146].

2.6 Antimicrobial surface modification

Bacterial infection is one of the reasons for osseointegration failure and inflammation, resulting in implant rejection. The microbial infection leads to biofilm formation, and microbes like *Streptococcus sanguinis* are among the first colonisers and contribute a leading role in early attachment and guide attachment of other colonisers. Later colonisers such as *Lactobacillus* *salivarius* contribute to biofilm maintenance, and their by-products contribute to biofilm formation [235]. For the success of the implant, antibiotics or other antimicrobial agent immobilization on the implant surface might be a potential alternative [151, 237]. Various research groups have tried to incorporate such agents onto the surface, summarized in **Table 2.3**. Pawlik et al. have tried attachment of a model drug, ibuprofen, via APTES to prolong the release and enhance the loading efficiency. For this purpose, the anodic titanium dioxide surface was modified using sodium hydroxide and APTES [151]. Liu et al. have encapsulated vancomycin in nanoparticles composed of poly(vinyl alcohol) and poly(lactide-glycolide acid) [PVA/PLGA]. These fabricated NPs were coupled on the implant surface via an APTES linker. Release of the vancomycin was pH dependent and occurred via swelling of the nano-encapsulation followed by ester bond rupture between vancomycin and PLGA. The highest antibacterial efficacy against *Staphylococcus aureus* was observed at a pH of 4.5. This fabrication strategy provided a dual benefit of osteoblast adhesion and antimicrobial activity [237].

Table 2.3: Surface modification strategies utilised for antimicrobial implant coatings

Modifiers	**Functional moieties**	**Properties**	**Significance**	**Remarks**	**Ref**
APTES	Amine; Melamine: antimicrobial peptide;	Melamine conc: 3.1×10^{-9}mol/cm^2	Melamine has the potential as an antimicrobial coating of biomaterials; Resistant against sterilization techniques: autoclave and ethylene dioxide;	% reduction: 62.5 % (*P.aeruginosa*); % reduction: 84.4% (*S.aureus*)	[238]
APTES	Amine; PVA/PLGA nanoparticles;	Drug release at 20 days: 7.1 µg/ml	Vancomycin encapsulation;	ZOI highest at pH 4.5: 20.7± 0.6 mm against *S. aureus*;	[237]
APTES; PEG;	Amine with PEG spacer;		Enoxacin immobilization;	MIC: 2 µg/ml (*S. aureus*, *S. epidermidis*), 4 µg/ml (MRSA), 0.5 µg/ml (MRSE) and 0.06 µg/ml (*E. coli*)	[239]
APTES; Polymer brush;	Amine;	63.5 ± 2.3°contact angle; Roughness:29.2 ± 4.1; Thickness: 6.8 ± 0.5 – 11.6 ± 2.5 nm;	Antimicrobial peptide: hLf1-11 attachment;	% inhibition: 60.6 ± 6.2 (*S. sanguinis*), 55.7 ± 1.1 (*L.salivarius*); Biofilm inhibition: 47.2 ±13.9 (*S.sanguinis*), 47.3 ± 14 (*L.salivarius*)	[240]
CPTES; micro-grooved surface;	Chloro;	Contact angle: Microgrooved: 60.68 ±2.89°; Alkali etching: 14.68 ±0.68°; CPTES silane: 77.69 ±9.28°; GL13K: 101.6 ±6.75°;	Antimicrobial peptide: GL13K attachment;	GL13K coating activity thrice compared to microgroove (*P. gingivalis);*	[157]
APTES; Chitosan; Alginate;	Amine terminal; Layer-by-layer;	Contact angle: Pristine Ti- 70°, modified Ti- 28°;	Minocycline loaded chitosan/ alginate;	Antimicrobial activity against *S. aureus*; Stable minocycline release; 85-98% bacterial inhibition;	[241]

APTES: 3-aminopropyltriethoxysilane; PEG: poly (ethylene glycol); PVA: poly(vinylalcohol); PLGA: poly (lactic-co-glycolic acid); CPTES: (3-Chloropropyl)triethoxysilane

2.6.1 Antimicrobial peptides

Titanium implants suffer from nosocomial infections at the site of a surgical incision. One solution is the construction of antimicrobial coatings, such as antimicrobial peptides (AMPs), directly onto the surface [242-245]. One advantage of antimicrobial peptides is that they are not susceptible to bacterial resistance development and have a broad spectrum of activity. This type of coating is not feasible using physical adsorption due to difficulty in controlling the release, as this method relies on the morphology and composition of the substance to be adsorbed. Further sudden burst release of the coating may cause cytotoxicity, attachment in the wrong orientation may reduce its efficacy, and its long-term stability is also an issue. Fabrication of antimicrobial titanium surfaces via click immobilisation of peptide onto the surface using silane coupling of an alkynyl group can be tried [242]. These issues can be easily addressed by covalent coupling, especially long-term stability. In a study, the fusion protein PEG-HHC36 was used by Chen et al. [242], and antimicrobial activity was determined against two clinically relevant strains, *Staphylococcus aureus (SA)* and *Escherichia coli (EC).*

Zhou *et al.* have utilised antimicrobial peptide (AMPs) GL13K to enhance the antimicrobial properties of the titanium surface. GL13K was attached to the micro-grooved surface using 3-(chloropropyl)-triethoxy silane (GPTES) as the linker. Further studies were performed to determine the antibacterial activity against *Porphyromonas gingivalis*, and the proliferation of the human gingival fibroblasts (HGFs) was analyzed. Chen et al. have utilised the same strategy of AMPs fabrication onto Ti surfaces for the attachment of melamine, a broad-spectrum antibiotic against fungi, bacteria, and even protozoa. Antimicrobial activity was determined against *Pseudomonas aeruginosa* and *Staphylococcus aureus*. AMPs fabrication was stable against sterilization methods such as ethylene oxide and heat sterilization [238]. Another research group, Gallardo et al., have tried to modify the surfaces of model Titanium implants using other silanes, such as triethoxysilypropyl succinic anhydride (TESPA), to incorporate the anhydride terminal functionality. The main aim of the study was to determine the antibacterial activity, thus evaluating the in vitro response [235].

2.6.2 Metallic antimicrobials

The following section summarizes the antimicrobial coating for implant-related applications involving metallic biomaterials. Metals can be utilized alone for the application or can be combined with other metals or metal oxides to impart antimicrobial properties. This section also included the usage of metallic nanoparticles for the same objective.

2.6.2.1 Metals:

Various metals have been utilized for implant-related applications. Thin-film coatings made of copper and titanium have been created, and the impact of these coatings on bacterial development has been investigated by Wojcieszak *et al.* The likelihood of copper ions migrating from the film surface to the interior of microorganisms may rise because of these coatings' improved wettability [246]. Chu *et al.* created several layers of material on the surface. They discovered that the antibacterial effect of the thin film metallic glasses (TFMGs) with Al or Ag content is comparable to that of the pure Ag coating. Lacking Ag or Al, the ZrTiSi TFMG exhibits subpar antibacterial activity. The antimicrobial effectiveness against *P. aeruginosa*, *E. coli*, and *S. aureus* has been evaluated, and it has been found that metal ion release has a significant impact on antimicrobial activity [247]. Lalitha *et al.* utilized cardanol in acrylate epoxidized linseed oil (AELO), a renewable resource, to synthesize the Schiff base complexes based on zinc and copper used to make antibacterial thin film coating materials. The antibacterial activity of the material compounds was effective against both Gram-positive and Gram-negative bacteria, and its efficacy rose with concentration. This manufactured material can create hydrophobic urinary catheter tubes resistant to microorganisms [248]. Wei *et al.* have integrated fine Cu and Cu salt particles into polymer-based coating systems. The fact that coatings with embedded fine Cu salt had higher antimicrobial properties than coatings with metallic Cu and that more Cu ions were released as a result suggests that the primary reason *E. coli* dies after coming into contact with polymer-Cu coatings is due to the effect on cell membrane integrity [249]. Thin metallic films can be coated on various implant-related surfaces to make them antimicrobial. Cu or Cu ions are the least explored for this application but can be utilized within their cytotoxicity limits. Other metals such as Zn, Ag, or Al can also be used for biomedical applications. Cytotoxicity of the various metals can be reduced by coating them with biologically benign materials. Film thickness and the nature of the addition, doping, or mixing will also tune the antimicrobial behavior to a more significant extent.

2.6.2.2 Metal oxides:

TiO_2 is well known for its antibacterial activity, mediated through photoactivity. Using the sol-gel dip coating technique, Cao *et al.* coated the bracket with a thin layer of TiO_2 to provide a photocatalytic antibacterial effect [250]. The bracket was coated with a thin layer of nitrogen-doped TiO2-xNy made by RF magnetron sputtering. The antibacterial activity of the bracket was found to be effective against *Streptococcus mutans*, *Lactobacillus acidophilus*, *Actinomyces viscous*, and *Candida albicans*, with percentages of 95.19% and 91% [251]. Chung *et al.* used a sol-gel dip-coating technique to create titania (anatase) and Ag-doped titania coatings on glass microscope slides. Antibacterial activity tests against *Bacillus cereus*, *Escherichia coli*, and *Staphylococcus aureus* revealed that coatings exhibited an exceptional antimicrobial response.

Compared to a conventional TiO_2 coating, Ag-doped coatings were much more photo-catalytically and antimicrobial active, lowering bacterial loads and addressing nosocomial infections. The effectiveness of these films depends on how easily the electron-hole pair produced by photosynthesis can be stabilized. Using the arc ion plating technique, TiO_2 film can be created on medical grade AISI 304 stainless steel. It provides medical tools with an efficient antibacterial surface coating approach, lowering the incidence of hospital-acquired illnesses [252]. It has been noted that the Zn(II)-tetracarboxy-phthalocyanine (TcPcZn) complex intensified the antibacterial activity of TiO_2, which has the potential to be an efficient photocatalytic agent on a variety of microbes and chemical pollutants under visible light irradiation [253]. It has been discovered that photocatalysts containing sulfur and nitrogen-doped atoms are bioactive. Therefore, they can be used as antimicrobial surfaces in healthcare settings. Researchers tested the synthetic photocatalyst for antibacterial activity and used white light as the irradiation source to successfully eradicate *Escherichia coli*. These were highly effective antibacterial thin film photocatalytic coatings [254].

It is possible to create ZnO films using aerosol-assisted chemical vapor deposition, a well-known antibacterial agent (AACVD) [255]. Ali *et al.* have generated highly c-axis oriented ZnO thin films with wurtzite structure on heated glass using the spray pyrolysis approach. The antibacterial efficiency of the manufactured films improved with increasing Al/Zn ratio when tested against *Escherichia coli* germs. Surgical tools, protective hospital clothing, medical implants, and storage containers could all benefit from antimicrobial coatings [256]. Ag_4O_4, commonly known as Ag(I)Ag(III) oxide, can also be utilized to create antimicrobial coatings [257]. By altering physical and chemical properties, antimicrobial activity can be imparted as Mandracci *et al.* executed by using plasma-assisted chemical vapor deposition to produce thin coatings of SiOx; the surfaces of dental materials were altered. *Streptococcus mutans* and *Streptococcus mitis* were investigated for surface adhesion [258]. Wojcieszak *et al.* investigated the bactericidal properties of (Cu, Ti, Nb)Ox thin films, whose antibacterial activity is linked to the copper ion migration process. Studies on antibacterial activity revealed that multi-oxide film, as it was created, had a potent bactericidal impact [259]. An efficient way to enhance the mechanical, tribological, and antibacterial properties of the widely used Ti6Al4V bio-alloy is through pulsed laser deposition (PLD) of ZrO_2 coating. *Staphylococcus aureus* and *Klebsiella pneumonia* were shown to adhere and grow less readily on coated samples. For the sample coated at 200 °C substrate temperature, an apparent reduction in CoF of 23 % at 2 N (tribological force) and a wear rate of up to 49 % at 5 N (tribological force) were observed [260].

2.6.2.3 Metallic nanoparticles:

Proanthocyanidins and cinnamaldehyde are the two antioxidants found in *Cinnamomum verum*. *Cinnamomum verum* and Fe_3O_4 nanoparticles produced films with potent anti-inflammatory and antibacterial action and few side effects. Pulsed laser evaporation was used to deposit magnetic nanoparticles measuring 9.4 nm in size onto gastrostomy tubes (G-tubes) for testing antibacterial efficacy against Gram-positive and Gram-negative microbial colonization [261]. By reacting N-methyl pyrrolidone with silver salt in a semi-dry polymer film, Lyutakov *et al.* successfully created nanoparticles. These AgNPs doped films were then examined for their antibacterial efficacy on Gram-negative bacteria [262]. Inoue *et al.* investigated the effectiveness of a hybrid nanoparticle called Ag/Si NPs, which has a core made of silver (Ag) NPs and an exterior made of silicon (Si) nanocrystals. The benign AgNPs have been created and immobilized on amine self-assembled monolayer (SAM) surfaces. We explored the fabricated antimicrobial coating effect on *Pseudomonas aeruginosa* adhesion to produce biofilms. Fabricated surfaces hindered bacterial adhesion, which inhibited biofilm development and reduced bacterial viability by 67% [263]. Compared to AgNP films with organic caps, the synthetic film displays a more significant zone of inhibition in agar diffusion assays of *Escherichia coli*, as shown in **Fig. 2.14 [264]**. Metallic nanoparticles are also promising due to their higher surface area and smaller size. Different metal-related NPs such as TiO_2, Fe_3O_4, Ag, or Si can be recruited to accomplish the task.

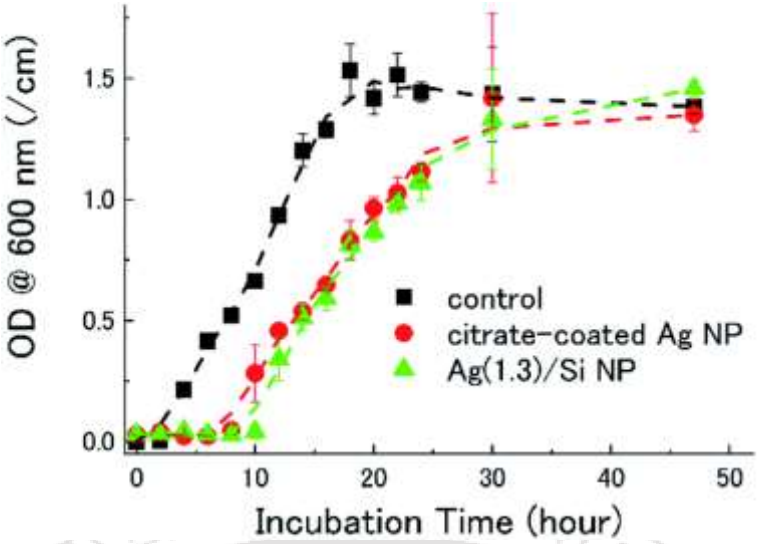

Figure 2.14: Growth kinetics of *E. coli* bacteria incubated with NPs (Adapted with permission under Creative Commons license).

2.6.3 Ceramic antimicrobials

Ceramic biomaterials made of metallic and non-metallic elements are divided into categories based on how they behave in a physiological milieu. Ceramics can be divided into bioinert, biodegradable/bioresorbable, and bioactive categories [77-80]. *Staphylococcus epidermidis* and *S. aureus* cause most infections connected to implants. Surgery is commonly necessary for recovery after antibiotic treatment. In static settings, *S. aureus* was less likely to stick to surfaces coated with diamond-like carbon (DLC) than those coated with titanium, tantalum, or chromium [265]. By applying the revised co-precipitation approach with cetyltrimethylammonium bromide, nitrogen, and bromine, Iconaru *et al.* produced NBrHAP suspension. Suspensions indicated their antibacterial solid activity and displayed exceptional *in-vitro* antimicrobial efficacy against bacterial and fungal strains [266]. Tyrosine silica/antibiotic nanocomposite was created by Balaure *et al.*, who also investigated the antibacterial activity against the pathogenic strain *Staphylococcus aureus*. The widths of the growth inhibition zones and the least inhibitory concentration values showed that the obtained nano biostructure considerably improves the antibacterial activity of three regularly used antibiotics against *S. aureus* [267].

2.6.4 Polymeric antimicrobials

By providing surface/local antimicrobial activity and facilitating the removal of attached microorganisms, Jones *et al.* hypothesized that the *in vitro* properties and *in vitro* resistance to encrustation of films made of poly(-caprolactone) (PCL) and blends of PCL and the polymeric antimicrobial complex, poly(vinylpyrrolidone)-iodine (PVP-I) coating system would lower the incidence of medical device-related infections[268]. An effective hydrophilic-antimicrobial thin film coating of functionalized polymaliamides has been created by Nagaraja *et al.* to limit pathogenic microorganisms' activity of the polymer and thin film against *Staphylococcus aureus*, *Escherichia coli*, and bacteria that cause tuberculosis variant. There are additional reports of *Mycobacterium smegmatis* and *Candida albicans* [269].

A quick and reliable photo grafting procedure can create thin polymer films that shield implantable medical devices from infection. Considering this, Shen *et al.* produced zwitterionic thin films of poly(dimethyl)siloxane (PDMS) that significantly decreased bacterial adherence in both *in vitro* and *in vivo* settings. Fabricated thin films can create films that resist bacterial adhesion and growth, which are remarkably robust antimicrobial films. These films are effective against the two bacterial strains that frequently cause medical device infection[270]. Martin *et al.* coated the clinically significant fabric with poly(dimethylaminomethyl styrene) and investigated its antibacterial effectiveness at concentrations up to 540 g/cm^2. They had excellent anti-gram-ve performance against *Escherichia coli* [271].

At an acidic pH, Richert *et al.* created a thin homogeneous coating of the polysaccharides chitosan and hyaluronan [272]. Bacterial adherence was reduced by 80% compared to a bare glass substrate in the films constructed at high salt concentrations. They were also found to be chondrocyte and bacterial-resistant [272]. According to Foster et *al.*, chitosan's final shape can considerably impact its antibacterial action. When tested on bacterial lawns and in liquid cultures, chitosan in solution form demonstrated nearly perfect suppression (98.2 %); however, chitosan films (20 µm) showed no inhibitory effects against *Escherichia coli*, *Staphylococcus aureus*, or *S. epidermidis* species [273]. The researchers created ultrathin chitosan films by spin-coating on gold/glass surfaces and crosslinking with genipin. The zeta potential of *H. pylori* changed from negative to positive when the pH was decreased. At pH 6, the shape of *H. pylori* changed from rod to coccoid because of pepsin adsorption before *H. pylori* adhesion [274].

2.6.5 Composite antimicrobials

Alias *et al.* applied a nanocomposite layer of silver (Ag) and tantalum oxide (Ta_2O_5) to the stainless steel 316L via physical vapor deposition magnetron sputtering. Manufactured composites also displayed a sizable zone of inhibition to *Escherichia coli* (B-axis: 26.00 ± 0.58 mm) and *Staphylococcus aureus* (A-axis: 16.33 ± 1.15 mm) [275]. The hip prosthetic surface was modified by Ferreri *et al.* using Ag-ZrCN coatings. One of the main nosocomial bacteria linked to infections connected to hip implants is *Staphylococcus epidermidis*. On stainless steel 316 L substrates, silver was incorporated in a zirconium carbonitride (ZrCN) matrix to give it an antibacterial property [276]. Dhall *et al.* used barium titanate (BTO)-based nanocomposite materials for biological purposes. While maintaining their mechanical and piezoelectric characteristics, it exhibit powerful antibiofilm properties against *Streptococcus mutans* without bactericidal effects, as shown in **Fig. 2.15**. Colony-forming units (*in vitro*) were reduced 10-fold because of the anti-adhesion impact. Nanocomposite on a negatively charged surface maintained strong antibacterial adhesion properties [277].

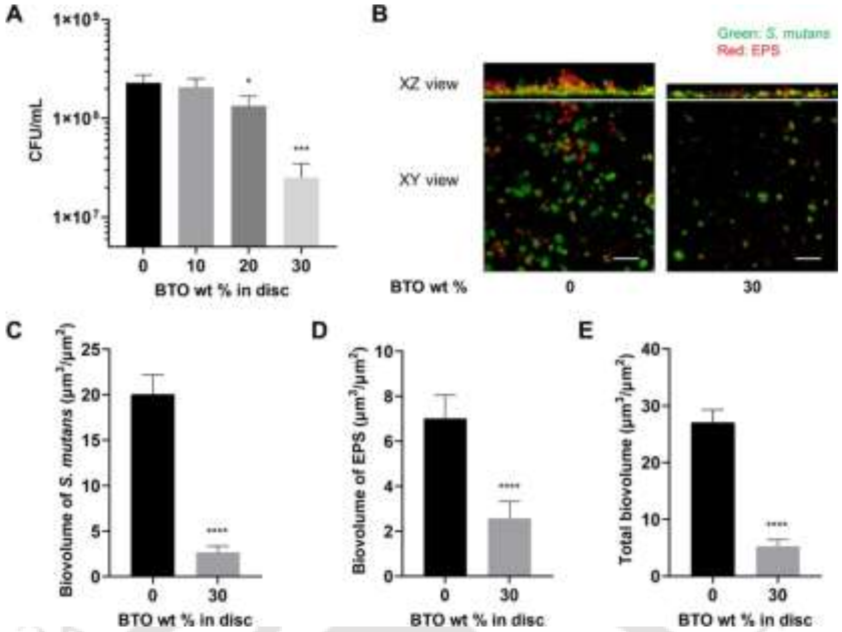

Figure 2.15: Graph depicting the antibiofilm capability (Adapted with permission from ACS Applied Materials & Interfaces 13.34 (2021): 40379-40391).

Ford *et al.* investigated the antimicrobial characteristics of detachable collagen/hyaluronic acid polyelectrolyte multilayers (PEMs) treated with LL-37, a naturally occurring human AMP. PEMs' antimicrobial and cytotoxic effects were evaluated using primary rat hepatocytes and the gram-negative *Escherichia coli* (*E. coli*, strain DH10B). The ability to neutralize *E. coli* and prevent microbial adherence were two functions of the investigated antibacterial characteristics. When LL-37 was added, PEMs developed that strongly inhibited microbial adherence [278]. Demircan *et al.* created straightforward cellulose nanocomposites that could obstruct the quorum-sensing (QS) molecules that controlled bacterial physiological processes. Several green, low-cost cellulose nanocomposites with organically modified montmorillonite were created, and they significantly inhibited the bacteria *C. violaceum* CV026 via quorum-sensing-regulated pigment production [279]. Positively charged polymeric coatings have the potential to be antimicrobial due to simple electrostatic interactions with negatively charged bacterial walls and membranes. Taking this into account, Wojciechowski *et al.* employed positively charged films that prevented the growth of yeast (*C. albicans*), as well as both Gram-negative (*E. coli*) and Gram-positive (*S. aureus*) bacteria [280]. Reis *et al.* produced functional amine-enriched thin-film composite polyamide (PA) membrane surfaces using plasma polymerization, a practical method. Higher silver binding to the changed surface and increased antibacterial effectiveness with clearly visible *E. coli* growth eradication served as evidence of increased metal affinity [281]. Various scaffolds of various biomaterials were also being tried for antimicrobial efficacy as explained in **Table 2.4**.

Table 2.4: Various approaches employed for scaffold fabrication

Fabrication method	Fabrication strategy	References
3D additive manufacturing	Intercalation of gentamicin and ciprofloxacin into the inter-lamellae of the double hydroxide layers of Mg: Al & Zr phosphate	[282]
	Ti6Al4V alloy scaffolds with silver (Ag), calcium phosphate (CaP) nanoparticles (NPs)	[283]
Coating	Calcium Phosphate coating with vanillin derivative	[284]
	Drug-loaded fluorous-cured collagen shell around CS nanorod coatings	[277]
Functionalization	PEGylated polyglycerol sebacate functionalized with Laponite nano silicates and an antimicrobial peptide (AMP)	[285]
3D printing	Poly(dopamine) mediated functional 3D porous scaffold of PLGA with immobilized BMP-2 and ponericin G1	[286]
Electrospinning	Radially aligned PCL nanofiber with 25-hydroxyvitamin D3 (25(OH)D3)	[287]

Aslan *et al.* investigated the antimicrobial properties of single-walled carbon nanotubes (SWNT) layer-by-layer (LbL) combined with polyelectrolytes. When compared to control films, the inactivation rates of *Escherichia coli* and *Staphylococcus epidermidis* were much more significant after 24-hour incubation with SWNT-containing films (ca. 20 %) [288]. To prevent the growth of biofilms, Ahmed *et al.* created polyvinyl-N-carbazole (PVK) (97 wt. %)

and single-walled carbon nanotubes (SWNT) (3 wt.%). SWNTs were combined with PVK, an electroactive polymer, to create stable PVK-SWNT nanocomposite dispersions and films, which were more effective against *E. coli* and *B. subtilis* than either SWNTs or PVK alone [289].

Ito *et al.* looked into the antimicrobial qualities of polymeric ultra-thin films made of poly(lactic acid) (also known as "PLA nanosheets") and silver sulfadiazine (AgSD). In an *in vitro* assay, an AgSD-loaded nanosheet demonstrated antibacterial activity against methicillin-resistant *Staphylococcus aureus* (MRSA) for more than 3 days. The Nanosheet considerably decreased the amount of MRSA germs on the lesion in an *in vivo* test utilizing a mouse model of infection in a partial-thickness burn wound (more than 105-fold) [290]. For surface coating on orthopedic metal plates, a tricomponent nanohybrid dispersion in water containing silver nanoparticles (AgNP), nanometer-thick silicate platelets (NSP), and water-based polyurethane (PU) was created. Surface antibacterial effectiveness was demonstrated for coating compositions of AgNP/NSP to PU ranging from 1/1 to 1/5 by weight ratio. A coating thickness of about 1.5 μm showed a robust composite surface with an effective microbicide capability (**Fig. 2.16**) [291]. Pulit-Prociak *et al.* created an antibacterial composition based on polyvinyl alcohol (PVA) and zinc oxide (ZnO). Gelatin, guar gum, and hydroxyethyl cellulose were added to the composition as three natural stabilizers to achieve the objective. Strong adhesion forces and microbial activity led to effective surface microbial treatment [292]. Tamayo *et al.* created porous nanogold/PU scaffolds for antibacterial applications. *Staphylococcus epidermidis* and *Klebsiella* spp., two pathogen microorganisms linked to implant infections, were the targets of antibacterial experiments [293].

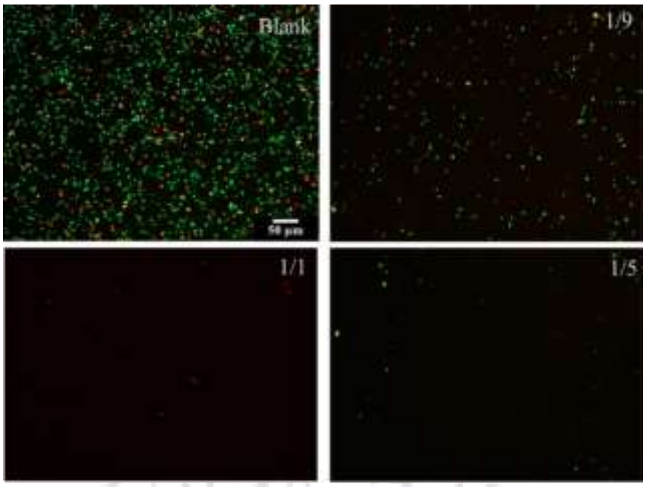

Figure 2.16: Live/Dead assay of the MRSA strain (Adapted with permission from ACS Applied Materials & Interfaces 6.22 (2014): 20324-20333).

2.7 Conclusion

Biomaterials are utilized for orthopaedic and dental implants, hip and knee joints, and many other load-bearing applications. Different metal alloys, polymers, ceramics, and composites are being explored as biomaterials. However, they suffer from certain limitations, which physical and chemical modification techniques can eliminate. Tuning the surface properties of the implant materials can be carried out to a certain degree depending on the desired applications, such as the fabrication of implants with reduced side effects and immunological responses. Biomaterials with self- antibacterial properties are needed to address the challenges of antimicrobial resistance and hospital-acquired infections. Thus, multifunctional biomaterials need to be designed for a given application.

Chapter 3

Surface modification and characterization of metallic implant surfaces

This chapter includes the surface modification of the titanium alloy surfaces using a silanization-based surface modification approach. Silane molecules with varied terminal moieties, such as octyl-, amine-, carboxyl-, hybrid-, mixed-, hexadecyl-, and octadecyl- were functionalized on the acid and UV-activated surfaces. These self-assembled monolayers (SAMs) of the various silane molecules were characterized after modification using the Contact Angle Goniometer, Fourier Infrared Transform Spectroscopy (FTIR), and Ellipsometer spectroscopy. Change in the surface energy and hydrophobicity, along with the change in the peak area of various functional groups (from FTIR), was quantified to get an insight into the silanization and surface tunability of various model implant surfaces.

3.1 Introduction

Biomaterials are utilized to fabricate implant materials such as orthopedic, dental, and other implants [1, 62]. The surface properties of the biomaterial rather than the bulk properties influence the fate of the implant material. Surface properties determine and influence the key physicochemical microenvironment events, such as protein interactions, cellular interactions, and immunological responses, to name a few [41, 294-297]. The physiological microenvironment interacts with the implants and causes the release of metal ions and deterioration of the implant surface. Released metal leachates interact with surrounding tissues, causing immunological responses [55, 298].

Protein adsorption is dependent on the substrate, protein, and microenvironment properties. Adsorption is affected by the charge distribution, size, and conformation of the proteins along with topography, chemistry, cationic site, hydrophobicity, crystalline phase, composition, and surface charge of the substrate [189, 205]. The ionic strength, temperature, and pH of the microenvironment also affect protein adsorption [189]. The secondary structure of the protein unfolds upon adsorption to irreversibly adsorb onto the surface. Non-specific protein adsorption might lead to biofouling, thus compromising the implant material.

The key surface features that are quite promising in determining the cellular interactions, namely protein adsorption, cell adhesion, and anti-biofouling, are governed by the surface energy of the functionalized surfaces [194, 210]. Enhancing the surface properties of the existing orthopedic materials without compromising their key features is a hot research area. Ensuring the implant-tissue interlocking and preventing micromotion, inflammation, and fibrosis are the most sought features.

Various physical and chemical modification strategies can be utilized to enhance the surface features. Physical modification strategies involve plasma spraying, electron beam sputtering, hydrothermal treatment, ion beam sputtering, and surface roughness tuning [15, 16]. In contrast, chemical modification involves the incorporation of thiolization, silanization, click chemistry, sol-gel method, electrochemical etching, anodization, apatite coating, electrochemical oxidation, doping of other elements, and other strategies to enhance the surface features [17, 18, 20, 21, 41]. Our strategy of silanization forms a thin, uniform coating on the surface, and the functionality can be altered by changing the terminal moiety of the silane molecules. This strategy helps to alter the surface chemical groups and the wettability and surface energy of the functionalized surfaces. Silane moiety can also be used as the coupling agent to incorporate other molecules and ligands onto the modified surfaces to enhance the overall features depending on the applicability. So, silane moieties provide ease of tunability and fabrication along with functional flexibility and application versatility.

This chapter includes the surface modification of the silica and titanium alloy surfaces using the silanization-based surface modification approach. Silane molecules with varied terminal moieties, such as octyl-, amine-, carboxyl-, hybrid-, mixed-, hexadecyl-, and octadecyl-, were functionalized on the acid and UV-activated surfaces. These self-assembled monolayers (SAMs) of the various silane molecules were characterized post-modification using the Contact Angle Goniometer, Fourier Infrared Transform Spectroscopy (FTIR), and Ellipsometer spectroscopy along with investigating the insights about the silanization and surface tunability of various model implant surfaces.

3.2 Materials and Methods

Ti6Al4V alloy sheet was procured from Metalfort, India, glove bag (cat.no. Z530220), anhydrous toluene (cat. no. 244511), Tri-ethoxy octyl silane (cat. no. 440213), 3-aminopropyl triethoxy silane (cat. no. 440140), hexadecyl trimethoxysilane (HDTMS, cat. no. 52360), trimethoxy(octadecyl) silane (TMODS, cat. no. 376213) p-Tolyl isocyanate (cat. no. 143634), dibutyltin dilaurate (cat. no. 291234), Bovine Serum Albumin (BSA, cat. no. A2153) was procured from Sigma-Aldrich; toluene, methanol, acetone, hydrochloric acid, sulfuric acid, hydrogen peroxide, and potassium permanganate, KCl, Na_2HPO_4, NaCl, diiodomethane and KH_2O_4 were purchased from Himedia and MilliQ water (18.2 MΩ.cm, make: Millipore) was utilized throughout the experiments. Polished samples were washed with acetone and kept in a vacuum desiccator post-drying for further use.

3.2.1 Pre-modification substrate cleansing strategy

Ti6Al4V sheets were cut into 1 X 1cm pieces using wire-electrical discharge machining (wire-EDM) followed by polishing with silicon carbide sandpapers of different grit sizes starting from the lowest to the highest (400, 600, 800, 1000, 1200, 1500, and 2000 μm). Surfaces were activated before the silanization-based self-assembled monolayers (SAMs) with slight modifications to the protocol previously described by our research group [145, 299-301]. Firstly, acid wash (MQ: H_2O_2: HCl, 3:1:1 v/v) was given for 30 min to remove all the hydrophobic patches, dust, and grease from the samples for the proper silanization to take place, followed by washing thrice with MQ water (10 min each) followed by acetone washing for 10 minutes [145, 299-301]. Acid wash followed by UV treatment (1 hour) to remove the reminiscent hydrophobic patches. Samples were immediately utilized for the surface modification.

3.2.2 Silane-based SAMs formation

3.2.2.1 Amine-, octyl-, hexadecyl-, octadecyl-, mixed-SAMs:

For the effective silanization, humidity in the glove bag was maintained at ≤35% using repeated purging of inert gas, i.e., nitrogen, to be carried out properly in the particular order to be effective, as mentioned below. Activated samples were kept in the anhydrous toluene containing the TEOS (octyl silane) under an inert nitrogen atmosphere for 24 hours to form uniformly distributed self-assembled monolayers (SAMs). Similarly, for the amine-terminated, mixed-, hexadecyl- and octadecyl- SAMs formation, samples were similarly immersed in the respective silane precursors (APTES, TEOS, HDTMS, TMODS) containing anhydrous toluene solution. Post-silanization, samples were shifted to clean beakers, and silane containing anhydrous toluene was discarded. Samples were washed with toluene, toluene-methanol (1:1 v/v ratio), and methanol for 10 minutes in a bath sonicator. SAMs modified Ti6Al4V substrates were kept in the vacuum desiccator until further experimentation.

3.2.2.2 Carboxyl SAMs formation:

Octyl SAMs were subjected to secondary modification using acidified $KMnO_4$ to impart carboxyl-terminal to the octyl SAMs, converting them to carboxyl SAMs. For the formation of carboxyl SAMs, acidified $KMnO_4$ using 2M H_2SO_4 was utilized to carry out the carboxylation of the terminal $-CH_2$ group of the octyl chain. For the modification, various percentages of the acidified $KMnO_4$ solution (1, 2, 3, 4,& 5%) were used with variable incubation time (5, 10, 15, 20, 25, 30, 60, 90, 120, and 150 min) at RT was carried with slight modification of the protocol previously described by our research group and elsewhere [62, 302, 303]. After modification, samples were washed thrice with MQ water for 10 min each, then dried under laminar airflow and stored in a vacuum desiccator.

3.2.2.3 Hybrid SAMs formation:

Hybrid SAMs are formed on the amine SAMs surfaces as the post-modification strategy. The amine terminal was coupled to the NCO- group of the p-tolyl isocyanate via urea linkage (NH-CO-NH). A hybrid terminal was formed using dibutyltin dilaurate as the catalyst; the reaction was carried out in the inert nitrogen atmosphere in the glove box at RT for 3 hours, followed by washing with the solvents, as mentioned in the above section [299].

3.3 Characterization

3.3.1 Contact Angle and Surface Energy

Surface Energy: A Contact Angle Goniometer (Holmarc) was used to determine the contact angle of the surface using MQ water and di-iodomethane. The sessile drop method was used for the measurement at RT. Samples in triplicates were used for the measurement. Young's equation was determinative and relates contact angle θ to interfacial tensions at solid-air, solid-liquid, and air-liquid interfaces:

$$\gamma_{sv} - \gamma_{SL} = \gamma_{LV} cos\theta \tag{1}$$

where γ_{LV}, γ_{SL} and γ_{sv} are the interfacial tensions in-between liquid-vapour, solid-liquid, and solid-vapour, respectively. Surface energy γ_{sv} was deduced based on the contact angle data of the MQ and DIM solutions on the surface-modified Ti6Al4V substrates based on geometric mean expression as reported previously by our research group [19, 62], shown below:

$$\gamma_{LV}(1 + cos\theta) = 2[(\gamma_L^P \gamma_S^P)^{1/2} + (\gamma_L^D \gamma_S^D)^{1/2}] \tag{2}$$

where γ_L^P and γ_L^D are the dispersive and polar components of the liquid surface energy and γ_S^P and γ_S^D are the respective dispersive and polar components of the solid surface energy, respectively.

3.3.2 Surface functional group characterization

Attenuated Total Reflectance-Fourier Transform Infrared Spectroscopy (ATR-FTIR) was used to characterize the various functional groups on the surface of the modified substrates. Vacuum desiccator stored samples were utilized for the ATR-FTIR (PerkinElmer Spectrum 2) measurement with a scan resolution of 4 cm^{-1} and range 4000 - 700 cm^{-1} at RT conditions. For all the samples, an unmodified Ti6Al4V substrate was used as the background prior to the sample measurement.

3.3.3 Thickness measurement

SEMILAB, Spectroscopic Ellipsometry Analyzer - SEA instrument (Model: GES5E), was used to analyze the thickness of the silane SAMs modified surfaces (AO-, HO-, HC-, HO-series, and others). The HeNe laser (632.8 nm) on the instrument was focused on the sample at a 70° angle of incidence. Optical constants fit the data: n = 3.871, k = 0.0158 for the substrate, n = 1.521, and k = 0 for the silane SAMs treated surfaces [304, 305].

3.4 Results and Discussion

3.4.1 Contact Angle and Surface Energy

3.4.1.1 Amine-, octyl- and mixed-SAMs:

The surface properties of the modified surfaces can be determined by knowing the hydrophilicity of the surfaces using the contact angle measurement. The surface energy of the modified substrates can be determined by measuring the contact angle of the polar and non-polar liquid with the known surface energy values. The contact angle of these liquids with respect to the modified substrates can help deduce the surface energies. The contact angle of the MQ (64.6±1.4°) and DIM (41.5±1°) on the amine SAMs modified silica substrates. Based on the measured contact angles of the MQ and DIM, the surface energy of the amine SAMs modified substrate was calculated to be 49.1±1 mJ/m^2. In addition to modifying the silica (glass coverslips) substrates, Ti6Al4V alloy was utilized as the model implant substrate for further silane modification and related experiments. In this direction, Ti6Al4V substrates were modified using the amine-SAMs modification and mixed-SAMs containing equal volumetric ratios of APTES (amine-SAMs precursor) and TEOS (octyl-SAMs precursor). The contact angle of the modified substrates was measured, and surface energy was deduced. The contact angle of the octyl-SAMs modified Ti6Al4V substrate was 107.7±1° (MQ) and 64.3±1° (DIM), and the surface energy calculated was 26.2±0.4 mJ/m^2; on the other hand, the contact angle of the mixed-SAMs was 83.4±1° (MQ) and 46.5±1° (DIM) and deduced surface energy was 39.3±0.4 mJ/m^2; somewhat in-between the contact angles measured for the amine- and octyl-SAMs modified substrates as evident from the data in **Table 3.1**.

Table 3.1: Surface parameters for various SAMs

SAMs	Surface parameters		
	Contact angle (θ)		Surface energy (mJ/m^2)
	MilliQ	DIM	
Amine	64.6±1.4°	41.5±1°	49.1±1
Octyl	107.7±1°	64.3±1°	26.2±0.4
Mixed	83.4±1°	46.5±1°	39.3±0.4
Octadecyl	121.6±1.2°	-	-
Hexadecyl	114.9±2°	-	-
Mixed$_{\textbf{(hexadecyl-octyl)}}$	117±2.8°	-	-
Carboxyl$_{\textbf{(hexadecyl-octyl)}}$	47±0.6°	-	-

3.4.1.2 Octadecyl-, hexadecyl-, mixed(hexadecyl-octyl)- and carboxyl(hexadecyl-octyl)-SAMs:

The Ti6Al4V substrate was further modified with different chain lengths in the linker region of the silane molecules. In the above section, we modified the Ti6Al4V substrate with the octyl-SAMs containing eight molecule carbon chain. Here, we have tried to modify the pre-treated substrates with sixteen and eighteen-carbon chain long mixer region, mixed-SAMs were also formed containing the eight and sixteen-carbon chain long mixer region, which was post-modified to carboxyl-SAMs converting the -CH_3 terminal moiety of the mixed-(hexadecyl-octyl) to the carboxyl terminated SAMs using the acidified potassium permanganate. The water contact angle measurement confirmed the successful modification. As clear from Table 1, the water contact angle of the octadecyl-SAMs was 121.6±1.2°, hexadecyl-SAMs was 114.9±2°, mixed$_{\text{(hexadecyl-octyl)}}$ SAMs was 117±2.8° and carboxyl$_{\text{(hexadecyl-octyl)}}$ SAMs was 47±0.6° respectively. Octadecyl-SAMs with the most extended chain length showed the highest contact angle followed by the mixed-SAMs, which might be due to intra-variation in the chain length of the SAMs on the surface, and carboxyl SAMs modified substrates showed the least contact angle due to an increase in the surface hydrophilicity.

3.4.1.3 Variable ratio mixed SAMs of amine-octyl, amine-carboxyl, hybrid-octyl, and hybrid-carboxyl silanes

In the following work, mixed SAMs were fabricated from the APTES and TEOS precursors and modified to carboxyl SAMs from the octyl-SAMs, and hybrid-SAMs from the amine-SAMs. Various volume ratios of the silane precursors were utilized for the mixed SAMs formation. Following ratios of the amine to octyl were utilized for the experimentation: 9:1, 8:2, 7:3, 6:4, 5:5, 4:6, 3:7, 2:8, and 1:9 along with the precursor SAMs at both ends as the control modification forming the AO series of the SAMs formation on the Ti6Al4V substrates. AO series samples were treated with the acidified $KMnO_4$ to form the AC series. In addition, HO series samples were formed upon the reaction of the AO series samples with the p-tolyl isocyanate in the presence of the dibutyltin dilaurate as the catalyst. HC series samples were formed when the native amine-SAMs and octyl-SAMs were converted to hybrid and carboxyl-SAMs, respectively. For the AO series samples, the highest water contact angle was for the octyl SAMs (105.6±2°) followed by the AO19 (101±1°), which gradually decreased with the decrease in TEOS fraction in the successive mixed SAMs ratios, and the least was for the amine SAMs surface (66.7±2°) as shown in **Fig. 3.1**. In the case of DIM for the AO series samples, the highest values were for the octyl SAMs (63.9±1.5°) followed by the AO19

(61.9±2.6º) and gradually decreased in the series and the least being for the amine SAMs (46.8±1.6º). Based on the MQ and DIM contact angle data for the AO series, surface energy was calculated using equations 1 and 2. The highest surface energy was calculated to be for the amine-SAMs surface (46.2±1.3 mJ/m^2), followed by the AO91 (43.6±0.5 mJ/m^2), which gradually decreased with the change in the precursor ratios and was least for the octyl SAMs surface (26.5±1 mJ/m^2) as depicted in **Fig. 3.1**. Here in the graph, X-axis represented the percentage of the silane used for the functionalization and that need not be the functionalized on the surfaces in the exact percentages depending on the reaction rate of different silane moieties. Similarly, the silane percentages mentioned in the X-axis throughout the thesis represented the actual silane percentages used for the functionalization, otherwise mentioned in the caption.

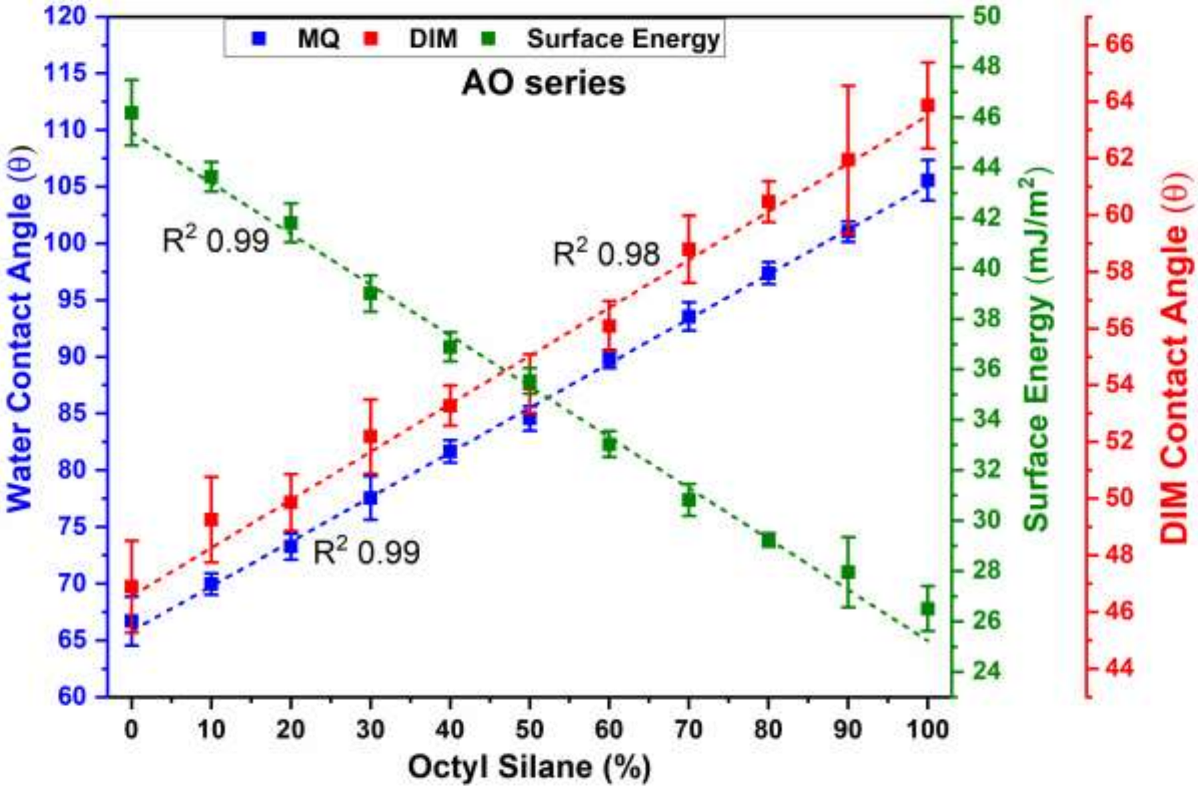

Figure 3.1: Contact angle measurement of the AO series samples with MQ and DIM; dotted lines represent the fitted data

In the AC series samples, the water contact angle was the highest for the amine SAMs (65.1±2.9º), which gradually decreased in the series as follows AC91 (64.4±1.2º)>

AC82(61.9±1.4°) and so on and least for the carboxyl SAMs surface (49±1.5°). A similar trend was followed for the DIM contact angle, with amine SAMs as the highest (46.6±1°) and least for the carboxyl SAMs (39.3±1°). The surface energy trend for the AC series was inverse to the water and DIM contact angles, with carboxyl SAMs samples having the highest surface energy (58.5±1 mJ/m^2) followed by the AC19 (57±0.5 mJ/m^2), AC28 (55.9±0.5 mJ/m^2) and so on and least being for the amine SAMs surface (47.1±1.5 mJ/m^2) as shown in **Fig. 3.2**.

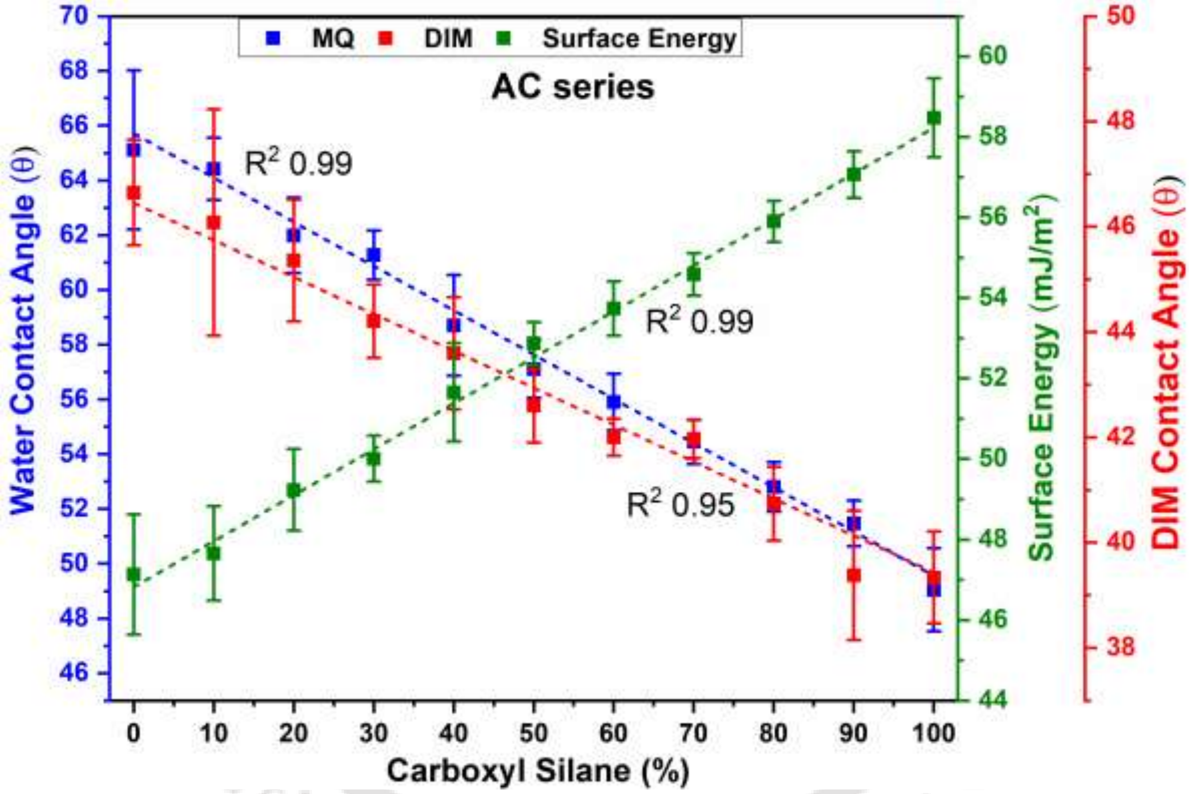

Figure 3.2: Contact angle measurement trend of the AC series samples with respect to the MQ and DIM, dotted lines represent the fitted data.

HO series samples were formed by the post-modification reaction of the octyl terminal with the p-tolyl isocyanate via urea linkage. The characterization based on the surface features, water, and DIM contact angle was measured on the HO series samples, followed by calculating the individual surface energies based on equations 1 and 2. The highest water contact angle was measured for the octyl SAMs surface (105.9±1.5°) followed by the HO19 (103.5±1.6°) < HO28 (101.7±0.8°) and so on, with the least for the hybrid-SAMs (87.3±0.5°). The same trend was also observed for the DIM contact angle with the octyl-SAMs (63.2±2°) > HO19

(62.8±1.2º) > HO28 (61.2±1.3º), so on, and the least for the hybrid-SAMs (51.6±1.8º). Surface energy values deduced based on the MQ and DIM contact angle values are inverse to the contact angle data with the highest surface energy for the hybrid-SAMs (35.8±0.8 mJ/m^2) > HO91 (35±0.5 mJ/m^2) > HO82 (33.8±0.5 mJ/m^2), so on and least for the octyl-SAMs surfaces (26.8±1.2 mJ/m^2) as shown in **Fig. 3.3**. The highest surface energy value signifies the tendency of the surface for a higher rate of adhesion or binding on the surface to minimize the overall free surface energy from the substrate. It might occur due to the attachment of the proteins or the adhesion of the bacteria or cellular components on the surface, making the surface susceptible to biofouling. However, it also signifies a higher potential for surface engineering to be flexible and form the next generation of biomaterials [306].

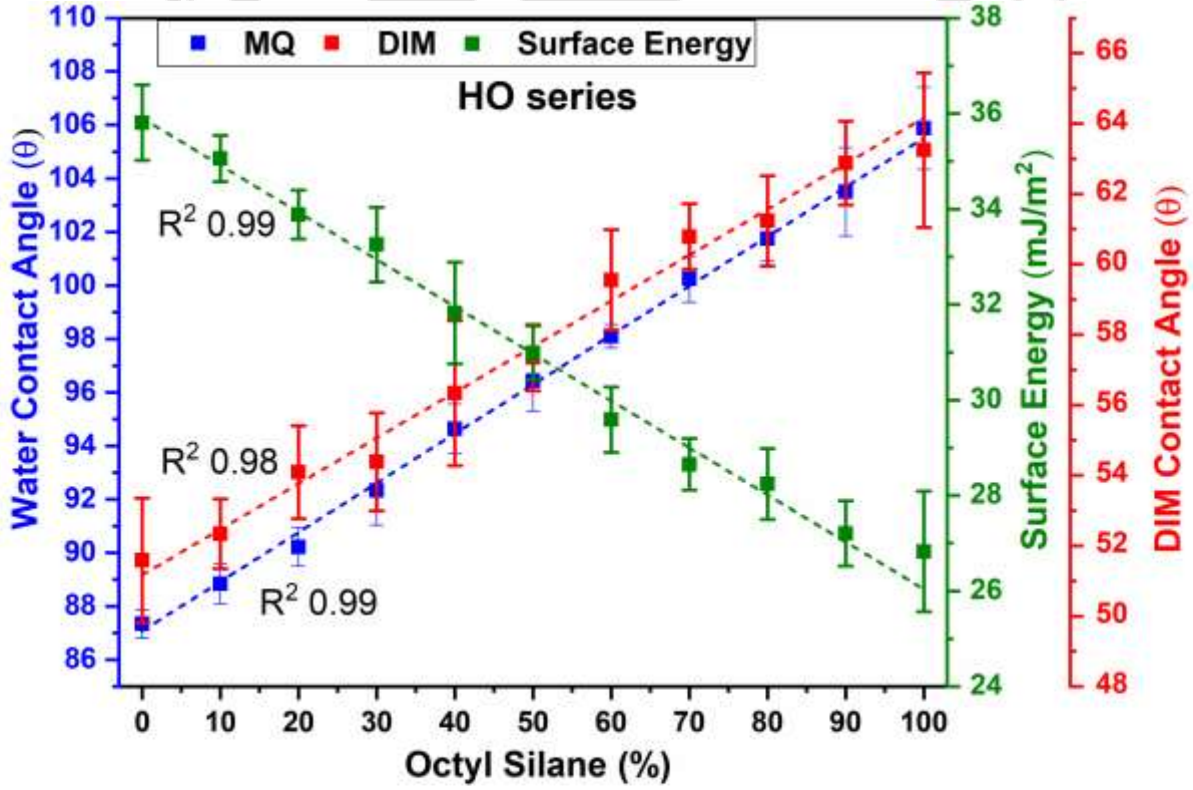

Figure 3.3: Contact angle data of the MQ and DIM for the HO series samples, fitted data is represented by the dotted lines

Amine-SAMs undergo post-modification to form hybrid-SAMs, and octyl-SAMs undergo post-modification to form the carboxyl-SAMs. So, the HC series samples involve double post-modification of the base SAMs attached to the Ti6Al4V surfaces. Water contact angle measurement on the functionalized surfaces revealed the highest value for the hybrid-SAMs surface (86±1º), proceeded by the HC91 (83±1.3º) > HC82 (79.5±0.8º), and so on, least water contact angle for the carboxyl-SAMs (52.1±1.7º). Similar decreasing behaviour was exhibited by the DIM contact angle for the HC series samples as follows: hybrid-SAMs (53.1±0.9º) > HC91 (51.7±0.6º) > HC82 (49.9±0.8º) and follows,s with the minimum angle exhibited by the carboxyl-SAMs sample (38.3±0.7º). Inverse behaviour was again exhibited by the trend for the surface energy values of the HC series samples, as follows; carboxyl-SAMs (56.9±1 mJ/m^2) > HC19 (56±0.8 mJ/m^2) > HC28 (53.5±1.2 mJ/m^2) and so forth with the least surface energy for the hybrid-SAMs (35.5±0.5 mJ/m^2) as quite clear from the data depicted as graph in **Fig. 3.4**.

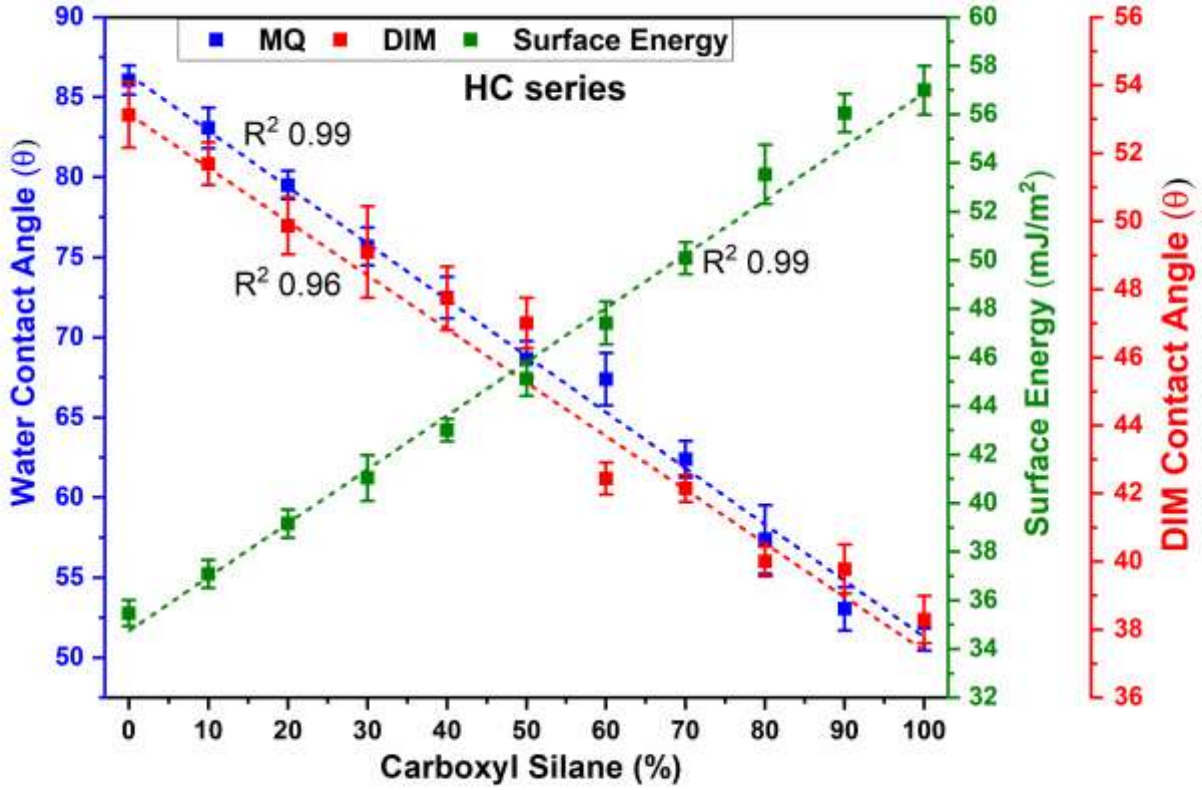

Figure 3.4: Contact Angle measurement of the HC series samples for the MQ and DIM, dotted lines represent the fitted data

3.4.1.4 Surface Energy and Carboxyl SAMs formation kinetics:

Material surface is the mediator in determining the fate of the biomaterial in the physicochemical microenvironment [307]. The surface energy of the modified substrates was determined using the MQ and DIM contact angles. Octyl-SAMs samples (0 min) showed the lowest surface energy (26.7±0.5 mJ/m^2), and the highest surface energy for the respective $KMnO_4$ concentrations (conc) was exhibited by the 150 min incubated samples, indicating the conversion of most of the octyl SAMs to carboxyl SAMs. Surface energy for all the $KMnO_4$ conc was further peak fitted using the ExpDec1 function in the OriginPro software, as shown in **Fig. 3.5**, to obtain the parameters related to the saturation surface energy, plateau time point, and time constant along with the derived parameter of saturation rate:

$$y = A1 * exp(-x/t1) + y0 \tag{3}$$

where, A1 is the amplitude and t1 is the time constant

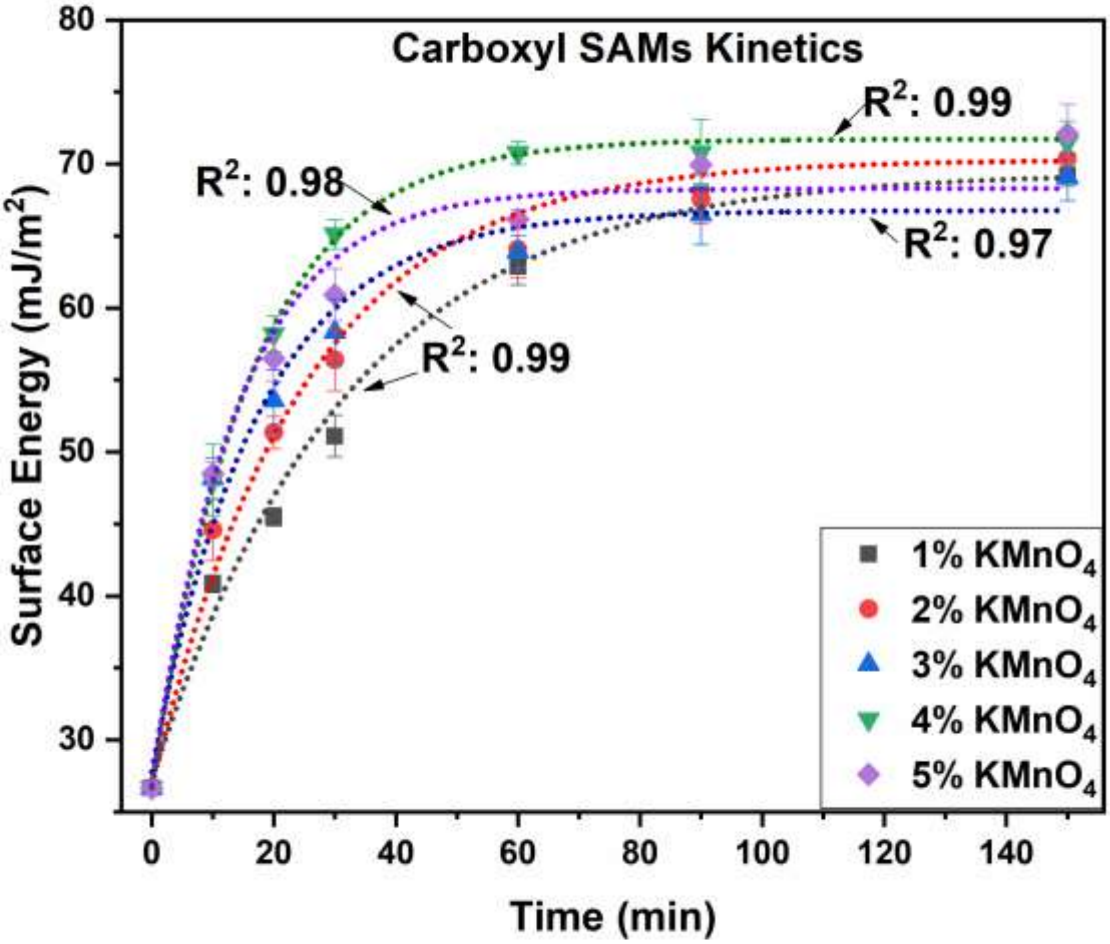

Figure 3.5: Graph showing the change in the surface energy of the octyl-SAMs modified Ti6Al4V substrates with the various concentrations of the acidified KMnO4 for the conversion to carboxyl-SAMs at variable time

Octyl SAMs surfaces incubated with 1% acidified $KMnO_4$ conc showed the least rate of 0.031 min^{-1} (R^2: 0.99), which showed a linear increase with the increase in the $KMnO_4$ concentration as follows: 0.041 min^{-1} (2%, R^2: 0.99), 0.058 min^{-1} (3%, R^2: 0.97), 0.062 min^{-1} (4%, R^2: 0.99) and 0.072 min^{-1} (5%, R^2: 0.98) clear from **Table 2**. This indicated a faster acid hydrolysis with an increase in the $KMnO_4$ concentration. A higher percentage (5%) of the acidified $KMnO_4$ showed ~3.5 times faster change in the surface energy than the lower percentage (1%). Based on the above data, the octyl-SAMs modified Ti6Al4V substrates showed the best result with the 5% acidified $KMnO_4$ condition for carboxyl-SAMs conversion. Surface energy is a crucial factor, but it achieves synergism with the surface topography to get the best properties for the implant material design [308]. It has been observed in a study conducted by Scotchford *et al.* that the cell adhesion behaviour on the modified surfaces can be enhanced by increasing the surface energy [309]. Lim *et al.* conducted experiments to study the long-term effects of the surface energy on cell-biomaterial and overall cellular behaviour, i.e., cell growth and mineralization behaviour. Studies showed that surface energy was responsible for changes in spatial cell growth behaviour, especially in cell differentiation and biomineralization in osteoblast cells [310]. In another study, researchers fabricated a surface energy gradient surface to study the effect on the fibronectin-mediated adhesion and proliferation of the MC3T3-E1 cells with precoated fibronectin on the surface prior to cell incubation. It was found that a 10° rise in the water contact angle reduced the doubling time by twice, though for the majority part, fibronectin mediated cell adhesion was independent of the surface energy [311].

3.4.2 Attenuated Total Reflectance-Fourier Transform Infrared Spectroscopy (ATR-FTIR)

FTIR was performed in the ATR mode in the 4000-700 cm^{-1} range to characterize the successful silanization on the Ti6Al4V surfaces and determine the various functional groups that were present. Surface functionalization kinetics was also determined based on the FTIR data. Silanization was performed on the silica substrate (glass coverslip) first, followed by functionalization on the titanium and Ti6Al4V substrates.

3.4.2.1 Amine-, octyl- and mixed-SAMs

The substrate was functionalized with amine-SAMs and was confirmed by the change in the contact angle compared to the bare sample, which was further confirmed by the ATR-FTIR measurement. Si-O-Si bending was observed at 758 cm^{-1} and stretching at 1043 cm^{-1}, indicating the successful silanization and silane bond formation between the silica substrate and the silane molecules. Si-C stretching due to the Si-CH_2R group was confirmed by the 833 cm^{-1} and 1146 cm^{-1} peaks, firmly confirming the successful SAMs formation on the substrate due to the silane molecules [145, 299-301]. The presence of the amine terminal moiety was confirmed by the peak at 1511 cm^{-1} due to the amide group.

Surface modification was also carried out on the Ti6Al4V substrates with octyl- and mixed-SAMs formation, as shown in **Fig. 3.6**. Si-O-Ti bending was confirmed at the 740 cm$^{-1,}$ and peak at 1020 cm^{-1} was due to stretching of the Si-O-Ti bond, confirming the successful silanization and siloxane bond formation between the substrate and the silane molecule. Si-C stretching at 870 cm^{-1} and 1140 cm^{-1} was due to the Si-CH_2R groups, which further confirmed the silanization [145, 299-301]. Mixed-SAMs contain both TEOS and APTES in an equal volume ratio (1:1), which means both amine and octyl terminal groups were equally distributed throughout the Ti6Al4V surface. Mixed-SAMs contain a peak at around ~1500 cm^{-1} due to the amine group and 2920 cm^{-1} due to the octyl group of the mixed-SAMs, whereas octyl-SAMs contain a peak at ~2920 cm^{-1} due to the octyl moiety.

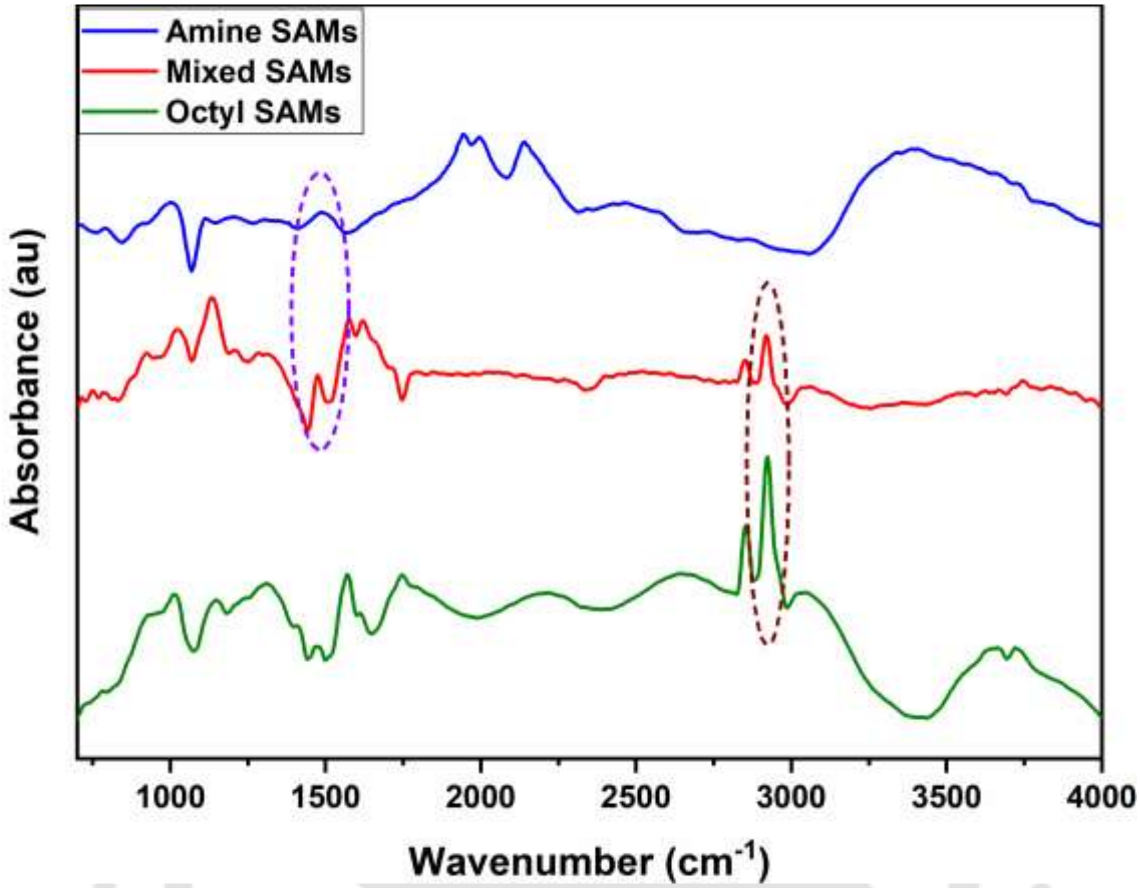

Figure 3.6: ATR-FTIR measurement of the amine-, mixed- and octyl-SAMs

3.4.2.2 Octadecyl-, hexadecyl-, mixed(hexadecyl-octyl)- and carboxyl(hexadecyl-octyl)-SAMs

Octadecyl-, hexadecyl-, and mixed-SAMs contain a peak at 2930 cm^{-1} due to -CH$_2$ stretching, while the carboxyl-SAMs contained a diminished portion of the -CH$_2$ stretching along with the peak centered at 1462 cm^{-1} due to hydroxyl stretching of the carbonyl group as shown in **Fig. 3.7**. Individual peak areas of all the SAMs functionalized surfaces in the -CH$_2$ stretching region were calculated using the OriginPro software to establish the relationship between the carbon chain length and the peak areas. Octadecyl-SAMs had the highest peak area (0.158±0.007), followed by the hexadecyl-SAMs (0.114±0.014), mixed-SAMs (0.05±0.005), and carboxyl-SAMs (0.059±0.002) as evident from the **Fig. 3.8**.

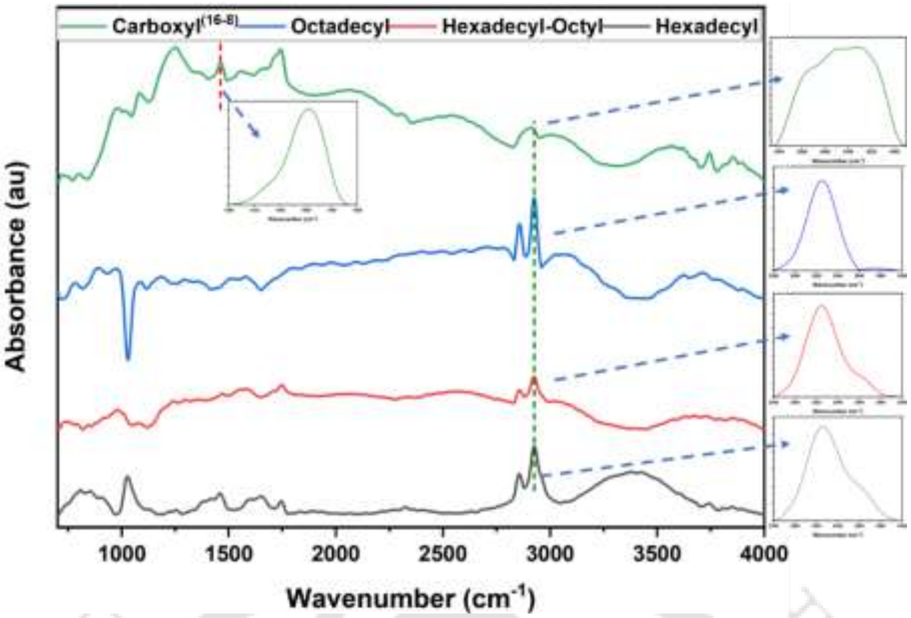

Figure 3.7: ATR-FTIR measurement of the hexadecyl-, octadecyl-, mixed-(hexadecyl-octyl) and carboxyl-(hexadecyl-octyl) SAMs functionalized Ti6Al4V surfaces

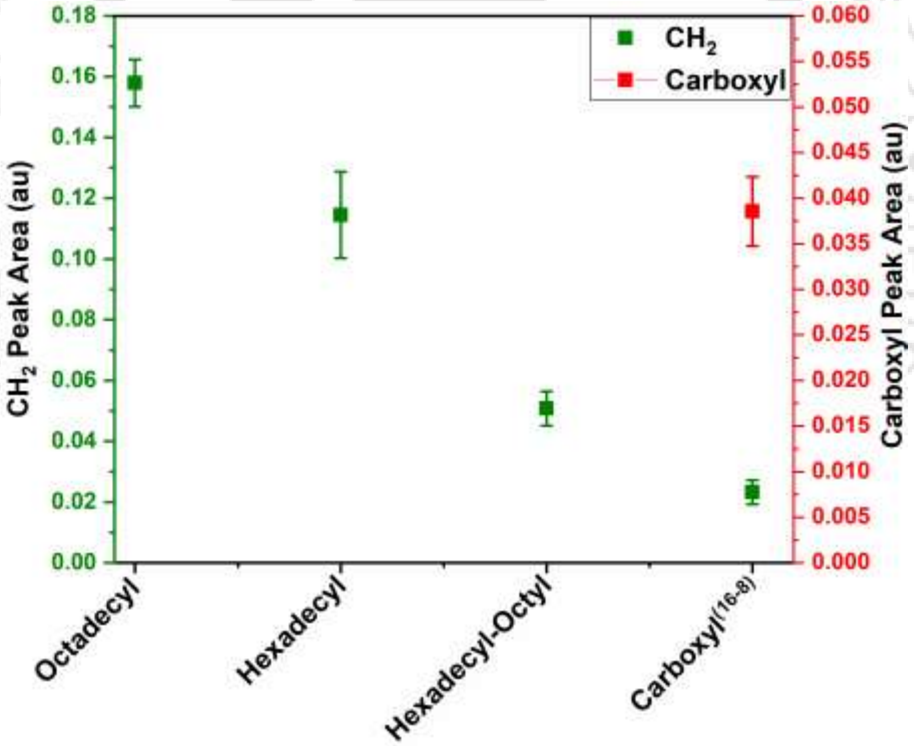

Figure 3.8: ATR-FTIR peak area of the modified surfaces in the CH$_2$ stretching region and for the amine group

3.4.2.3 Variable ratio mixed SAMs of amine-octyl, amine-carboxyl, hybrid-octyl, and hybrid-carboxyl silane

AO series samples involve the variable volumetric ratios of the precursor’s amine and octyl.

ATR-FTIR was carried depicting the peaks at ~760 cm^{-1} due to the Si-O-Ti bending and ~1020

cm^{-1} peak for the Si-O-Ti stretching with slight variation throughout the series, confirming the successful silanization on the Ti6Al4V surfaces. Peaks at 880 cm^{-1} and ~1136 cm^{-1} with slight variation among the samples in the AO series due to siloxane bond formation, further confirming the successful silanization as shown in **Fig. 3.9(a)**. Peaks due to the amine group were prominent in the range 1500-1600 $cm^{-1,}$ and the peak due to the octyl group in the range of 2880-2985 cm^{-1} as depicted in **Fig. 3.9(b & c)**, along with the trend in the peak area of the amine and octyl group in the AO series samples in **Fig. 3.9(d).** The highest peak area of the amine group was exhibited by amine-SAMs (0.36±0.02) > AO91 (0.26±0.03) > AO82 (0.19±0.03) and so on, showing a gradual decrease in the peak area and the least was for octyl-SAMs (0.017±0.004). As evident, the peak area trend for octyl group was opposite to the above trend, with octyl-SAMs having the highest peak area (0.66±0.02), followed by AO19 (0.46±0.04) > AO28 (0.4±0.008) and it keeps on decreasing in the following direction up to amine-SAMs surface (0.025±0.004), decrease and increase in the peak area for the two considered functional groups is slightly exponential. Actual ratios of the precursor silanes functionalized on the Ti6Al4V surfaces can be determined using the amine group peak area as the basis for the amine surface fraction investigation, C_{amine} using the protocol of another research group [312] as follows:

$$C_{amine}(\%) = \left(1 - \frac{AO_{series} - A_{octyl}}{A_{amine} - A_{octyl}}\right) \times 100$$

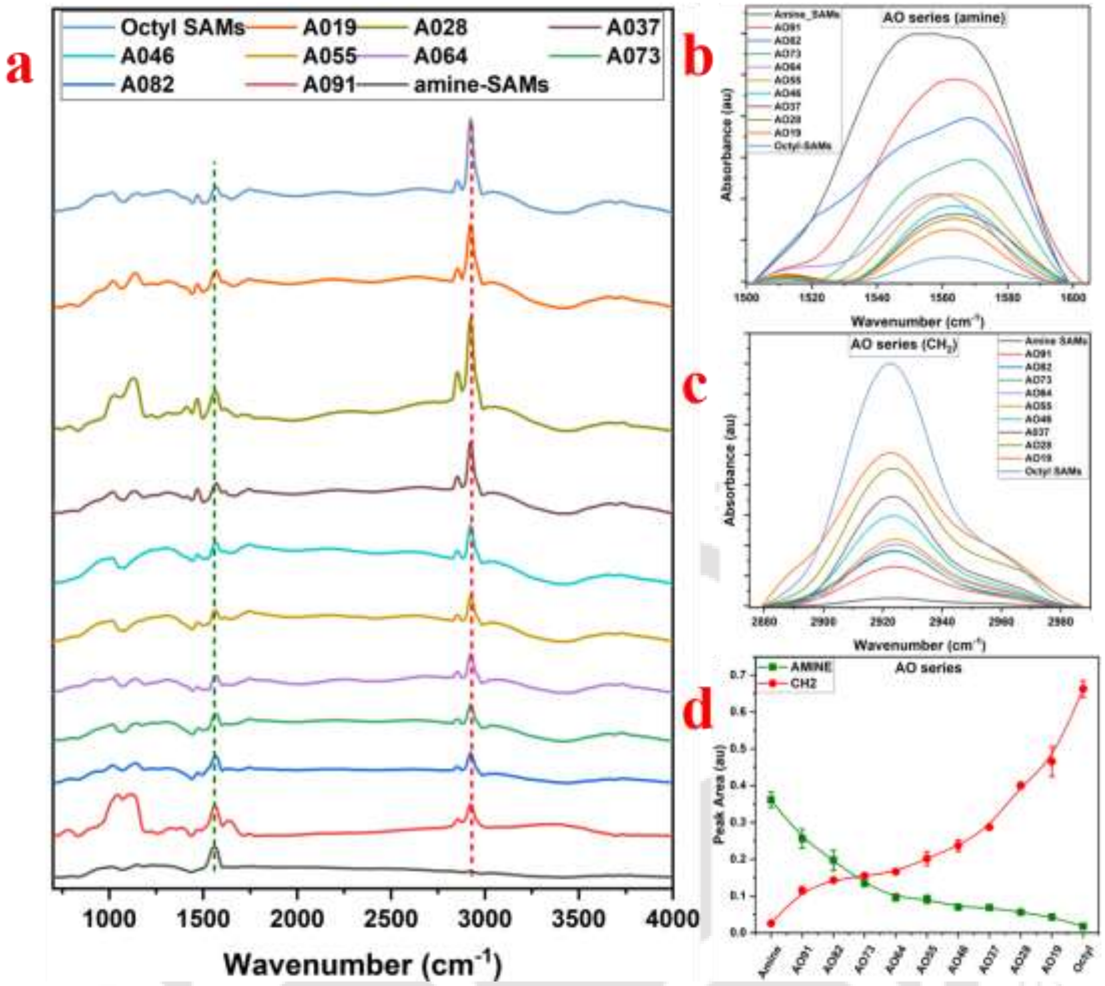

Figure 3.9: (a) ATR-FTIR in the 400-700 cm^{-1} region for the AO series SAMs modified Ti6Al4V substrates, (b) FTIR peak area for the AO series samples due to the amine group, (c) FTIR peak area due to the CH$_2$ stretching, (d) change in the peak area trend due to the APTES and TEOS ratios for the AO series samples

For the AC series samples, AO series samples were further modified using acidified KMnO$_4$ to convert the octyl terminal into the carboxyl. In the ATR-FTIR measurement, peaks at ~780 cm^{-1} and ~1040 cm^{-1} with slight peak shifts throughout the AC series due to bending and stretching due to Si-O-Ti confirming the successful silanization. Si-C stretching at ~1140 cm^{-1} and ~850 cm^{-1} with slight variation throughout the series due to Si-CH$_2$R groups further confirming silanization on the surface, as shown in **Fig. 3.10(a).** AC series samples contain the uniform distribution of the octyl and amine-SAMs depending on the ratios of the precursor silane moieties. FTIR peaks in the range of 1458-1638 cm^{-1} were utilized to assess the behaviour of change in the peak area of the amine terminal, reflecting the proportion of the amine-SAMs present throughout the modified Ti6Al4V surfaces as shown in **Fig. 3.10(b)**. Carboxyl-SAMs moieties also decreased in number throughout the modified surfaces as the relative ratio of the carboxyl decreased in the series, investigated by the FTIR peaks in the range 1350-1530 cm^{-1}, as shown in **Fig. 3.10(c)**. Carboxyl-SAMs showed the highest peak area of 0.176±0.012 for the carbonyl functional group, followed by AC19 (0.126±0.006) > AC28 (0.1±0.009) and so on, with the least for the amine-SAMs surface (0.007±0.0007). On the other hand, the least peak area for the amine group was for the carboxyl-SAMs (0.028±0.001) < AC19 (0.034±0.002) < AC28 (0.037±0.002) and others and amine-SAMs showed the least peak area of 0.2±0.02 as clearly visible from the **Fig. 3.10(d).**

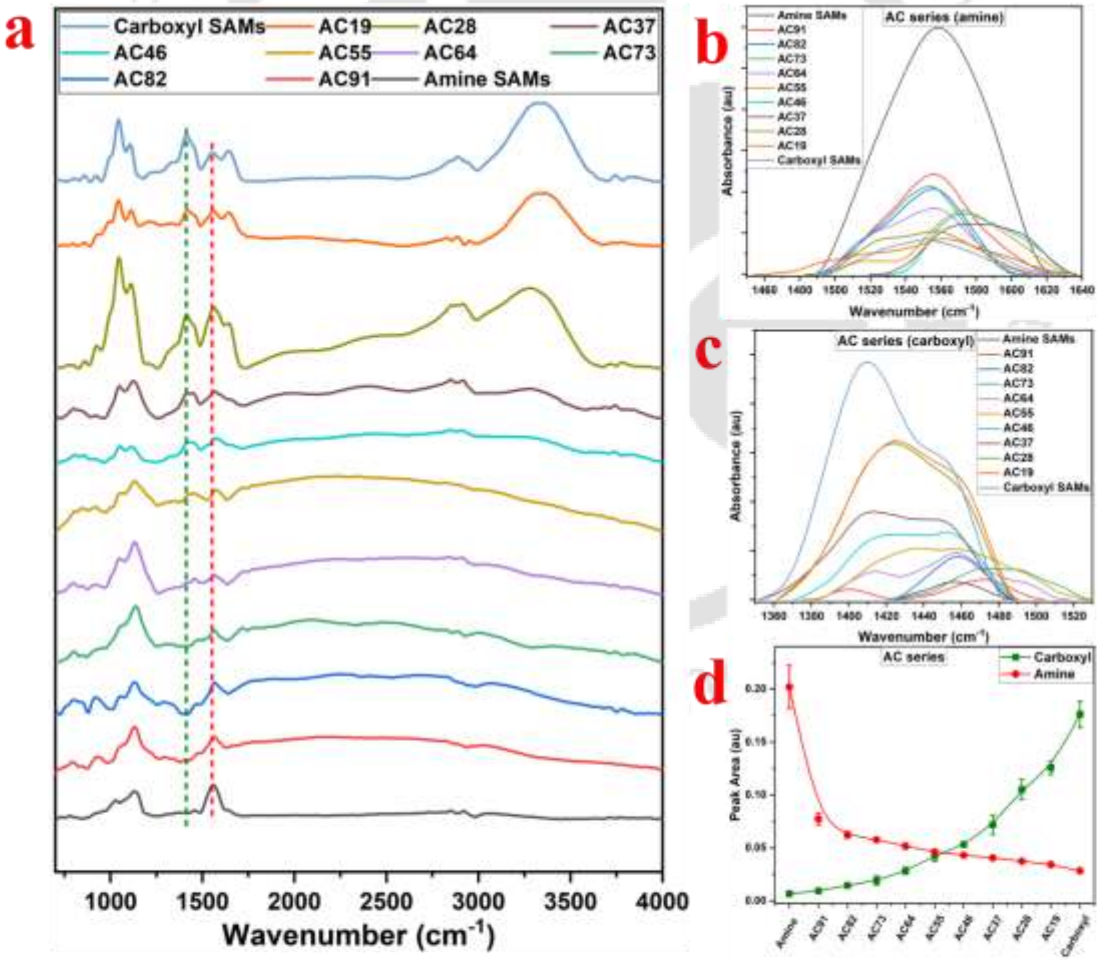

Figure 3.10: ATR-FTIR measurement of the AC series samples in the 4000-700 cm^{-1} range, (b) ATR-FTIR peaks for the AC series samples due to amine group, (c) FTIR peak due to the carbonyl group for the AC series functionalized surfaces, (d) peak area trend for the AC series samples due to the variation in the ratio of the amine and carboxyl ratios

ATR-FTIR measurement was carried out for a better understanding of the distribution of the various silane moieties across the modified surface and to confirm the successful silanization for the HO series samples; Silanization was confirmed by the Si-O-Ti bending (~760 cm^{-1}) and stretching (~1025 cm^{-1}) along with the Si-C stretching (~1145, ~870 cm^{-1}) due to the Si-CH$_2$R groups as shown in **Fig. 3.11(a)**. FTIR peaks corresponding to the hybrid and octyl moieties are shown in **Fig. 3.11(b and c)**, respectively. Changes in the peak area corresponding to the hybrid and octyl functional groups are mentioned in **Fig. 3.11(d)**. Investigation of the change in the peak in the range of the hybrid group showed the highest peak area for the hybrid-SAMs (0.065±0.005) and the least for the octyl-SAMs (0.003±0.001), the rest of the ratios of the two precursors fell in between the two control silanes. Inverse behaviour was observed for the change in the peak area of the octyl group, with the least for the hybrid-SAMs (0.078±0.005) and the highest for the octyl-SAMs (0.38±0.017), rest of the ratios in between the hybrid and octyl-SAMs groups as depicted in **Fig. 3.11(d).**

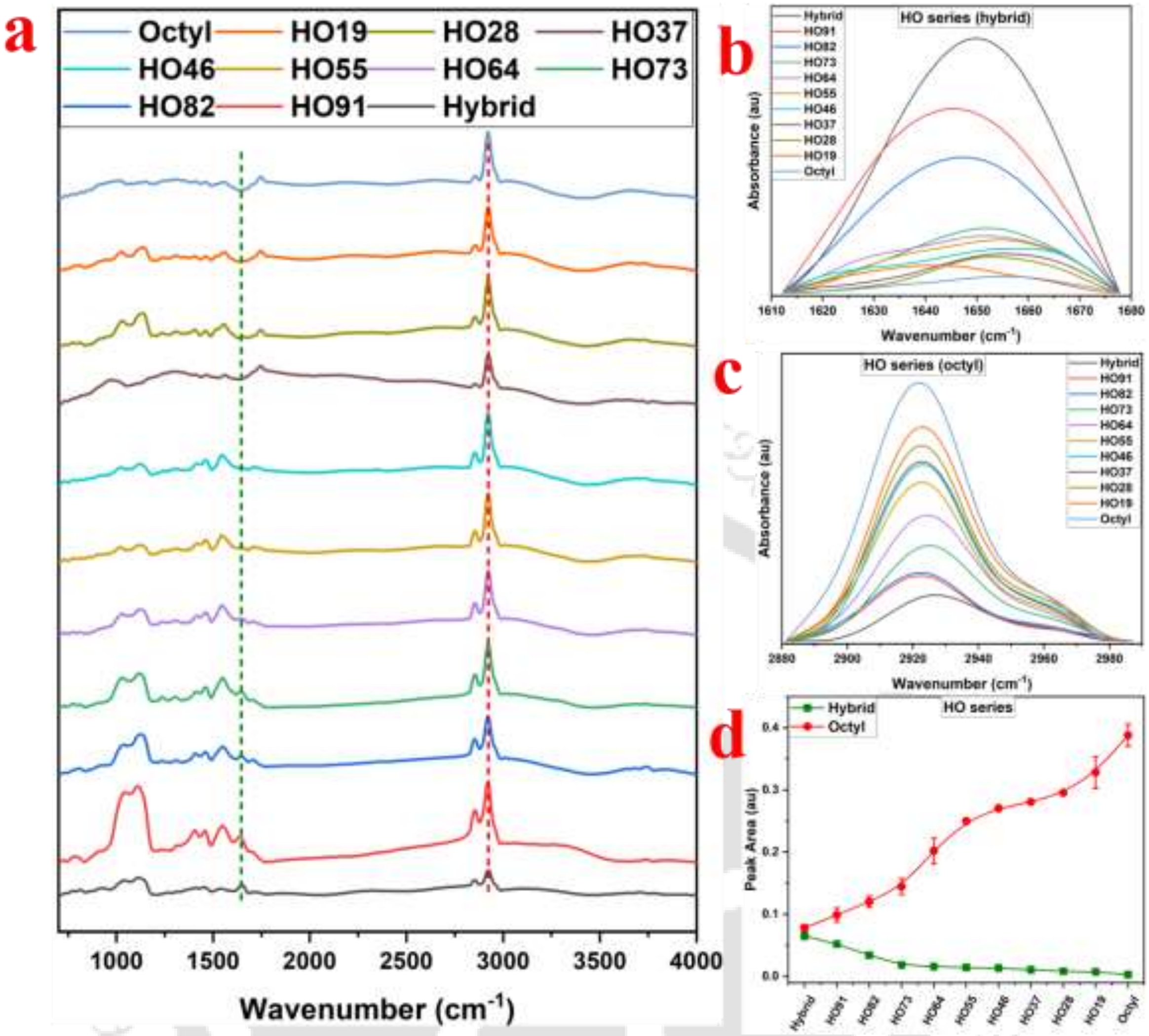

Figure 3.11: (a) ATR-FTIR graph of the HO series samples in the range of 4000-700 cm^{-1}, (b) FTIR peak due to the hybrid group of the HO series samples, (c) FTIR peaks due to octyl group present in the HO series samples, (d) change of the peak area of the hybrid and octyl groups due to change in the respective volume ratios of the precursor silane molecules

Similarly, the HC series was also characterized using the FTIR in the ATR mode. As apparent from the name, this series involves dual post-modification functionalization to the existing AO series samples and FTIR graphs shown in **Fig. 3.12(a)**. Changes in the peak area due to hybrid-SAMs and carboxyl-SAMs were predicted in **Fig. 3.12(b and c)**. Behavioural change in the peak area of the precursors with the relative change in the ratios throughout the series is shown in **Fig. 3.12(d)**. Peak area change in both the precursors is inverse, as in the case of the hybrid group, highest peak area for the hybrid SAMs (0.064±0.005) and least for the carboxyl-SAMs

(0.002±0.0007) whereas for the carbonyl group, least peak area exemplified by the hybrid-SAMs (0.007±0.001) and highest for the carboxyl-SAMs (0.22±0.02).

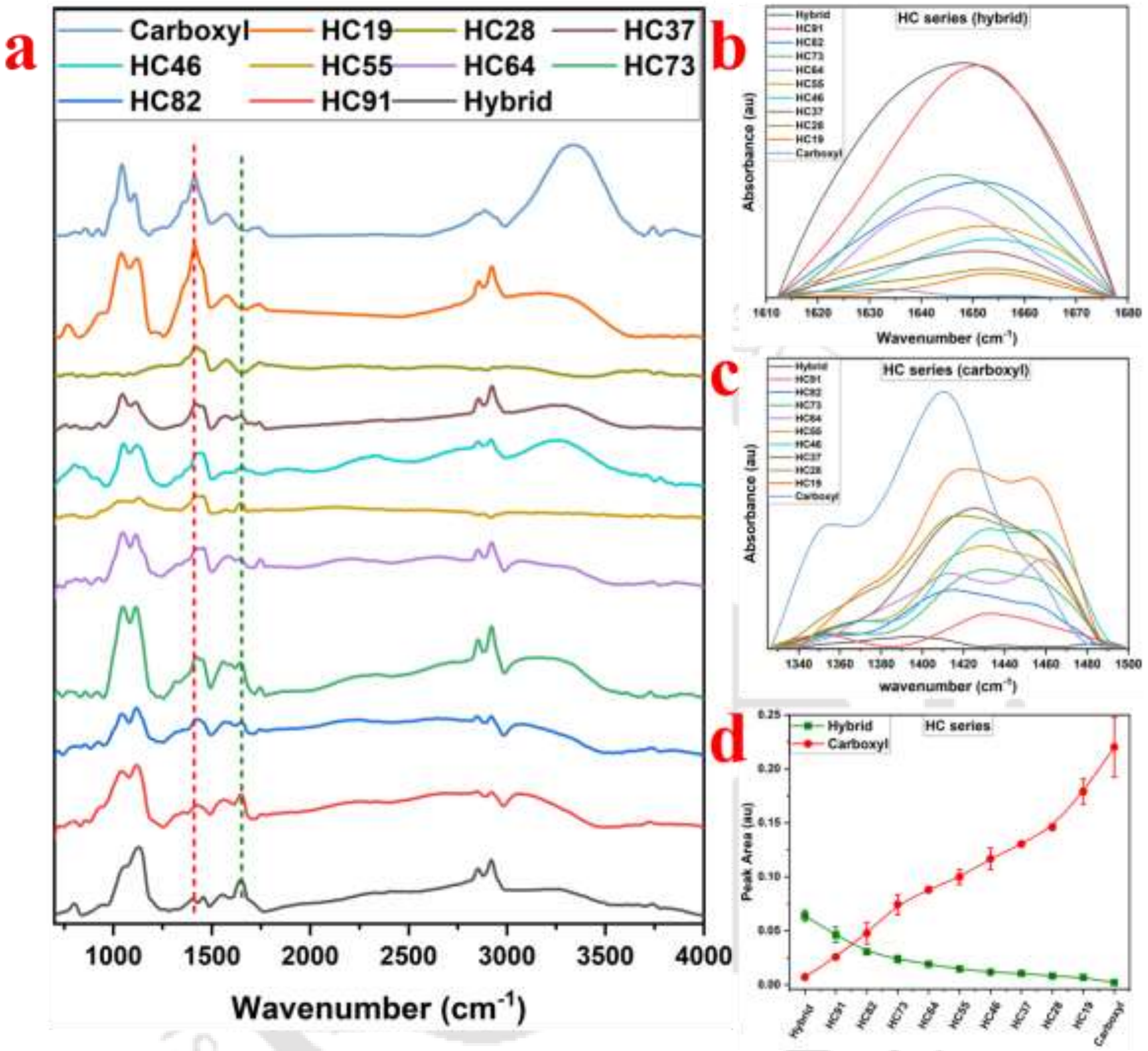

Figure 3.12: (a)ATR-FTIR graph showing change in the peak areas of the HC series samples in the 4000-700 cm-1 range, (b) change in the FTIR peaks for the HC series samples due to hybrid group, (c) FTIR peaks showing the change in the HC series samples in the carboxyl region, (d) trend showing the peak area change due to variation in the ratio of the hybrid and carboxyl precursors of the HC series samples

3.4.2.4 Carboxyl SAMs formation Kinetics:

In the current work, carboxyl SAMs formation occurs by the conversion of the terminal methylene moiety of the octyl SAMs to the carboxyl moiety. Elucidating the rate and trend of the carboxyl SAMs formation kinetics is the main theme of the current work. For the kinetics, surface energy derived from the contact angles (MQ & DIM) and ATR-FTIR mediated peak areas of the carboxyl and methyl groups were utilized. The formation of the carboxyl SAMs was reflected in the change in the surface energy of the modified substrates. On the same grounds, changes in the peak areas of the methylene and carboxyl moieties were utilized.

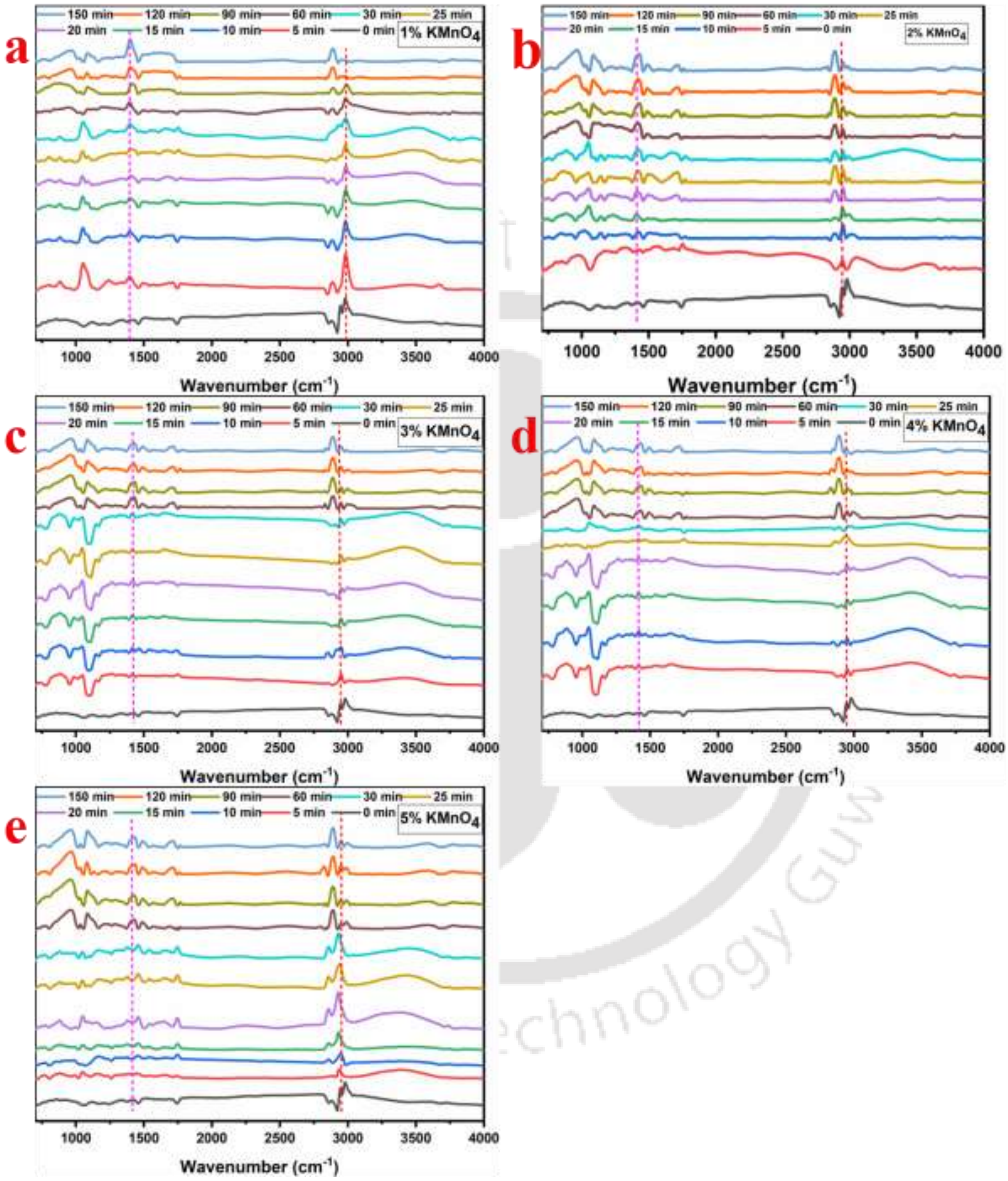

Figure 3.13: ATR-FTIR spectra of the octyl silane and carboxyl SAMs post modified Ti6Al4V samples, (a) 1% acidified $KMnO_4$ treated octyl SAMs substrates, (2) 2% acidified $KMnO_4$ treated samples, (c) 3% acidified $KMnO_4$ treated samples, (d) 4% acidified $KMnO_4$ treated samples, and (5) 5% acidified $KMnO_4$ treated samples.

Modified Ti6Al4V samples underwent FTIR measurement to elucidate the successful silane modification and compare octyl and carboxyl-SAMs. FTIR was recorded in the range of 4000-

700 cm^{-1} at RT in the ATR mode with a resolution of 4 $cm^{-1,}$ as shown in **Fig. 3.13**. Successful silanization and siloxane bond formation were confirmed by the peaks at 760 cm^{-1} and 1054 cm^{-1}, signature peaks for the bending and stretching due to Si-O-Ti[145, 301, 313, 314]. Silane-based SAMs formation on the Ti6Al4V substrates was cross-confirmed by the 880 and 1140 cm^{-1} for the Si-C stretching of the Si-CH_2R groups. Usually, the siloxane bond is attributed to the FTIR peak in 1300-800 cm^{-1} [315]. The presence of the octyl terminal moiety was confirmed by the peak of the asymmetric CH_2 stretching in the range of 2920-3030 cm^{-1} with a blue shift[62, 315], whereas successful post modification of the octyl SAMs to the carboxyl SAMs was confirmed by the carbonyl bending due to the carboxyl group in the range of 1350-1460 cm^{-1}, confirming the presence of the carboxyl group [316-319].

Carboxyl SAMs formation was monitored by determining the change in the peak area of the -CH_2 asymmetric stretching (2920-3030 cm^{-1}) due to terminal octyl moiety and carbonyl bending (1350-1460 cm^{-1}) due to terminal carboxyl moiety with a red shift [316-319]. Sun *et al.* found a peak at 1413 cm^{-1} due to carboxylate species arising due to the interaction of the carbonyl and hydroxyl groups [320]. **Fig. 3.14** exemplifies the change in the peak area due to the carbonyl bending of the carboxyl group of the modified terminal moieties. **Fig. 3.14(a, c, e, g, and i)** shows the increase in the FTIR peak area with the acidified $KMnO_4$ incubation time interval, whereas **Fig. 3.14(b, d, f, h, and j)** exemplifies the change in the peak area which is subjected to peak fitting using the BiDoseResp fitting function in the OriginPro software as shown below:

$$y = A1 + (A2 - A1)\left[\frac{p}{1 + 10^{(LOGx01 - x)h1}} + \frac{1 - p}{1 + 10^{(LOGx02 - x)h2}}\right] \tag{4}$$

where, A1 is the initial value of Y, A2 is the value of Y at the top plateau phase, LOGx01 & LOGx02 are the first and second EC50, p is the proportion, and h1 & h2 are the slope1 & slope 2, respectively.

In the above fitting data, we were interested in the Y value at the plateau phase (A2) and slopes (h1& h2), giving insight into the rate and onset behaviour of the carboxyl SAMs formation. Solver add-in in Excel was used to find out the value of time at the plateau phase (A2); samples incubated with 1% acidified $KMnO_4$ took 819.2 minutes to saturate, whereas saturation time drastically decreased with the increase in the acidified $KMnO_4$ concentration. Samples with 2% conc achieved saturation at 90.6 min, 3% conc at 82 min, 4% conc at 90.9 min and 5% conc at 91.4 min. An increase in the carboxyl peak area exhibited two slopes, i.e., varied rates. In the initial phase, samples were incubated with 1% (0.19 area/min) and 2% (0.26 area/min) conc showed a shallow rise of the peak area, i.e., the rate of change in the peak area was slow, whereas 4% (2.82 area/min) conc samples showed a medium rise and 3% conc (11.95 area/min) incubated samples showed the steepest rise in the peak area. Samples incubated with 5% conc of the acidified showed only one slope and completely lacked the initial slope. The second slope is shallow for all the samples, indicating a very small or little change in the peak area with the gradation of the time interval. There is a slight increase in the second slope up to 4% acidified $KMnO_4$ incubated samples, 1% (0.020 area/min), 2% (0.035 area/min), 3% (0.048 area/min), and 4% (0.057 area/min). It can be concluded that the rise of the change in the peak area at the carboxyl region gets saturated gradually with the increase in the concentration of the acidified $KMnO_4$ subjected to the conversion of the methylene terminal moiety of the octyl SAMs samples to carboxyl-terminal moiety of the carboxyl SAMs samples. Zhai *et al.* utilized the FTIR-based strategy to investigate the behaviour of the methoxy silane-based coupling agents for the hydrolysis kinetics. Temperature and acidity effect on the hydrolysis kinetics of the vinyltrimethoxysilane, (1H, 1H, 2H, 2H-perfluorooctyl) trimethoxysilane, (3, 3, 3-trifluoropropyl)trimethoxysilane, 3-chloropropyltrimethoxysilane, phenyltrimethoxysilane and 3-mercaptopropyltrimethoxysilane [321]. In another work by the same research group, the hydrolysis kinetics of the silane molecules was detected, and it concluded that kinetics followed second-order reaction kinetics with electrophilic substitution [322]. In a study carried out by Jonas *et al.*, triethoxysilane-based derivates were synthesized with succinimidyl ester being the headgroup (amine-reactive), termed as the linker silane and other silane termed as the matric silane with an unreactive ethylene -glycol headgroup. FTIR-based kinetics analysis was performed to determine the various reaction parameters. 1698 cm^{-1} peak of the succinimidyl ring was investigated, and 50 min was found to be the reaction completion time [323]. Suys *et al.* fabricated a biosensor by optimizing the conditions for 11-mercaptoundecanoic acid grafting and investigation using the ATR-FTIR strategy. The disappearance of the mercaptoundecanoic acid-COOH stretching and the appearance of the three ester bonds were monitored using the ATR-FTIR [324]. An in-situ kinetics based on a silicon dioxide-coated layer on the ATR crystal was utilized to detect for the detection of the diphenyl chlorosilane from the carbon tetrachloride solution using ATR-FTIR [325].

Carboxyl SAMs conversion can be cross-verified by the change in the CH_2 peak area and with the carboxyl peak area as shown in **Fig. 3.15(a, c, e, g, and i)**. Peak area change of both the functional groups was inversely related to one another, i.e., an increase in the carboxyl peak area will be reflected as a decrease in the -CH_2 peak area. Taking forward this hypothesis, we measured the ATR-FTIR of the samples in the region of 2920-3030 cm^{-1}[145, 326], calculated the peak area in the region, and carried out peak fitting of the data using the ExpDec1 fitting function in the OriginPro software as shown:

$$y = y0 + Ae^{-x/t} \tag{5}$$

where, y0 is the y offset, A is the amplitude, and t is the time constant

Samples incubated with 1% conc took longer to saturate (409.6 min), while saturation drastically reduced for the other samples and became constant (51.2 min), meaning there was no further decrease in the peak area beyond this time interval. The decrease rate was slowest for the 1% conc (0.07 area/min), highest for the 2% conc (0.49 area/min), and almost constant for other concentrations, 3% (0.41 area/min), 4% (0.40 area/min), and 5% (0.41 area/min), respectively **Fig. 3.15(b, d, f, h, and j)**.

FTIR region (3000-2800 cm^{-1}) corresponds to symmetric and asymmetric stretching due to the $-CH_2$ group. Naik *et al.* also studied the behaviour of the $-CH_2$ peaks for asymmetric and symmetric stretching with the passage of the incubation time in the case of octadecyl trichloro silane on the silica substrate. It was observed that alkyl chains of the silane showed a higher degree of disorder up to 30 minutes of the immersion time, but trans and rigid chain conformation was achieved by 1 hour of immersion time, indicating 1 hour is sufficient time to form crystalline SAMs on the surface [326]. However, for the silanization reaction to be completed correctly and for the orderly formation of the SAMs, our research group carried out the reaction for 24 hr under inert conditions. Real-time ATR-FTIR based quantification strategy was devised by Barros et al. to investigate the kinetics parameters for the extrusion process for the polymer-blends (PP/PA6) development [327]. In a research work contributed by Carrer *et al.*, percutaneous absorption models for the synthetic membrane systems based on lanolin for the trans-dermal drug delivery optimization. For the characterization of the lipid (lanolin), $-CH_2$ symmetric and asymmetric stretching vibrations were investigated via ATR-FTIR-based non-invasive technique. An increased in the vibrational frequency was observed, indicative of increased disordered conformational changes [328]. Further, ATR-FTIR was utilized to deduce the polymerization kinetics of various methacrylate monomers such as bisphenol A glycidyl methacrylate, hydroxyethyl methacrylate, and 10-methacryloyloxydecyl dihydrogen phosphate for various dental applications. The methacrylate peak at 1320 cm^{-1} was investigated to deduce the polymerization rate and conversion degree [298].

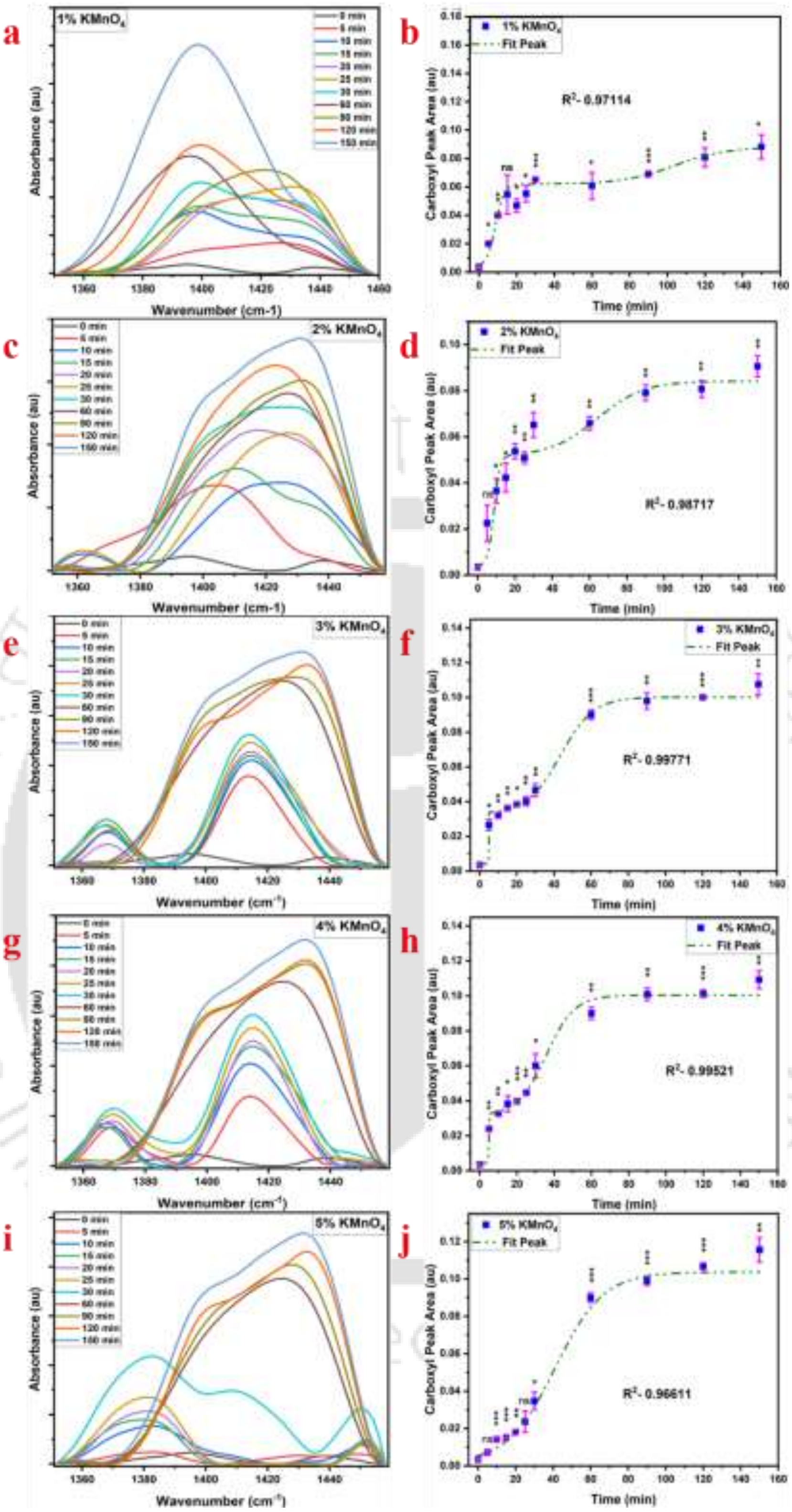

Figure 3.14: ATR-FTIR graph showing the change in the carboxyl group peak area; change in the ATR-FTIR peaks due to (a) 1%, (c) 2%, (e) 3%, (g) 4% and (i) 5% acidified $KMnO_4$; change in the peak area and peak fit due to, (b) 1%, (d) 2%, (f) 3%, (h) 4% & (j) 5%; all the p values were calculated in comparison to the control sample (0 min) using GraphPad Prism software, where ns > 0.05, * ≤ 0.05, ** ≤ 0.01, *** ≤ 0.001.

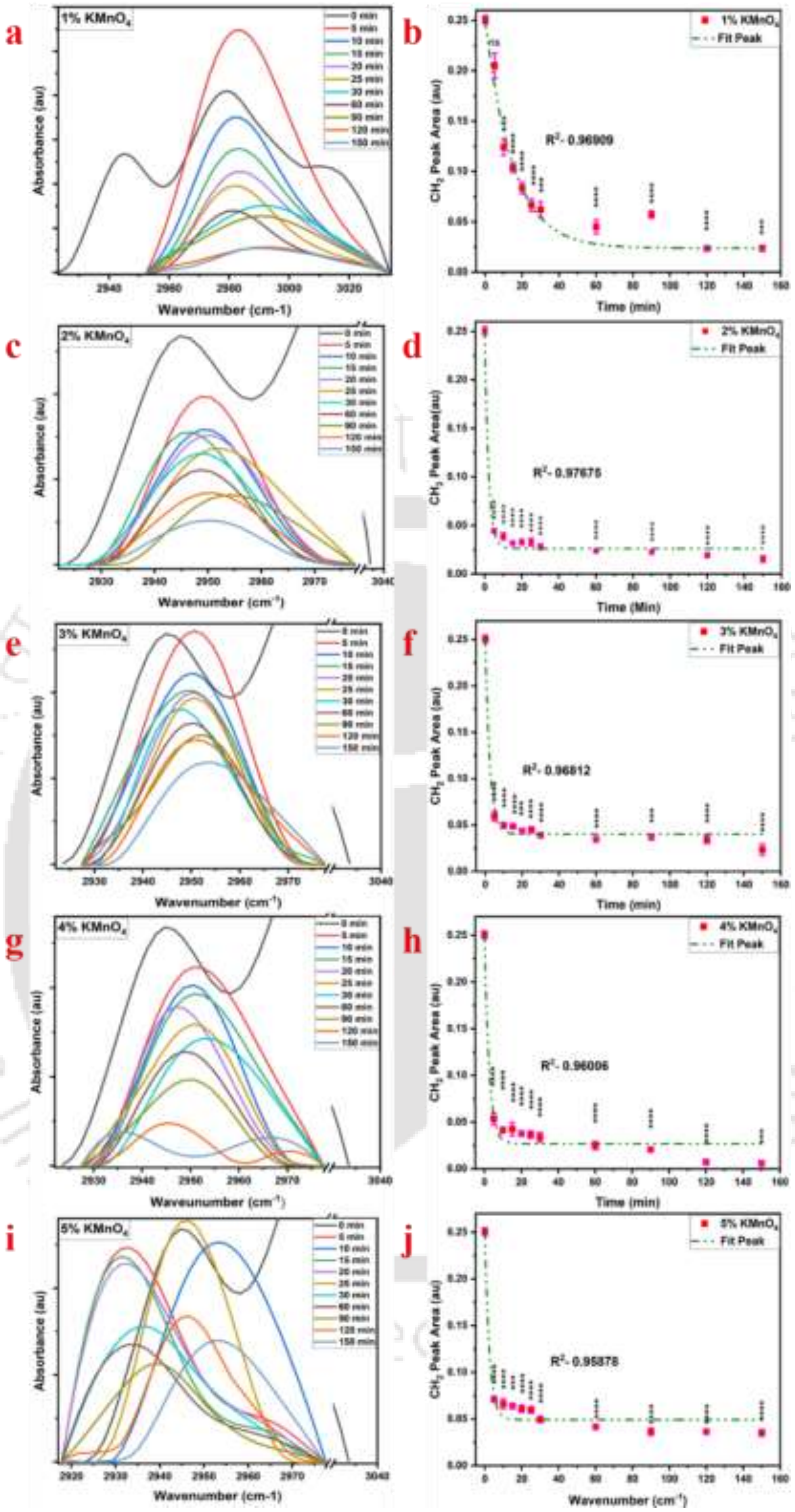

Figure 3.15: ATR-FTIR graph showing the change in the methylene group peak area; change in the ATR-FTIR peaks due to (a) 1%, (c) 2%, (e) 3%, (g) 4% and (i) 5% acidified $KMnO_4$; change in the peak area and peak fit due to, (b) 1%, (d) 2%, (f) 3%, (h) 4% & (j) 5%; all the p values are calculated in comparison to the control sample (0 min) using GraphPad Prism software, where ns > 0.05, * ≤ 0.05, ** ≤ 0.01, *** ≤ 0.001.

3.4.3 Thickness measurement

3.4.3.1 AO, AC, HO, and HC series:

The thickness of the silane SAMs fabricated on the Ti6Al4V surfaces was quantified using ellipsometry spectroscopy, as shown in **Fig. 3.16.** In the AO series, the following trend was observed: 1.89 (amine) < 2.09 (AO91) < 2.32 (AO82) < 2.34 (AO73) < 2.35 (AO64) < 2.38 (AO55) < 2.40 (AO46) < 2.43 (AO37) < 2.47 (AO28) < 2.52 (AO19) and 2.53 nm (octyl); AO series samples showed a two-phase increase in the thickness, first phase increased by a rate of 0.089 $\%^{-1}$ while the second phase increased by a rate of 0.0089 $\%^{-1}$. AC series exhibited an increase in the thickness the increase in the carboxyl moieties as follows: amine (1.89) < AC91 (1.92) < AC82 (2.09) < AC73 (2.16) < AC64 (2.24) < AC55 (2.33) < AC46 (2.38) < AC37 (2.59) < AC28 (2.67) < AC19 (2.91) and carboxyl (2.93 nm) with a slope of 0.01 $\%^{-1}$. SAMs thickness on the Ti6Al4V surfaces for the HO series increased in the following manner: 2.05 (hybrid) <2.15 (HO91), 2.14 (HO82), 2.09 (HO73) < 2.17 (HO64) < 2.20 (HO55) < 2.33 (HO46) < 2.42 (HO37) < 2.49 (HO28), HO19 (2.45) and 2.53 nm (octyl) with a slope of 0.005 $\%^{-1}$. On the other hand, the HC series showed a slope of 0.008 $\%^{-1}$ with the thickness trend as follows: 2.05 (hybrid) < 2.16 (HC91) < 2.25 (HC82) < 2.42 (HC73), 2.34 (HC64) < 2.58 (HC55) < 2.63 (HC46) < 2.65 (HC37) < 2.67 (HC28) < 2.79 (HC19) < 2.93 nm (carboxyl) as shown in **Fig. 3.16**.

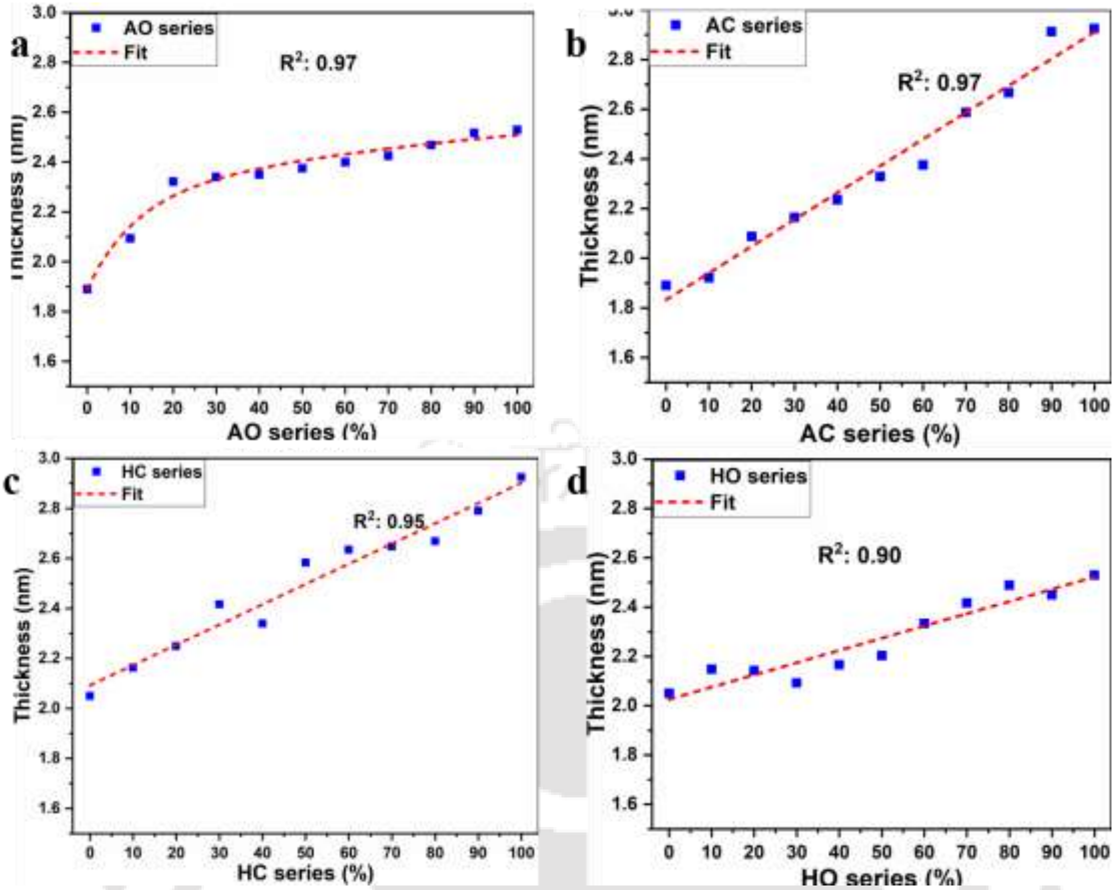

Figure 3.16: Graph showing the ellipsometer spectroscopy data of the thickness measurement of the silane SAMs of (a)AO-,(b) AC-,(c) HO-, and (d) HC- series samples.

3.4.3.2 Ellipsometry spectroscopic analysis of the long chain silane SAMs:

Octadecyl SAMs exhibited a chain length of 3.2 nm, while hexadecyl SAMs with a chain length of 36.5 nm. On the other hand, Carboxyl$_{(16-8)}$ showed the highest silane length of 3.33 nm due to the effect of the acidified potassium permanganate treatment, as the mixed$_{(16-8)}$ SAMs of same precursor silanes showed a thickness of 2.87 nm. Octyl SAMs with a thickness of 2.62 nm and amine with 1.91 nm gave rise to mixed$_{(amine-octyl)}$ SAMs with a thickness of 2.32 nm, as shown in **Fig. 3.17**.

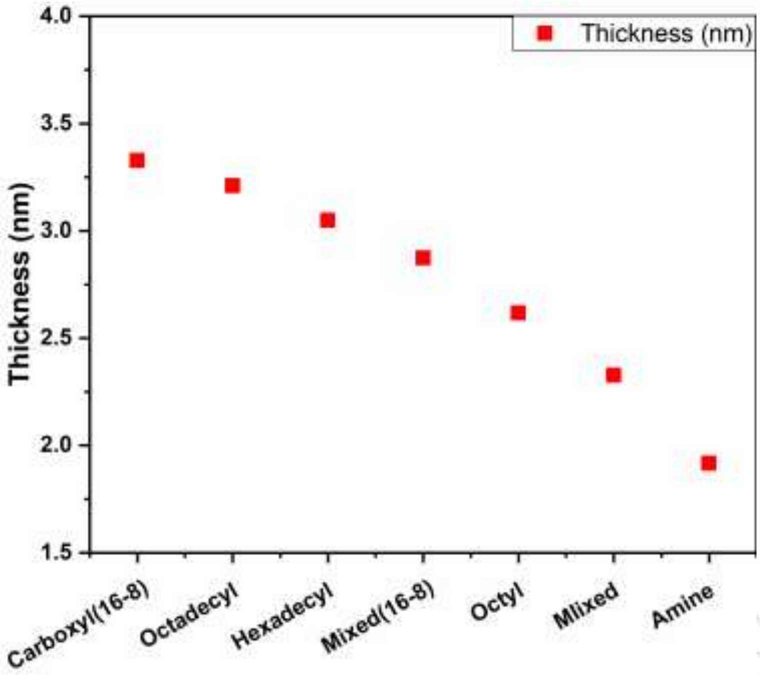

Figure 3.17: Graph showing the ellipsometer spectroscopy data of the thickness measurement of the silane SAMs on the Ti6Al4V surfaces.

3.5 Conclusion

Mixed SAMs incorporate the features of the involved silane precursor, as evident from the intermediate surface energy of the mixed SAMs and an increase in the SAMs moiety resulted in a rise in hydrophobicity. So, the AO-, AC-, HO-, and HC- series on the mixed SAMs were explored for various parameters to tune surface parameters. It was observed that the equal proportions of the precursor silanes resulted in intermittent hydrophobicity and surface energy. Carboxyl SAMs with varied acidified $KMnO_4$ and incubation time showed the lowest surface energy for the 0 min sample (26.7±0.5 mJ/m^2), which increased with the incubation time for all the conc of the acidified $KMnO_4$. 5% conc incubated samples took the least saturation time, while 2%, 3%, and 4% conc samples took twice the time to attain the saturation phase. Response time was also slow for the 1% conc, almost twice for the 2, 3, and 4 conc, while 1% conc took 5 times the response time. It was also observed that the decrease in the CH_2 peak area is inversely proportional to the rise in the peak area due to the carboxyl group. The thickness of the various silanes was quantified and showed the highest thickness for the octadecyl SAMs surfaces and the least for the amine SAMs surfaces.

Chapter 4

Bio-interfacial study of protein interaction with functionalized model implant surfaces

---

This chapter focuses on the protein adsorption studies (BSA, FBS, Col-I, and FN) on the silane-functionalized Ti6Al4V surfaces. BSA and FBS adsorption studies were performed on the AO-, AC-, HO-, and HC- series surfaces, followed by the carboxyl SAMs surfaces with varied acidified $KMnO_4$ and incubation time. Moreover, mixed$_{(16\text{-}8)}$ and carboxyl$_{(16\text{-}8)}$ SAMs were investigated for BSA adsorption insights, along with hexadecyl SAMs for protein adsorption (BSA, Col-I, and FN) investigation.

4.1 Introduction

Titanium and its alloy are a promising candidate for orthopedic implants. They exhibit many advantages, such as relatively low Young's modulus, fatigue strength, toughness, mechanical strength, biocompatibility, and corrosion resistance [41, 295-297]. Titanium has poor wear resistance and antimicrobial activity and a bioinert surface due to the formation of the titanium dioxide layer onto the surface [210, 329]. It hinders the chemical bonding and interactions between material and surrounding tissues. This leads to the micromotion at the implant site and prevents osseointegration. It also exhibits a stress shielding effect to a certain extent, which results in the wearing and generation of the debris and release [210] of the particles [330]. It may result in aseptic loosening and fibrous growth at the site, leading to the recruitment of the inflammatory agents and activation of the coagulation cascade [218, 331, 332]. Surface wearing may also release toxic vanadium and aluminum ions in the microenvironment, resulting in harmful side effects leading to implant failure [333].

Protein adsorption is the critical player in determining the biocompatibility of the implants. The implant surface comes in contact with the physiological microenvironment, and various proteins rapidly start adsorbing onto the surface and saturate it [189, 217]. So, protein adsorption is the crucial factor for the success of the implant and depends on the conformation, orientation, and nature of the proteins adsorbed on the surface. Protein adsorption study is important because it adsorbs onto the surface after water molecules and mediates between the implant surface and cells/tissues. Also, ECM secreted by the cells to the surroundings comprises proteins majorly [31, 98, 218].

Protein adsorption depends on the substrate, protein, and microenvironment properties. Adsorption is affected by the charge distribution, size, and conformation of the proteins along with topography, chemistry, cationic site, hydrophobicity, crystalline phase, composition, and surface charge of the substrate [189, 205]. The ionic strength, temperature, and pH of the microenvironment also affect protein adsorption [189]. The concentration, composition, and conformation of the adsorbed protein depend on the type of implant [212]. Protein adsorption occurs due to electrostatic interaction between charged adsorbent and oppositely charged amino acid side chains.

It has been observed that the success of the implant is determined by the surface properties rather than the bulk properties. Therefore, all the issues related to titanium and alloys can be addressed easily by modulating the surface properties. Enhancing the protein adsorption capability of the surfaces will lead to better osseointegration. Protein adsorption behaviour of the titanium surfaces can be easily tuned by using techniques such as physical (plasma spraying, electron beam sputtering, hydrothermal treatment, ion beam sputtering, surface roughness tuning)[15, 16], chemical (sol-gel method, electrochemical etching, anodization, silanization, apatite coating, electrochemical oxidation, doping of other elements) [17, 18, 20, 21, 41], and biological (surface protein grafting, bioactive molecule grafting) [22] modifications. Modification can tune the surface morphology, roughness, chemical composition, and surface chemistry. Modulating the surface morphology may lead to tuning biochemical signals related to cell adhesion and increasing the surface area, imparting better bone-implant mechanical interlocking. Extensive work has been carried out to overcome the disadvantages of titanium alloy implants [23, 24].

This chapter focuses on the protein adsorption studies (BSA, FBS, Col-I, and FN) on the silane-functionalized Ti6Al4V surfaces. BSA and FBS adsorption studies were performed on the AO-, AC-, HO-, and HC- series surfaces, followed by the carboxyl SAMs surfaces with varied acidified $KMnO_4$ and incubation time. Moreover, $\text{mixed}_{(16\text{-}8)}$ and $\text{carboxyl}_{(16\text{-}8)}$ SAMs were investigated for BSA adsorption insights, along with hexadecyl SAMs for protein adsorption (BSA, Col-I, and FN) investigation.

4.2 Materials and methods

Bovine Serum Albumin (BSA) [catalog no. A2153], lyophilized bovine fibrinogen (FN) [catalog no. F8630], and type-I collagen from calf skin (Col-I) [catalog no. C9791-10MG], were procured from Sigma-Aldrich. Sodium chloride (NaCl) [catalog no. MB023], potassium chloride (KCl) [catalog no.TC010], dibasic sodium phosphate (Na_2HPO_4) [catalog no. MB024], and monobasic potassium phosphate (KH_2PO_4) and SDS were procured from Himedia, India.

BSA stock solution was prepared in 1xPBS solution (pH 7.4) at RT conditions, and concentration was determined using the Implen spectro nanophotometer (Implen GmbH, Munich, Germany). followed by preparation of different dilutions (0.5, 1, 2, 3, 4, & 5 mg/ml). Likewise, fibrinogen (FN) stock was also prepared in PBS buffer at pH 7.4, followed by dilution preparations (5, 10, 20, 30, 40, 50 µg/ml) and added to the hexadecyl SAMs samples. Type-I collagen (Col-I) was mixed in 0.1M glacial acetic acid (1 mg/ml), followed by vortexing and storing at 4 °C to completely solubilize the protein in the buffer. After that, the collagen solution was diluted in the PBS solution to attain a pH of 7.4. Protein dilutions of 5, 10, 20, 30, 40, and 50 µg/ml were prepared, and hexadecyl SAMs (1x1 cm^2) surfaces were placed in the 24 well plates. Individual proteins with varied concentrations were added to the wells with the samples. Moreover, mixed solutions of BSA/Col-I, BSA/FN, and FN/Col-I were added to the samples at various concentrations and incubated for 2 hours at 37 °C. Post adsorption, the remaining protein solution was discarded, and samples were rinsed thrice with sterile PBS and kept aside. Samples were dried in the laminar flow hood and stored in a vacuum desiccator, followed by FTIR (Perkin Elmer, Spectrum Two) spectra measurement in the amide-I region under ATR mode. FTIR data in the amide-I region was deconvoluted in the OriginPro by taking the second derivative for deconvolution of the secondary structure of the various proteins.

4.3 Results and discussion

4.3.1 AO-, AC-, HO- and HC- series samples

4.3.1.1 BSA adsorption studies

AO series samples contained the varied percentage proportions of the amine and the octyl SAMs. BSA adsorption was performed at 37 °C for 2 hours under static conditions with 1 mg/ml BSA, followed by washing thrice with PBS and drying the protein adsorbed surfaces under laminar airflow and storage in a vacuum desiccator. Samples were quantified for protein adsorption by determining the change in the protein secondary structure in the amide-I region using FTIR, followed by protein deconvolution guided by the second derivative of the FTIR spectra as shown in **Fig. 4.1**. In the secondary structure, the percentage of β-sheet conformation increased with the increase in the octyl SAMs percentage, with a slight variation throughout the series. It varied in the following manner: 15±2 (amine), 25.7±0.7 (AO91), 29.2±0.7

(AO73), 31.2±1.4 (AO37), 32±0.4 (AO19), 35.2±1.9% (octyl). The bare Ti6Al4V surfaces showed a β-sheet percentage of 35.2±1.9%.

Similarly, there was a rise in the α-helicity with the rise in the octyl SAMs proportionality as follows: 46.2±2 (amine), 46.3±2.2 (AO82), 45.4±2 (AO73), 48.37±3.4 (AO64), 52.6±1.7 (AO55), 52.8±1.5 (AO46) and 51.4±1.2% (octyl). The bare substrate, however, showed alpha helicity of 55.4±3%. Amine SAMs (32.6±1.9%), octyl SAMs (10.5±1.5%), and a bare showed a β-turn proportion of 19.5±3 (**Fig. 4.2**). Silane-based mixed SAMs of carboxyl and amine were fabricated by another research group that investigated the adsorption behaviour and change in the secondary structure of fibronectin. Covalent binding or adsorption of the fibronectin on the functionalized surfaces resulted in the change in the β-turn conformation to the random coils with an increase in the β-sheet content. However, there was no significant change in the α-helicity of the native and surface-bound fibronectin [334].

Indian Institute of Technology Guwahati

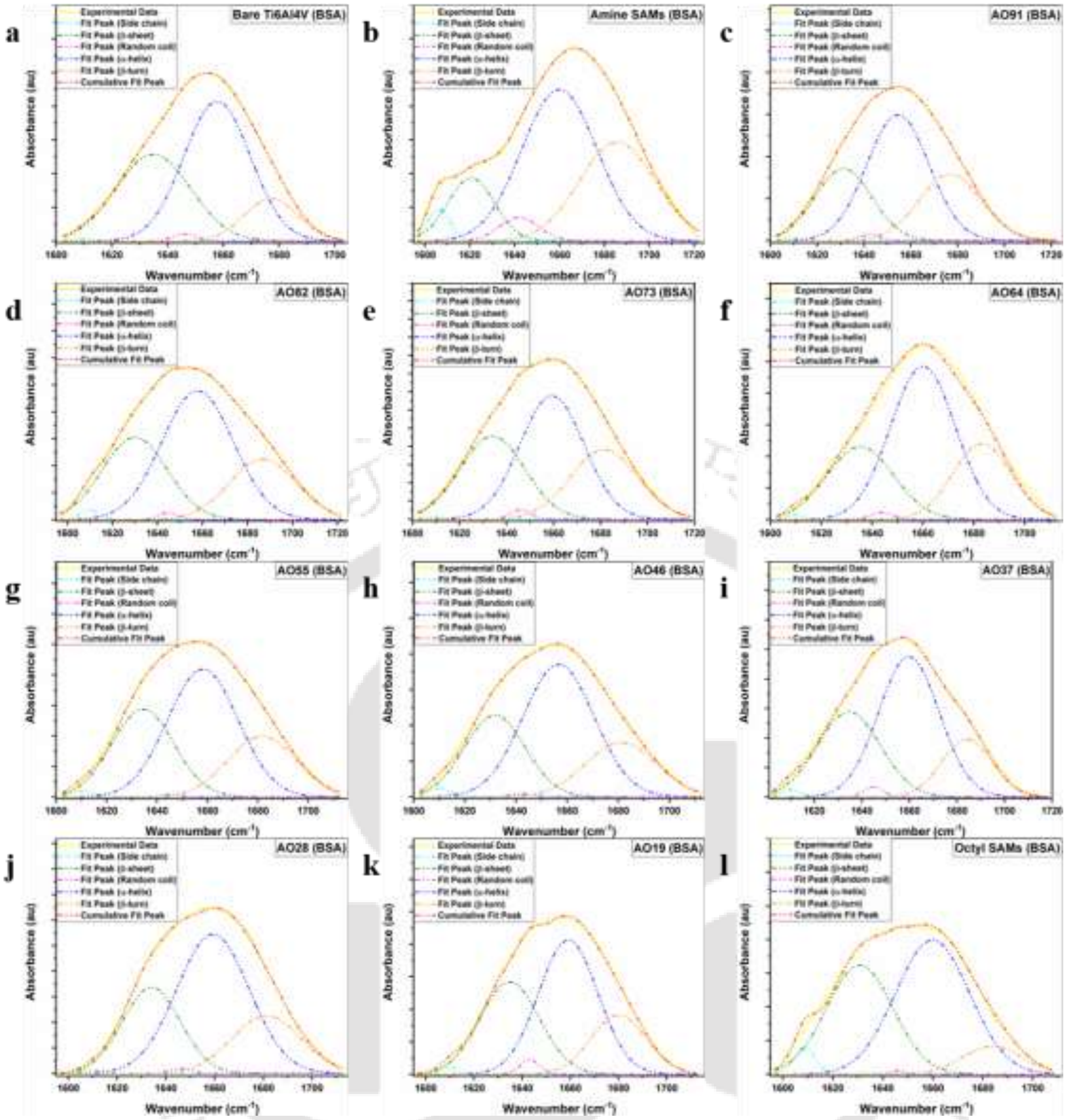

Figure 4.1: Graphs showing FTIR deconvolution of amide-I peak to investigate the change in the secondary structure of BSA on, (a) bare, (b) amine SAMs, (c) AO91, (d) AO82, (e) AO73, (f) AO64,

Institute of Technology

(g) AO55, (h) AO46, (i) AO37, (j) AO28, (k) AO19, and (l) octyl SAMs functionalized Ti6Al4V surfaces

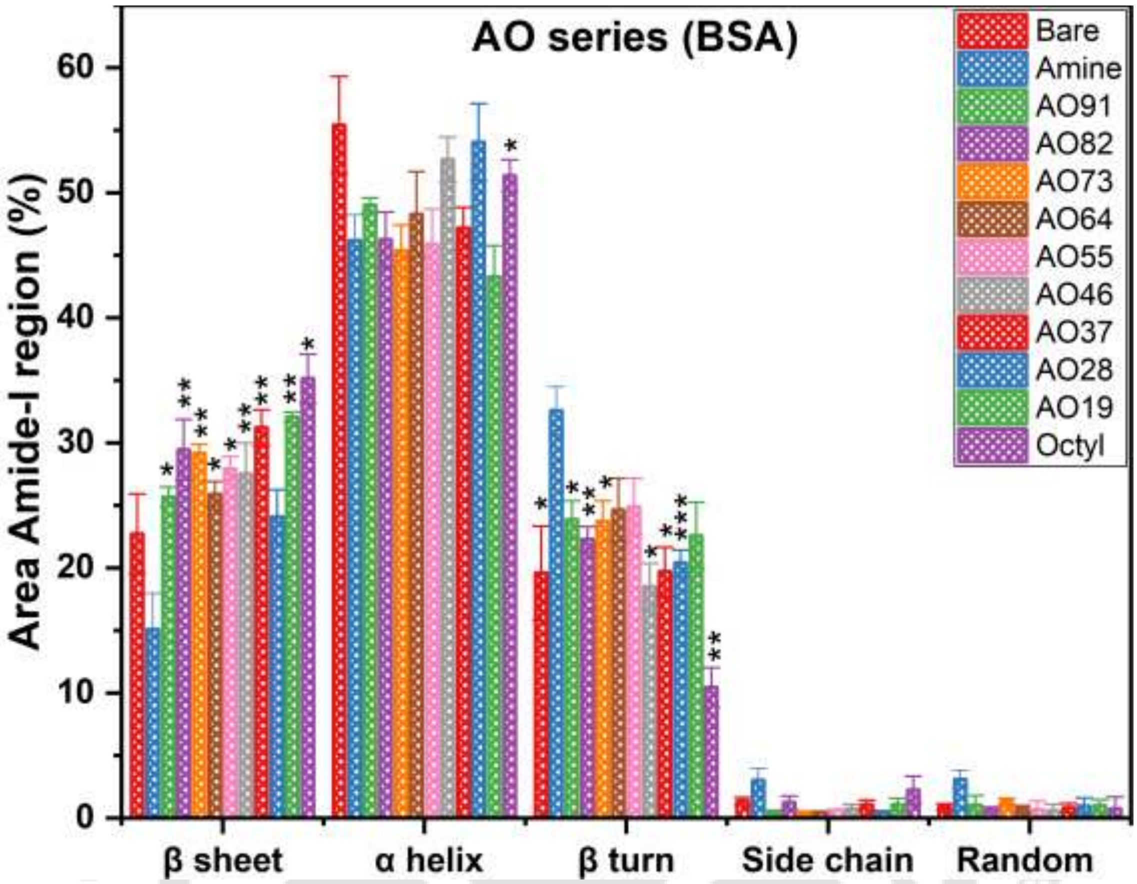

Figure 4.2: Bar graph showing the change in the secondary structure of the BSA in the amide-I region for the AO series samples; statistical analysis was performed using GraphPad Prism, where ns > 0.05, * ≤ 0.05, ** ≤ 0.01, *** ≤ 0.001.

Octyl SAMs underwent secondary modification to form the carboxyl SAMs, as mentioned in Chapter 3 in detail. So, the AC-series samples comprised primary (amine) and secondary (carboxyl) modifications at varying proportionalities. The secondary structure of the BSA exhibited an increase in the β-sheet conformation and a decrease in the α-helix conformations (**Fig 4.3**). The percentage decrease in the α-helicity was obtained as follows: 51±2 (amine), 50.9±2 (AC91), 42.7±2 (AC82), 42.6±1.1 (AC64), 40.7±5 (AC55), 40.2±3.7 (AC46), 36±5 (AC28), 37.8±2.4 (AC19), 39.7±19% (carboxyl), and 55±8% for the bare substrate. On the other hand, the rise in the β-sheet was in the following manner: 27.8±1.6 (amine), 28.6±1.8 (AC91), 42±2.9 (AC82), 48.9±3.6 (AC73), 46.6±0.9 (AC64), 48±1.1 (AC46), 53.3±3.5%

(carboxyl) with slight variation in the trend throughout the series. At the same time, there was no significant trend in the β-turn conformation in the series, as shown in **Fig. 4.4**.

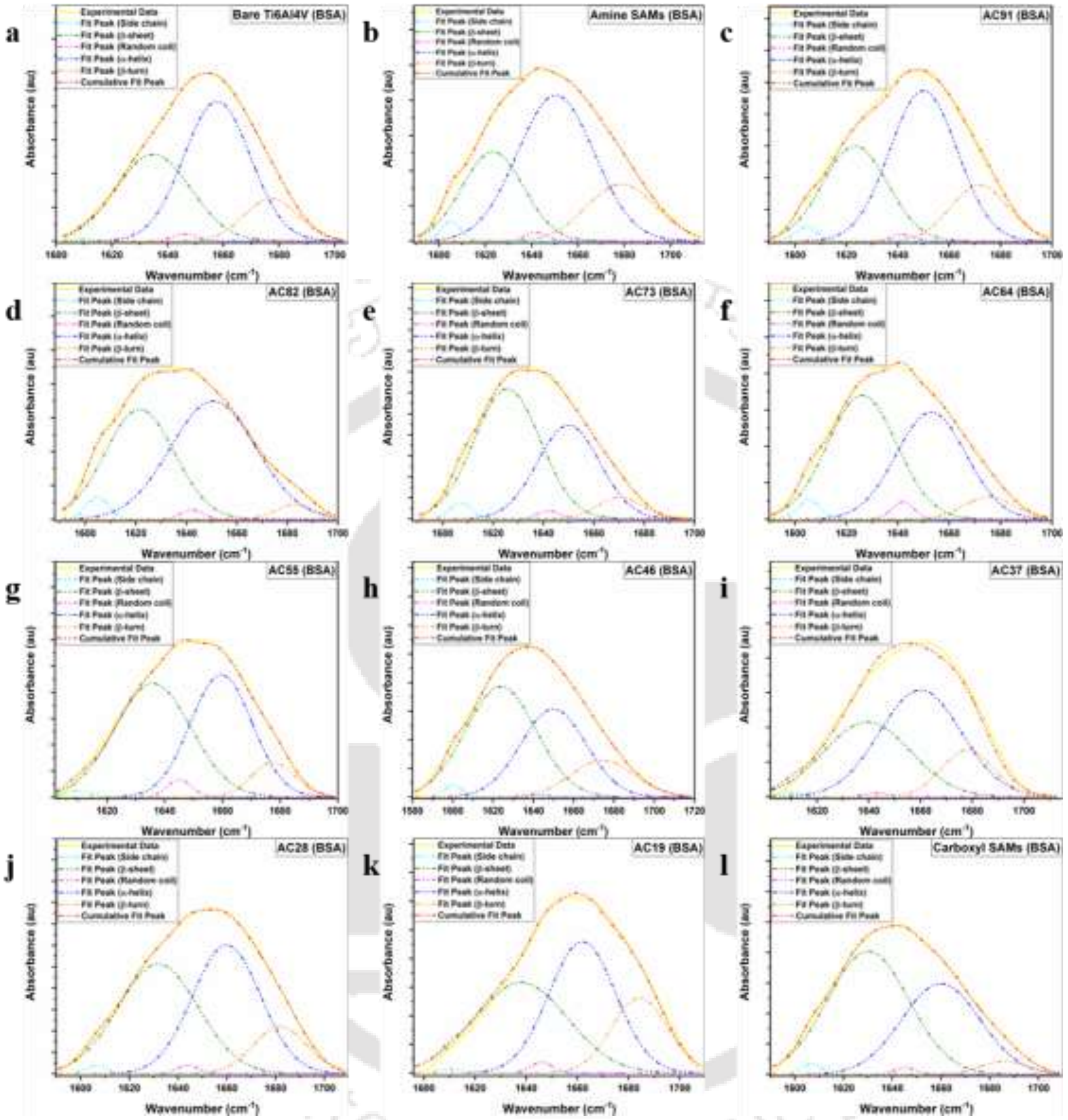

Figure 4.3: Graphs showing FTIR deconvolution of amide-I peak to investigate the change in the secondary structure of BSA on (a) bare, (b) amine SAMs, (c) AC91, (d) AC82, (e) AC73, (f) AC64, (g) AC55, (h) AC46, (i) AC37, (j) AC28, (k) AC19, and (l) octyl SAMs functionalized Ti6Al4V surfaces.

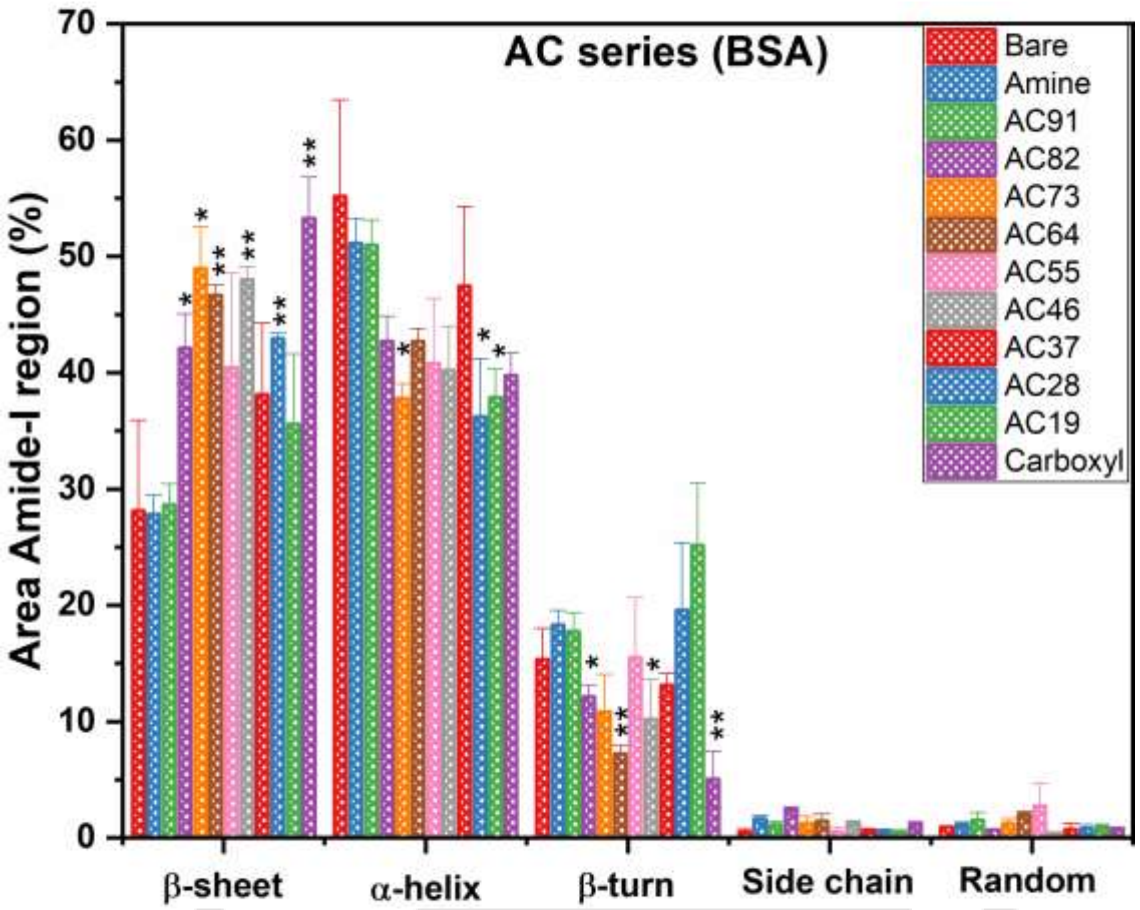

Figure 4.4: Bar graph showing the change in the secondary structure of the BSA in the amide-I region for the AC series samples; statistical analysis was performed using GraphPad Prism, where ns > 0.05, * ≤ 0.05, ** ≤ 0.01, *** ≤ 0.001.

HO series samples comprise hybrid SAMs (secondary modification of amine SAMs) and octyl SAMs at varying percentages. BSA adsorption on the surfaces was explored to investigate the protein adsorption behaviour at the varying proportionalities of two silane moieties. Secondary structure interpretation post FTIR deconvolution exhibited a decrease in the β-sheet conformation and an increase in the α-helicity (**Fig. 4.5**). Reduction in the β-sheet conformation as follows: 46.5±4 (hybrid) > 46±3.3 (HO91) > 44±1.9 (HO82) > 39.2±3.3 (HO64) > 37.4±3.2 (HO46) > 36.3±1 (HO28) > 34.4±5% (octyl) and 32.8±2 (bare Ti6Al4V) surfaces and the rise in the α-helicity in the following order: 35.2±5 (hybrid) < 35±2.2 (HO82) < 36.5±5 (HO55) < 44±3.2 (HO37) < 47±2 (HO28) < 48±3 (HO19) < 50±6 (octyl) as shown in **Fig. 4.6**.

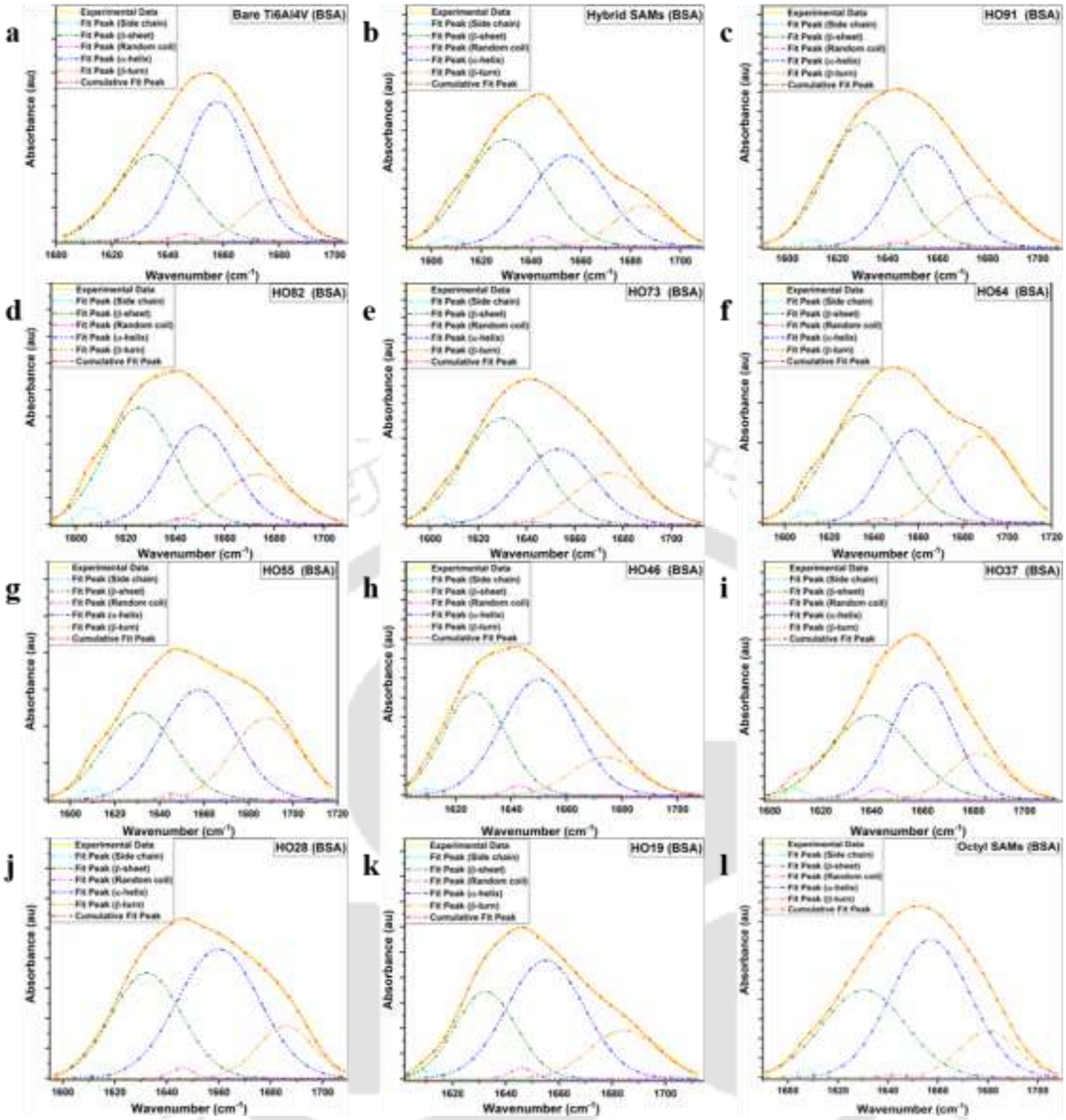

Figure 4.5: Graphs showing FTIR deconvolution of amide-I peak to investigate the change in the secondary structure of BSA on (a) bare, (b) hybrid SAMs, (c) HO91, (d) HO82, (e) HO73, (f) HO64, (g) HO55, (h) HO46, (i) HO37, (j) HO28, (k) HO19, and (l) octyl SAMs functionalized Ti6Al4V surfaces.

ute of Technology

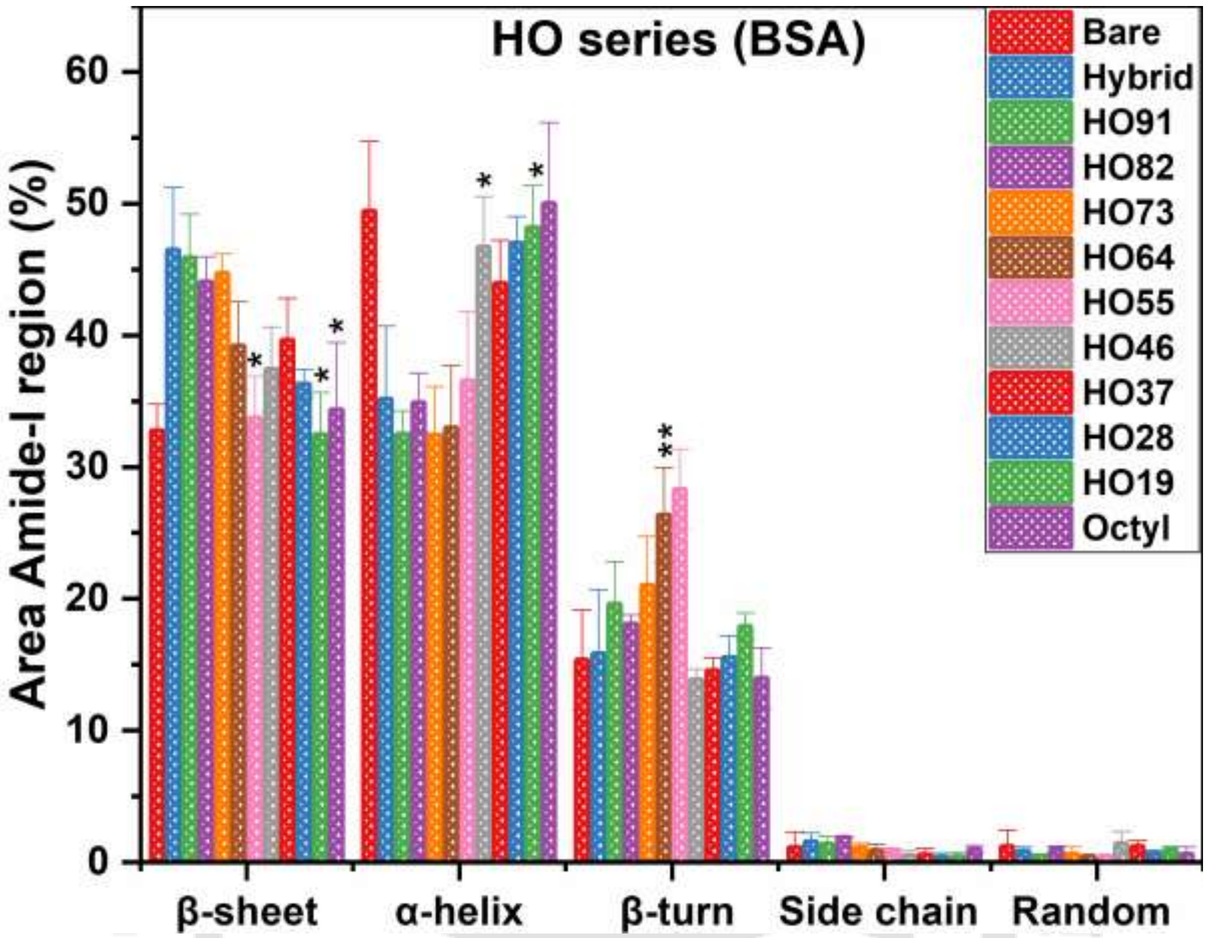

Figure 4.6: Bar graph showing the change in the secondary structure of the BSA in the amide-I region for the HO series samples; statistical analysis was performed using GraphPad Prism, where ns > 0.05, * ≤ 0.05, ** ≤ 0.01, *** ≤ 0.001.

HC series samples comprise the secondary medication of amine SAMs (hybrid SAMs) and octyl SAMs (carboxyl SAMs), as shown in **Fig. 4.7**. There was no generalized trend in the change in the β-sheet conformation with carboxyl SAMs (43.3±1.7%), hybrid SAMs (40.4±1.2%), and bare Ti6Al4V (32.8±2%) surfaces. However, α-helicity showed an increase with the increase in the hybrid proportionality, as follows: hybrid (35.6±3) < HC73 (35±2.7) < HC55 (37.4±4) < HC37 (41.4±3.6) < HC28 (42±1.2) <carboxyl (43.2±2.9%) and bare (49.4±5%) as clear from **Fig. 4.8**.

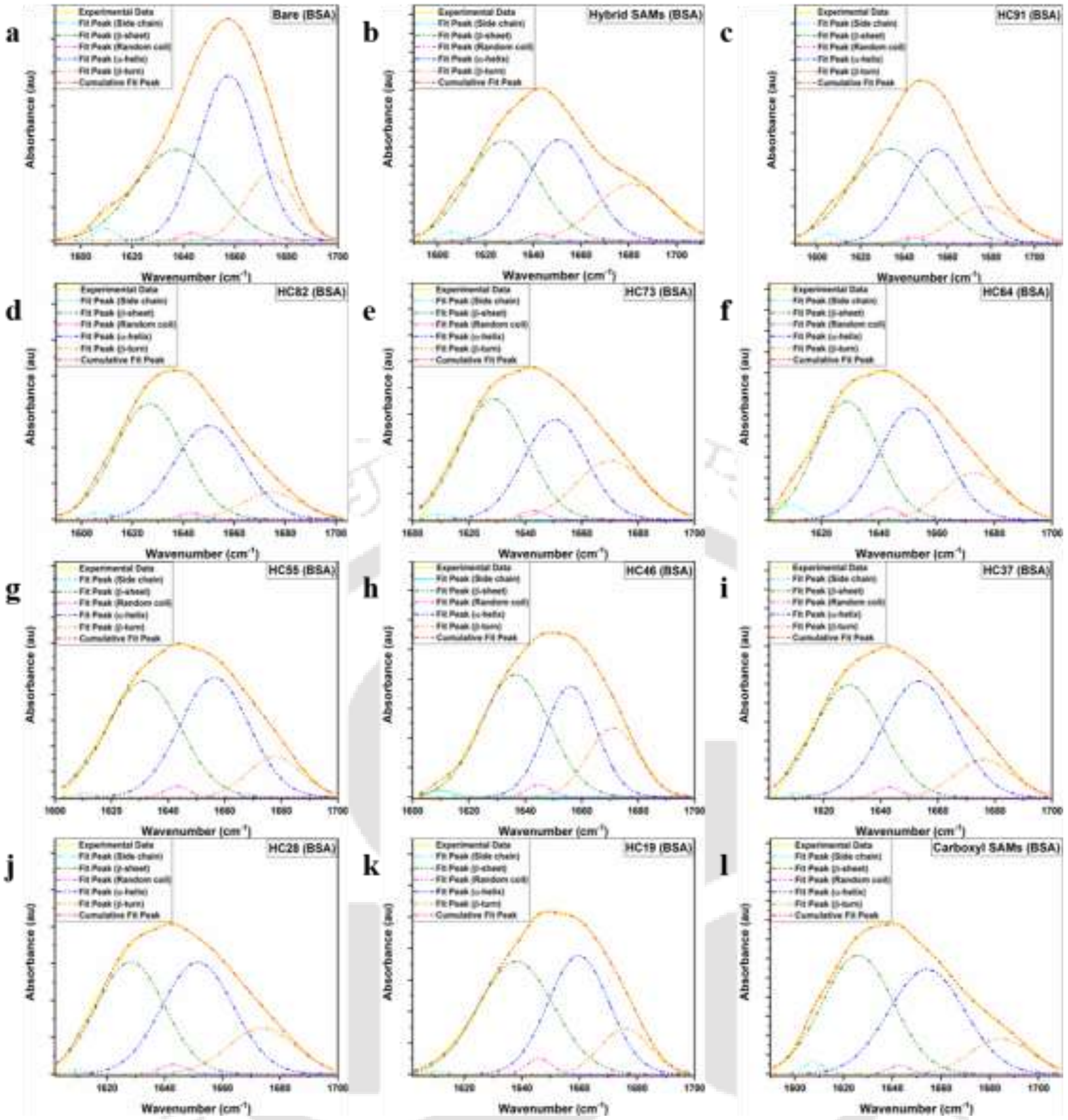

Figure 4.7: Graphs showing FTIR deconvolution of amide-I peak to investigate the change in the secondary structure of BSA on, (a) bare, (b) Hybrid SAMs, (c) HC91, (d) HC82, (e) HC73, (f) HC64, (g) HC55, (h) HC46, (i) HC37, (j) HC28, (k) HC19, and (l) carboxyl SAMs functionalized Ti6Al4V surfaces

Institute of Technology

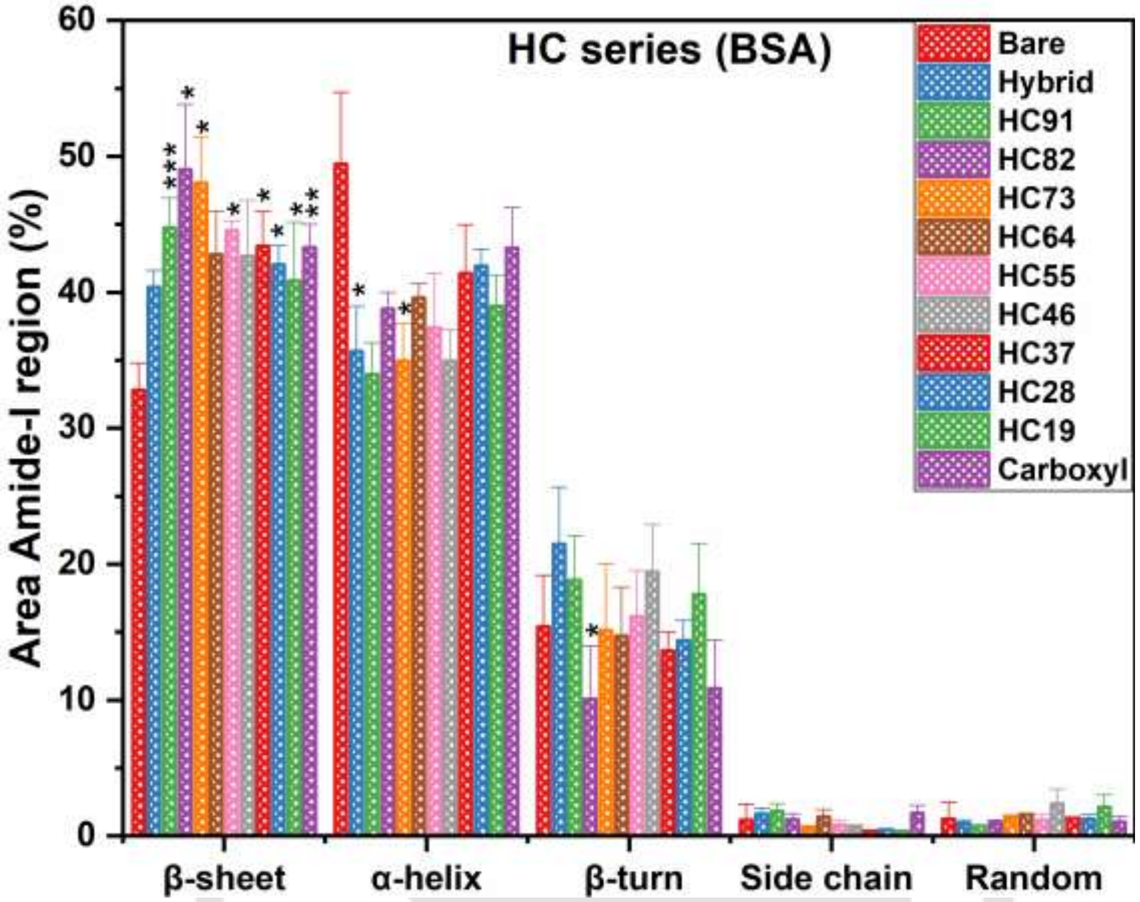

Figure 4.8: Bar graph showing the change in the secondary structure of the BSA in the amide-I region for the HC series samples; statistical analysis was performed using GraphPad Prism, where ns > 0.05, * ≤ 0.05, ** ≤ 0.01, *** ≤ 0.001.

4.3.1.2 FBS adsorption studies

AO-, AC-, HO-, and HC- surfaces were subjected to FBS adsorption as it is a mixed system of various blood proteins (albumin being the most abundant). FBS was also adsorbed on the silane functionalized surfaces for 2 hrs at 37 °C (**Fig. 4.9**). There was no significant change in the β-sheet conformation for the AO series samples, though there was a decrease in the α-helicity and an increase in the β-turn conformation. α-helicity decreased in the following manner: 51±2.3 (amine) > 48±2.3 (AO91) > 48±1.6 (AO82) > 45.8±1.3 (AO73) > 45.5±0.3 (AO64) > 43.5±1.8 (AO46) > 40.3±2.2 (AO37) > 39.7±3.2 (AO28) >37±2.7 (AO19) > 35.7±2% (octyl) and 50.2±2.4% (bare), whereas β-turn conformation increased in the following manner with the increase in the octyl proportionality: 24±3.4 (amine) < 24±3.2 (AO91) < 28.6±2.5 (AO73)

Indian Institute of Technology Guwahati

< 29±2.3 (AO64) < 33.6±2.2 (AO46) < 32.3±2.5 (AO37) < 35.6±2.8 (AO28) < 35.7±0.6 (AO19) < 36.4±1.8% (octyl), and 27.2±0.6 (bare) surfaces as clear from **Fig. 4.10**.

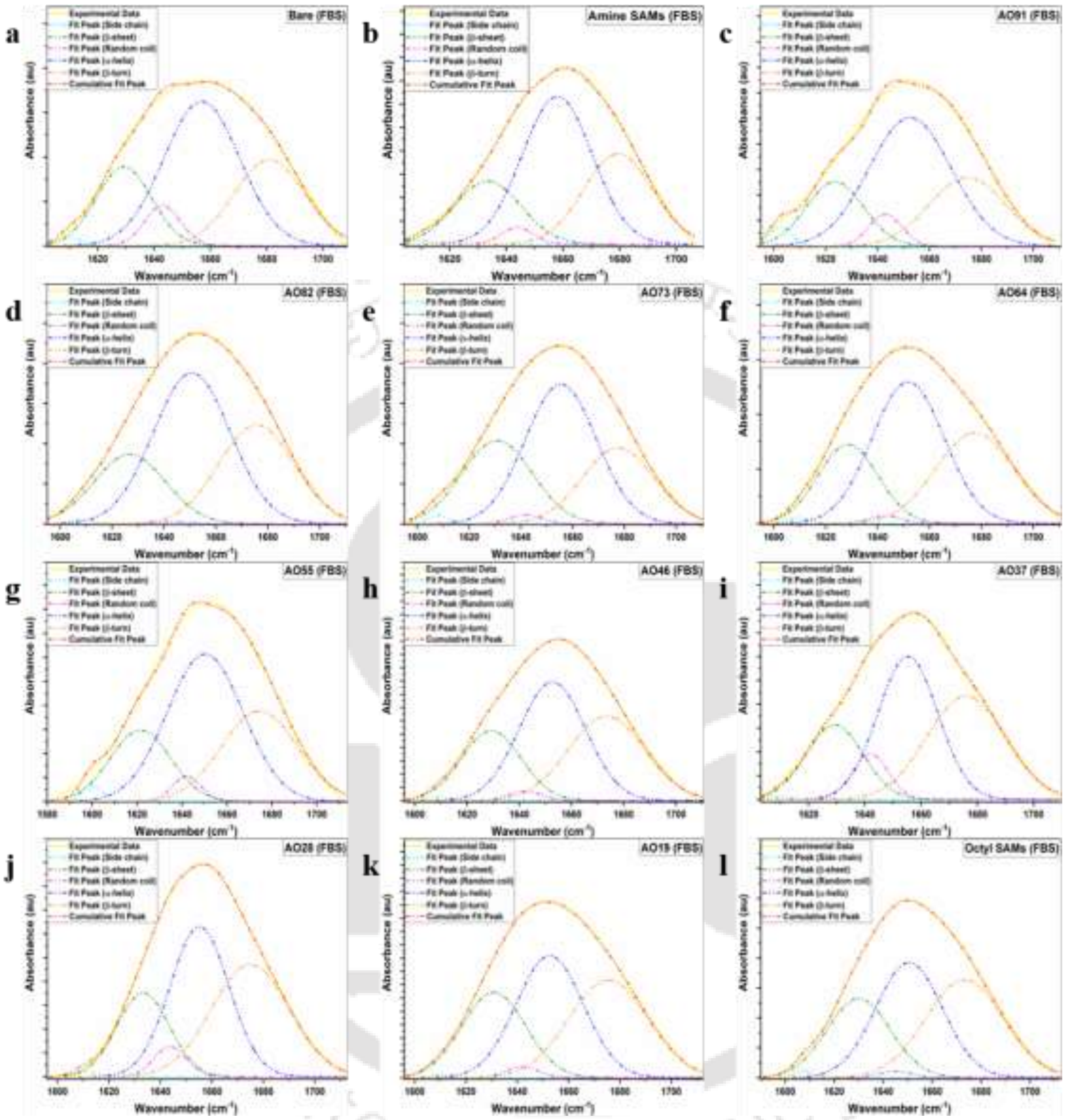

Figure 4.9: Graphs showing FTIR deconvolution of amide-I peak to investigate the change in the secondary structure of FBS on, (a) bare, (b) amine SAMs, (c) AO91, (d) AO82, (e) AO73, (f) AO64, (g) AO55, (h) AO46, (i) AO37, (j) AO28, (k) AO19, and (l) octyl SAMs functionalized Ti6Al4V surfaces

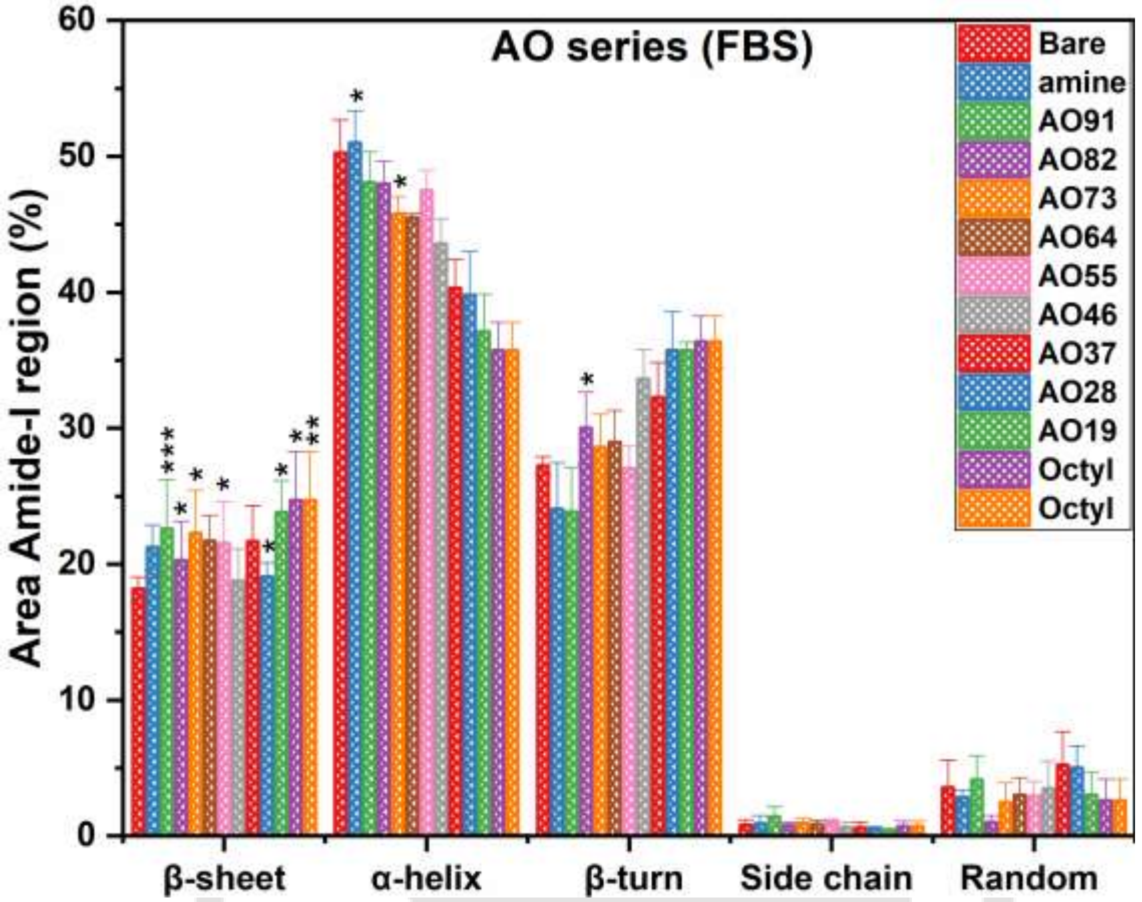

Figure 4.10: Bar graph showing the change in the secondary structure of the FBS in the amide-I region for the AO series samples; statistical analysis was performed using GraphPad Prism, where ns > 0.05, * ≤ 0.05, ** ≤ 0.01, *** ≤ 0.001.

In the case of the AC series samples, there was a decrease in the α-helicity and an increase in the β-sheet conformation (**Fig. 4.11**). However, there was an insignificant change in the β-turn conformation for carboxyl SAMs (24.8±2%), amine SAMs (21.7±1.4%) and bare Ti6Al4V (24±0.5%). α-helicity showed the following decremental trend in the conformation: amine (54±2.2), AC91 (54.5±2.7) > AC82 (53.3±3) > AC73 (50.5±1.5), AC55 (51.1±0.9) > AC46 (47.3±2.1) > AC37 (43.4±1.4), AC19 (44.5±1.3) > carboxyl (38.5±0.7%), and bare (49.3±2.1%), whereas increase in the β-sheet conformation was as follows: amine (23±0.7), AC91 (21.6±3.7), AC73 (28.2±2.5) > AC64 (28.7±1) > AC46 (32.2±1.6) > AC19 (33±1.8) > carboxyl (35±2.5%), and bare (20.3±3%) as apparent from **Fig. 4.12**. A study was conducted to evaluate the effect of the β-1,3-glucan conjugation onto the chitosan matrix on the adsorption behaviour of serum proteins. An increase in the surface hydroxyl group due to conjugation on the chitosan matrix resulted in increased serum protein adsorption compared to the unconjugated surfaces. Enhanced protein adsorption on the modified chitosan resulted in better osteoblast cell adhesion, spreading, and proliferation [335]. Secondary structure graphs have not been incorporated for the rest of the studies to avoid overcrowding the chapter.

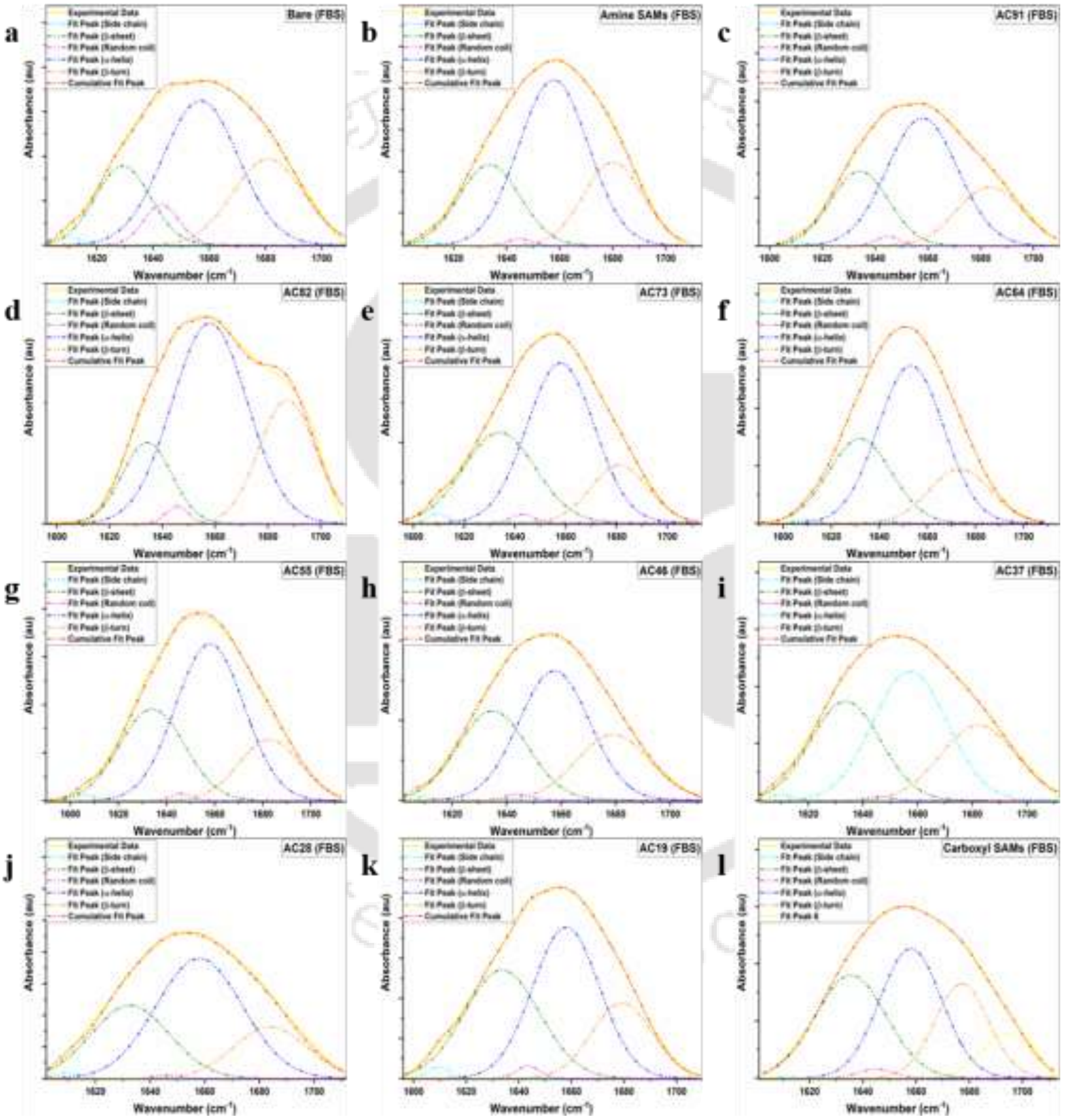

Figure 4.11: Graphs showing FTIR deconvolution of amide-I peak to investigate the change in the secondary structure of FBS on, (a) bare, (b) amine SAMs, (c) AC91, (d) AC82, (e) AC73, (f) AC64, (g) AC55, (h) AC46, (i) AC37, (j) AC28, (k) AC19, and (l) carboxyl SAMs functionalized Ti6Al4V surfaces

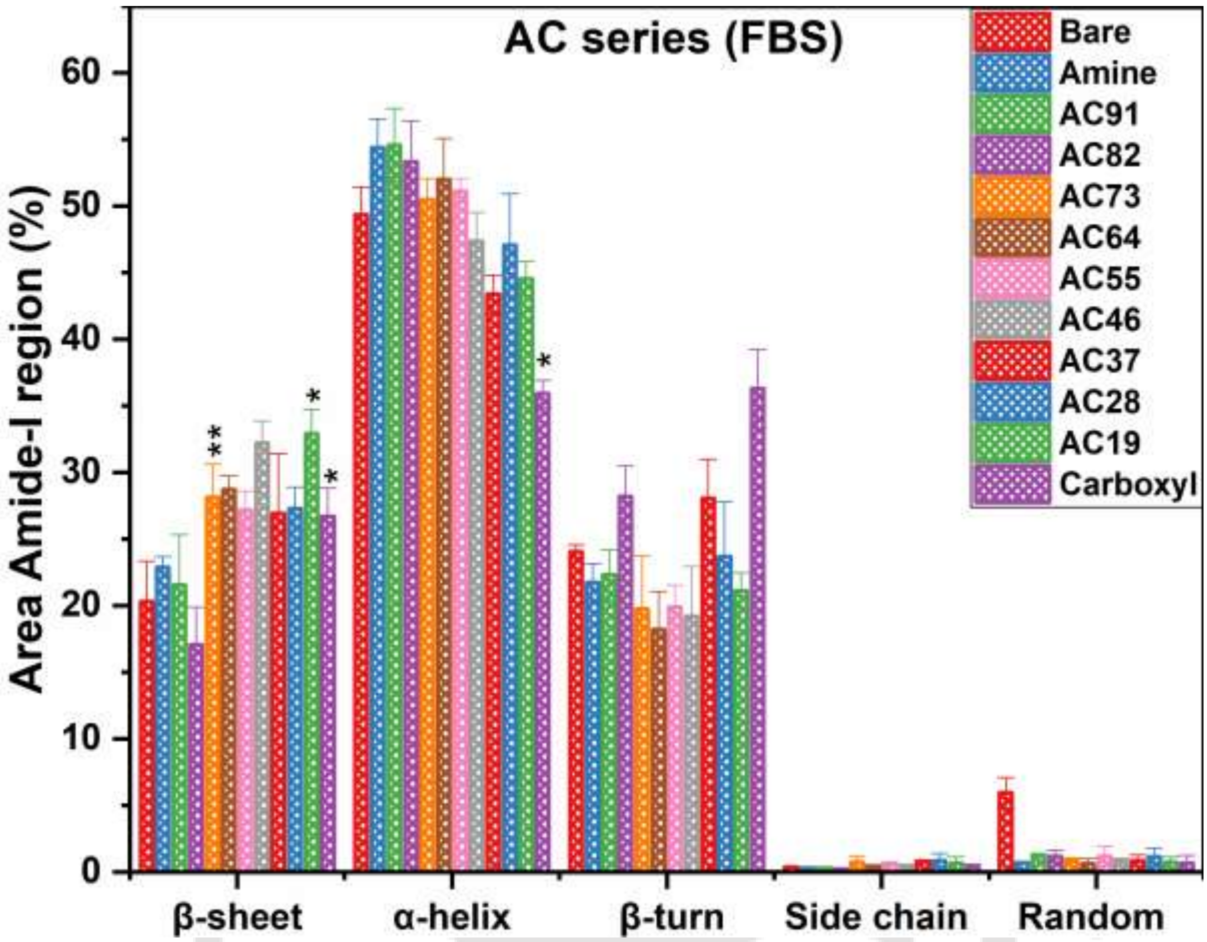

Figure 4.12: Bar graph showing the change in the secondary structure of the FBS in the amide-I region for the AC series samples; statistical analysis was performed using GraphPad Prism, where ns > 0.05, * ≤ 0.05, ** ≤ 0.01, *** ≤ 0.001.

Similarly, HO series samples were also investigated for the FBS adsorption behaviour. There was an increase in the β-sheet conformation and a decrease in the α-helicity with increased octyl proportionality in the HO series samples. β-sheet conformation varied in the following manner: hybrid (21±3) < HO91 (23±3) < HO82 (26.5±0.4) < HO64 (27±1.6) < HO46 (27.3±1.7) < HO37 (27.5±1.5) <HO28 (28±1.2) < octyl (28±1.9%), and 25.4±2.3% for the bare Ti6Al4V surfaces, α-helicity decreased in the following manner with the increase of the octyl proportionality: 43±3.6 (hybrid) > 42.2±0.2 (HO91) > 38±5.4 (HO82) > 38.5±3.6 (HO73) > 35.3±1.6 (HO37) > 35.3±2% (octyl), and 42.6±1.6% (bare) surfaces. β-turn conformation was independent of the change in the percentages of the carboxyl and hybrid SAMs with slight variability throughout the series with 34±1.5% (hybrid SAMs), 33.8±3.5% (octyl SAMs) and 28.5±2.6% (bare) surfaces as clear from **Fig. 4.13**.

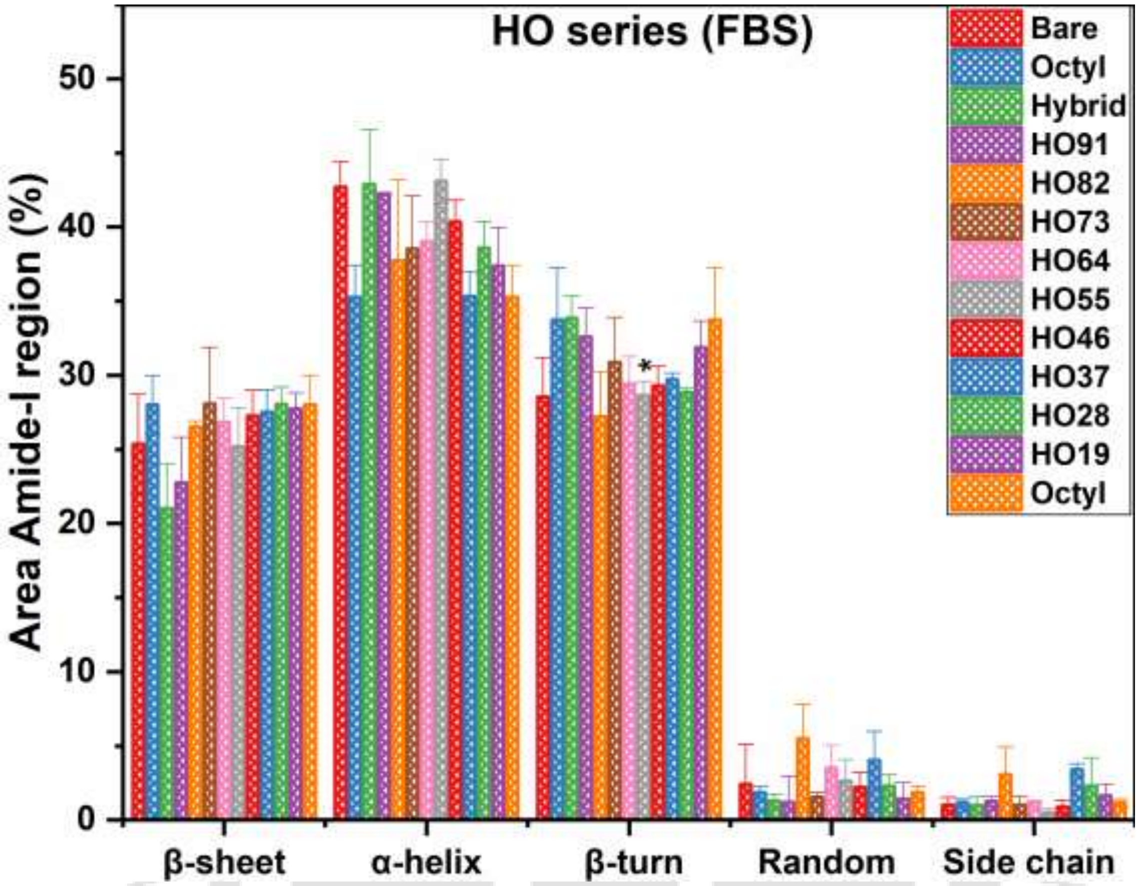

Figure 4.13: Bar graph showing the change in the secondary structure of the FBS in the amide-I region for the HO series samples; statistical analysis was performed using GraphPad Prism, where ns > 0.05, * ≤ 0.05, ** ≤ 0.01, *** ≤ 0.001.

Indian Institute of Technology Guwahati

HC series comprises the secondary modification of hybrid and carboxyl SAMs, resulting in the urea linkages in the SAMs for hybrid and converting methylene terminal to carboxyl-terminal for the carboxyl SAMs. There was a significant increase in the β-sheet conformation and a decrease in the β-turn conformation with increased carboxyl proportionality. An increase in the β-sheet showed the following trend with some variations in the series: 20.2±2.3 (hybrid) < 20±2.8 (HC91) < 21.3±1.9 (HC82) < 26±3 (HC73) < 30.2±3.8 (HC64), 28±4.7 (HC55), 28.5±2.2 (HC46) < 33±3.4 (HC37) < 38.6±2.6 (HC28) < 41.6±1.2 (HC19) < 43±1% (carboxyl), and 25.4±3.3 (bare) surfaces. A decremental change in the β-turn conformation showed the following trend: hybrid (35.4±0.9) > HC91 (36±0.8), HC82 (38±2.8) > HC73 (25±1) > HC55 (24.4±3), HC46 (25±2.4) > HC37 (22.6±0.4) > HC28 (16±3.7) > HC19 (15.3±2), carboxyl SAMs (15.8±1.3%) and bare (28.5±2%) surfaces. On the other hand, there was a slight change in the α-helicity with hybrid (42±1%), carboxyl (39±0.5%), and bare (42.6±1.7%) surfaces, as shown in **Fig. 4.14**.

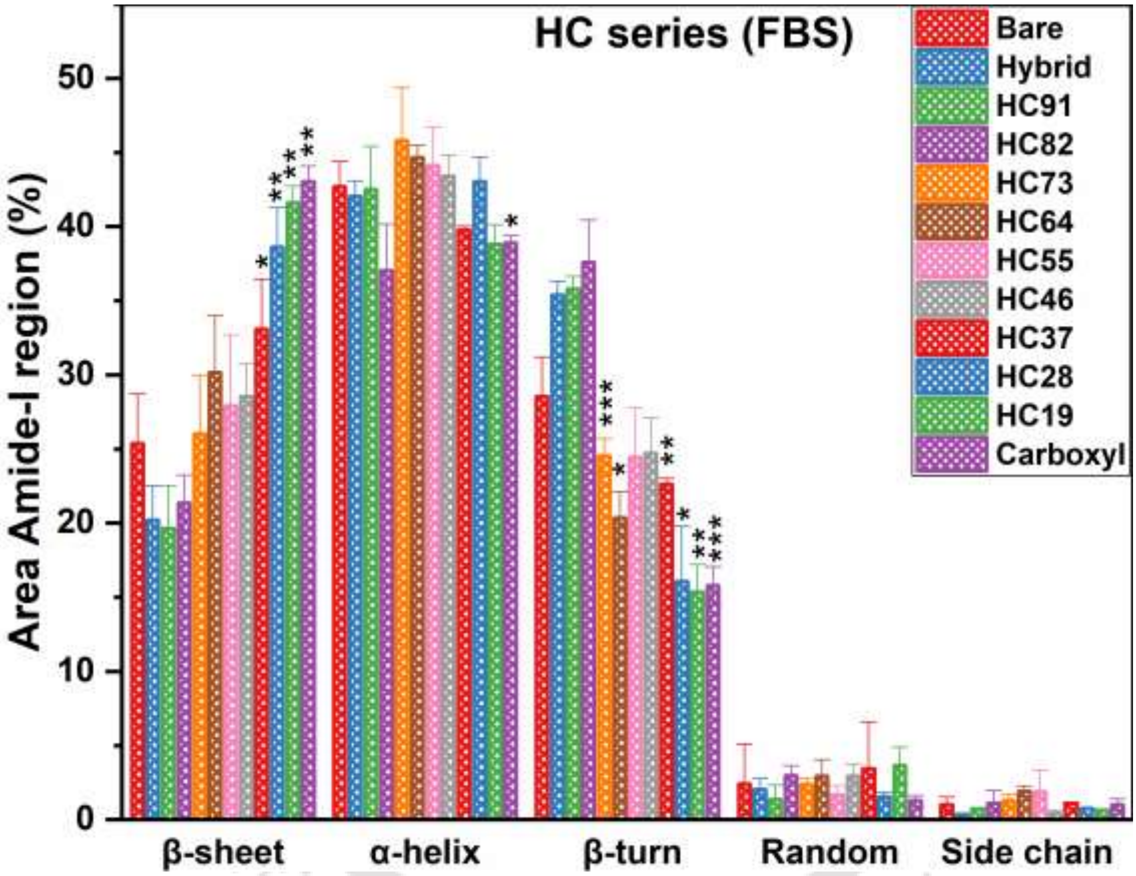

Figure 4.14: Bar graph showing the change in the secondary structure of the FBS in the amide-I region for the HC series samples; statistical analysis was performed using GraphPad Prism, where ns > 0.05, * ≤ 0.05, ** ≤ 0.01, *** ≤ 0.001.

4.3.2 BSA adsorption on carboxyl SAM surfaces

BSA adsorption was performed on the modified substrates using the acidified $KMnO_4$ (1-5%) and time duration (0, 60, 90, 120, 150 min). BSA adsorption was performed at 37 °C for 2 hour at static conditions; all the samples were performed in triplicates. After adsorption, samples were dried under laminar airflow and stored at a vacuum desiccator before FTIR measurement in the amide-I region. FTIR peaks were deconvoluted, taking the respective peak second derivative as the reference in the OriginPro software, as shown in **Fig. 4.15 & 4.16**. Octyl SAM samples were taken as the control (0 min) sample and exhibited 42.08±2.52% α-helicity, 32.43±1.27% β-sheet structure, and 19.39±2.90% β-turn structure. 1% acidified $KMnO_4$ incubated samples showed a decrease in the β-sheet structure with the increase in the incubation time compared to control as follows: 14.91±4.43% (60 min), 14.52±2.89% (90 min), 9.68±1.10% (120 min) and 13.64±0.98% (150 min). There is a rise in the β-turn structure as 13.96±4.05% (60 min), 17.74±3.50% (90 min), 48.73±1.65% (120 min), and 34.50±11.3 3% (150 min), respectively. For the proper adsorption of the protein with the surface, all the adhesion points of the protein need to attach to the surface for decisive and irreversible adsorption behaviour. For making solid contacts, protein needs to unfold its native structure to a certain degree to make room for all the adhesion points to be accessible for binding to the surface [19, 41, 314, 336].

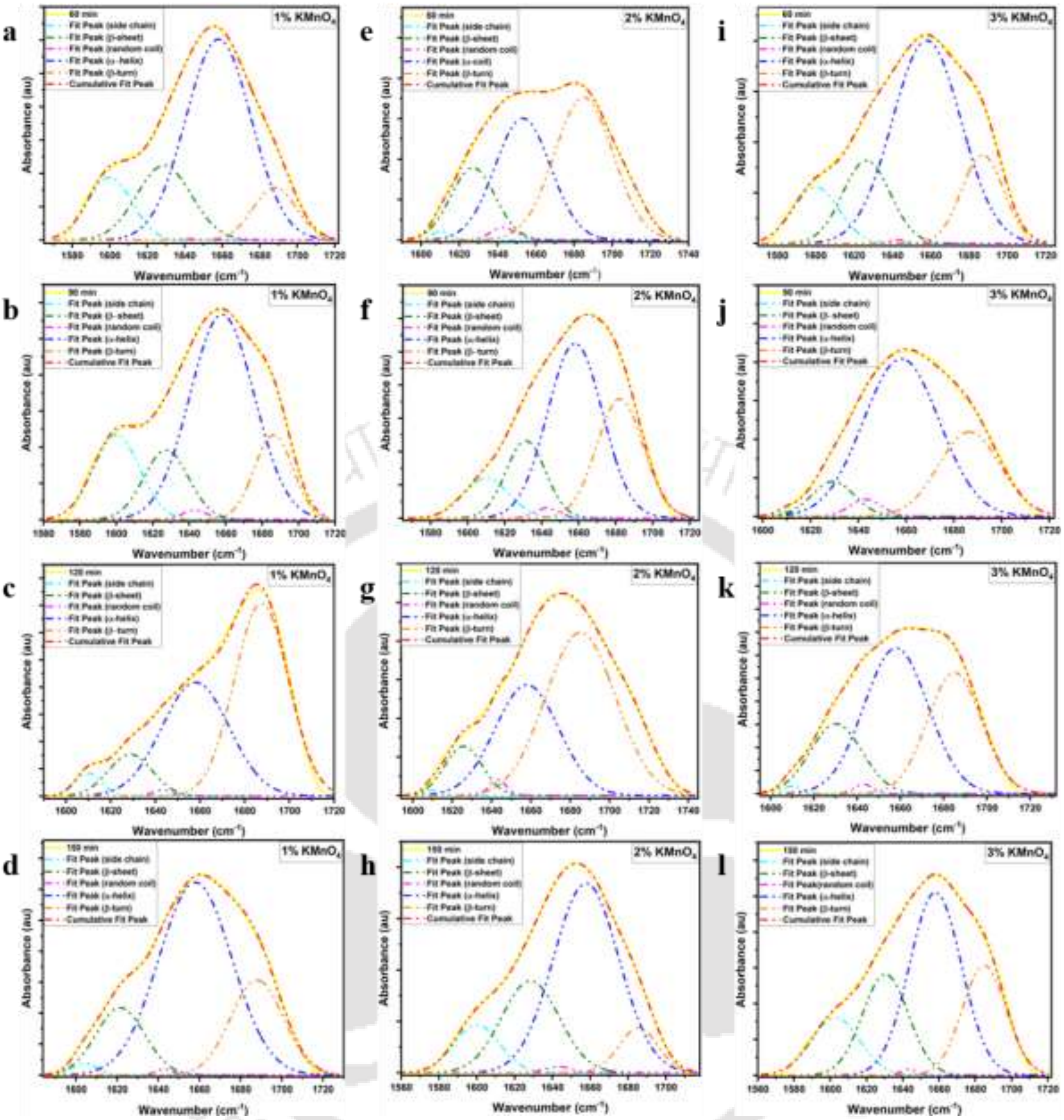

Figure 4.15: Graphs showing FTIR deconvolution of amide-I peak to investigate the change in the secondary structure of BSA on, (a-d) 1% KMnO$_4$, (e-h) 2% KMnO$_4$, (i-l) 3% KMnO$_4$ treated samples

Institute of Technology

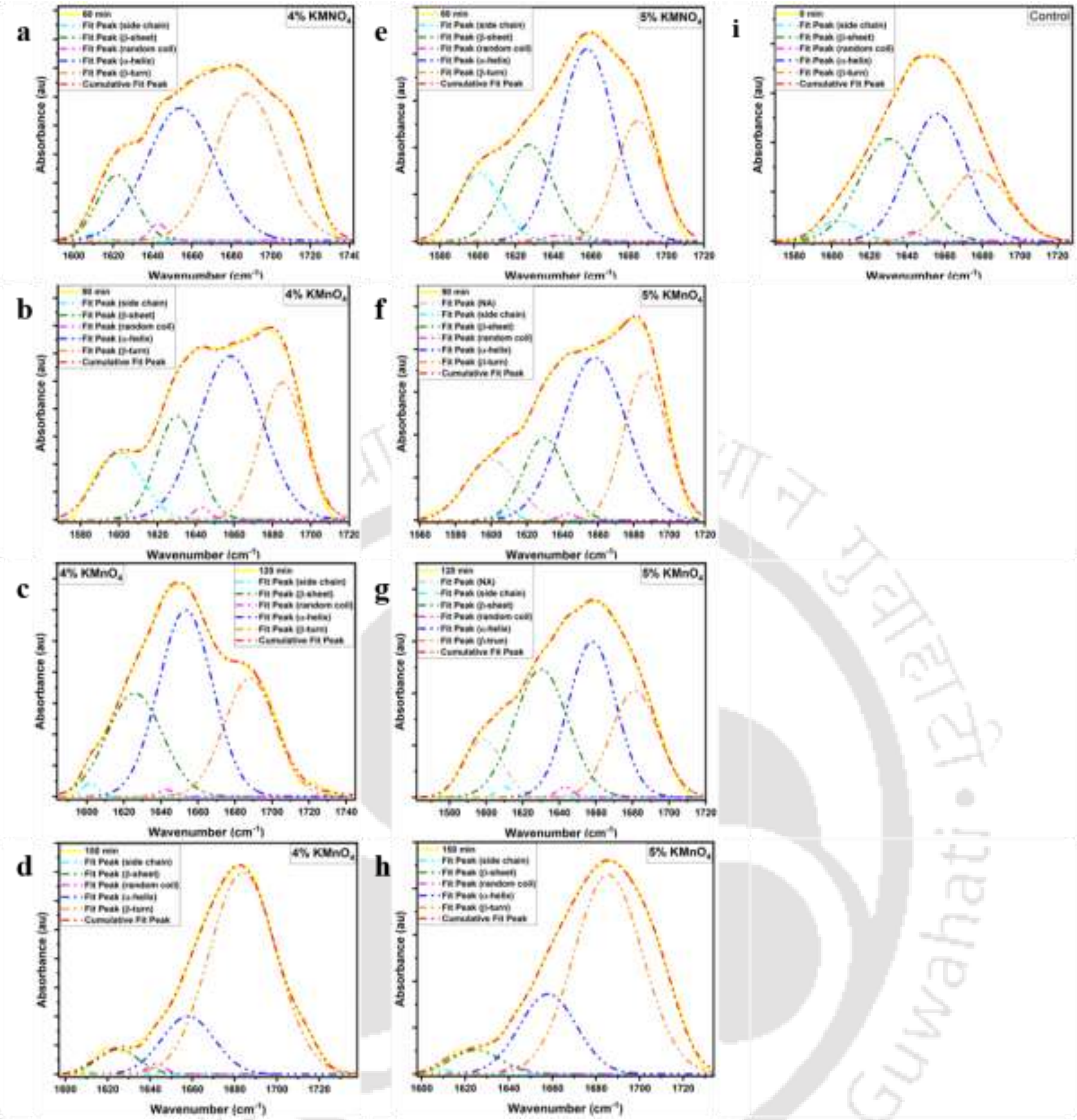

Figure 4.16: Graphs showing FTIR deconvolution of amide-I peak to investigate the change in the secondary structure of BSA on, (a-d) 4% KMnO$_4$, (e-h) 5% KMnO$_4$, treated samples, and (i) control samples

In the case of the 2% conc (KMnO$_4$), the native BSA structure unfolded to accommodate the effective adsorption. Most prominent behaviour was observed in the β-sheet structure compared to the control with a gradation of time interval, 60 min (16.26±3%), 90 min (13.82±1.30%), and 120 min (11.17±2.72%), while the 150 min (25.92±1.94%) sample showed the slight increase in the conformation. In the case of the 3% conc (KMnO$_4$) incubated samples, there is a decrease in the β-sheet and α-helix in the 60 min and 90 min samples compared to the 0 min samples. Still, it showed an overall increase in the β-sheet, 14.51±1.50% (60 min), 12.0±3.85% (90 min), 17.68±3.38% (120 min) and 19.08±2.37% (150 min); and decrease in the α-helix, 55.79±1.45% (60 min), 53.57±7.88% (90 min), 49.76±2.57% (120 min) and 45.58±5.22% (150 min), respectively. In the 4% conc ($KMnO_4$) incubated samples, there was a change in the secondary structure of the protein on the variously incubated modified samples. Still, there was a lack of any trend in the behaviour. Samples incubated with 5% conc ($KMnO_4$) at variable time intervals exhibited remarkable and distinctive trends in the conformational unfolding behaviour. There was a noteworthy increase in the α-helicity as follows: 60 min (58.63±2.15%) > 90 min (47.33±8.40%) > 120 min (40.39±4.15%) > 150 min (26.20±4.51%), respectively. A slightly descending trend was observed in the case of β-turn as follows: 19.74±1.57% (60 min), 32.11±3.24% (90 min), 26.54±2.39% (120 min), and 61.53±7.33% (150 min) as shown in Fig. **4.17**. Barberi *et al.* observed the albumin and fibronectin adsorption onto the bioactive glass doped with silver ions. FTIR peaks in the amide-I region were utilized to interpret the secondary structure. BSA native structure slightly changed from the native conformation on adsorption on the undoped bio-glass, whereas the secondary structure drastically denatured upon adsorption to the silver-doped bioglass [337]. Another study regarding the effect of the BSA adsorption on the Mo-doped SiO_2-CaO-P_2O_5 composite was performed by Lucacel *et al.* in simulated biological media. It was observed that the native structure of the BSA was well preserved prior to and after adsorption onto SiO_2-CaO-P_2O_5 composites with molybdenum dopant [338].

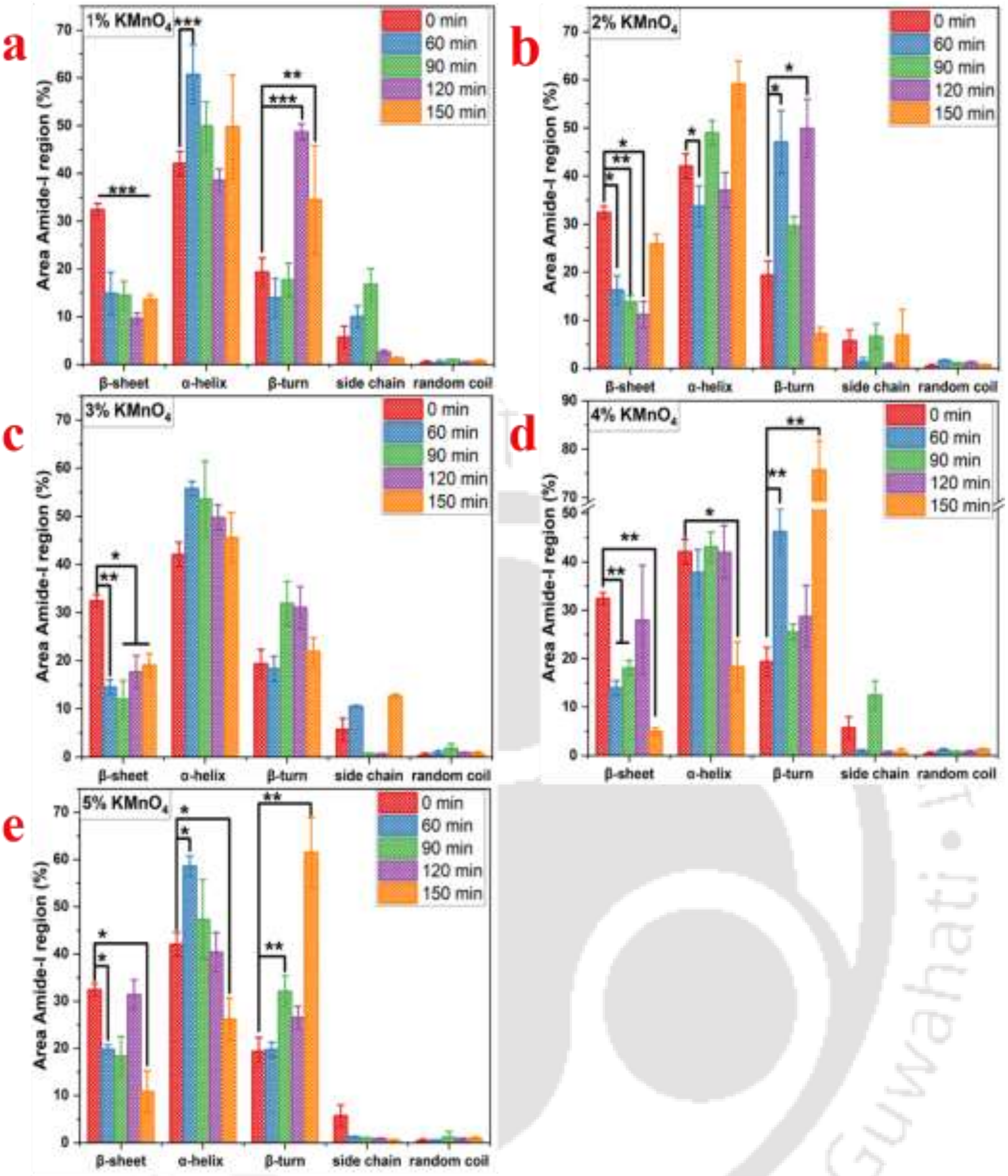

Figure 4.17: BSA secondary structure obtained post-deconvolution of the ATR-FTIR peaks in the amide-I region, (a) 1%, (b) 2%, (c) 3%, (d) 4% and (e) 5% acidified $KMnO_4$; statistical analysis was performed using GraphPad Prism, where ns > 0.05, * ≤ 0.05, ** ≤ 0.01, *** ≤ 0.001.

4.3.3 BSA secondary structure interpretation on octadecyl SAMs modified surfaces

Hydrophobic octadecyl SAMs were fabricated on the bare Ti6Al4V surfaces and were explored for the BSA adsorption behaviour. To investigate the change in the secondary structure, BSA was adsorbed on the octadecyl SAMs surfaces for 2 hrs at 37 ºC at a variable protein concentration (0.5, 1, 2, 3, 4, & 5 mg/ml). Change in the secondary structure at the varied BSA concentrations was compared to the native BSA incubated at 37 ºC for 2 hrs. Change in the secondary structure was independent of the concentration used for the protein adsorption, though the change was significant compared to the native BSA incubated at the same conditions. Native BSA exhibited a β-sheet conformation of 35.4±0.8%. At the same time, the BSA adsorbed octadecyl SAMs samples showed the following results: 23±2.6 (0.5 mg/ml), 20.8±1.7 (1 mg/ml), 18±1.7 (2 mg/ml), 20.7±2.9 (3 mg/ml), 20±0.6 (4 mg/ml) and 23±1.5% (5 mg/ml). In contrast, the native BSA showed α-helicity of 43±0.3% and the octadecyl SAMs adsorbed with BSA exhibited the decrease in the change in the conformation with the increase in the BSA conc as follows: 62.6±2.2 (0.5 mg/ml) > 61.7±3.7 (1 mg/ml) > 60.7±4.8 (2 mg/ml) > 60.5±4 (3 mg/ml) > 59.5±1.4 (4 mg/ml) > 56.6±2.3% (5 mg/ml). β-turn conformation changed for the lower BSA conc, but higher adsorbed conc showed the conformation equivalent to native BSA (19.3±0.6%); trend as follows: 12.6±0.9 (0.5 mg/ml) < 14.8±1.6 (1 mg/ml) < 18.2±2.4 (2 mg/ml), 16.7±2.2 (3 mg/ml) < 18±0.7 (4 mg/ml) < 19.1±1.2% (5 mg/ml) as clear from **Fig. 4.18**.

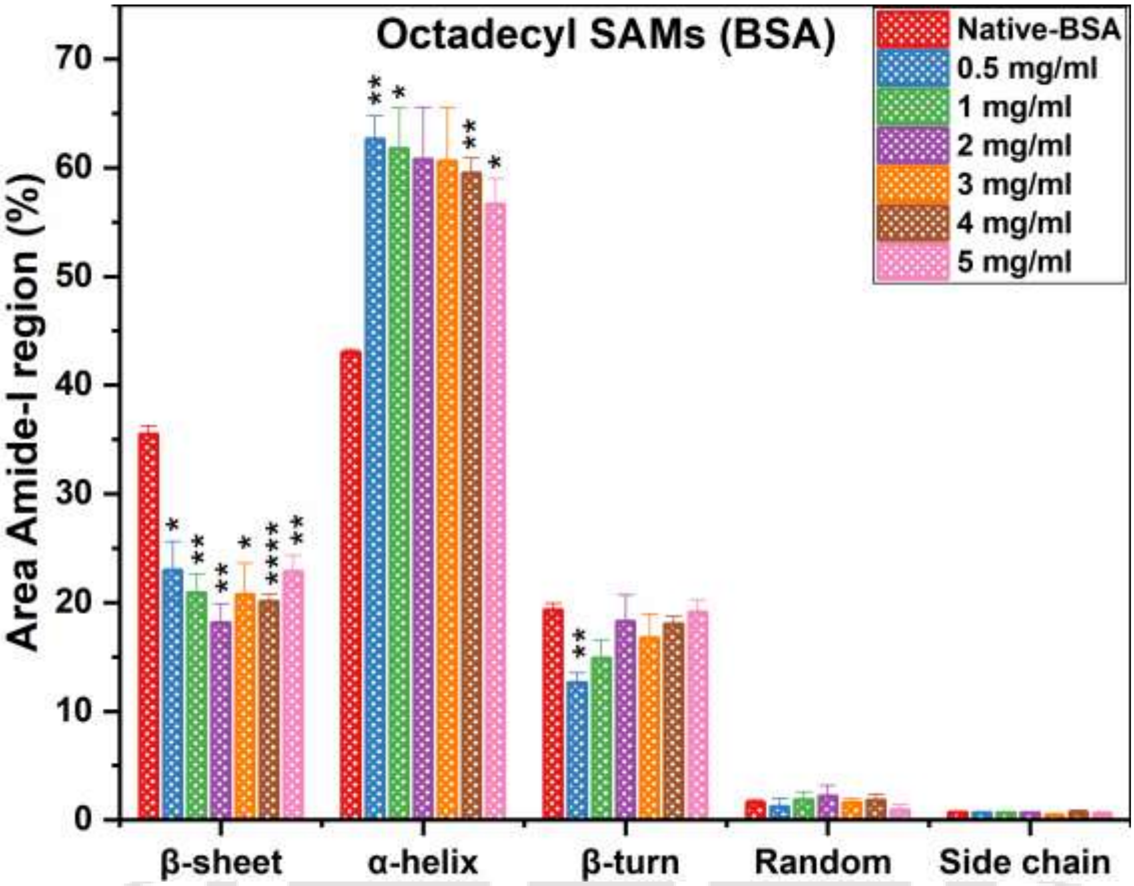

Figure 4.18: Bar graph showing the change in the secondary structure of the BSA in the amide-I region for the octadecyl SAMs samples; statistical analysis was performed using GraphPad Prism, where ns > 0.05, * ≤ 0.05, ** ≤ 0.01, *** ≤ 0.001.

4.3.4 Protein adsorption on the hexadecyl SAMs-modified Ti6Al4V surfaces

Hexadecyl SAMs functionalized surfaces were adsorbed with various proteins (BSA, FN, and Col-I) to investigate the insight into the surface behaviour in the physiological microenvironment. There was no significant change in the adsorbed BSA on hexadecyl SAMs surfaces compared to the native BSA incubated at 37 °C for the β-sheet conformation, β-sheet conformation (%) was as follows: native (35±1), 0.5 mg/ml (39.6±2.2), 1 mg/ml (41±1.9), 2 mg/ml (37.1±2.3), 3 mg/ml (38.2±2.3), 4 mg/ml (40±2.6) and 5 mg/ml (30.6±2.7%). A higher concentration of the BSA showed α-helicity comparable to the native BSA that decreased with a decrease in the concentration of the adsorbed BSA, as follows: native BSA (43±0.3), 41±3 (5 mg/ml), 35.3±2.2 (4 mg/ml), 35.5±3.7 (3 mg/ml), 36.8±1 (2 mg/ml), 30±1 (1 mg/ml), 27.8±1.4 (0.5 mg/ml) as shown in **Fig. 4.19**. There was a slight change in the β-turn conformation (25-30%) compared to the native BSA (19.3±0.35), though the change was insignificant among the BSA adsorbed surfaces with the change in the BSA concentration. Cristina et al. investigated the effect of the protein pre-adsorption on the cell behviour with fibronectin and vitronectin as the model proteins. Both proteins exhibited 90% surface retention capability upon adsorption from single protein systems, while adsorption from the multicomponent system (FBS) fibronectin showed a weaker binding capability due to competitive effects from other proteins[339]. In another study, the researcher grafted PCL polymer with heparin and investigated its effect on the adsorption behaviour of the fibronectin and BSA. It was observed that fibronectin adsorption increased with an increase in the heparin conc, while BSA showed an inverse relation with the heparin, indicating the heparin specificity for the fibronectin adsorption [340].

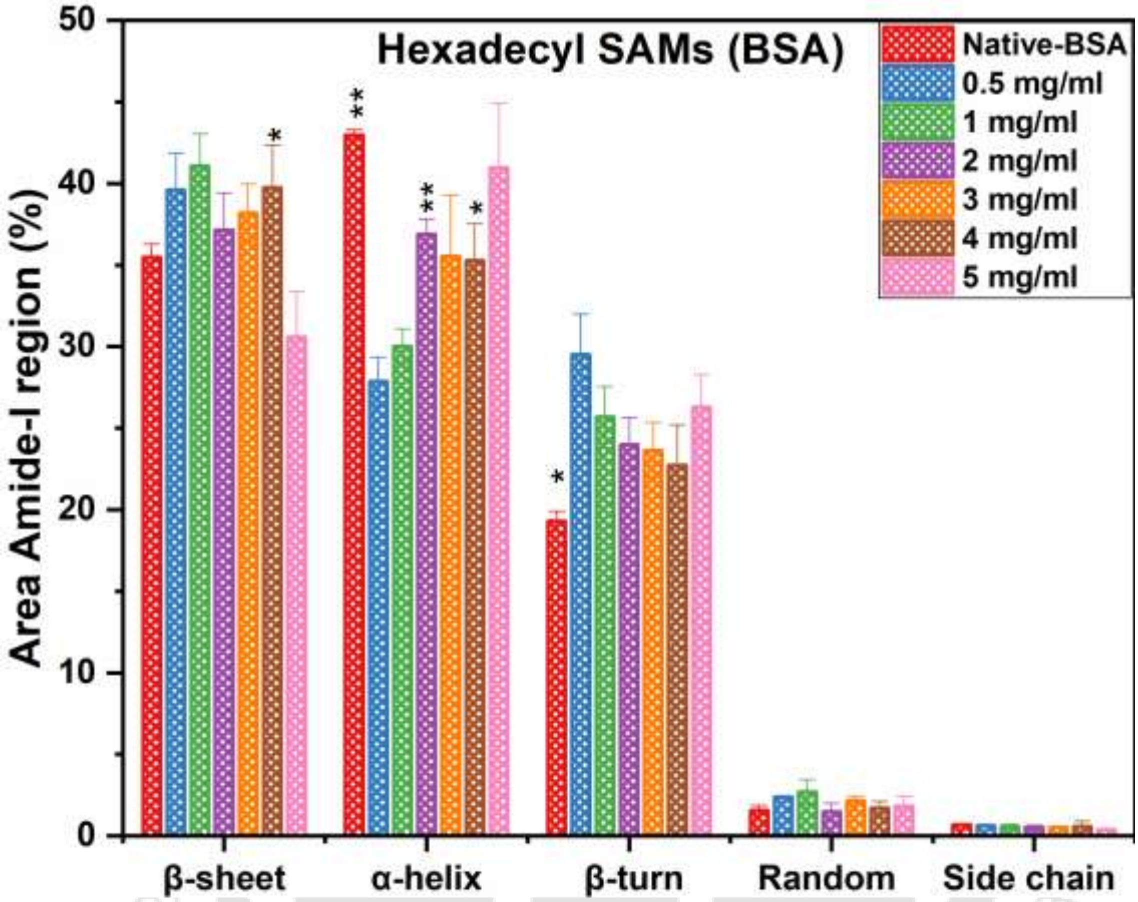

Figure 4.19: Bar graph showing the change in the secondary structure of the BSA in the amide-I region for the hexadecyl SAMs samples; statistical analysis was performed using GraphPad Prism, where ns > 0.05, * ≤ 0.05, ** ≤ 0.01, *** ≤ 0.001.

Fibrinogen is the critical protein involved in the blood clotting cascade, and its non-specific binding on the surfaces might result in surface biofouling. So, fibrinogen adsorption was also investigated on the hexadecyl-modified surfaces for 2 hr at 37 °C. β-sheet conformation remained independent of the FN concentration and adsorption parameters (~30%). At the same time, the α-helicity increased with the decrease in the adsorbed FN concentration, and β-turn conformation decreased with the decrease in the adsorbed protein conc. α-helicity varied in the following manner: 60±2.2 (5 µg/ml) > 52.7±3.1 (10 µg/ml) > 51.7±3 (20 µg/ml) >50.6±1.9 (30 µg/ml) > 46±0.7 (40 µg/ml), 47.2±1% (50 µg/ml) and 48±1.5% (native FN); whereas β-turn conformation showed the following trend: 9.8±1.5 (5 µg/ml) < 13.8±2 (10 µg/ml) < 15.8±0.9 (20 µg/ml) < 18.4±2.6 (30 µg/ml) < 18.4±1.8 (40 µg/ml) < 19.2±2.5% (50 µg/ml), and 18±1.6% (native FN) as shown in **Fig. 4.20**.

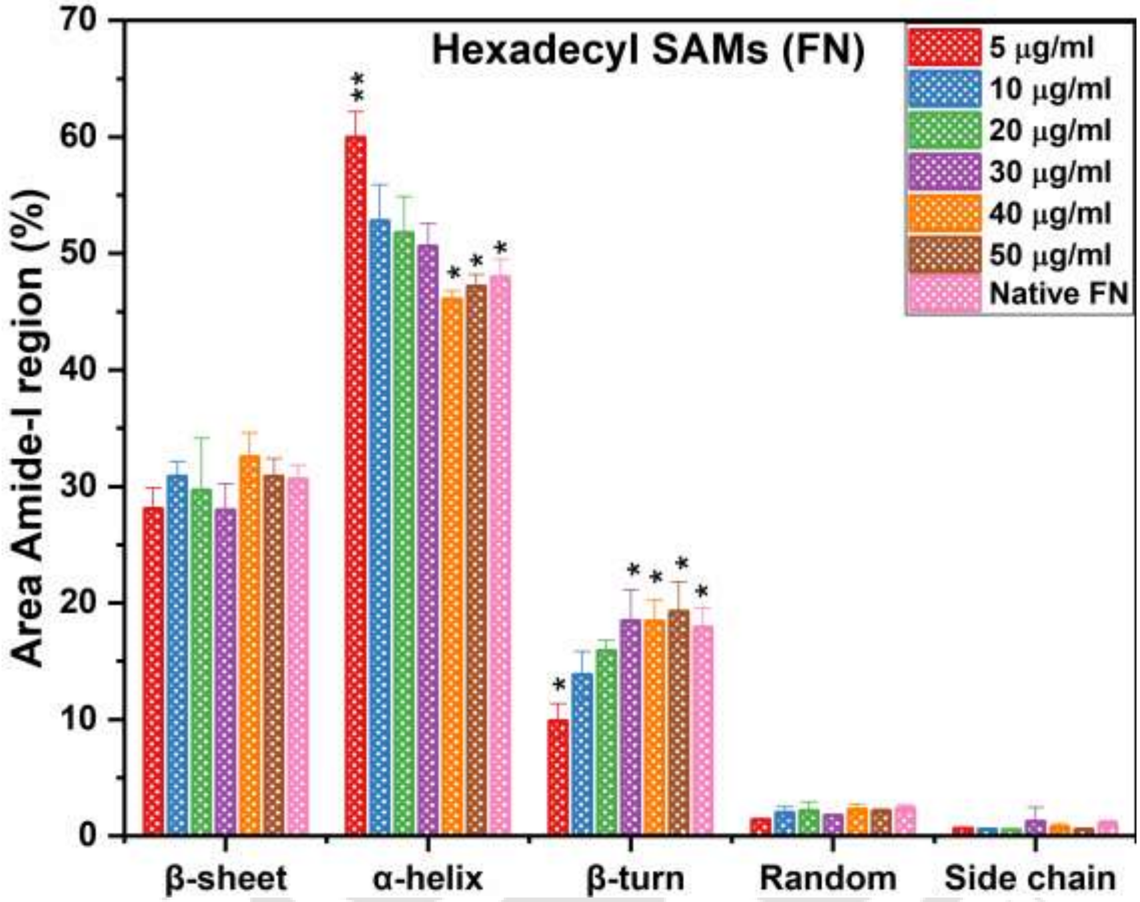

Figure 4.20: Bar graph showing the change in the secondary structure of the FN in the amide-I region for the hexadecyl SAMs samples; statistical analysis was performed using GraphPad Prism, where ns > 0.05, * ≤ 0.05, ** ≤ 0.01, *** ≤ 0.001.

4.3.5 BSA adsorption insights on the mixed$_{(16-8)}$ and carboxyl$_{(16-8)}$ SAMs

Hexadecyl and octyl silane moieties were utilized to fabricate the mixed and carboxyl SAMs containing equal ratios of the precursor moieties. BSA was explored for the adsorption behaviour on the mixed and carboxyl SAM surfaces. β-sheet conformation changed from 35±1% (native BSA) to 22-28% for the adsorbed surfaces with 21.4±0.6% (0.5 mg/ml) and 26±4% (5 mg/ml). α-helicity decreased with the increase in BSA conc as follows: 63.5±1.3 (0.5 mg/ml) > 63±2.6 (1 mg/ml) > 59.6±1.4 (4 mg/ml), 54±5% (5 mg/ml) and 43±0.3%

(native); β-turn exhibited the following result: 19±1% (native), 13.7±2.3% (0.5 mg/ml), 12.8±1.7% (3 mg/ml), 14.2±0.6 (4 mg/ml) and 17.7±4 (5 mg/ml) as shown in **Fig. 4.21**.

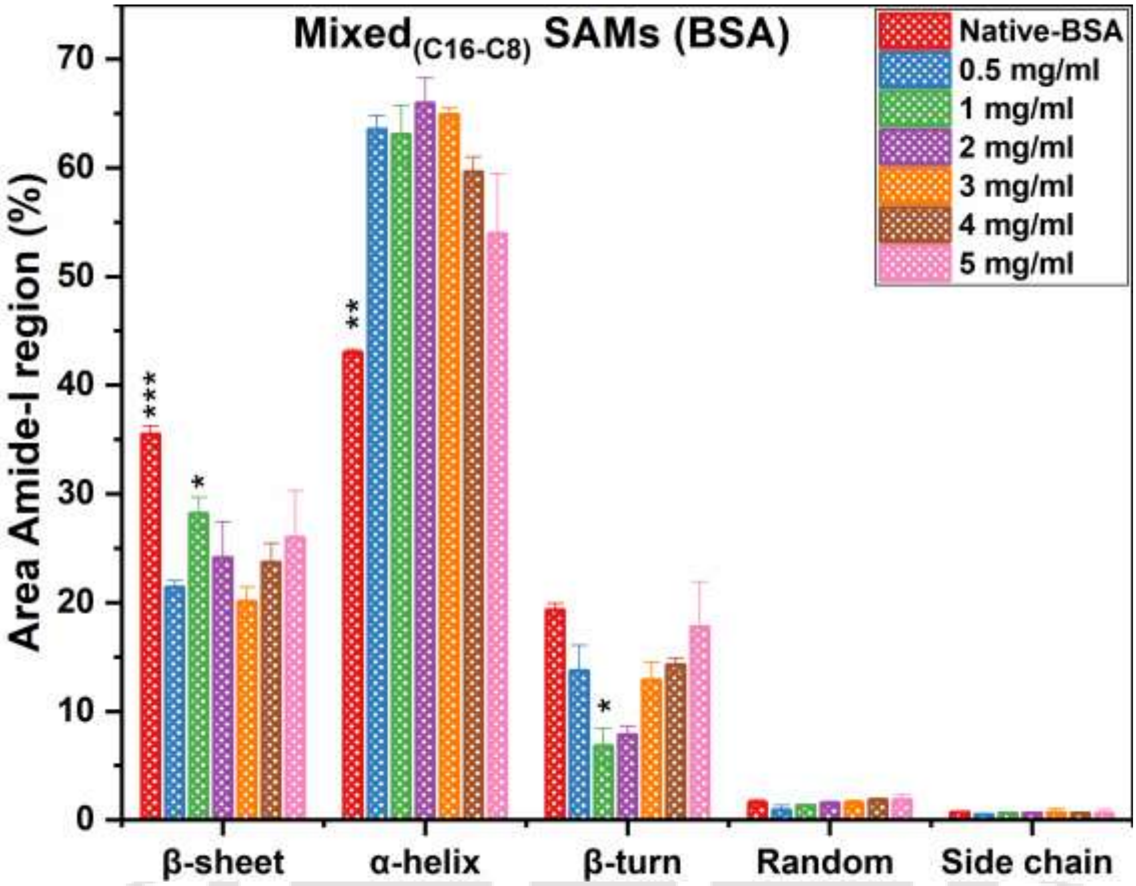

Figure 4.21: Bar graph showing the change in the secondary structure of the BSA in the amide-I region for the mixed SAMs samples; statistical analysis was performed using GraphPad Prism, where ns > 0.05, * ≤ 0.05, ** ≤ 0.01, *** ≤ 0.001.

Carboxyl$_{(16-8)}$ SAMs were fabricated by the secondary modification of the mixed SAMs with acidified potassium permanganate to form the carboxyl terminals. Carboxyl$_{(16-8)}$ SAMs were also investigated for changes in the BSA secondary structure post-adsorption on the functionalized surfaces. β-sheet conformation was 22.7±3% (0.5 mg/ml), 30±1.3% (5 mg/ml), and 35.5±0.8% (native), α-helicity decreased with the increase in the BSA conc.as follows: 60.3±3.6 (0.5 mg/ml) > 57.6±3 (1 mg/ml), 58.6±1.7 (2 mg/ml) > 56±2.6 (3 mg/ml) > 54.2±1.2 (4 mg/ml) > 44.4±0.6% (5 mg/ml), and native (42.9±0.2). There was an increase in the β-turn with an increase in the adsorbed BSA conc with slight variation among the surfaces as follows:

14.7±0.8 (0.5 mg/ml) < 17.4±2.4 (1 mg/ml), 16.7±2.6 (3 mg/ml) < 23.8±1.7% (5 mg/ml) and 19±1 (native) as shown in **Fig. 4.22**.

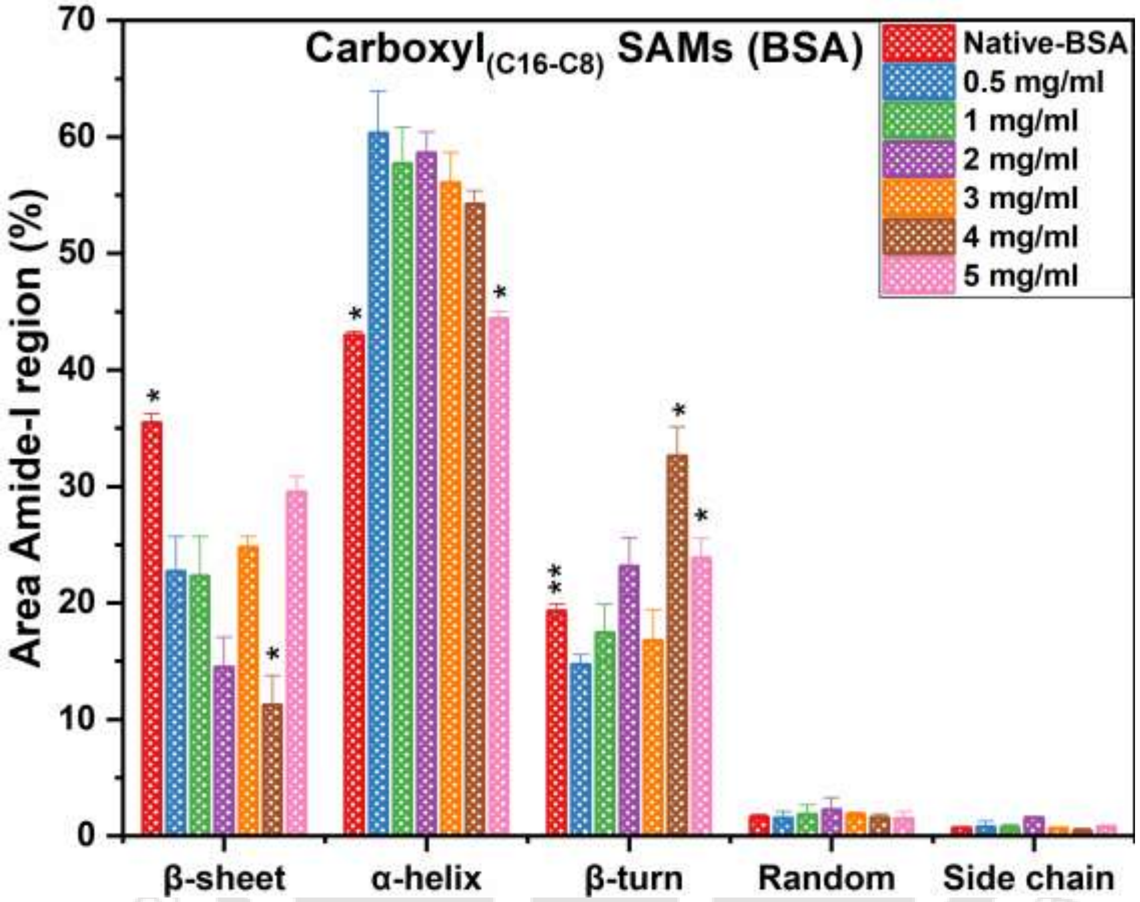

Figure 4.22: Bar graph showing the change in the secondary structure of the BSA in the amide-I region for the carboxyl SAMs samples; statistical analysis was performed using GraphPad Prism, where ns > 0.05, * ≤ 0.05, ** ≤ 0.01, *** ≤ 0.001.

4.4 Conclusion

BSA and FBS adsorption was carried out on the AO-, AC-, HO-, and HC- series samples to investigate the change in the secondary structure. AO series showed an increase in the β-sheet and a decrease in the β-turn conformation, increasing the octyl proportionality for BSA. On the other hand, there was a decreasing trend in the α-helicity and an increase in the β-sheet conformation with the rise in the carboxyl proportionality. FTIR deconvolution exhibited a decrease in the β-sheet conformation and an increase in the α-helicity for the HO series; α-helicity showed an increase with the increase in the hybrid proportionality in the HC series.

FBS adsorption on the AO- and AC- series samples showed a decrease in the α- helicity but an increase in the β-turn conformation for the AO- series and β-sheet conformation for the AC- series samples. There is a slight increase in the β-sheet conformation for HO- and HC- series and a decrease in the α-helicity with increased octyl proportionality in the HO series samples and a decrease in the β-turn conformation with increased carboxyl proportionality for the HC- series.

Carboxyl SAMs surfaces showed a decrease in the β-sheet structure with increased incubation time compared to octyl SAMs for 1% and 2% acidified $KMnO_4$ incubated samples. 3% incubated surfaces showed an increase in the β-sheet with an initial lag phase, while α-helicity increased, but the β-turn conformation decreased for the 5% incubated surfaces. BSA exhibited a decrease in the change of α-helicity with the increase in the conc for the octadecyl and hexadecyl SAMs surfaces; samples adsorbed with lower BSA conc exhibited unfolding behaviour as reflected by the change in the conformation of protein adsorbed on the functionalized substrates. α-helicity increased while the β-turn conformation decreased with the increase of the adsorbed FN conc on the hexadecyl SAMs functionalized surfaces. Mixed$_{(16-8)}$ and carboxyl$_{(16-8)}$ SAMs functionalized surfaces showed a decrease in the α-helicity and an increase in the β-turn conformation of the adsorbed BSA secondary structure. Choice of surface will depend on the application, say for the fabrication of the BSA based anti-biofouling surface, silane functionalization showing the highest change in the protein secondary structure along with high surface energy might be the suitable surface. Similar approach can be used to fabricate collagen coated surfaces for various tissue engineering related applications.

Chapter 5

Bio-interfacial study of cellular interactions with functionalized model implant surfaces mediated by adsorbed proteins

This chapter focuses on cell adhesion studies using MG63 cell lines on various silane-functionalized titanium surfaces. The first section explores the cell adhesion behavior of the MG63 cell line on the AO-, AC-, HO-, and HC- series Ti6Al4V surfaces. The following section dealt with the effects of the FBS pre-adsorption on the Octyl and Bare Ti6Al4V surfaces to enhance the cell-material interactions. The third section discussed the longer Hexadecyl SAMs and their cellular interactions with and without pre-adsorption of proteins (BSA, Col-I, and FN).

5.1 Introduction

Interactions of proteins, cells, and body fluid with the biomaterial are crucial for the success of an implant [341, 342]. The type of cellular-biomaterial interactions varies from implant to implant. For example, reconstructive implants require osseointegration with surrounding cells and tissues [343] without toxic leachate from the implant surface. The success of an implant is determined by tissue-level events such as blood clotting, surface fouling, and bone resorption, which are derived from molecular and cellular interactions at the implant-tissue interface [344]. The environment inside the body is electrically, mechanically, and chemically active. Many dynamic biological events occur at the interface due to alteration of the typical biochemical environment around the implant site [232]. The implant surface (metallic, polymeric, or ceramic) contains various surface ions arising from functional groups on the implant surface, incorporating the biological ions and forming a surface oxide layer [233].

Implant interacts typically with the bloodstream or extracellular matrix, leading to the first binding of constituent proteins followed by cell-implant interactions [345]. Interaction of proteins and other biological molecules with the implant surface causes a temporary or permanent change in the conformation, leading to a shift in function [346, 347]. Controlling cell-biomaterial interactions is a prerequisite for developing successful implants [348]. Various surface modification strategies can be utilized to tune the various surface properties. Silanization is a surface modification strategy, as Silane is well known to enhance cell adhesion and promote osteoblast differentiation. In a study done on the SaOS-2 osteoblast cell line, it was found that triethoxysilypropyl succinic anhydride silane (TESPA) enhances the osteoblast activity by increasing the gene expression of the RUNX2 gene involved in the osteoblast differentiation on the titanium surface. Upregulation of COL1A1 and BMP-2 expression hundredfold confirms the role of the TESPA silane in promoting osteoblast growth differentiation and maturation [235]. In another cell adhesion study conducted using the HLE and rat pheochromocytoma (PC12) cells on the bare and silane-modified glass surfaces, it was found that ECM protein pre-adsorption shortened the adhesion time and increased the cell adhesion on the surfaces without the serum supplementation in DMEM compared to the bare substrates indicating their potential for biomedical applications [349].

This chapter focused on biomaterial-cell interactions. Various silane modifications, such as amine, octyl, and hexadecyl, were utilized to tune the surface properties of Ti6Al4V surfaces, along with secondary modifications of carboxyl and hybrid SAMs. In the first section, the proportionalities of the amine, octyl, hybrid, and carboxyl SAMs were varied to determine the best strategy for enhanced cell adhesion. Apart from these, pre-adsorption of various proteins such as FBS, collagen, BSA, and fibrinogen was carried out on the hydrophobic silanes (octyl and hexadecyl SAMs) to enhance the cell adhesion capability.

5.2 Materials and methods

Bovine Serum Albumin (BSA) [catalog no. A2153], lyophilized bovine fibrinogen (FN) [catalog no. F8630], type-I collagen from calf skin (Col-I) [catalog no. C9791-10MG], Fluorescein isothiocyanate (FITC) labeled phalloidin [catalog no. P5282], Propidium iodide (PI) [catalog no. 537059] and PenStrep antibiotic [catalog no. P0781] were procured from Sigma-Aldrich. The human osteoblast cell line (MG63) was procured from NCCS, Pune. Dulbecco's modified Eagle's medium (DMEM) [catalog no. AL066A], sodium chloride (NaCl) [catalog no. MB023], potassium chloride (KCl) [catalog no.TC010], dibasic sodium phosphate (Na_2HPO_4) [catalog no. MB024], and monobasic potassium phosphate (KH_2PO_4) [catalog no. MB050], paraformaldehyde [catalog no. TCL119], and tritonX100 [catalog. No.TC286] were procured from Himedia, India. Fetal Bovine Serum (FBS) [catalog no. 10082147] from Thermo Fischer, India.

5.2.1 Silane-based SAMs formation

Please refer to the Materials and Method section of Chapter 3 for more detail regarding the sample preparation and silane-based SAMs formation.

5.2.2 Protein pre-adsorption

5.2.2.1 Fetal Bovine Serum Pre-adsorption on octyl-SAMs modified Ti6Al4V surfaces

Bare Ti6Al4V and octyl SAMs surfaces (1x1 cm) were sterilized by dipping the samples in 70% ethanol for 1 hour under the laminar flow, followed by washing the samples thrice with sterile Phosphate Buffered Saline (PBS)[350]. They were dried aseptically under laminar air flow conditions, followed by transferring the samples to sterile 24-well plates for further experimentation. FBS aliquot was thawed in the water bath at 37 °C. FBS dilutions of 5, 10, 15, 20, 25, and 30 (v/v) were prepared in sterile PBS under aseptic conditions. 1 ml of the FBS dilutions was added to the sterile bare and octyl SAMs samples and transferred to an incubator at 37 °C for 2 hours [351]. After the pre-adsorption step, the remaining FBS was discarded, and the samples were washed thrice with sterile PBS and kept aside.

Meanwhile, the MG63 cell line with 85-90% confluency was passaged post-trypsinization, cells were counted on the hemocytometer, and cell stock ($1x10^4$ cells/ml) was prepared in the DMEM media. Cells were incubated on the functionalized surfaces with pre-adsorbed FBS (varied conc) and kept in the incubator for 12 hours for the cell adhesion experiments. Surfaces with the pre-adsorbed proteins were incubated with incomplete DMEM media (lacking 10% FBS but with 1% PenStrep solution). Samples without FBS pre-adsorption and samples incubated with complete DMEM media were used as the control samples.

5.2.2.2 Albumin, fibrinogen, and collagen-I pre-adsorption on hexadecyl SAMs modified Ti6Al4V surfaces.

Bovine Serum Albumin (BSA) stock was prepared in 1xPBS solution (pH 7.4) at RT conditions, and concentration was determined using an Implen spectro nanophotometer (Implen GmbH, Munich, Germany). BSA stock was sterilized using the 0.2 µm syringe filter in the cell culture hood, followed by dilution preparations (0.5, 1, 2, 3, 4, & 5 mg/ml). Fibrinogen stock was also prepared in PBS buffer at pH 7.4, and the stock was filter sterilized (0.2 µm) in the cell culture cabinet followed by dilution preparations (5, 10, 20, 30, 40 & 50 µg/ml) and added to the sterile hexadecyl SAMs samples. Type-I collagen was mixed in 0.1M glacial acetic acid (1mg/ml), followed by vortexing and storing at 4 °C to completely solubilize the protein in the buffer. After that, the collagen solution was diluted in the PBS solution to attain a pH of 7.4. Before the pre-adsorption studies, collagen was filtered and sterilized (0.2 µm), and 5, 10, 20, 30, 40, and 50 µg/ml protein dilutions were prepared for the cell culture experiments[152, 352]. Sterilized hexadecyl SAMs ($1x1\ cm^2$) surfaces were placed in the 24 well plates, and individual proteins with varied concentrations were added to the wells with the samples. Moreover, mixed solutions of BSA/Col-I, BSA/FN, and FN/Col-I were added to the samples at various concentrations and incubated in the cell culture incubator for 2 hours at 37 °C. Post adsorption, the remaining protein solution was discarded, and samples were rinsed thrice with sterile PBS and kept aside[353, 354]. As mentioned in the previous section regarding the cell adhesion studies, pre-adsorbed surfaces were incubated with 1 ml DMEM media (without FBS) with a cell density of $1x10^4$ cells/ml for 12 hours in the incubator. Samples without pre-adsorbed protein and complete DMEM media were used as the controls.

5.2.2.3 Cell Adhesion studies, fluorescence staining, and microscopy

Sterilized AO-, AC-, HO-, and HC- series (as mentioned in Chapter 3) samples were incubated with complete DMEM media containing the MG63 cell line ($1x10^4$ cells/ml) in the incubator for 12 hours for cell adhesion. The bare Ti6Al4V surface without the silane modification was the control sample. Post-cell adhesion experiments spent DMEM media discarded from the samples, and the sample surfaces were gently rinsed thrice with sterile PBS to remove the unadhered MG63 cells from the sample surfaces [19, 62, 152]. Cell adhesion was visualized and quantified using fluorescence microscopy post-experiments. Samples were fixed with 4% (v/v) paraformaldehyde solution overnight at 4 °C. Post fixation, the unreacted paraformaldehyde was discarded, and samples were rinsed thrice with PBS. To avoid non-specific staining on the surface, surfaces were blocked with 2% (w/v) BSA and permeabilized with 0.2% (w/v) Triton X100 for 6 hours, followed by staining the actin filaments with phalloidin-FITC dye for 12 hrs. Surfaces were stained with propidium iodide (PI) at 20 µg/ml to stain the cell nuclei for 2 hours. After each step, samples were thoroughly rinsed with the PBS thrice to remove the unreacted reagents and dyes. Cell imaging was carried out using a Nikon fluorescent microscope. Based on the cell images obtained, further image processing and data quantification were carried out using ImageJ software (developed at the National

Institute of Health, USA) to analyze cell area, cell circularity, and surface coverage of the cells on the various modified surfaces [19, 62, 152].

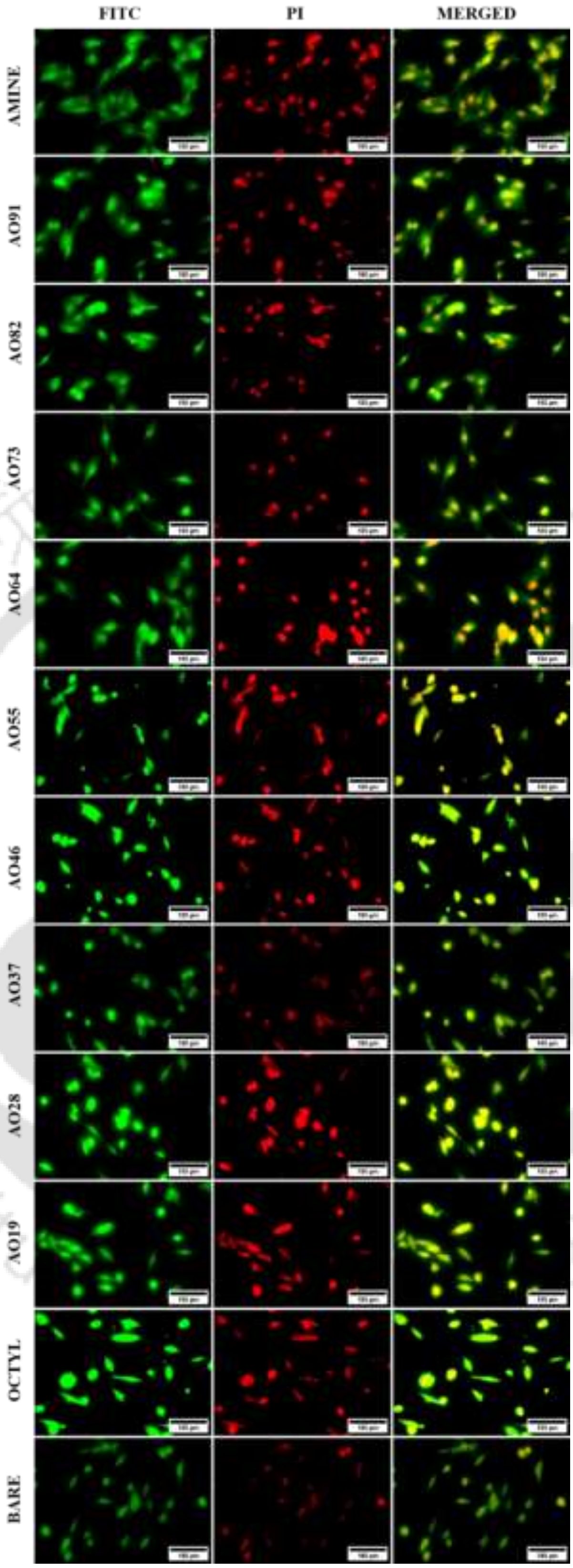

Figure 5.1: Fluorescent cell images of the MG63 cell line adhered to the AO series samples.

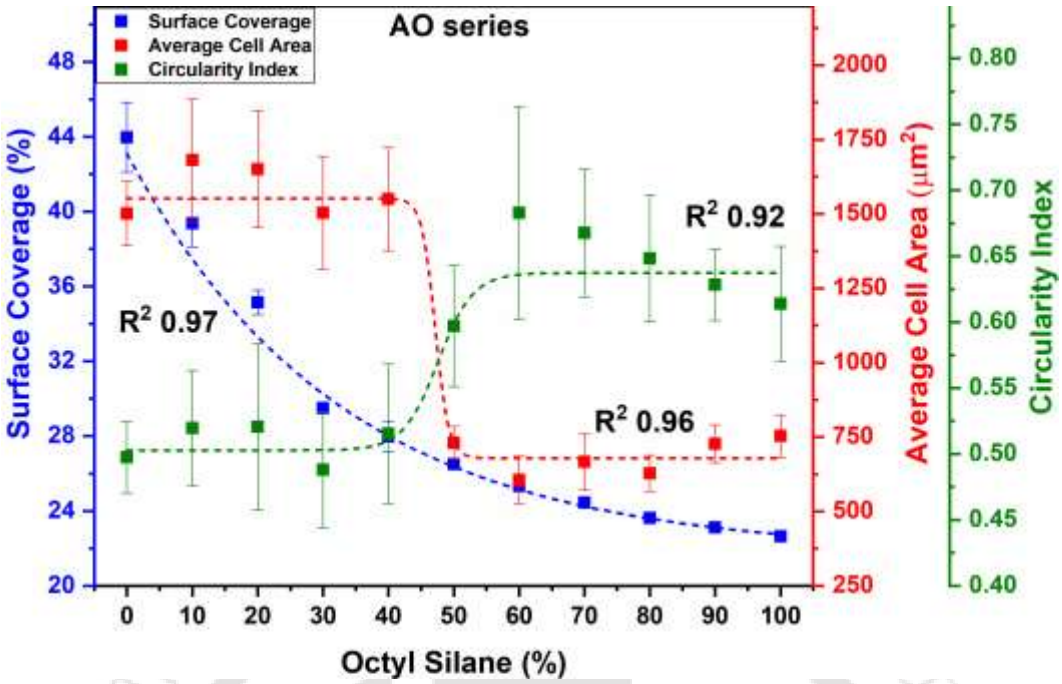

Figure 5.2: Graph showing the data for the surface coverage, average cell area, and cell circularity index for AO series samples; dotted lines show the fitted data.

5.3 Results and Discussion

5.3.1 AO-, AC-, HO- and HC- series

AO series contained the variable ratio (v/v) of the amine and octyl SAMs precursors; the AC series comprised the variable ratios (v/v) of the amine and carboxyl; HO series comprised the variable ratios of hybrid (secondary modification of amine SAMs) and octyl while the HC series contained the variable precursor volume ratios of the secondary modifications of the amine (hybrid SAMs) and octyl (carboxyl SAMs). Cell adhesion studies were conducted on the various modified surfaces to evaluate the effect and extent of the variable precursor silanes. As evident from **Fig. 5.1**, the octyl SAM surface showed the least surface coverage, cell spreading, and proliferation among the silane-modified surfaces. As the octyl SAMs surface is hydrophobic, the least cell adhesion is comparable to that of the Bare Ti6Al4V surfaces. Cell surface coverage (%), cell circularity index, and average cell area (μm^2) were the cell adhesion parameters evaluated based on the fluorescent cell images, as shown in **Fig. 5.2**. A cell circularity index of 1 implies a perfect circle, whereas 0 implies an extensively elongated polygon; the better the cell spreads, the more likely the cells will exemplify a value approaching 0. ImageJ software was used to extract the quantitative data from the cell images.

Surface coverage of the bare sample was 14.2±0.1%, while 43.9±1.8% (amine SAMs) and 22.6±0.1% (octyl SAMs). The average cell areas were 690±60, 753±70.9 and 1501±108 μm^2 for bare, octyl, and amine SAMs, respectively. Bare and octyl surfaces exhibited similar circularity (~0.61), which reduced to 0.49±0.02 for the amine SAMs. Amine SAMs surfaces with moderate surface wettability and terminal amine group showed remarkable surface coverage and cell spreading. In contrast, the rest of the samples showed a trend between the two extremes, and cell adhesion parameters improved with an increase in the amine precursor ratio.

Furthermore, OriginPro software was used to perform the data fitting function to determine the trendline for the various cell adhesion parameters. In the case of the AO-series samples, the Exponential function was utilized to fit the surface coverage (%) data, where average cell area and circularity index data were fitted using the sigmoidal function. Surface coverage showed a decrease rate of 0.03 $\%^{-1}$ with the increase in the octyl percentage (R2: 0.97), whereas average cell area increased by a rate of 0.97 $\%^{-1}$ (R2: 0.97) with the rise in the amine proportionality and started growing after the amine proportion increased by 45.1% in the series. On the other hand, circularity showed a transition point when the octyl fraction increased by 42.2% with a rate of 0.37 $\%^{-1}$ based on the fitted data (R^2: 0.92), indicating lesser cell spreading with the increase in the octyl content, as shown in **Fig. 5.2**.

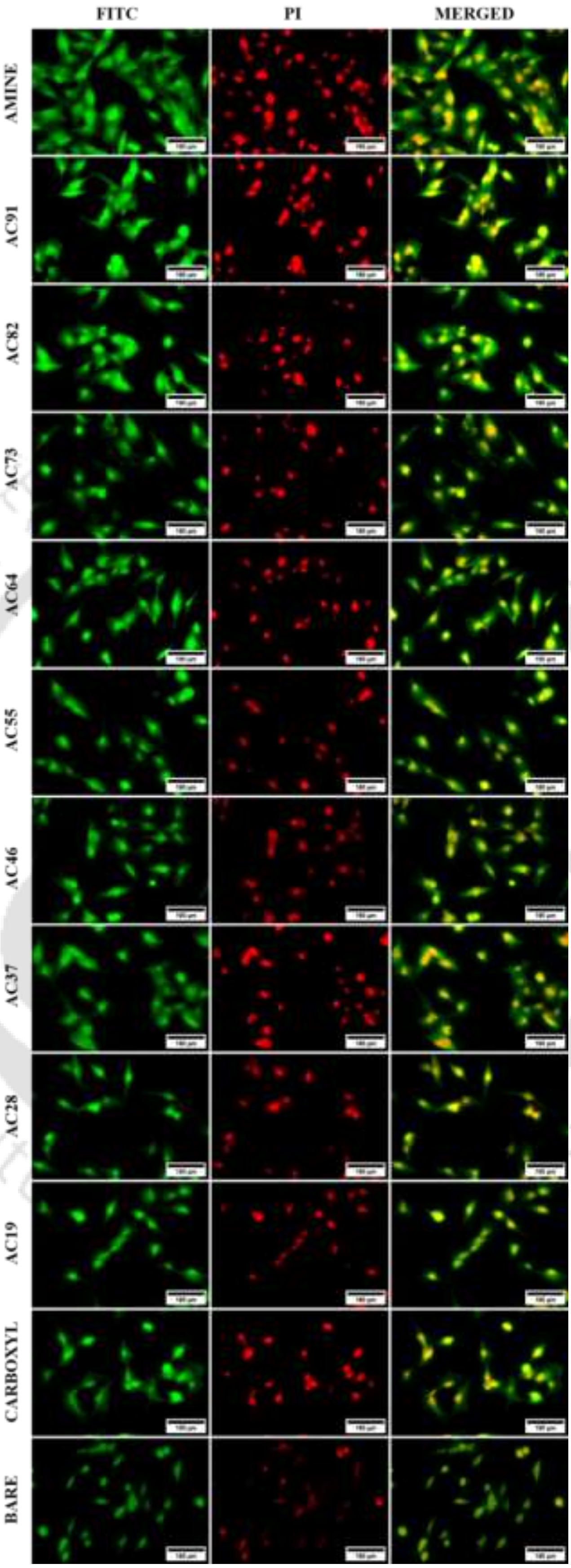

Figure 5.3: Representative fluorescent cell images of the MG63 cell line on the AC series surfaces.

Indian Institute of Technology Guwahati

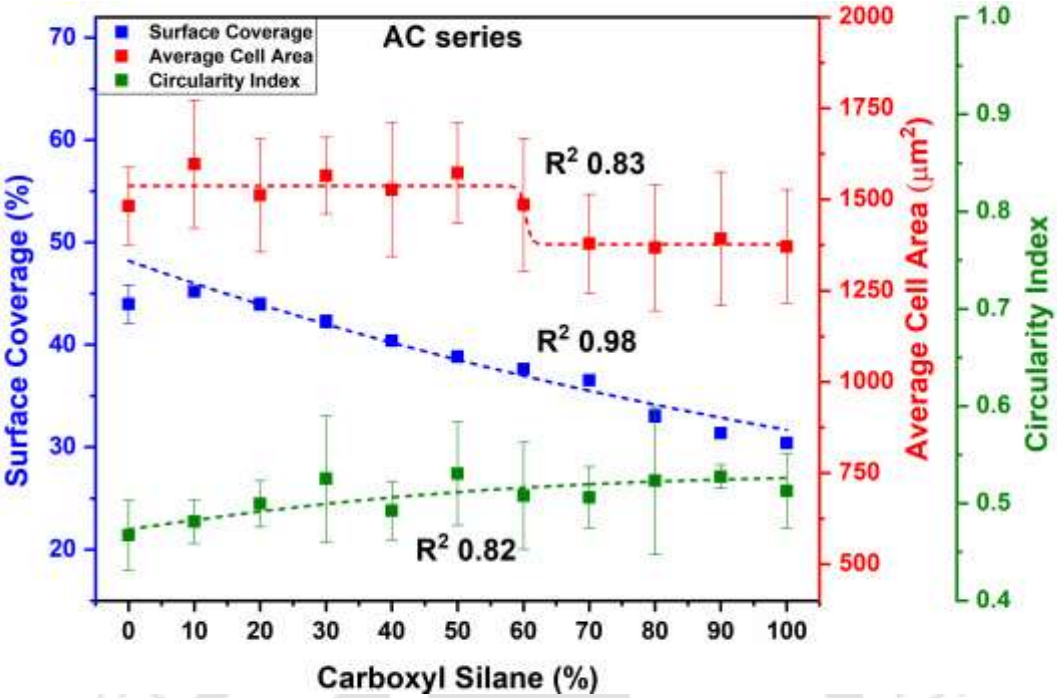

Figure 5.4: Graph showing the data for the surface coverage, average cell area, and cell circularity index for AC series samples; dotted lines represent the fitted data.

Cell adhesion was best for the AC series samples on the amine SAMs-modified substrates. Still, it gradually decreased with the increase in the ratio of the carboxyl SAMs precursor exhibiting the least cell adhesion on the carboxyl SAMs surfaces (**Fig. 5.3**). Though there is no steep decrease in the circularity for the amine and carboxyl SAMs surfaces, there is a slight decrease in the average cell area for the samples with carboxyl SAMs precursor ratios. Amine SAMs exhibited a higher surface coverage (43.9±1.8%) compared to the carboxyl SAMs (30.4±0.2%); there was a slight change in the circularity for amine SAMs (0.46±0.03) and carboxyl SAMs (0.51±0.03) while the average cell area was 1481±105 μm^2 (amine SAMs) and 1370±155 μm^2 (carboxyl SAMs) as shown in **Fig. 5.4**. The decrease in the surface coverage with the increase in the carboxyl proportionality was as follows: 60.6±3.6 (amine only), 45.2±0.3 (AC91), 43.9±0.3 (AC82), 42.3±0.6 (AC73), 40.4±0.3 (AC64), 38.8±0.5 (AC55), 37.6±0.2 (AC46), 36.5±0.2 (AC37), 33±0.6 (AC28), 31.4±04 (AC19) and 30.4±0.2% (carboxyl only), respectively. Surface coverage showed a decrease rate of -0.006 (R^2: 0.95) due to an increase in the hydrophobic octyl SAMs, whereas the circularity increased by a rate of 0.03 $\%^{-1}$ with the increase in the octyl proportionality (R^2: 0.82). The average cell area transitioned at a 59.44% decrease in octyl proportionality with a rate of $2.25\%^{-1}$ (R^2: 0.83), increasing the average cell area.

Indian Institute of Technology Guwahati

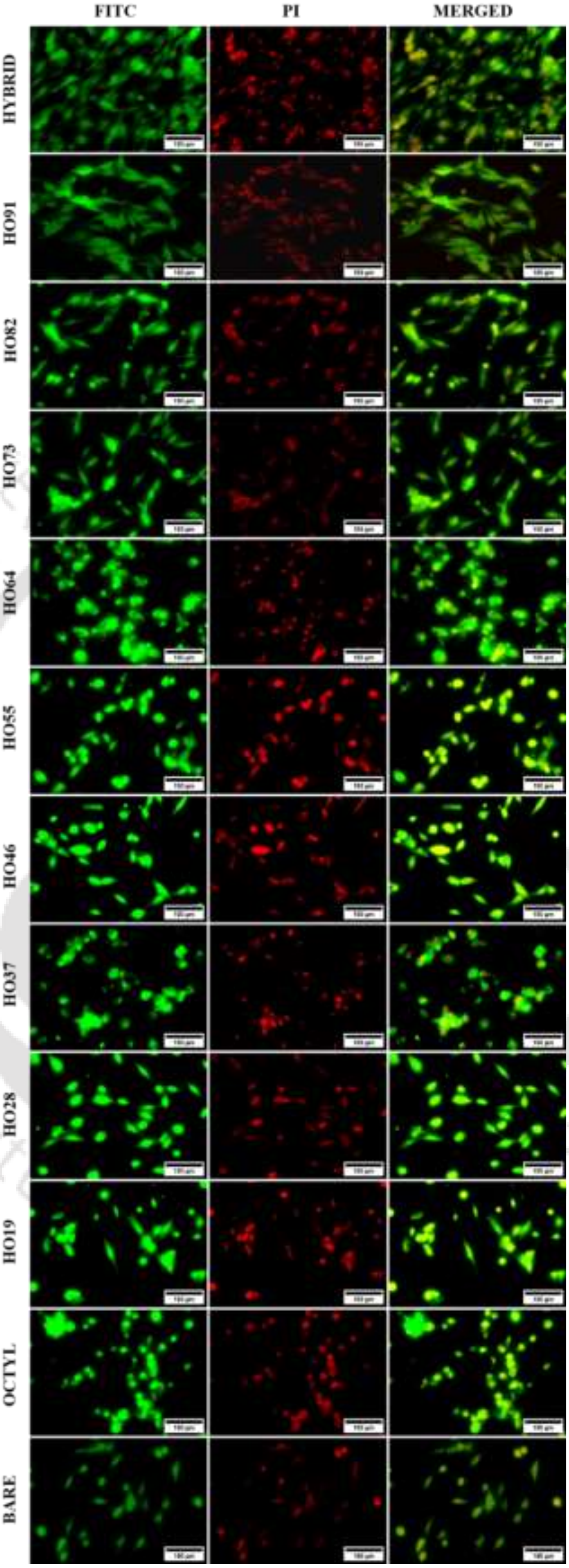

Figure 5.5: Representative fluorescent images of the MG63 cell line on the HO series surfaces.

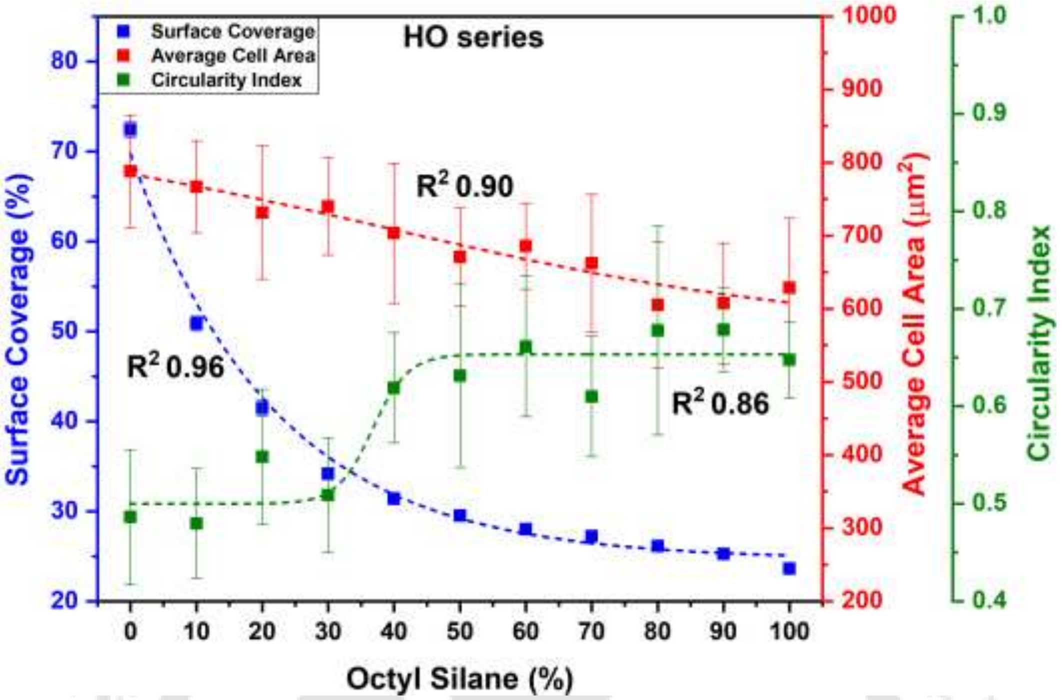

Figure 5.6: Graph showing the data for the surface coverage, average cell area, and cell circularity index for HO series samples; dotted lines show the fitted data.

Amine SAMs undergo secondary modification to form hybrid SAMs of the AO series samples, resulting in HO series samples. The cell adhesion study showed a result similar to the AO series samples, as the hydrophobicity of the octyl SAMs compromised the biological features of the modified surfaces, as shown in **Fig. 5.5**. The higher the precursor octyl silane ratio, the lower the feature of the resultant cell adhesion parameters. Hybrid SAMs exhibited the highest surface coverage (72.4±0.96%) and least by the octyl SAMs (23.6±0.24%), highest circularity for the octyl SAMs (0.64±0.04) and least for amine SAMs (0.48±0.06); least average cell area for the octyl SAMs (629±94.5 µm^2) and highest for the amine SAMs (788±77 µm^2) surfaces. Surface coverage showed the following trend: 72.4±0.96 (hybrid), 50.8±0.8 (HO91), 41.4±0.8 (HO82), 34±0.6 (HO73), 31.4±0.6 (HO64), 29.5±0.4 (HO55), 28±0.4 (HO46), 27.2±0.2 (HO37), 26±0.3 (HO28), 25.2±0.2 (HO19), and 23.6±0.2% (octyl), respectively; decrease in the average surface area was as follows: 788±77 > 766±62 > 731±91 > 740±66 > 703±95 > 670±67 > 685±58 > 662±93 > 605±85 > 607±82 > 629±94 µm^2. The circularity index increased with the increase in the octyl proportionality in the series with slight variation in the trend as follows: 0.48±0.06 < 0.47±0.05 < 0.54±0.06 < 0.5±0.05 < 0.61±0.05 < 0.63±0.09 < 0.66±0.07 <0.61±0.06 < 0.67±0.1 < 0.67±0.04 < 0.64±0.04. Surface coverage decreased with a rate of -0.045%$^{-1}$ (R^2: 0.97) with the octyl SAMs increase; on the other hand, an increase in the amine percentage resulted in an increase in the rate of the average cell area by 0.029%$^{-1}$ (R^2: 0.90). Circularity index showed a sigmoidal curve with transition begin at 31.3% octyl SAMs proportion with a rate of 0.36 %$^{-1}$ (R^2: 0.9) as shown in **Fig. 5.6**.

Indian Institute of Technology Guwahati

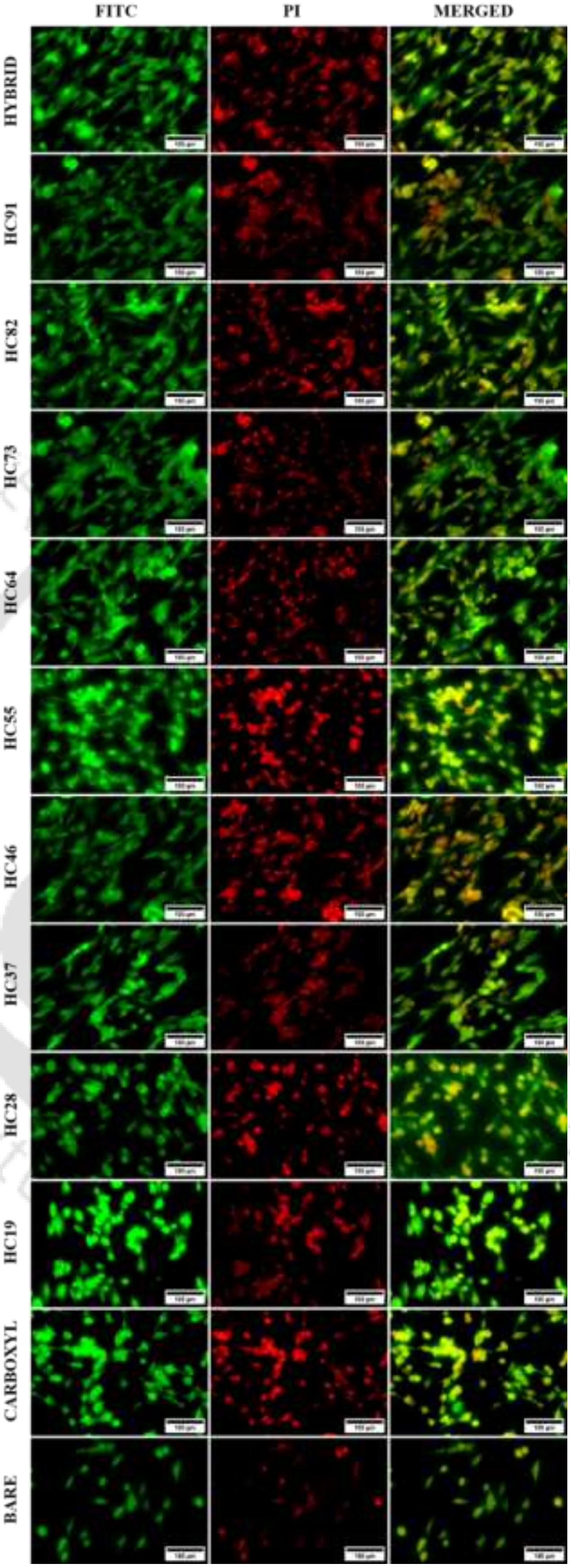

Figure 5.7: Representative fluorescent images of the MG63 cell line on the HC series surfaces.

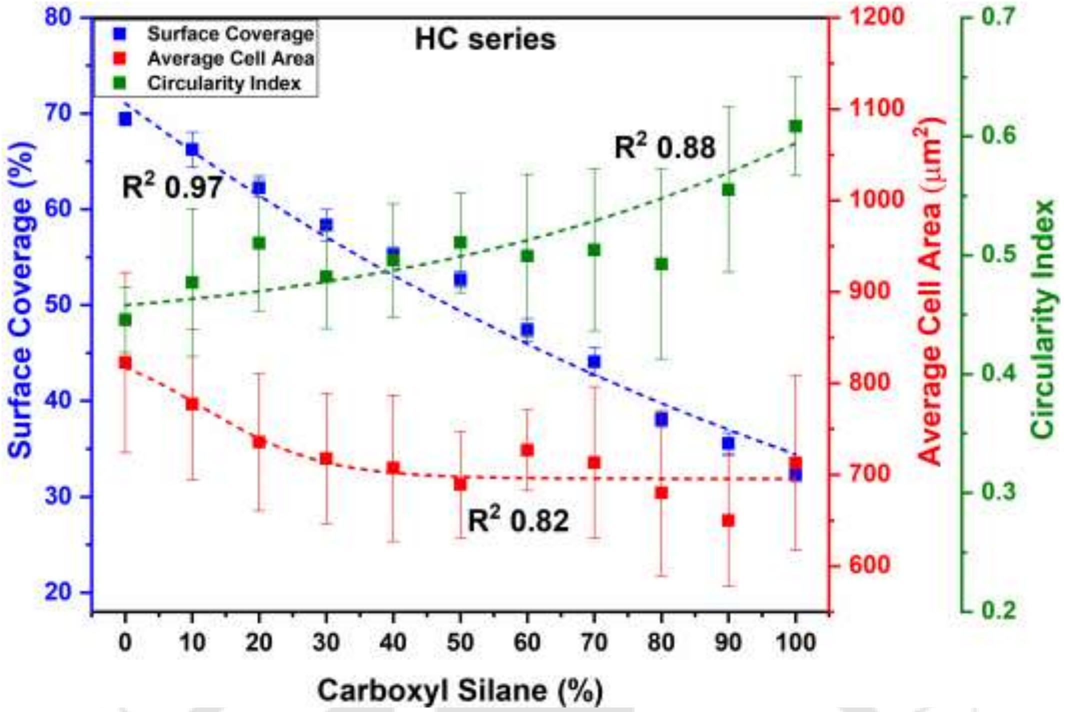

Figure 5.8: Graph showing the data for the surface coverage, average cell area, and cell circularity index for HC series samples; dotted lines show the fitted data.

Secondary modification of the amine and octyl SAMs resulted in the formation of the hybrid and carboxyl SAMs, so the double secondary modification of the precursor silanes fabricated the HC series samples. Lower performance of the octyl SAM surfaces due to hydrophobicity can be enhanced by turning the octyl group into carboxyl, resulting in the carboxyl SAM modification. **Fig. 5.7** shows the fluorescent cell images of HC series samples that showed remarkable cell adhesion of the MG63 cells on all the series variants with better surface coverage, circularity index, and average cell area. The least surface coverage and average cell area were shown by carboxyl SAMs (32.3±0.84%, 712±95 μm^2) and highest for hybrid SAMs (69.4±0.7%, 822±98 μm^2). In contrast, carboxyl SAMs exhibited the highest circularity (0.6±0.04) and the least for the hybrid SAMs (0.44±0.02), as evident from **Fig. 5.8**. Surface coverage decreased for the HC series samples as follows: 69.4±0.7 > 66.2±1.8 > 62.2±1 > 58.3±1.6 > 55.2±0.8 > 52.6±0.8 > 47.4±1 > 44±1 > 38±0.7 > 35.5±1 > 32.3±0.8% and the average cell area showed a decreasing trend with slight variation as follows: 822±98 >777±82

> 735±75 > 717±71 > 707±80 > 689±57 > 726±44 > 713±83 > 679±90 > 649±71 > 712±95 μm^2.

Table 5.1: Derived cell adhesion parameters based on fitted data

Series	Rate constant of surface coverage (%$^{-1}$)	Transition point (%)	Maximum coverage/surface (%)
AO	-0.03	45.1	43.9±1.8 of amine SAMs
AC	-0.006	59.4	45.9±2.2 of amine SAMs
HO	-0.045	31.3	72.4±01 of hybrid SAMs
HC	-0.007	-	70.2±1.6 of hybrid SAMs

Surface coverage decreased at -0.007 %$^{-1}$, with an increase in the carboxyl proportion (R^2: 0.97). The average cell area increased at a rate of 0.12 %$^{-1}$ with increased hybrid proportionality in the series (R^2: 0.82); circularity reflecting the cell spreading increased at a rate of 0.022 %$^{-1}$ with an increase in the carboxyl fraction in the system (R^2: 0.88). All the derived cell adhesion parameters based on the fitted data are tabulated in **Table 5.1**, and the range of the circularity, average area, and surface coverage are mentioned in **Table 5.2**.

Table 5.2: Range of the various cell adhesion parameters

	Range		
Series	**Average Area (μm^2)**	**Surface coverage (%)**	**Circularity**
AO	600 - 1500	22.6 - 44	0.48 – 0.68
AC	1370 - 1600	30 - 44	0.46 – 0.53
HO	605 - 790	23.5 – 72.4	0.48 – 0.67
HC	822 - 650	32 - 70	0.44 – 0.6

Among the AO-, AC-, HO- and HC- series samples, hybrid SAMs exhibited the best surface coverage of 72.4±0.9%; the least circularity was shown by the hybrid followed by the amine SAMs modified surfaces (0.46); the highest cell area attained by the amine SAMs surfaces (~1500 μm^2). The highest rate of decrease of the surface coverage (~ -0.04) was shown by the samples containing the octyl SAMs fractions (HO- AO- series), while the carboxyl conversion of the octyl fractions reduced the decrease rate by 10 folds (~ -0.007).

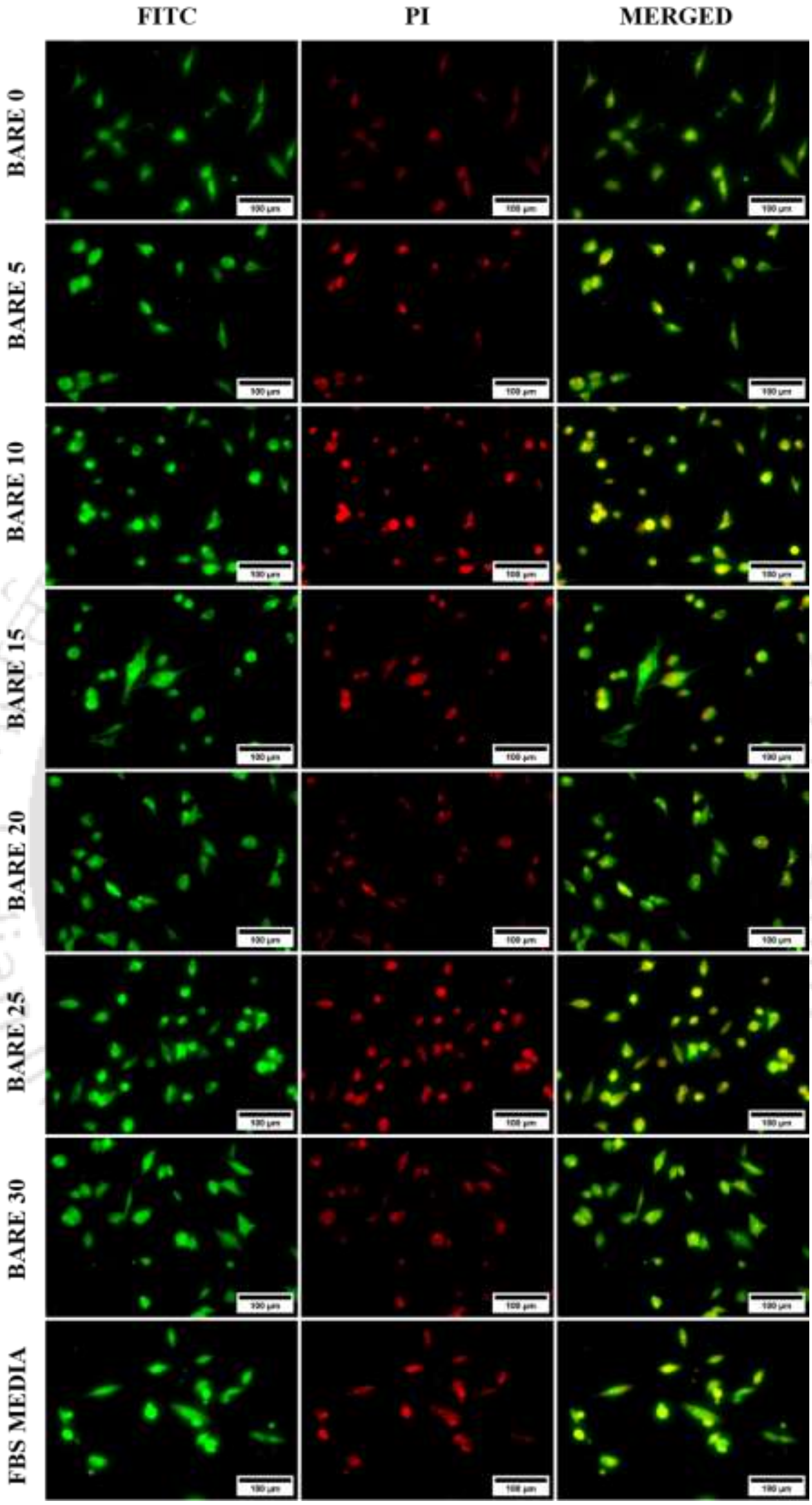

Figure 5.9: Representative fluorescent images of the MG63 cell line on the FBS pre-adsorbed bare Ti6Al4V surfaces.

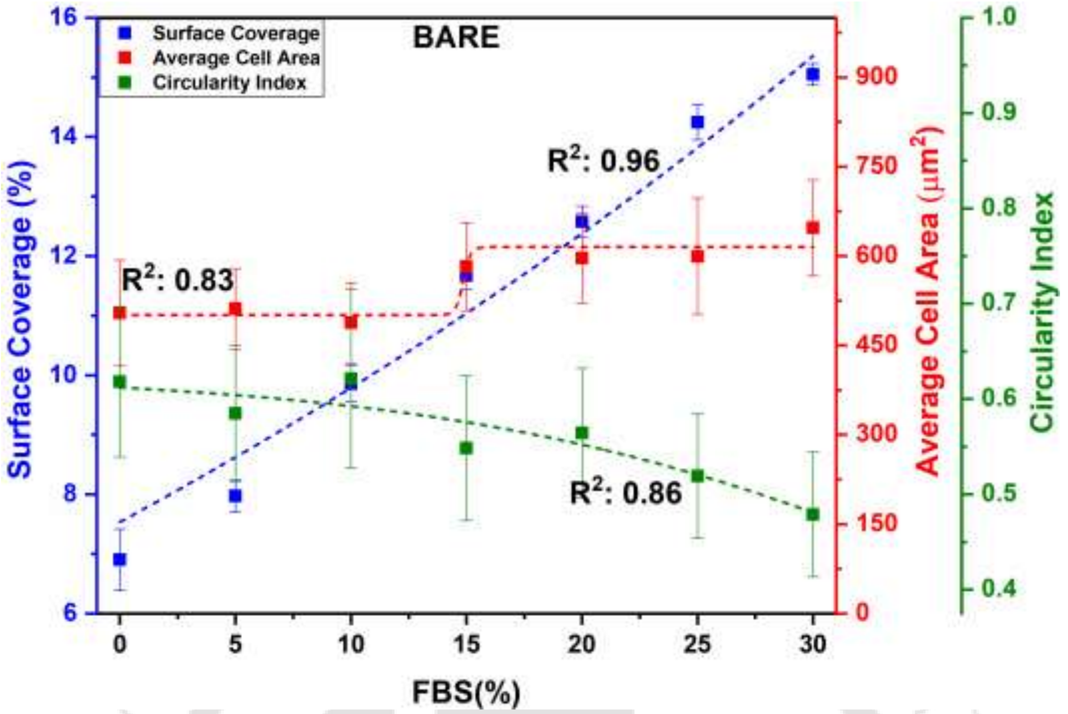

Figure 5.10: Graph showing the data for the surface coverage, average cell area, and cell circularity index for the FBS pre-adsorbed Bare Ti6Al4V surfaces; dotted lines show the fitted data.

5.3.2 Fetal Bovine Serum pre-adsorbed octyl-SAMs surfaces

Usually, the cell culture media (DMEM) is supplemented with 10% FBS (undefined supplement) to sustain cell growth and progress. As evident from the above section, the hydrophobicity of the octyl SAMs functionalized surfaces compromises the biological features of the functionalized surfaces. To tackle this issue, we tried incorporating the FBS on the functionalized surfaces in the pre-adsorbed form. Various percentages of the FBS (0, 5, 10, 15, 20, 25, and 30%) were pre-adsorbed on bare Ti6Al4V and octyl SAMs functionalized surfaces for 2 hr at 37 °C. As shown in **Fig. 5.9**, the least cell adhered to the surface with 0% pre-adsorbed FBS for the bare surfaces. Cell surface coverage increased gradually with an increase in the percentage of the pre-adsorbed FBS, and the highest was reported for the surface with 30% pre-adsorbed FBS. However, it was less than the bare surface incubated with FBS-supplemented DMEM media. Surface with 0% pre-adsorbed FBS showed a surface coverage of 6.9±0.5% < 7.9±0.2% (5% FBS) < 9.8±0.3% (10% FBS) < 11.6±0.2% (15% FBS) and so on with 15±0.1% (30% FBS) and 9.2±0.7% for the complete DMEM incubated surfaces as clear from **Fig. 5.10**. Cell circularity was highest for 0% FBS (0.62±0.07) and least for 30% FBS (0.47±0.06) and supplemented DMEM incubated surfaces (0.54±0.05), while the least average cell size for 0% (504±88 μm^2) and highest for 30% (647±80 μm^2) and FBS supplemented media surface (587±91 μm^2). Compared to the bare Ti6Al4V surfaces, octyl SAMs perform better with the cell adhesion studies mediated by pre-adsorbed FBS.

Indian Institute of Technology Guwahati

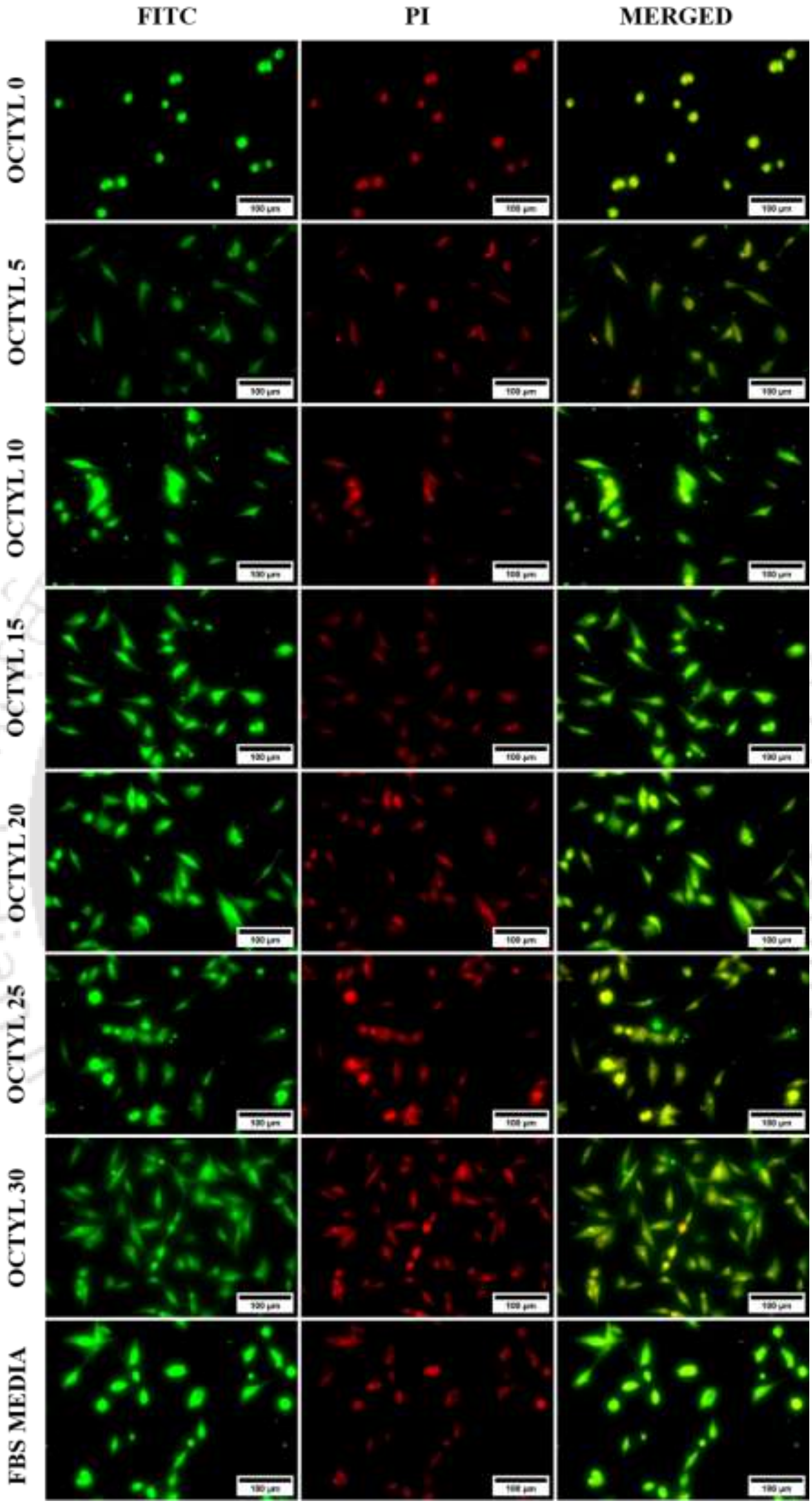

Figure 5.11: Representative fluorescent images of the MG63 cell line on the FBS pre-adsorbed octyl SAMs surfaces.

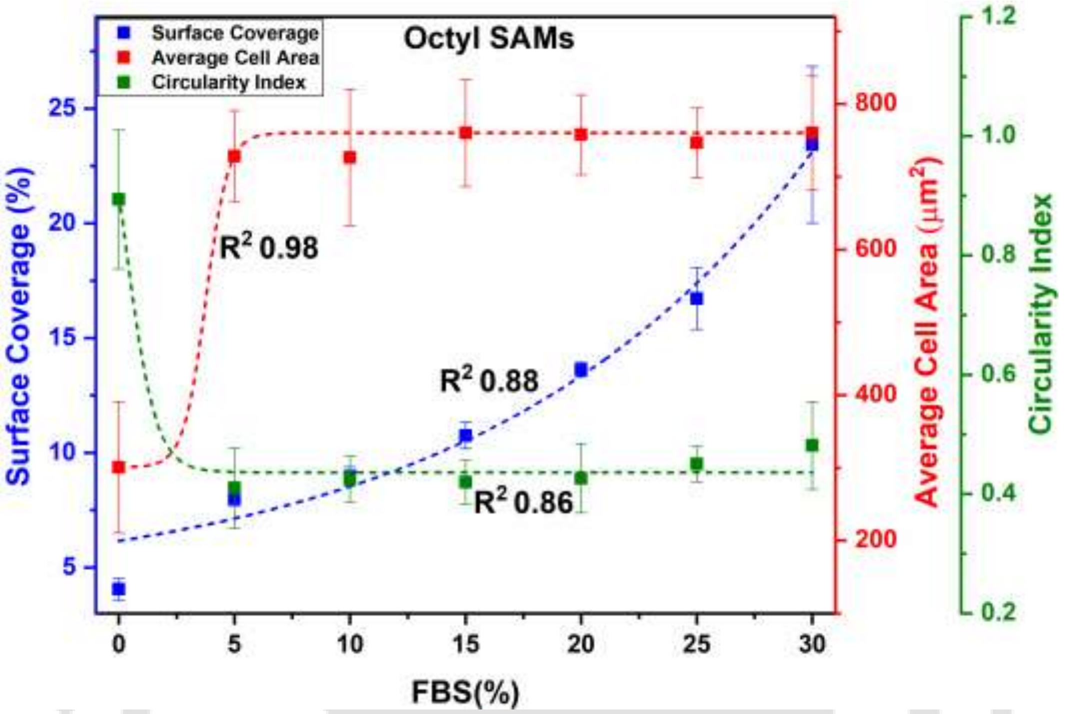

Figure 5.12: Graph showing the data for the surface coverage, average cell area, and cell circularity index for the FBS pre-adsorbed Octyl SAMs modified surfaces; dotted lines show the fitted data.

Octyl SAMs surfaces with 0% pre-adsorbed FBS showed the least circularity and cell number compared to the octyl SAMs incubated with FBS-supplemented DMEM (no pre-adsorbed FBS). At the same time, there was a linear relation between the surface coverage and the FBS concentration, as shown in **Fig. 5.11**. 0% pre-adsorbed FBS samples showed a surface coverage of 4±0.4%, average cell area of 300±90 μm^2, and circularity of 0.89±0.1 compared to the surface coverage of 13±0.95%, average cell area of 698±55 μm^2, and circularity of 0.56±0.04 for the octyl SAMs surfaces incubated with FBS supplemented DMEM media. Surface coverage response was 7.9±0.3% (5% FBS) < 8.9±0.4% (10% FBS) < 10.7±0.5% (15% FBS) < 13.6±0.3% (20% FBS) < 16.7±1% (25% FBS) <23.4±3% (30% FBS) respectively (linear response). On the other hand, there was no significant change in the average cell area with the increase of the FBS concentration; it got saturated as follows: 728±62 μm^2 (5%), 726±93 μm^2

(10%), 760±73 μm^2 (15%), 757±55 μm^2 (20%), 746±48 μm^2 (25%) and 760±77 μm^2 (30%), respectively. The circularity index data exhibited almost the same behavior with 0.41±0.06 (5%) and 0.48±0.07% (30%), respectively, as quite clear from the graph in **Fig. 5.12**.

Surface coverage increased by 0.014 for bare surfaces and 0.07 for the octyl SAMs surfaces, a two-fold increase in the surface coverage rate for the functionalized surfaces. Average cell area increased by a rate of 6.35 %$^{-1}$ for the bare surfaces, with the transition state at 14.54% of the pre-adsorbed FBS; on the other hand, octyl SAMs exhibited a rate of 2.09 %$^{-1}$ with a transition at 2.80% pre-adsorbed FBS, indicating quick saturation of the average area (~760 μm^2), circularity was also quickly saturated for the octyl SAMs surfaces (0.43) with a rate of 2 %$^{-1}$ whereas 0.08 %$^{-1}$ for the bare surfaces based on the fitted data and the various range of the various parameters are tabulated in **Table 5.3**. Rezek et al. also performed the FBS pre-adsorption studies on the hydrophobic and hydrophilic diamond surfaces, and it was observed that post-FBS pre-adsorption, cell adhesion by 40% on the hydrophilic surfaces compared to the hydrophobic diamond surfaces under shaking conditions. There was an insignificant change in the cell adhesion behaviour at static conditions, and the hydrophilic surface was independent of the cell adhesion conditions [351]. In another study, chitosan matrices were functionalized with β-1,3-glucan to fabricate bone scaffold. It was observed that better serum protein adsorption enhanced cell adhesion, spreading, and proliferation due to the pre-adsorbed fibronectin and vitronectin on the surfaces [335].

Table 5.3: Range of the various cell adhesion parameters

	Range		
FBS pre-adsorbed surface	**Surface coverage (%)**	**Avg cell area (μm^2)**	**Circularity**
Bare (Ti6Al4V)	7 - 15	488 - 650	0.47 - 0.62
Octyl SAMs	4- 24	300 - 760	0.42 – 0.90

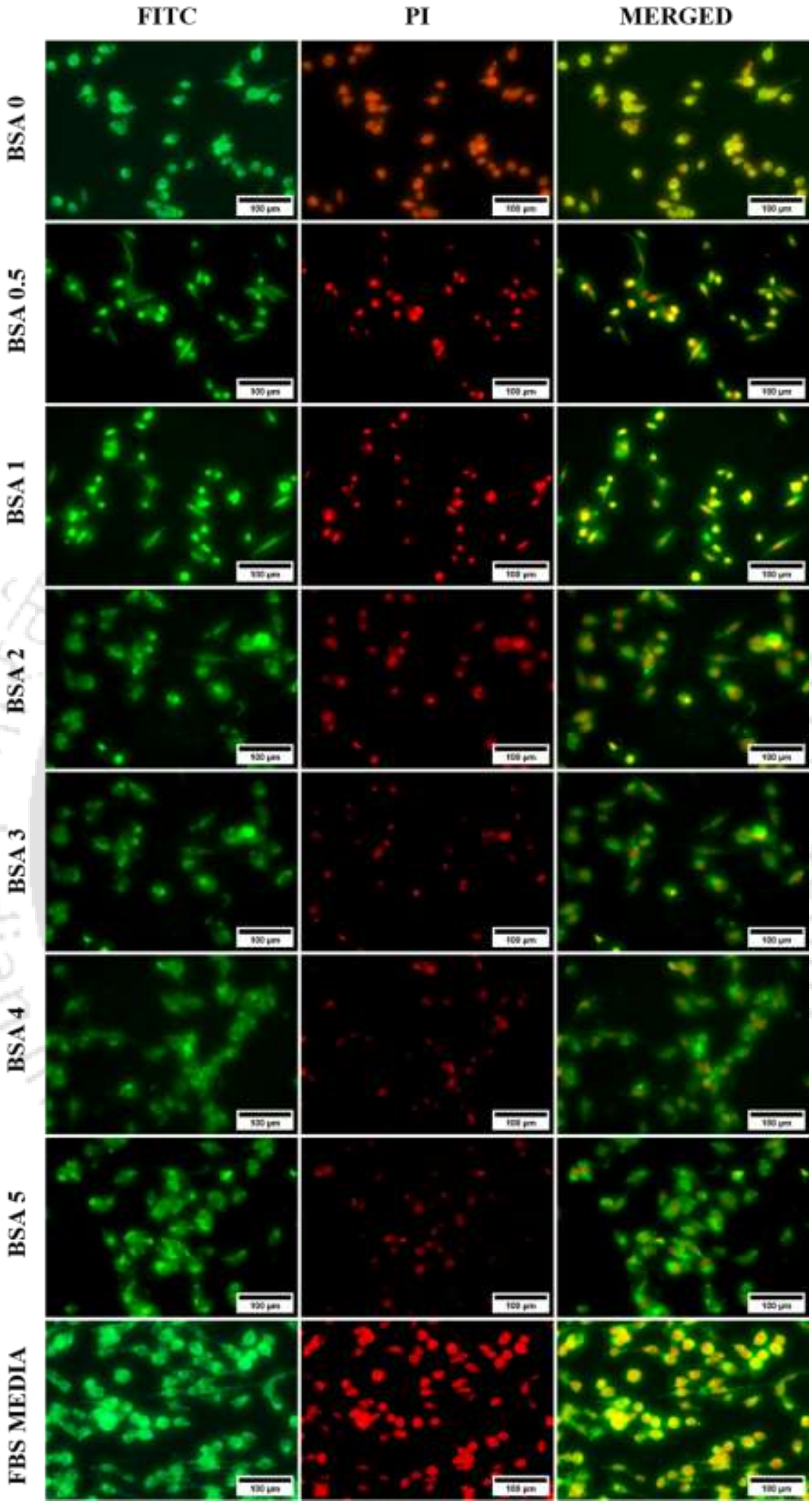

Figure 5.13: Representative fluorescent images of the MG63 cell line on the BSA pre-adsorbed hexadecyl SAMs surfaces.

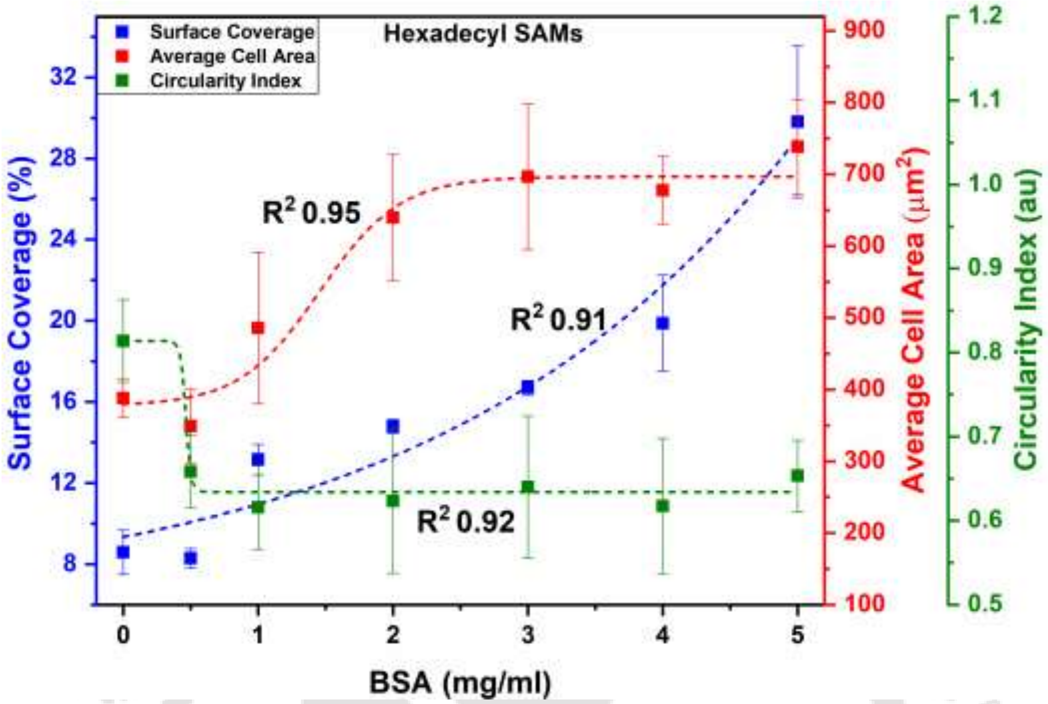

Figure 5.14: Graph showing the data for the surface coverage, average cell area, and cell circularity index for BSA pre-adsorbed hexadecyl SAMs surfaces.

5.3.3 Protein pre-adsorbed hexadecyl SAMs functionalized Ti6Al4V surfaces

Compared to octyl SAMs, hexadecyl SAMs have a longer chain length and higher hydrophobicity. So, instead of simply exploring the pre-adsorption of the complex cocktail of the FBS, we tried exploring the pre-adsorption of individual proteins (BSA, Col-I & FN) separately and mixed pre-adsorption of the proteins (BSA/col-I, BSA/FN, FN/col-I) on the hexadecyl surfaces. Molar concentrations used for the various protein as follows: BSA (7.5, 15, 30, 45, 60, 75 µM); fibrinogen (0.01, 0.03, 0.06, 0.09, 0.12, 0.15 µm) and Collagen-I (0.02, 0.03, 0.07, 0.10, 0.13, 0.17 µM). Due to longer chain length and steric hindrance imparted roughness; and orientation of the SAMs will play a crucial role that will be difficult to explore for a complex system like FBS, which contains growth factors, hormones, vitamins, and other biomolecules in addition to the proteins. Blank surfaces without pre-adsorbed BSA showed the highest circularity with low surface coverage and a small average cell area, as depicted in the fluorescent images in **Fig. 5.13**. An increase in the BSA concentration increased the surface coverage, circularity index, and average cell area. **Fig. 5.14** shows the cell adhesion data; control samples without pre-adsorbed showed a surface area of 8.5±1%, an average cell area of 387±26.9 μm^2, and a circularity of 0.81±0.04.

In contrast, the control samples incubated with FBS-supplemented DMEM media showed a surface coverage of 45.6±2.4%, average cell area of 643.9±47.9 μm^2, and circularity of 0.5±0.05 for the hexadecyl SAMs samples. Surface coverage increased by 8.2±0.47% (0.5 mg/ml BSA) and 29.8±3% (5 mg/ml BSA), the least average cell area for the 0.5 mg/ml BSA (348.7±51 μm^2) and highest for 5 mg/ml BSA (738.4±66 μm^2); but there was no significant change in the circularity as all the samples showed the circularity in the range of ~0.6 with slight variations among the samples. Surface coverage (%) showed an exponential increase of 0.37 μg/ml^{-1} (R^2: 0.93) with an increase in the pre-adsorbed BSA concentration, and circularity attained a faster plateau phase of 0.63 with a transition point around 0.5 mg/ml of the BSA concentration (R^2: 0.92). The average cell area was also quickly saturated at 0.86 of the BSA concentration with an increased rate of 3.36 μg/ml^{-1} (R^2: 0.94). A study on the heparinized PCL surfaces showed an increase in the endothelial cells (EC) cell adhesion behaviour and a decrease in the smooth muscle cells. Enhanced cell adhesion behaviour of the EC cells correlated with enhanced fibronection adsorption on the heparinized surfaces, as the fibronectin is the key mediator in the cell adhesion of the EC cells [340].

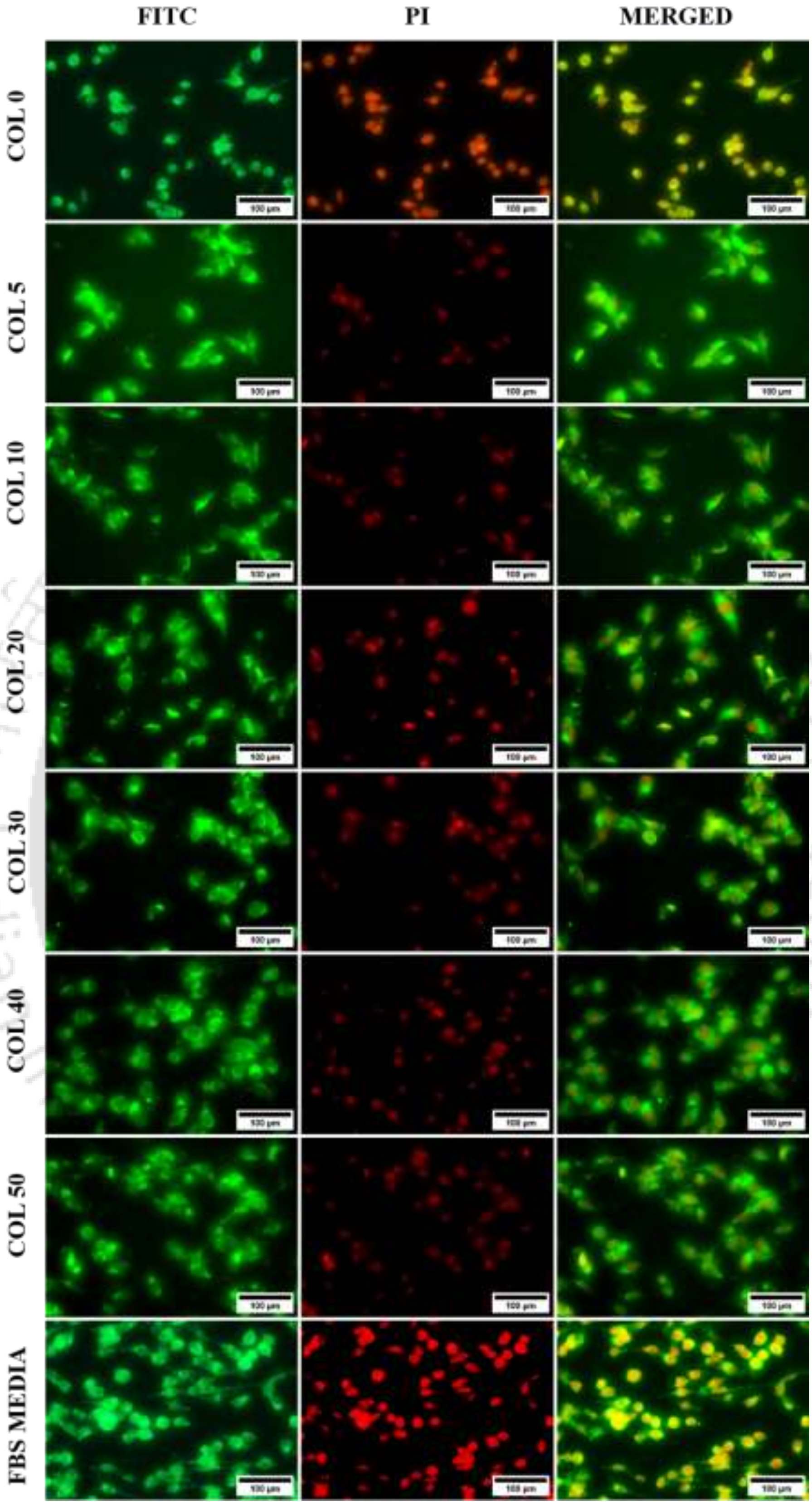

Figure 5.15: Representative fluorescent images of the MG63 cell line on the Col-I pre-adsorbed hexadecyl SAMs surfaces.

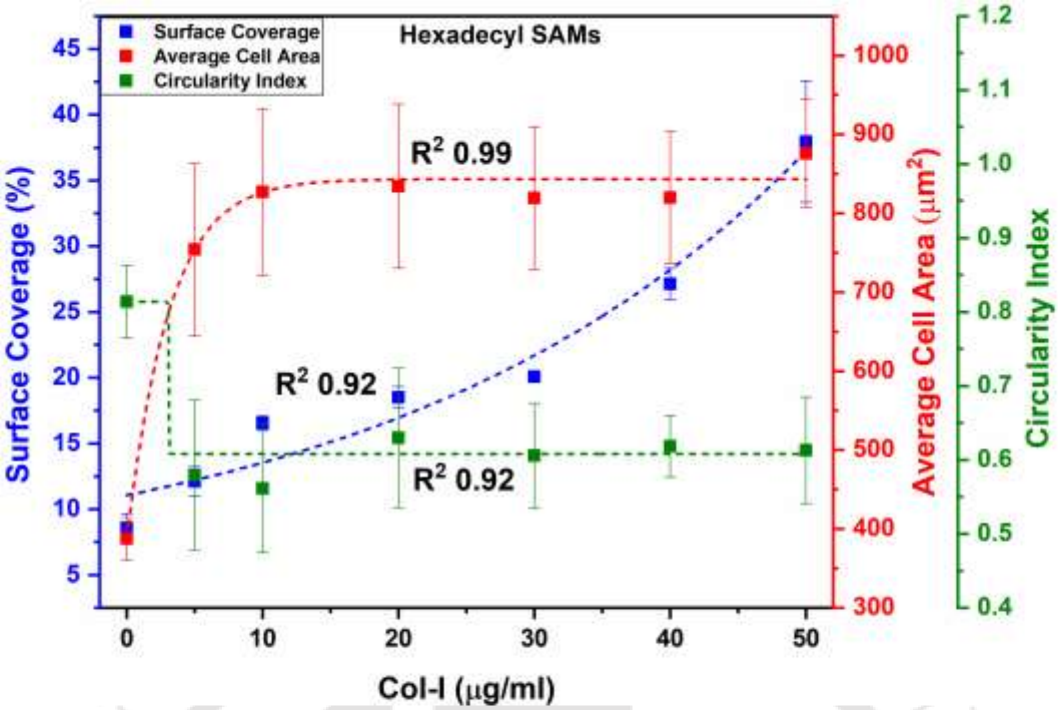

Figure 5.16: Graph showing the data for the surface coverage, average cell area, and cell circularity index for Col-I pre-adsorbed hexadecyl SAMs surfaces.

Collagen is the most promising protein in biomedical engineering, particularly for tissue engineering, to enhance the biological features of biomaterials. The pre-adsorption studies used Collagen type-I in various concentrations (5, 10, 20, 30, 40, and 50 µg/ml). Results were similar in trend to the BSA pre-adsorbed hexadecyl SAMs surfaces, with the increased adsorbed protein concentration enhancing cell adhesion, as illustrated in **Fig. 5.15**. Surface coverage showed the following behavior: 12±1% (5 µg/ml) < 16.5±0.5% (10 µg/ml) < 18.5±0.8% (20 µg/ml) < 20±0.2% (30 µg/ml) < 27±1% (40 µg/ml) < 37.9±4% (50 µg/ml), while average cell area showed the least area for 5 µg/ml (754±109 µm^2) and highest for 50 µg/ml (876±68 µm^2); circularity index was independent of the pre-adsorbed protein concentration (~0.6) for all the samples with slight variations as illustrated by the graph in **Fig. 5.16**. Surface coverage increased by 0.03 µg/ml^{-1} (R^2: 0.94) with the increase in the Col-I concentration (R^2: 0.94). Circularity was independent of the collagen-I concentration and showed no significant change with the collagen adsorption; the sharp transition occurred at 3.09 µg/ml Col-I concentration (R^2: 0.92), but the average cell area increased by a rate of 0.34 µg/ml^{-1} (R^2: 0.99).

भारतीय प्रौद्योगिकी संस्थान गुवाहाटी • Indian Institute of Technology Guwahati •

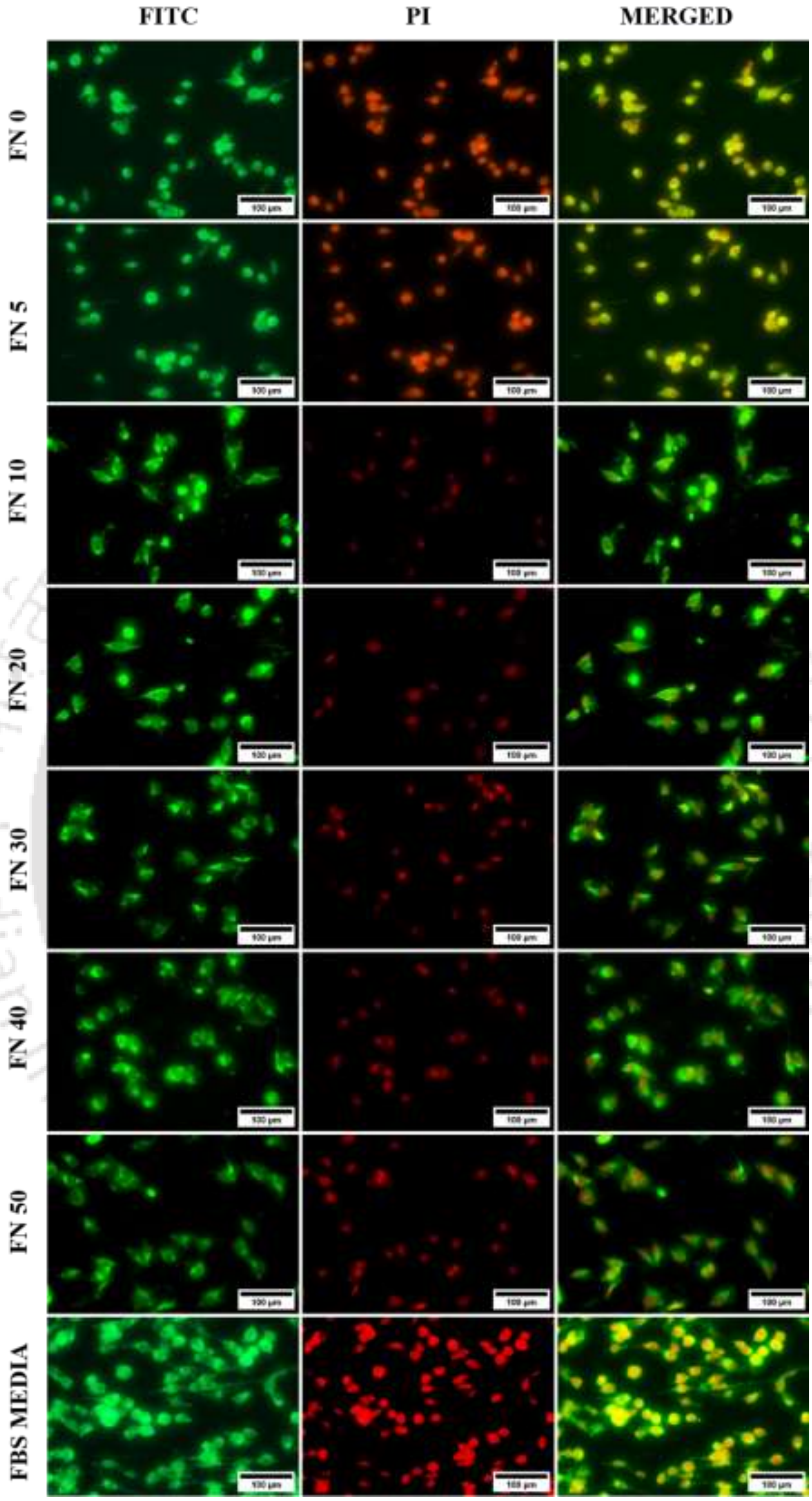

Figure 5.17: Representative fluorescent images of the MG63 cell line on the fibrinogen pre-adsorbed hexadecyl SAMs surfaces.

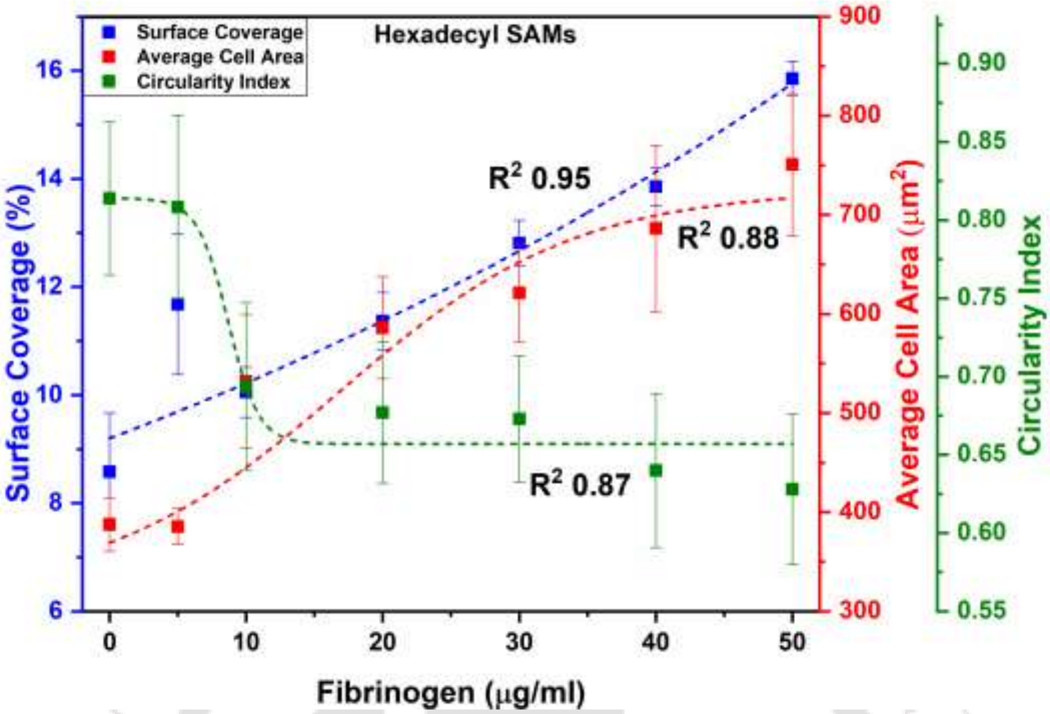

Figure 5.18: Graph showing the data for the surface coverage, average cell area, and cell circularity index for fibrinogen pre-adsorbed hexadecyl SAMs surfaces.

Fibrinogen (FN) is the main protein of the coagulation cascade, resulting in blood clotting. The type and the concentration of the protein adsorbing on the biomaterial surface determine the fate of the implants in the body. FN adsorbing on the biomaterial surface marks the biomaterial for rejection and clotting, resulting in implant failure. So, exploring the nature of FN is of utmost importance for biomaterial fabrication. as shown in **Fig. 5.17**. There was a slight increase in the surface coverage with the increase in the FN concentration. However, the cell adhesion is less than the BSA and Col-I pre-adsorbed surfaces, and other cell adhesion parameters. As apparent from **Fig. 5.18**, there was no drastic change in the surface coverage area for the FN samples, with 11.6±1% (5 μg/ml) and 15.8±0.3% (50 μg/ml), though there was a significant change in the average cell area with 385.5±18 μm^2 (5 μg/ml) and 750.9±72 (50 μg/ml); there was higher circularity for the 5 μg/ml (0.8), which reduced to 0.69 (10 μg/ml) and 0.62 (50 μg/ml). Surface coverage increased at a rate of 0.012 μg/ml^{-1} with the FN concentration (R^2: 0.97), and circularity changed at a rate of 0.88 μg/ml^{-1} (R^2: 0.87) with the transition point at 6.41 µg/ml FN concentration. In contrast, the average cell area changed at a rate of 0.11 µg/ml^{-1} with the FN pre-adsorption (R^2: 0.88).

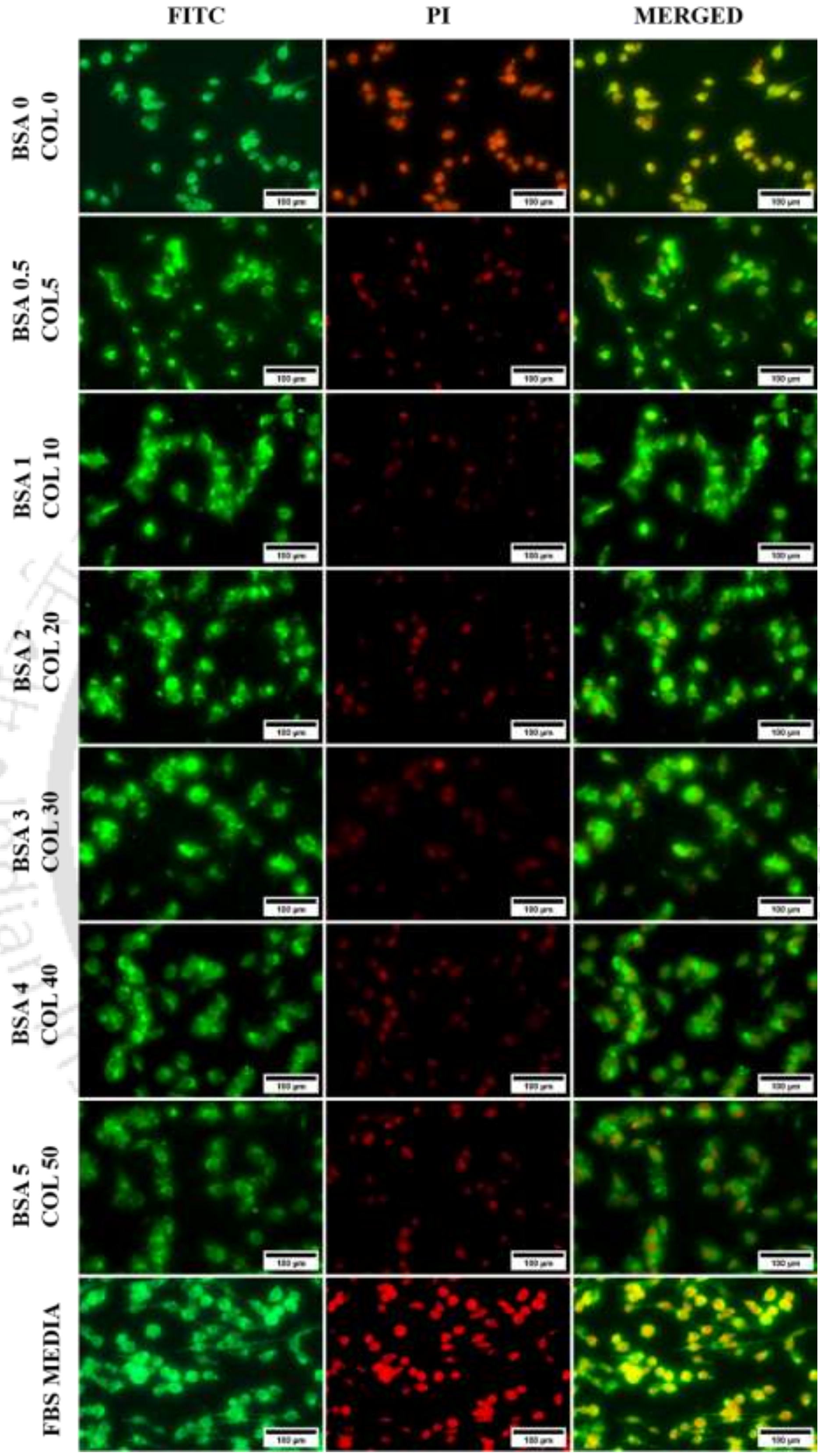

Figure 5.19: Representative fluorescent images of the MG63 cell line on the surfaces of BSA/Col-I pre-adsorbed hexadecyl SAMs.

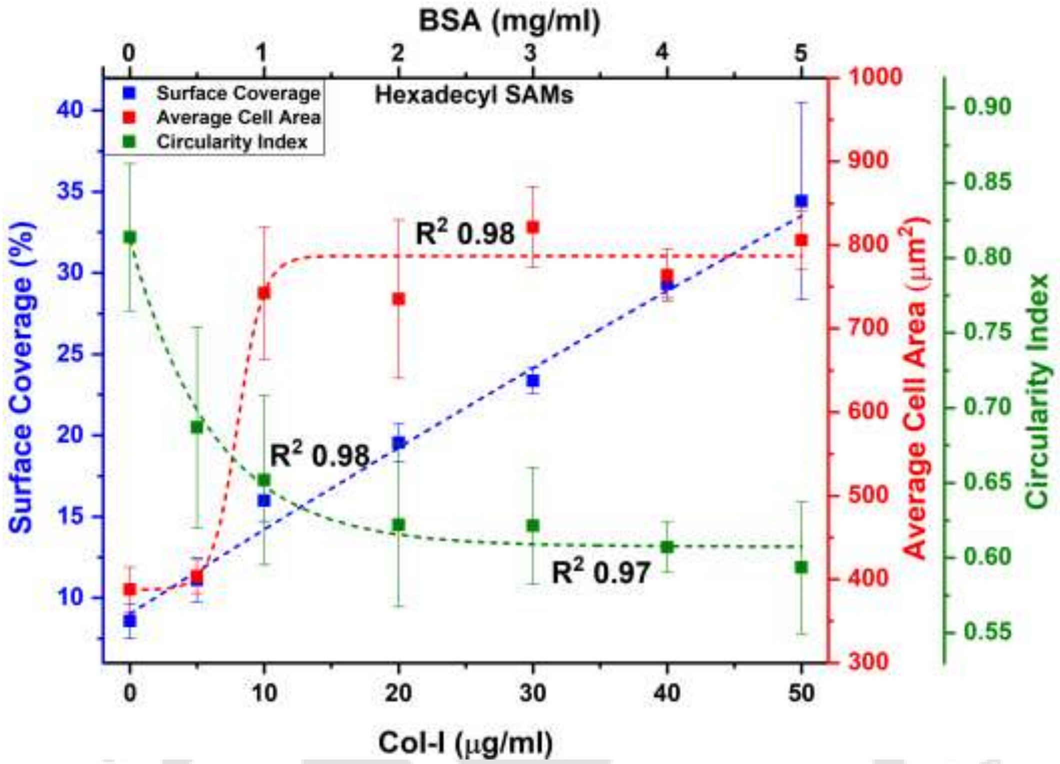

Figure 5.20: Graph showing the data for the surface coverage, average cell area, and cell circularity index for BSA/col-I pre-adsorbed hexadecyl SAMs surfaces.

In the previous section, the cell adhesion behavior of three proteins was separately explored; ~~now~~, the pre-adsorption of mixed proteins was explored. BSA/Col-I cell adhesion studies showed a gradual increase in the surface coverage with the increase in the concentrations of both proteins, as clear from the fluorescent cell images in **Fig. 5.19**. Substrate pre-adsorbed with the lowest concentration of the protein (0.5 mg/ml BSA & 5 μg/ml Col-I) showed the least surface coverage of 11±1%, average cell area of 403.7±20 μm^2 and circularity of 0.68±0.06. In contrast, the substrate with the highest protein concentration (5 mg/ml BSA & 50 μg/ml Col-I) showed a surface coverage of 34.4±6%, average cell area of 806±34 μm^2 and circularity of 0.59±0.05 as shown in **Fig. 5.20.** Surface coverage changed at a rate of 0.03 μg/ml^{-1} for BSA and 0.003 μg/ml^{-1} for Col-I, with an R^2 of 0.98, circularity at a rate of 0.16 μg/ml^{-1} (Col-I) and 1.6 μg/ml^{-1} (BSA) with a transition point at 6.17 μg/ml (Col-I) and 0.617 mg/ml (BSA) for the change in the circularity (R^2: 0.97). On the other hand, the average cell area exhibited a rate of 1.04 μg/ml^{-1} (Col-I) and 10.4 μg/ml^{-1} (BSA) with a transition point at 6.11 μg/ml (Col-I) and

0.611 mg/ml (BSA) for the binary protein system of BSA/col-I (R^2: 0.98). In a study conducted by a research group for the cell adhesion behviour in the presence of protein pre-adsorption, it was observed that vitronectin and fibronectin significantly influence the cell adhesion behaviour. Incorporation of the antibodies against both proteins reduced the cell adhesion, signifying protein-mediated cell adhesion on the hydroxyl methyl mixed SAMs [339].

Indian Institute of Technology Guwahati

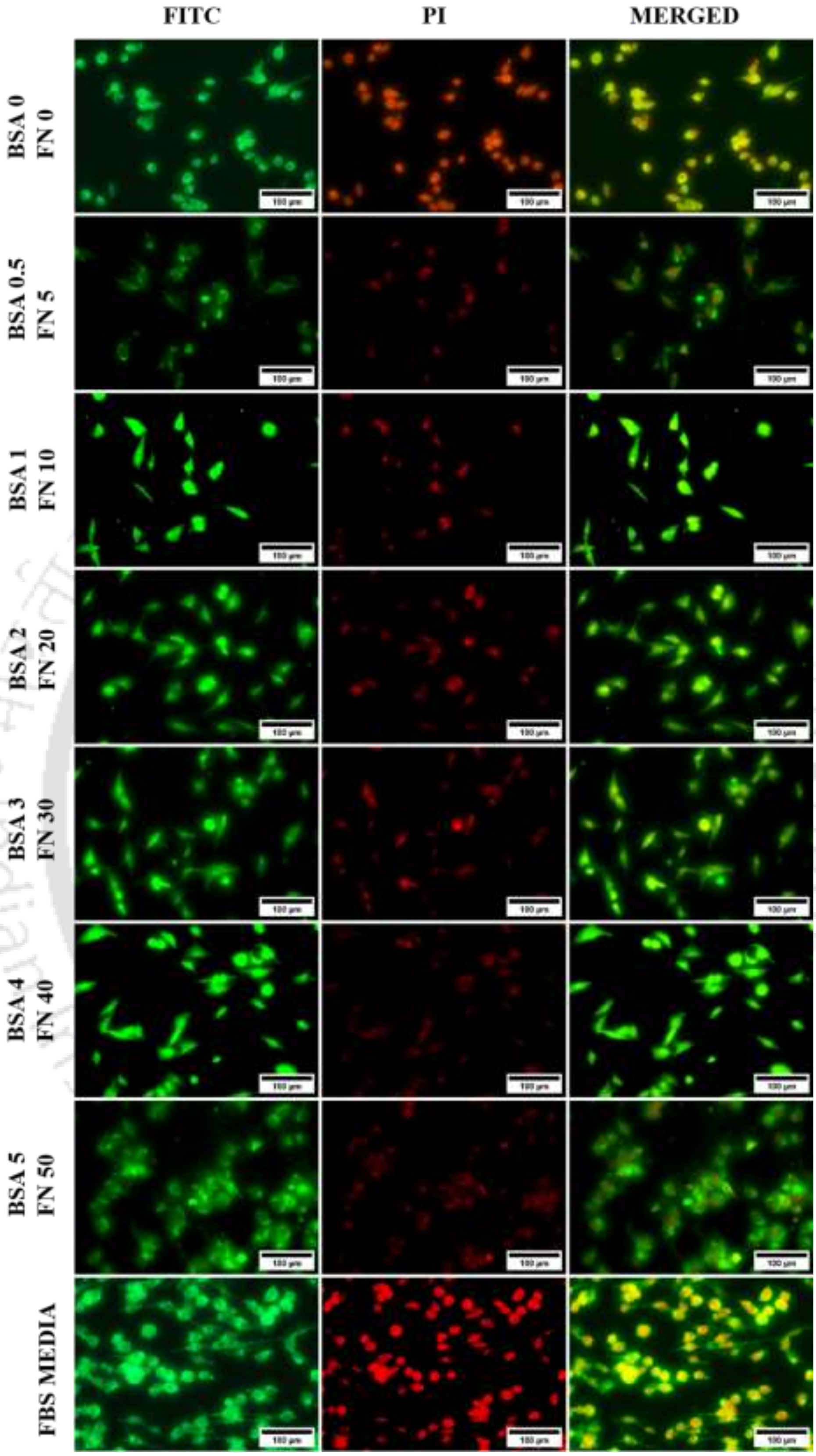

Figure 5.21: Representative fluorescent images of the MG63 cell line on the surfaces of BSA/fibrinogen pre-adsorbed hexadecyl SAMs.

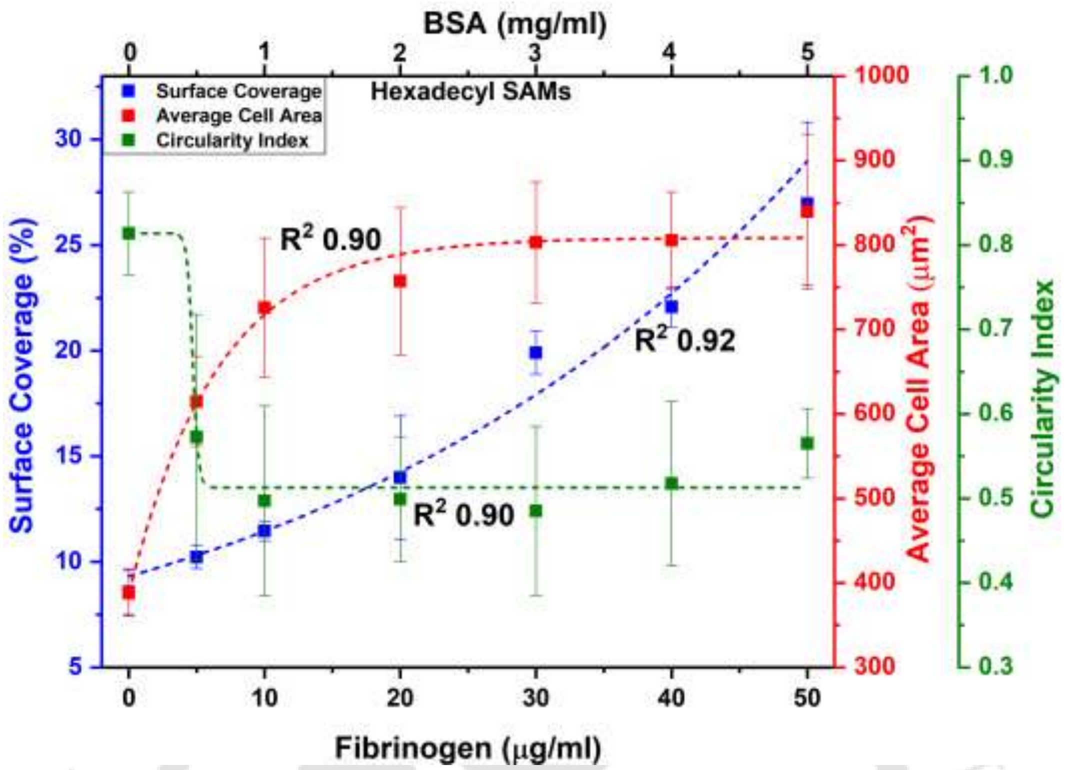

Figure 5.22: Graph showing the data for the surface coverage, average cell area, and cell circularity index for BSA/fibrinogen pre-adsorbed hexadecyl SAMs surfaces.

BSA is a slightly hydrophobic protein, and FN is a protein responsible for biofouling in the physiological microenvironment. **Fig. 5.21** shows that the binary protein systems of BSA and FN were pre-adsorbed on the surfaces of the hexadecyl SAMs and explored for cell adhesion behavior. Based on the graph in **Fig. 5.22**, cell adhesion gradually increases with the increase in the concentrations of both proteins. The highest surface coverage was 26.9±3% (5 mg/ml BSA & 50 µg/ml FN), and the least was 10.2±0.5% (0.5 mg/ml BSA & 5µg /ml FN); the same samples exhibited the highest (839.5±91 µm^2) and least (614±53 µm^2) average cell area among the samples. There was no drastic change in the circularity index (~0.5) among the surfaces. Surface coverage (R^2: 0.96) increased with the amount of the protein concentration and was 0.02 µg/ml^{-1} (FN) and 0.2 µg/ml^{-1} (BSA); circularity was independent of the protein concentration in the binary system and showed a transition at 0.302 mg/ml (BSA) and 4.28

μg/ml (FN) for the system (R^2: 0.89). The average cell area varied at a rate of 1.53 μg/ml^{-1} (BSA) and 0.15 μg/ml^{-1} (FN) for the system (R^2: 0.90).

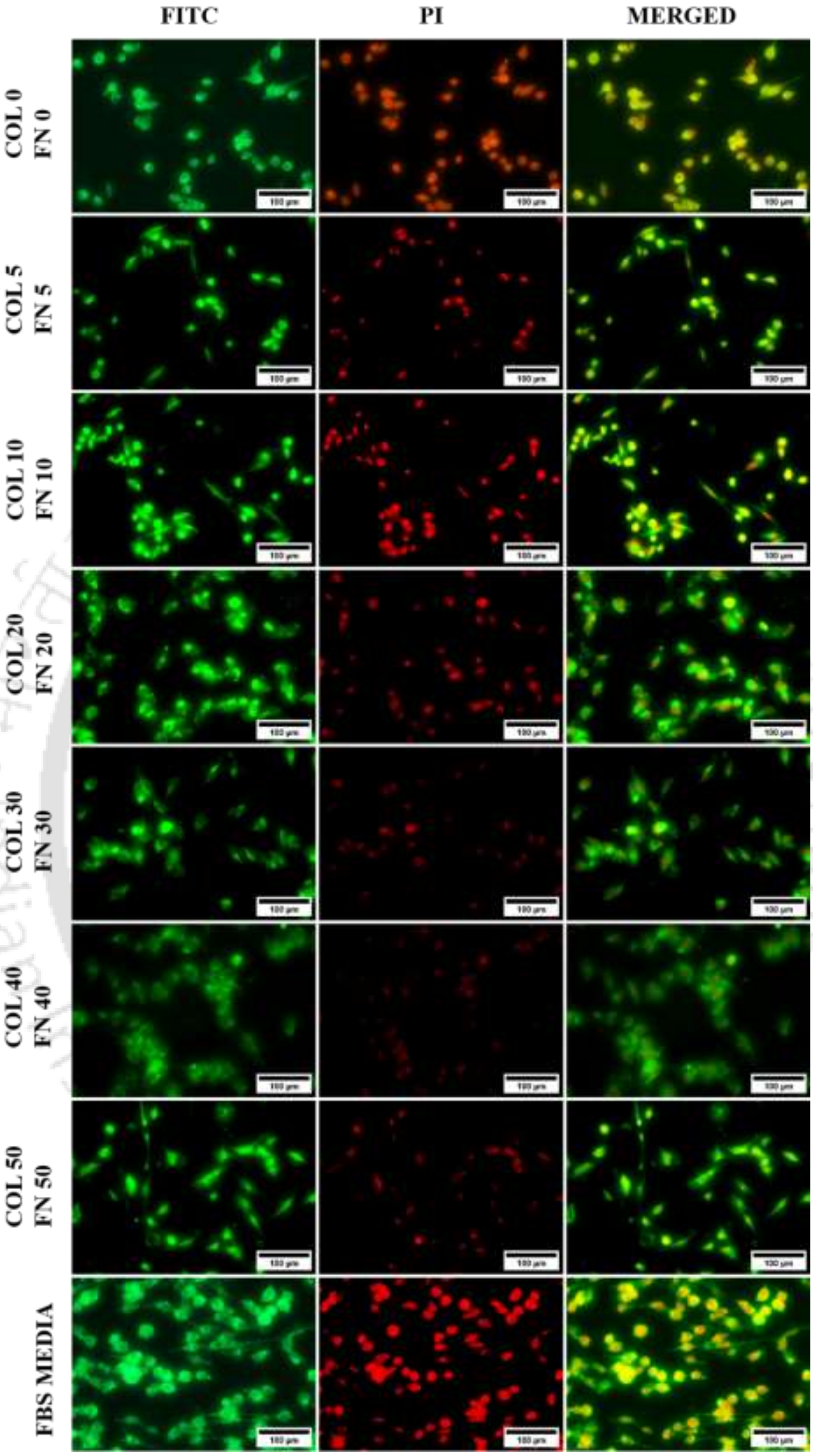

Figure 5.23: Representative fluorescent images of the MG63 cell line on the surfaces of fibrinogen/Col-I pre-adsorbed hexadecyl SAMs.

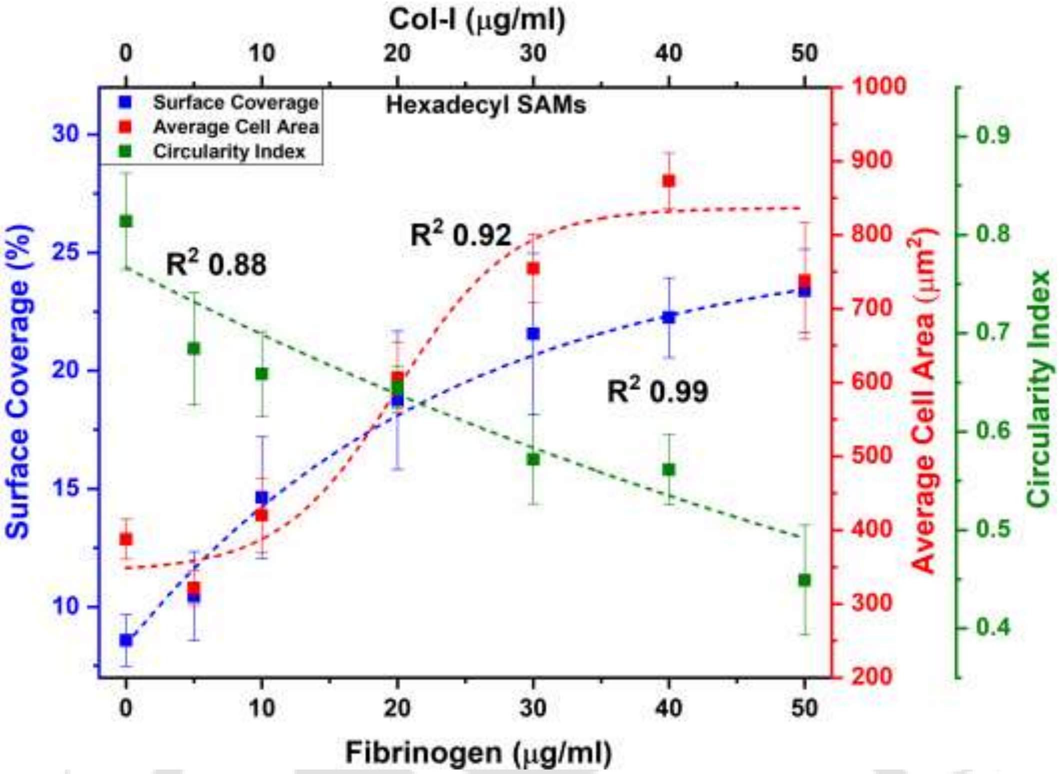

Figure 5.24: Graph showing the data for the surface coverage, average cell area, and cell circularity index for fibrinogen/Col-I pre-adsorbed hexadecyl SAMs surfaces.

Col-I and FN were also tried as the mixed system for pre-adsorption on the hexadecyl SAMs surfaces. An increase in the concentration of both proteins resulted in the slightly enhanced adhesion of the MG3 cell line on the surfaces, as shown in **Fig. 5.23**. The least surface coverage of 10.4±1% and the highest 23.4±1% were observed for the samples, and the least average cell area of 321.4±23 μm^2 and the highest cell area of 737.7±78 μm^2 were seen; on the other hand, the highest circularity was 0.68 and least was 0.44 for the surfaces as depicted in **Fig. 5.24**. Circularity varied at a rate of 0.011 μg/ml^{-1} (R^2: 0.88) and for average cell area at 0.24 μg/ml^{-1} with the transition point at 11.38 μg/ml (R^2: 0.92), while the surface coverage varied at a rate of -0.04 μg/ml^{-1} (R2: 0.99) with the increase in the pre-adsorption. All the derived parameters of the cell adhesion studies on the protein pre-adsrobed hexadecyl SAMs surfaces are tabulated in **Table 5.4**.

Table 5.4: Derived parameters of the cell adhesion study on pre-adsorbed hexadecyl SAMs surfaces.

Pre-adsorbed protein		**Average cell area (μm^2)**		**Circularity**		**Surface coverage rate (%)**
		Rate Constant (μg/ml^{-1})	Transition point	Rate Constant (μg/ml $^{-1}$)	Transition point	
BSA		3.36	0.86	50.7	0.42	0.375
Col-I		0.34	-	-	3.09	0.03
FN		0.11	-	0.88	6.41	0.012
BSA/Col-I	BSA	10.4	0.61	1.6	0.62	0.03
	Col-I	1.04	6.11	0.16	6.2	0.003
BSA/FN	BSA	1.53	-	-	0.30	0.2
	FN	0.15	-	-	4.28	0.02
FN/Col-I	Col-I	0.24	11.4	0.01	-	0.04
	FN	0.24	11.4	0.01	-	0.04

5.4 Conclusion

Functionalizing the titanium and alloy surfaces with silane-based SAMs will enhance the overall biological properties of the functionalized surfaces. Primary medication of the amine and octyl SAMs was carried out, and variations in the proportionalities of both moieties were undertaken to evaluate the best fabrication parameters. Amine and octyl can be secondarily modified into hybrid and carboxyl SAMs. Amine and hybrid SAMs exhibited remarkable cell proliferation with a circularity of ~0.4, whereas carboxyl gave intermittent circularity of 0.5, and the least was ~0.6 for the octyl SAMs. Amine and hybrid SAMs with a >50% surface coverage for the 12-hour duration and high average cell area were the most desirable silane functionalities for biomaterial fabrication. Further, another silane moiety with hydrophobicity was tried for the functionalization, hexadecyl SAMs with twice the chain length of octyl SAMs. Poor biological features of the octyl and hexadecyl SAMs were attempted to be addressed by using the ECM pre-adsorption strategy. FBS pre-adsorption was tried with a circularity of ~0.4

for the octyl SAMs, indicating better cell spreading. However, the surface coverage increased to only 23.4% without FBS supplementation, compared to the bare Ti6Al4V surfaces, a 1.5fold increase in the cell adhesion activity. Hexadecyl was subjected to single and mixed protein pre-adsorption to determine the cell adhesion activity. The study found that Col-I had the best surface coverage at 37%, followed by BSA at 30% and FN at 15% while a mixed system of BSA/col-I showed 34% coverage. FN introduced reduced coverage but enhanced cell proliferation, with the best concentration at ~0.45. BSA, Col-I, and FBS pre-adsorption improved hydrophobicity and cell adhesion properties.

Indian Institute of Technology Guwahati

Chapter 6

Design of antimicrobial coatings on functionalized model implant surfaces without compromising biocompatibility

---

This chapter focuses on fabricating various antimicrobial coatings for biomedical applications. In the first section, benign silver nanoparticles were fabricated and coated on the amine SAMs-modified silica surfaces and explored for their antimicrobial and anti-biofilm properties. The second section explored natural biopolymer chitosan as an antimicrobial agent and drug-loading vehicle.

Section 6.1.1: Silver nanoparticles based antimicrobial surface coating

6.1 Introduction

At a global level, nosocomial infections are one of the most severe consequences of surgical procedures, especially in developing countries. Patients suffering from orthopedic disorders are implanted with prosthetics of metallic, ceramic, polymeric, or composite-type biomaterials to mimic the normal biological counterpart(s) required for the normal functioning of the host [345, 355-359]. These implant sites are vulnerable to microbial infection throughout post-operative procedures. As a preventive measure, patients are medicated with heavy dosages of antibiotics to avoid sepsis and microbial infection, which causes systemic side effects [360] and the development of drug resistance [361]. These factors ultimately lead to the failure of an implanted biomaterial [362]. Therefore, removing and replacing the implant from the damaged site inevitably spreads [363]. The development of antibiotic-resistant microbial strains necessitates focusing on alternate antimicrobial agents and biocompatible surfaces to prevent systemic side effects [364]. Hence, designing antimicrobial surfaces for various biomedical research and applications is clinically relevant for biomedical research and applications, i.e., anti-biofouling devices[286, 365, 366].

In this direction, nanoparticles (NPs) have a broad spectrum of antimicrobial activity [367] and have shown promising size-dependent antimicrobial activity due to the high surface area-to-volume ratio. NPs can penetrate the cell membrane and disrupt the normal functioning of the cellular components compared to bigger particles [368]. Hence, NPs can be tailored to their various applications [19, 344, 369-372]. The antimicrobial activity of NPs is also reported to be size-dependent; the smaller the size, the higher the antimicrobial activity. NPs can be used directly as an antimicrobial agent and may be encapsulated inside hydrogels or polyethylene glycol (PEG) to enhance bioavailability [373, 374]. Among all the metal and metal oxide NPs, silver nanoparticles (AgNPs) are one of the most extensively studied NPs, which have been explored as antimicrobial agents [375, 376]. Researchers have employed various methodologies for AgNPs synthesis, including physical, chemical, and biological (plant-mediated, fungal, bacterial) routes [377, 378]. However, physical and chemical methods require harmful chemicals and a significant input of energy [378]. Hence, green (plant-mediated) synthesis of AgNPs is the most plausible synthesis route as it does not demand harsh reaction conditions required in the chemical synthesis or the stringent sterility required for microbial synthesis [379]. Various plants have been utilized for synthesizing [377-380] AgNPs, including medicinal plants, to exert a synergistic effect. [381, 382]. AgNPs exhibit antimicrobial activity through various mechanisms, including disruption of membrane integrity and inactivation of respiratory enzymes, resulting in the generation of reactive oxygen species and affecting membrane potential [368, 383].

In this study, an amine self-assembled monolayer (SAMs) on a silica surface was explored to immobilize AgNPs, which were synthesized using the leaf extract of *Miscanthus khasiana* (Silvergrass), one of the abundant and least exploited plants [384]. The synthesized NPs were characterized using X-ray diffractometer (XRD), Fourier Transform Infrared Spectroscopy (FTIR), Raman, UV-Vis spectroscopy, and Field Emission Transmission Electron Microscopy

(FETEM) to confirm the successful synthesis. The synthesized AgNPs were tested for their antibacterial activities against clinically relevant *E.coli*, and then the Inhibitory Concentration (IC_{50}) value was determined. Further AgNPs were adsorbed on the amine-SAMs surface to design an antibacterial surface and to confirm the successful attachment of AgNPs over the modified surface; several techniques were employed, such as RAMAN spectroscopy, FTIR spectroscopy, Atomic Force Microscopy (AFM), and Field Emission Scanning Electron Microscopy (FESEM). Antimicrobial activity was determined against *E.coli* in the first sub-section, followed by the determination of anti-biofilm activity against *Pseudomonas aeruginosa*.

6.2 Materials and methods

6.2.1 Materials

(3-aminopropyl) triethoxysilane (APTES, cat. no. 440140, purity 99%), anhydrous toluene (cat. no. 244511, purity 99.8%), and silver nitrate (cat. No. 209139, purity 99.0%) were purchased from Sigma-Aldrich, India. Sulfuric acid, sodium hydroxide, hydrochloric acid, methanol, toluene, sodium chloride, potassium chloride, monobasic potassium phosphate, dibasic sodium phosphate, Luria Bertani broth, and hydrogen peroxide were procured from Himedia, India. Ammonia solution was procured from Rankem, India. Micro cover glasses (No. 1/10) were obtained from Axiva, India. Milli-Q water (18 MΩ.cm) was utilized throughout the work.

6.2.2 Preparation of plant leaf extract

Fresh leaves of the *Miscanthus Khasiana* plant were collected from the Indian Institute of Technology Guwahati campus. The following protocols synthesized NPs with slight modification [380, 385]. In brief, 10 gm of plant leaves were thoroughly washed thrice using deionized water to remove the dust particles on leaf surfaces. Plant leaves were mixed with 100 ml of deionized double distilled water (10% w/v) and boiled at 100°C for 10 minutes. The mixture was then cooled and filtered through a Whatman filter paper (pore size 11 µm), and the filtrate was used for further experiments.

6.2.3 Synthesis of AgNPs using plant leaf extract

100 ml of leaf extract of *Miscanthus khasiana* was mixed with 15 mM of freshly prepared NaOH solution, followed by 100 ml of 10 mM $AgNO_3$[380]. In the chemical synthesis of AgNPs, the concentration used for the NaOH was higher in the range of 15 mM to 1M [380, 386]. Also, the synthesis occurred at a higher temperature. In the present study, NaOH acts as a reaction accelerator and size stabilizer. Compared to other research groups, we have utilized a lower concentration of NaOH [380, 386] under mild conditions (25 ºC). Nitrogen purging was utilized to avoid the oxidation of $AgNO_3$, which aided the removal of oxygen from overhead space. The mixture was stirred in the dark for two hours at 150 rpm and 25°C. After two hours, the pale-yellow colored solution was turned into a stable brown-coloured solution, indicating the successful synthesis of AgNPs.

6.2.4 Characterization of the synthesized AgNPs

6.2.4.1 Physical Characterization of AgNPs:

The absorbance values of the synthesized AgNPs were recorded in the wavelength range of 400 - 600 nm at a resolution of 1 nm using a UV-Vis spectrophotometer (Electronics India 2306). The diffraction pattern of the synthesized AgNPs was recorded using a high-resolution XRD (Bruker X-ray Powder diffractometer) in the 2θ range of 10 to 70. FTIR and Raman spectroscopy data were also recorded to confirm the successful synthesis of AgNPs. Raman spectra were recorded at 488 nm using a LASER micro Raman system (Horiba Jobin Vyon, LabRam HR), and FTIR spectra were recorded in the range of 400-4000 cm^{-1} using an FTIR spectrophotometer (PerkinElmer Spectrum Two). Zeta potential and hydrodynamic diameter of the synthesized AgNPs were also measured using Anton-Paar Litesizer 500. Before DLS measurement, the AgNPs stock solution (1 mg/ml) was diluted in water at a 1:100 ratio, followed by sonicating for 20 minutes. The synthesized AgNPs samples' morphology and particle size were examined using FETEM (JEOL 2100F) in the standard bright field mode. Further, the Selected Area Electron Diffraction (SAED) pattern, fringe pattern, and EDS were analyzed for crystallographic analyses.

6.2.4.2 Inhibitory concentration of the synthesized AgNPs:

An overnight-grown culture of *E. coli* strain DH5α in Luria Bertani broth was used for the experiment. The absorbance of the culture was taken at 600 nm after pelleting out the culture at 5000 rpm for 10 minutes, followed by suspension in 1X phosphate buffer saline (PBS). The culture was diluted in sterilized PBS buffer to seed 1×10^7 CFU/ml. Working concentrations of the synthesized AgNPs were made after diluting the 1 mg/ml stock. The working concentrations ranged from 1024 to 2 µg/ml. A total volume of 200 µl per well comprised of 10 µl inoculum, 40 µl AgNPs solution(s), and 150 µl Luria Bertani broth. For this purpose, 10 µl inoculum of 1×10^7 CFU/ml of *E.coli* in autoclaved phosphate buffered saline was seeded in 96 well plate containing serial dilutions of AgNPs in triplicates and sterilized LB media. Incubation was done for 12 hours, followed by recording the OD at 600 nm. The plate was incubated at 37ºC under non-stirring conditions, followed by absorbance measurement at 600 nm using a plate reader (Tecan; model: Infinite 200 Pro). Kanamycin at its minimum inhibitory concentration (MIC) was taken as the positive control [387], and media was taken as the negative control.

6.2.5 Design of an Antibacterial Surface

The amine-SAMs surface was prepared to design an antibacterial surface, followed by the attachment of AgNPs over it.

6.2.5.1 Preparation of amine-SAMs surface:

Glass coverslips were washed using the protocol previously described by our research group[19, 314]. Briefly, coverslips were sonicated in piranha solution (H_2SO_4:H_2O_2 [7:3]) for one hour and rinsed with MilliQ water. Further, the coverslips were sonicated in a base solution (H_2O:H_2O_2:NH_3 [5:1:1]) for 30 minutes and washed in MilliQ water. Afterward, the coverslips were sonicated in an acid solution (HCl:H_2O:H_2O_2 [1:6:1]) for 30 minutes and rinsed with MilliQ water. Later, coverslips were sonicated in acetone for 10 minutes and were dried overnight. Dried coverslips were modified by forming self-assembled monolayers of amine (NH_2) using APTES. The surface modification was performed by dipping unmodified coverslips in 1% (v/v) APTES solution in anhydrous toluene for 24 hours at room temperature (25°C) under an inert nitrogen atmosphere[19, 314]. Postmodification, washing the modified surface was done by sonication in toluene, toluene: methanol (1:1 v/v) solution, and methanol for 5 minutes each. Later, the above-modified surfaces were dried in laminar air flow and stored in a vacuum desiccator for further experiments.

6.2.5.2 Attachment of AgNPs on amine-SAMs surface:

The attachment of AgNPs on the amine-SAMs glass coverslip surface was performed by dipping the amine-SAMs surface into AgNPs solution, and the surface reaction was analyzed using ATR-FTIR and was recorded with time, as shown in **Fig. 6.1(a)**. Positively charged amine groups on the surface and negatively charged groups on AgNPs interacted to form the cyano group that resulted in the attachment of AgNPs. The reaction kinetics was studied from 1975 cm^{-1} to 2300 cm^{-1}, assigned to the cyano group [388]. With the passage of reaction time, peak intensity increased and reached saturation within ten minutes. **Fig. 6.2(b)** shows the scatter graph of peak area from 1975 cm^{-1} to 2300 cm^{-1} with time. The peak area reached a plateau within ten minutes of the reaction time. However, the surface kinetics was performed for two hours to ensure the completion of the reaction between the amine group present on the surface and plant sap capping present on AgNPs.

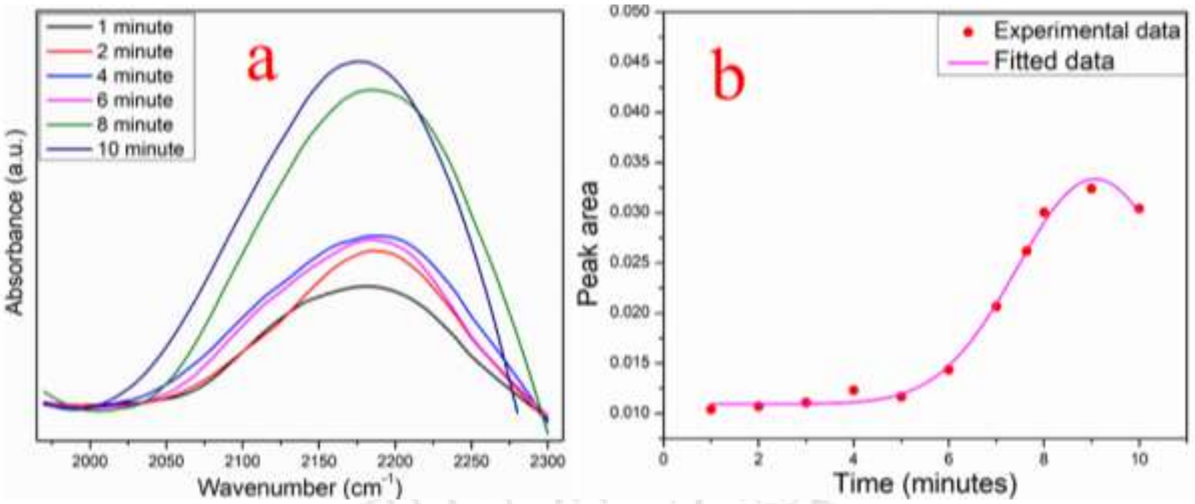

Figure 6.1: FTIR analysis of the AgNPs attachment on the amine-SAMs surface in the range 1975 cm^{-1} - 2300 cm^{-1} (a), Attachment kinetics of AgNPs on amine SAM surface (b).

6.2.6 Characterization of the Amine-SAMs and AgNPs-amine surfaces

The morphology of the modified surfaces was analyzed using FESEM (Zeiss, Model: Sigma) and AFM (Oxford, Model: cypher) [tip radius: 7 ± 3 nm; mode: tapping]. The functional groups of the modified surface were confirmed using an ATR-FTIR and Raman spectroscopy at 488 nm. AgNPs and plant sap were also analyzed using FTIR.

6.2.7 Stability analysis

The stability of a surface is an important aspect related to the actual application. AgNPs adsorbed modified surfaces were kept in duplicates in sterilized PBS at 37°C for 24 hours [389]. The stability evaluation protocol was modified slightly. Samples were then washed thrice with sterilized PBS. Changes in the surface chemistry of the modified surfaces at 0 and 24 hours were analyzed using Raman spectroscopy to conclude their stability, and changes in the water contact angle were also investigated.

6.2.8 Anti-biofilm properties of the benign silver nanoparticles

For FESEM and FACS analysis, *P. aeruginosa* suspension (1 X 10^7 CFU/ml) was used, and surfaces were incubated with the bacteria overnight. For FESEM, surfaces were washed with PBS, fixed with glutaraldehyde, dehydration with different percentages of ethanol, and dried

Indian Institute of Technology Guwahati

to eradicate water content. For the FACS, bacteria attached to the surfaces were collected and incubated with propidium iodide (PI) and analyzed using a flow cytometer.

Cell viability of the *P. aeruginosa* on various fabricated surfaces was determined using BD FACS flow cytometry (BD Biosciences, USA). *P. aeruginosa* suspension (10^7 CFU/ml) was incubated with the fabricated surfaces (bare, amine-SAMs and AgNPs-amine) overnight. Post-incubation cells were harvested and washed thrice with PBS, followed by centrifugation for 5 minutes at 5000 rpm. Cells were incubated with propidium iodide (PI) for 15 minutes at room temperature, followed by centrifugation and PBS washing to remove unattached dye. PI labeled dead and live cells were taken as the dead and live controls.

6.3 Results and Discussion

6.3.1 Characterization of AgNPs

The optical properties of AgNPs are dependent on the diameter of the particles exhibiting a single absorption peak in the range of 400 - 450 nm [390, 391]. The synthesized AgNPs displayed a strong absorbance at 423 nm, as shown in **Fig. 6.2(a)**, indicating the successful synthesis. The morphology, particle diameter, crystallinity, fringe pattern, interplanar d-spacing, and elemental analysis of AgNPs were analyzed using FETEM. **Fig. 6.2(b)** shows the spherical AgNPs morphology (15 ± 3 nm). **Fig. 6.2(c)** shows the EDS spectra of synthesized AgNPs, indicating the presence of silver (68.76% (w/w)). The presence of carbon from the organic compounds of plant leaf extract was also detected at 27.03% (w/w), indicating the coating of organics on AgNPs [384]. **Fig. 6.2(d)** displays the SAED pattern of AgNPs showing concentric rings, which indicate a polycrystalline nature. **Fig. 6.2(e)** shows the lattice fringes of AgNPs, a characteristic pattern displayed by crystalline substances. Furthermore, the inset displays the d-spacing between crystal planes, which was found to be 0.255 nm (corresponds to [111] atomic plane of Ag). The hydrodynamic diameter and the surface potential of the aqueous AgNP solution were also measured (**Fig. 6.2(f-g)**). The intensity average hydrodynamic diameter was 15.82 nm (**Fig. 6.2(f)**), corresponding to the TEM data. The Zeta potential of AgNPs (**Fig. 6.2(g)**) was found to be -27.8 ± 1.1 mV. This indicated the negatively charged surface potential of AgNPs, which facilitated their attachment onto the positively charged amine-SAMs surface.

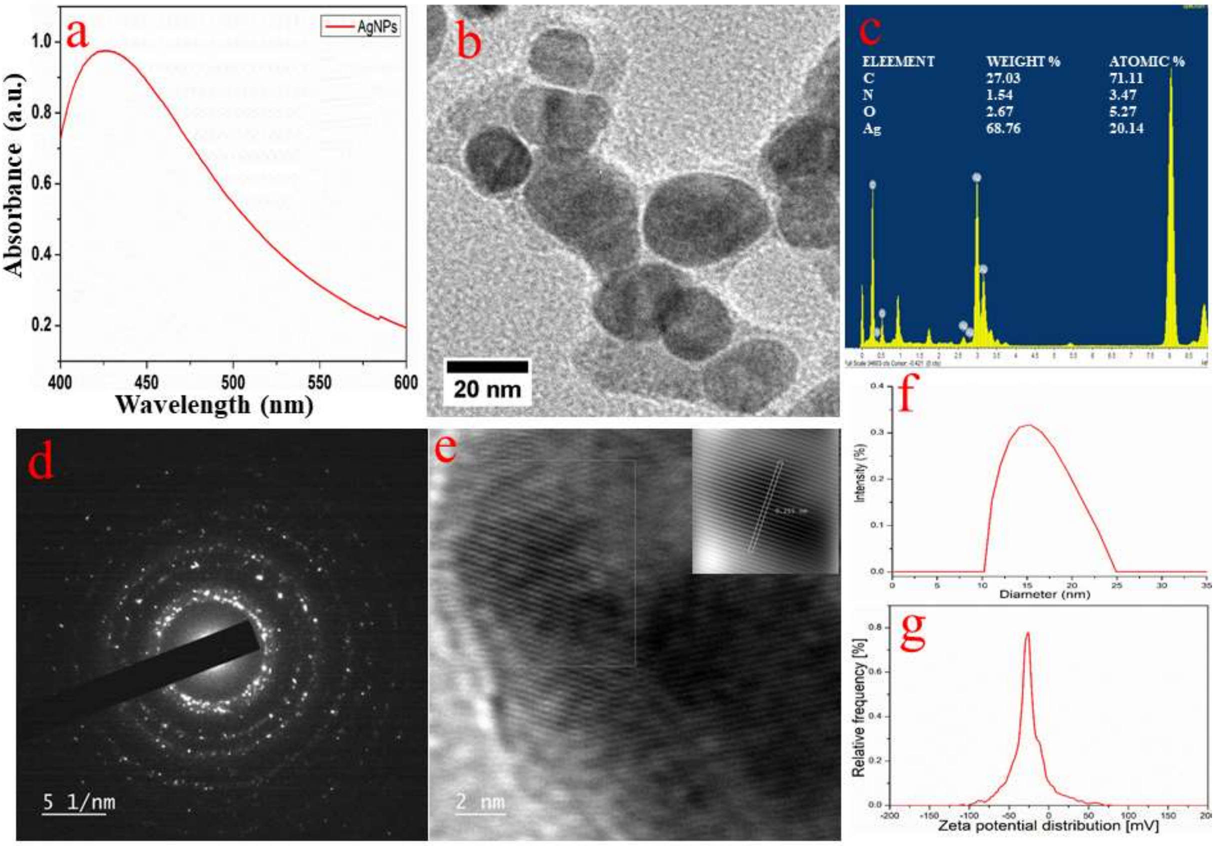

Figure 6.2: Characterization of AgNPs (a) UV-Vis spectrophotometer analysis for primary confirmation of AgNPs showing SPR at 423 nm, (b) Morphology of AgNPs in FETEM (c) EDS of AgNPs, (d) SAED pattern of AgNPs indicating polycrystalline nature of NPs, (e) Fringe pattern of AgNPs indicating the d-spacing value of NPs (inset), (f) DLS analysis, (g) Zeta potential of NPs.

XRD analysis of the fabricated biogenic AgNPs was carried out in the 2θ range of 35 to 80. AgNPs showed peaks comparable to the scientific literature (ICDD file no. 04-0783) at 38° (111), 44.38° (200), 64.42° (220), 77.38° (311) and 81.53° (222), as shown in **Fig. 6.3(A)** corresponding to the signature peaks of the silver. D-spacing of 0.24 nm was computed using Bragg's equation ($2dsin\theta = n\lambda$)[392]. Further, many additional peaks correspond to the plant extract synthesizing and capping the AgNPs [393, 394]. The crystal size of the AgNPs was found to be 3.42 nm, as calculated using the Scherrer equation. Sangappa *et al.* obtained an

XRD pattern for the biogenic spherical AgNPs comparable to our material, and the crystal structure was found to be face-centered cubic (FCC)[395]. XRD peaks of the fabricated AgNPs were sharper than the XRD pattern obtained by other research groups [393]. FTIR analyses of plant sap and AgNPs were recorded to analyze functional groups present on AgNPs compared to plant sap (**Fig. 6.3(B)**). Peaks at 1054 cm^{-1} and 1190 cm^{-1} of plant sap and AgNPs, respectively, were due to the C-N stretching of amine. C-N stretching at 1266 cm^{-1} and 1342 cm^{-1} of plant sap and AgNPs were due to aromatic groups in both samples. N-H bending at 1585 cm^{-1} [396] and 1548 cm^{-1} [286] and N-H stretching at 2927 cm^{-1} and 2828 cm^{-1} were detected for plant sap and AgNPs, respectively [380, 397, 398]. The antimicrobial activity of AgNPs was also determined against *E.coli* (**Fig. 6.4**). OD of cells decreased with an increase in the conc of NPs. The experimental data was explained through a double exponential expression indicating a first sharp decrease followed by a gradual decrease [399]. The IC_{50} value (corresponds to a 50 % decrease in initial OD) was found to be 109 µg/ml, which agreed with the reported data of AgNPs [400].

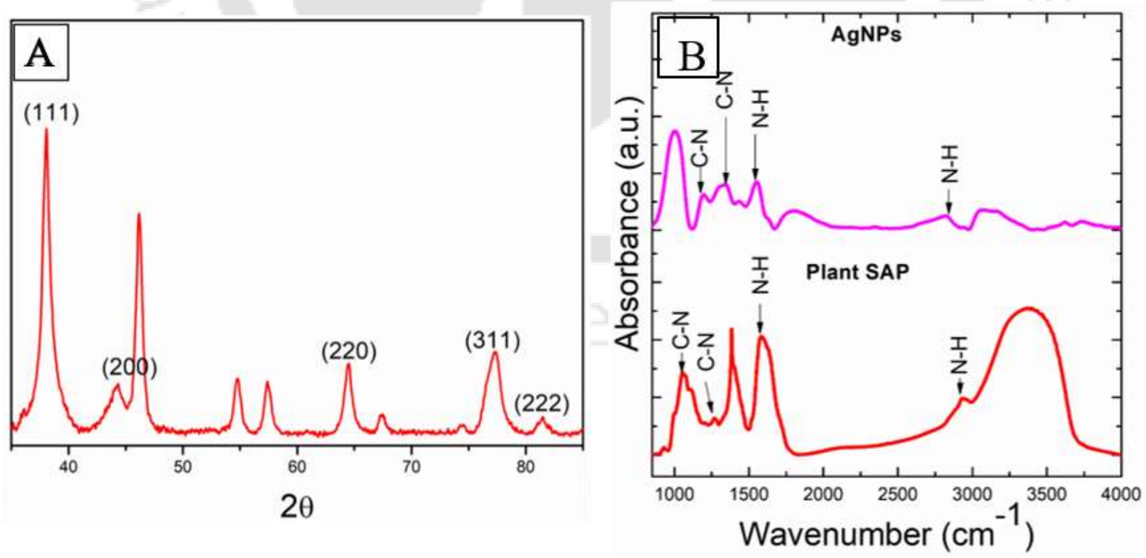

Figure 6.3: Graph showing (A) XRD of biogenic AgNPs along with the standard XRD of silver[394], (B) FTIR data of AgNPs and plant sap.

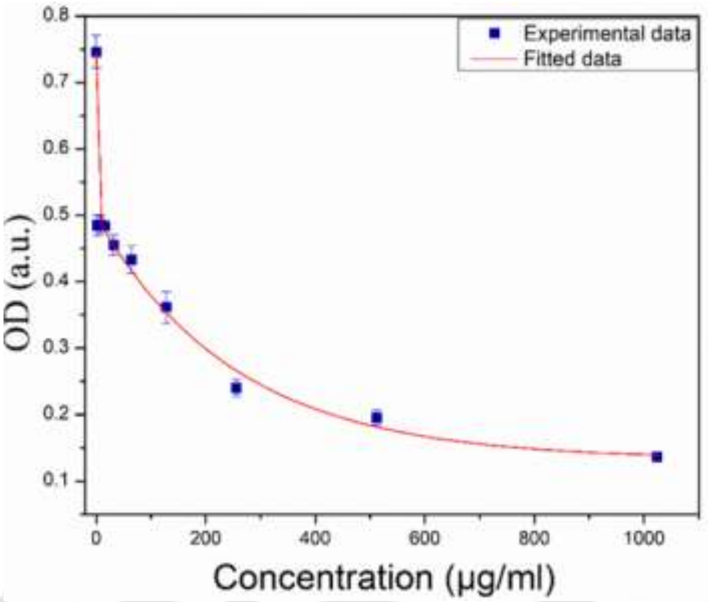

Figure 6.4: Graph showing the antimicrobial activity of the AgNPs against *E.coli* strain.

6.3.2 Characterization of AgNPs attachment

The synthesized AgNPs were attached to the amine-SAMs surface, confirmed by FTIR and AFM analyses. **Fig. 6.5(A)** shows the FTIR-ATR spectra of amine-SAMs and AgNPs-amine surfaces. The peaks at 1090 cm^{-1} and 1095 cm^{-1} of AgNPs-amine and amine-SAMs surfaces corresponded to Si-O-Si bending, indicating siloxane bond formation between silane molecules and successful silanization of the modified surfaces [336]. The peaks at 1632 cm^{-1} and 1643 cm^{-1} corresponded to the N-H group of amine-SAMs and AgNPs-amine surfaces, respectively [19]. The peak at 2695 cm^{-1} of both surfaces corresponded to C-H stretching. The peak at 1388 cm^{-1} of AgNPs-amine surface was assigned to C-N stretching [401]. The peak at 2222 cm^{-1} in the AgNPs-amine surface indicated C-N stretching due to an interaction between the amine group of the modified surface and the organic capping of the AgNPs. These observations confirmed the successful syntheses of amine-SAMs and AgNPs-amine surfaces. Water Contact angle was measured to determine surface hydrophobicity. For the unmodified surface, the contact angle was 23 ± 1°, which increased to 63 ± 1° for the amine surface [19] and 71 ± 1° for AgNPs-amine surfaces, respectively. The increase in the contact angle in the AgNPs-amine surface compared to the amine surface might be due to polyphenolic groups capping NPs. The morphology and size of the synthesized AgNPs were confirmed using an Atomic Force Microscope (AFM), as depicted in **Fig. 6.5(B)**. AFM analysis was conducted in non-contact mode at a 1.2 Hertz scan rate. The shape of the NPs is also a key parameter in determining the biological properties [402]. It was clear from the AFM data that the AgNPs are almost the same size. Other research groups have also reported the morphology and size of the biogenic AgNPs using AFM [403]. AFM analysis was performed to analyze the pattern of AgNPs distributed on the surface. Roughness parameters were determined for the surfaces. Ra value of amine-SAMs was found to be 1.062 nm, similar to the reported data [19, 314]. The Ra values of the AgNPs-amine surface was 4.28 nm, and the percentage area coverage of AgNPs-amine surfaces was 3 ± 0.5%.

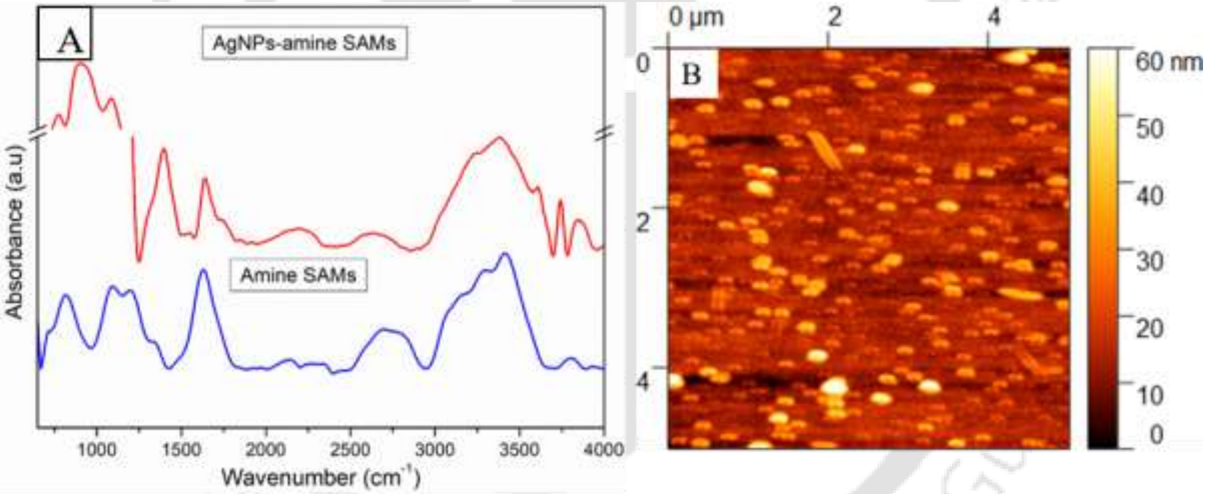

Figure 6.5: FTIR analysis of surfaces with amine-SAMs and AgNPs (A), AFM analysis of the AgNPs-amine surfaces showing uniform attachment of the AgNPs (B).

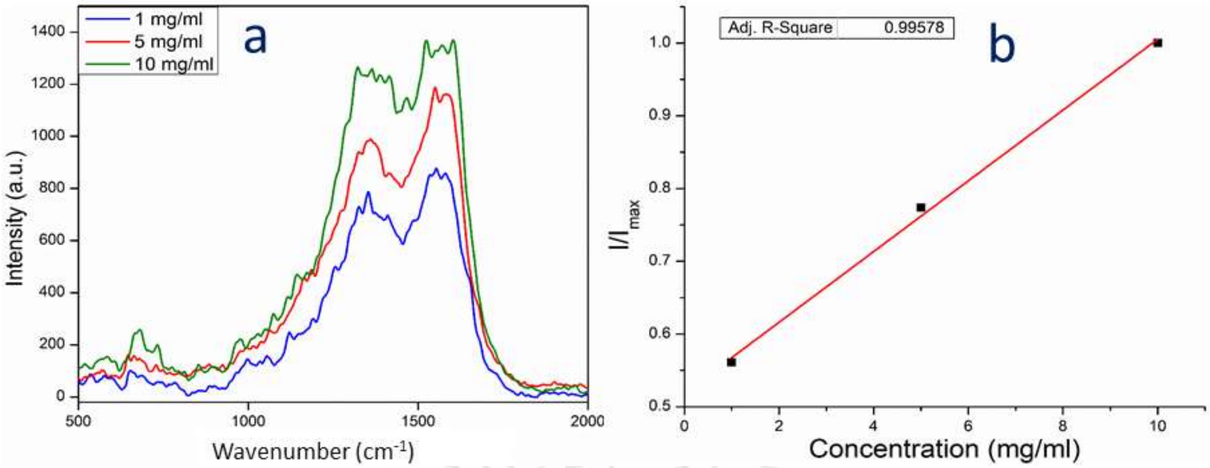

Figure 6.6: RAMAN spectroscopy analysis of AgNPs at 488 nm and 100X magnification, (b) change in the peak area corresponding to change in AgNPs concentrations.

RAMAN analysis of AgNPs-amine surfaces with varying concentrations was performed to monitor the attachment (**Fig. 6.6(a)**). The peak at 1550 ± 25 cm^{-1} was assigned to asymmetric C=O stretching vibrations of the carboxylate group [404]. The peak at 1350 ± 25 cm^{-1} corresponded to the C-N stretching of amine. Peak broadening at 10 mg/ml concentration may be due to phonon confinement [405]. Due to the high concentration of AgNPs on the surface, signal saturation occurs, which results in the peak broadening [406]. With the increased concentration of AgNPs used for the adsorption, RAMAN peak intensities were also increased (**Fig. 6.6(b)**). The peak area increased linearly with an increase in the concentration, indicating a higher surface coverage at 10 mg/ml concentration.

6.3.3 Stability studies

AgNPs-amine surface was analyzed for its stability in PBS (pH 7.4). The experiment was carried out at a physiological temperature of 37 ºC for 24 h, followed by washing with MilliQ water. Post- washing, the surface dried in a hot air oven at 37 ºC, followed by wettability and RAMAN spectroscopy analyses. The contact angle of 24 hour treated AgNPs-amine surface was analysed using deionized double distilled water, which decreased to 69 ± 1º compared to 0 hour sample (71 ± 1º). In RAMAN analysis, both peaks (1350 ± 25 cm^{-1} and 1550 ± 12 cm^{-1}) of 0 hour sample were conserved/observed in 24 hour sample. However, the intensity of the 1350 cm^{-1} peak decreased for 24 hour treated sample, presumably due to hydrolysis of AgNPs-amine. Also, both peaks exhibited redshifts due to phonon confinement [405]. In **Fig. 6.7**, the peak at 1352 cm^{-1} was assigned to the C-N stretching of amine for 0-hour surface [407]. A peak shift from 1352 cm^{-1} for 0-hour sample to 1322 cm^{-1} for the 24-hour sample was observed. The peak position of 1550 cm^{-1} obtained for 0 hour surface was assigned to asymmetric C=O stretching vibrations of a carboxylate group, which was shifted to 1538 cm^{-1} in 24 hour sample. In the current work, the adsorption of biogenic AgNPs was tried on amine-SAMs surfaces. An alternative strategy may be employed to covalently attach the AgNPs onto amine-SAMs so that the stability of the antimicrobial coating can be enhanced. Previously, our group has explored and stabilised various SAMs as potential surface modifiers of biomaterials to tune surface-protein and cell-surface interactions [19, 314, 336, 399, 408]. However, an ideal biomaterial should possess both antimicrobial and biocompatible properties. In this direction, the present work complements previous works incorporating antibacterial features. A similar strategy can be implemented to impart antimicrobial properties of other SAMs apart from amine SAMs.

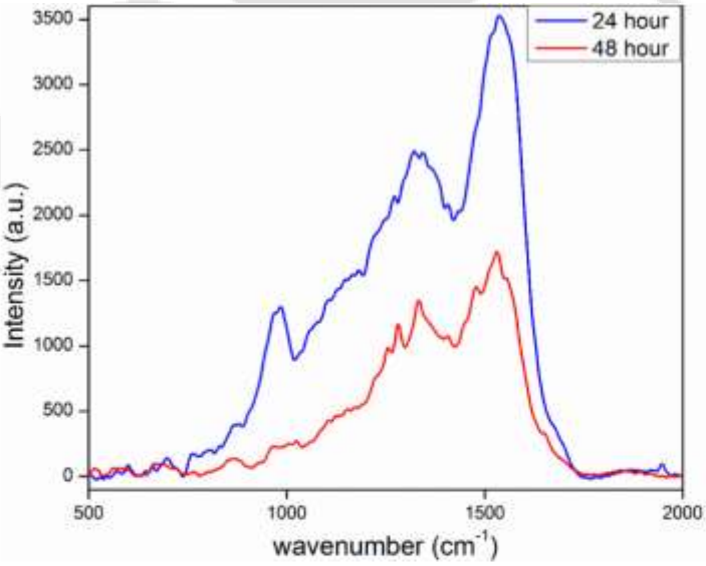

Figure 6.7: Stability analyses of 24h treated AgNPs-amine surface using RAMAN spectroscopy analysis at 488 nm wavelength.

6.3.4 Anti-biofilm properties of the benign silver nanoparticles

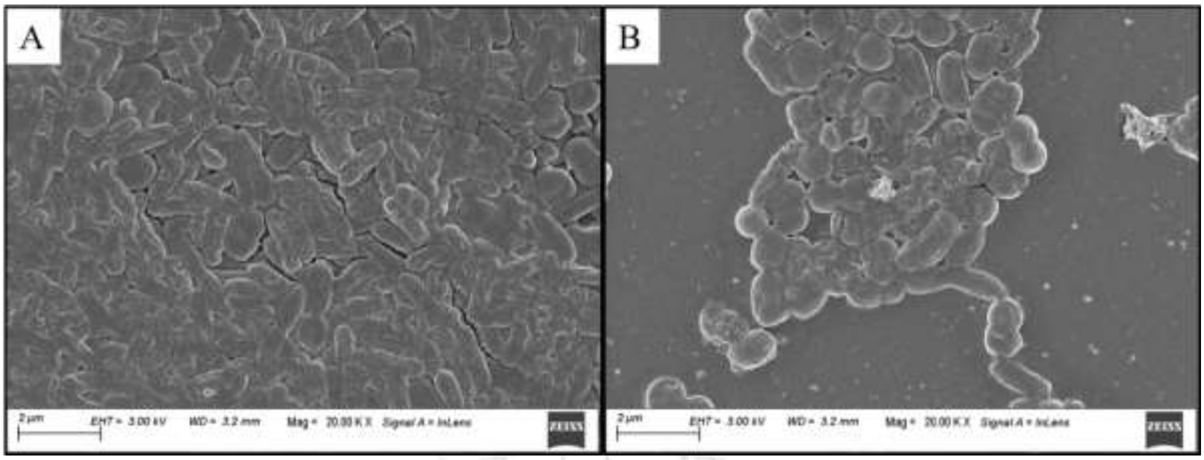

Figure 6.8: FESEM image showing the *Pseudomonas aeruginosa* biofilm on amine SAMs (A) and AgNPs-amine surfaces (B).

FESEM analysis of the *Pseudomonas aeruginosa* biofilm on the amine-SAMs and AgNPs-amine surfaces was carried out. FESEM revealed that AgNPs adsorbed amine SAMs surfaces inhibited the biofilm formation of *P. aeruginosa* compared to the amine SAMs modified surfaces, as apparent from **Fig 6.8**. Holdan *et al.* also characterized the *P. aeruginosa* biofilm using SEM for the morphological features of the biofilm. It is clear from **Fig. 6.8(B)** that AgNPs hampered bacterial attachment by disrupting the release of the polysaccharides needed for the bacterial colonization of the surfaces and releasing silver ions from the surface. This indicated the efficacy of the fabricated surfaces for restricting biofilm formation. FESEM indicates the presence or absence of the biofilm. However, it does not account for the viability of the bacteria present on the surface. FACS analysis is more reliable for determining antimicrobial activity against various clinically relevant bacterial strains [409]. FACS analysis of the different surfaces was carried out to quantify the degree of bacterial viability of various surfaces (**Fig. 6.9**). It was found that amine SAMs showed the highest live population of the *P. aeruginosa* (61.3%) and lowest dead population (38.69%) due to the presence of the positively charged amine surface that readily interacts with the negatively charged bacterial cell wall.

On the other hand, bare glass coverslip surfaces showed a slightly lesser population of live bacteria (53.94%) and a higher dead population (46.06%) than the amine-SAMs modified surface. AgNPs-amine surfaces showed the lowest live population (32.55%) and highest dead population (67.45%) of all the surfaces used for the studies, thus confirming the potential of the fabricated surfaces as antimicrobial. Kiruba *et al.* incubated the *P. aeruginosa* for different time intervals with hydroquinone and characterized the viability using FACS analysis. They found that the *P. aeruginosa* incubated with hydroquinone (4X MIC) for 2 hours showed a dead population of 56.57%, slightly lower than the one obtained by the AgNPs-amine surfaces incubated with the bacteria overnight [409]. In a similar study, Verma *et al.* assessed the viability of the AgNPs coated gutta-percha for endothelial applications. It was found that 71.24% percentage of the *E. faecalis* cells were killed by the 2% AgNPs- gutta-percha exposure [410]. From the above discussion, it is clear that the fabricated antimicrobial surfaces are highly effective in eradicating the biofilm formation by *P. aeruginosa.* These studies indicate the potential of antimicrobial surfaces for various biomedical applications, such as modifying surfaces involved in surgery and implantation.

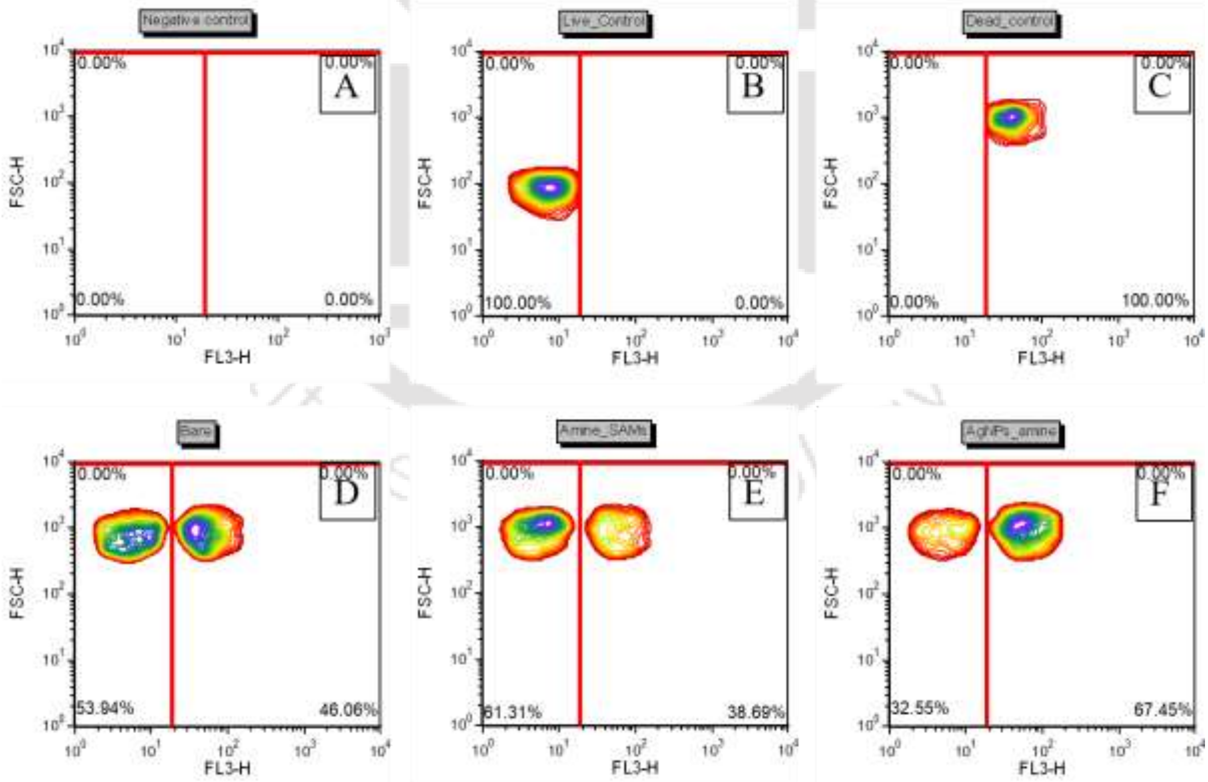

Figure 6.9: FACS analysis of the different surfaces, negative control (A), live bacteria (B), dead bacteria (C), bare surface (D), amine-SAMs (E), and AgNPs-amine (F) surface.

6.4 Conclusions

Biogenic AgNPs were successfully synthesized using plant leaf extract of *Miscanthus khasiana*. A UV-Vis spectrophotometer was used to confirm the completion of the synthesis. XRD showed signature peaks of silver at 2θ values 37.99, 44.04, and 64.42, which SAED further confirmed. The size of AgNPs and d-spacing value were 20-22 nm and 0.255, respectively. The IC_{50} value of AgNPs against clinically relevant bacteria was 109 µg/ml. Amine-SAMs were formed on a glass substrate, confirmed by the contact angle and FTIR analyses. Further, AgNPs attachment on the amine surface was confirmed using AFM and FTIR. A stability study of the AgNPs-amine surface in PBS at 37 ºC for 24 h showed a durable antimicrobial coating for biomedical applications. Conclusively, this new approach can produce cost-effective antimicrobial surfaces for various prospective applications.

AgNPs-amine surfaces inhibited bacterial attachment and colonization, as evident from the FESEM data showing lesser bacterial attachment. FACS analysis provided greater insight regarding the viability status of the adhered bacteria. It was clear from the FACS data that AgNPs-amine surfaces showed the highest bacterial death (67.45%) compared to the amine-SAMs and bare surfaces. It is clear from the data that the fabricated surfaces can address the nosocomial to some extent without compromising the basic features of the medical material.

Section 2: Chitosan biopolymer mediated NPs as the antimicrobial agents and ampicillin loading vehicles

6.5 Introduction

Various next-generation biomaterials such as polymers [3, 4], ceramics [5, 6], metals [7, 8], composites [9, 10], and scaffolds [411, 412] are being explored throughout the scientific community to fabricate a material with the desirable features for implant-related applications. All the materials mentioned above have pros and cons, so addressing various issues related to biomaterials is the most promising research. Alternatively, antibiotic dosages can be alternated with fabricating antimicrobial surface coatings to easily tackle localized infections at the implantation site [413]. Antimicrobial moieties can directly attach to the surface of the implant material as the physiological microenvironment interacts with the implant surface but not with the bulk material. So, attaching, crosslinking, or immobilizing the alternate or conventional antimicrobial agents directly to the surface will suffice the current needs [414-416].

Nanoparticles (NPs) with various multimodal mechanisms of antimicrobial actions can be directly utilized or used synergistically with conventional drug-loading vehicles [417]. In this regard, extensive research has been conducted thoroughly with the metal and metal oxide nano-entities for antimicrobial applications. Though they showed promising antimicrobial efficacy, they have serious nano-toxicological issues that limit their medical applicability [418]. So, using bioderived molecules with simple molecular structures will show less immunological response. In this regard, various bio-polymers are being investigated, such as lignin, cellulose, hemicellulose, gelatin, collagen, pectin, sodium alginate, chitin, chitosan, silk fibroin, albumin, tannins, and others. They are biocompatible in nature and exhibit ease of surface functionalization [419]. Among all the biomolecules, chitosan has been explored in the current research work due to its various favorable features. Chitosan has excellent potential due to its polycationic makeup and adaptability as a drug-loading vehicle or conjugation framework for the numerous functional moieties on the surface [420]. Additionally, chitosan has a mucoadhesive characteristic, biocompatible, and is simple to synthesize [421].

TH-3560_176106117

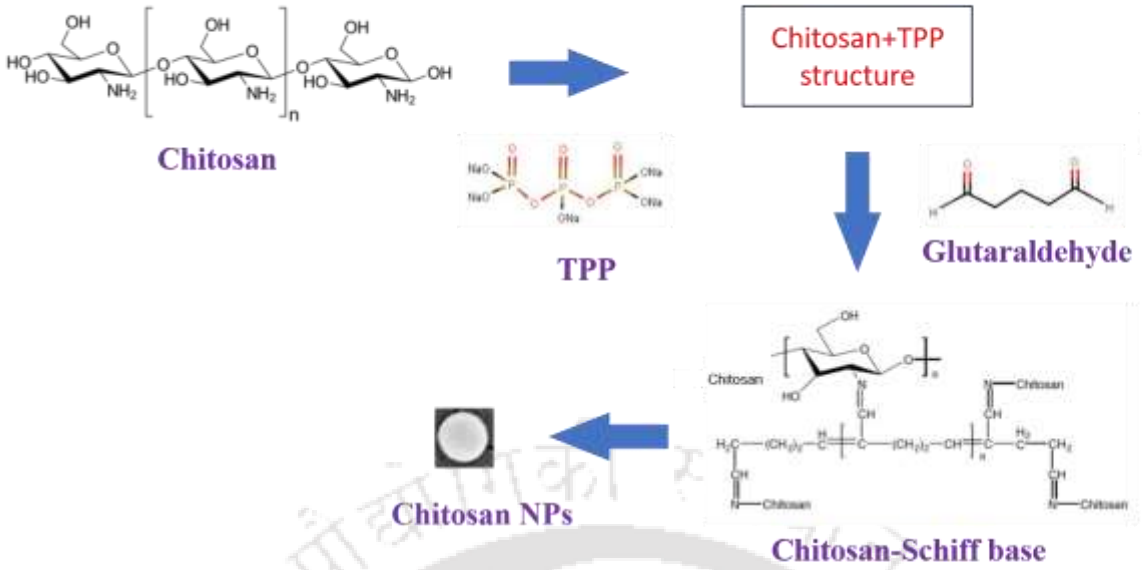

Figure 6.10: Schematic showing the chitosan NPs fabrication strategy.

Our research aims to fabricate chitosan NPs on the surface of the titanium and its alloy to give the implant surface antibacterial properties, eliminating the requirement for external antibiotic therapy. For microbial eradication from the surface, our research aims to impart an antimicrobial property by silane-mediated coupling of the antibiotic-encapsulated chitosan nanoparticles (NPs). Chitosan NPs were fabricated using the modified ionotropic gelation method using sodium tripolyphosphate and glutaraldehyde crosslinking. The antimicrobial effect and cytocompatibility of the prepared metal surfaces were investigated using gram-positive bacteria and murine fibroblasts, respectively.

6.6 Materials and Methods

6.6.1 Materials

Chitosan-high molecular weight (HMW; 310 000-375 000 Da), chitosan-low molecular weight (LMW; 50 000-190 000 Da), and sodium tripolyphosphate (TPP) were procured from Sigma-Aldrich Japan. Glacial acetic acid, sodium acetate, phosphate buffered saline, 25% glutaraldehyde solution, ampicillin, 3-aminopropyl trimethoxy silane (APTMS), and dehydrated toluene were purchased from FUJIFILM Wako Pure Chemical Corporation, Japan. 2-(4-Iodophenyl)-3-(4-nitrophenyl)-5-(2,4-disulfophenyl)-2H-tetrazolium, monosodium salt

(WST-1) was obtained from DOJINDO LABORATORIES, Japan. Eagle's minimum essential medium (E-MEM, AccuDia^{TM} Eagle's MEM 1) was obtained from Shimadzu Diagnostics Corporation, Japan. Fetal bovine serum was obtained from Biowest, France. Nutrient broth medium was procured from EIKEN CHEMICAL CO., LTD, Japan. Murine fibroblast L929 (ATCC CCL-1) was purchased from Summit Pharmaceuticals International Corporation, Japan. Bacteria for antibacterial assays (*Escherichia coli* and *Staphylococcus aureus*) were purchased as EZ-PEC^{TM} kits (cat. No. 0483-PEC and 0485-PEC, respectively) from Microbiologics, St Cloud, USA.

6.6.2 Chitosan NPs synthesis

The strategy of chitosan NPs synthesis is shown in **Fig. 6.10.** The dynamic nature of the fabricated NPs was addressed using glutaraldehyde as the covalent crosslinker, resulting in a fluorescently active Schiff base formation [401].

Chitosan stock solution (20 mg/ml) was prepared in 0.2 M glacial acetic acid and stirred overnight to dissolve the chitosan (HMW & LMW) completely in the solution until a gel-like uniform texture was achieved. In the same flask, the chitosan working solution of pH 5 was prepared by diluting the stock solution 10 times with 0.5M sodium acetate (acetic acid: sodium acetate ratio was 1:9 v/v). Another chitosan working solution of pH 3 was formed by diluting the stock solution 10 times with Milli-Q (ultrapure) water and stirred until a uniform solution was obtained. TPP solution (0.5 mg/ml) was added dropwise to the working solution using the peristaltic pump at the flow rate of 80 µg/ml for 50 min. Post-TPP addition, the chitosan-TPP solution was stirred for 30 min to equilibrate the reaction mixture. Post equilibration, glutaraldehyde was added dropwise to be 1/5 of the chitosan weight, and the reaction mixture was kept on stirring for an extra 30 min for the glutaraldehyde to crosslink the chitosan chains completely. To monitor the progression of the synthesis and crosslinking reaction, aliquots of the reaction mixture were collected at every 10 min interval, and the following measurements:

Fourier Transform Infrared Spectroscopy in the Attenuated Total Reflectance mode (FTIR-ATR, IRAffinity-1S, SHIMADZU CORPORATION, Japan, in the range of 4000-700 cm^{-1} with a scan interval of 4 cm^{-1}), and dynamic light scattering analysis (DLS, ELSZ-2000ZS, Otsuka Electronics Co., Ltd.) were used. The blank reaction was run with the buffer solution not containing the reaction precursors (chitosan, glutaraldehyde and TPP) with sample collection every 10 min.

The molarity of the glutaraldehyde (2, 4, 6, and 8 mM) was varied to control the crosslinking level for tuning the drug release kinetics. Synthesized NPs were aged and separated from the unreacted precursor molecules by centrifugation at 30000 g for 30 min, followed by thrice washing with Milli-Q water. Purified NPs samples were freeze-dried and kept in the vacuum desiccator before further experimentation.

6.6.3 Characterization of NPs

Freshly fabricated NPs solution was drop-cast on a carbon tape, followed by drying in the laminar airflow and storing the samples in a desiccator. Then, the sample surface was coated with Pt using an ion sputter coater (E-1030, Hitachi High-Tech Corporation, Japan) prior to the observation of NP morphologies by scanning electron microscopy (SEM, S-4800, Hitachi High-Tech Corporation, Japan).

6.6.4 Ampicillin Loading

Ampicillin was chosen as a model drug to be encapsulated inside the chitosan NPs by in-situ loading during the NP synthesis. Ampicillin was added to the chitosan working solution (pH 3 and 5) before adding TPP. Then, the TPP was added as previously described, followed by the glutaraldehyde crosslinking. First, glutaraldehyde concentration was set as 2 mM for pH 3 and 5 conditions with varying the weight ratio of ampicillin: chitosan (1:30, 1:20, 1:15, 1:12) to find the ideal ratio for ampicillin loading. Then, the ampicillin: chitosan ratio was kept at 1:30 with varying the glutaraldehyde molarity (2, 4, 6, and 8 mM) to find its effect on ampicillin loading. Synthesized NPs were collected from the reaction mixture by centrifugation (30,000 g for 30 min), followed by washing with Milli-Q water and freeze-drying.

The amount of ampicillin encapsulated in the NPs was decided by quantification of remaining ampicillin in the supernatant after centrifugation; the absorbance at 240 nm was measured using a UV-Vis spectrophotometer (GeneQuant^{TM} 1300, Harvard Bioscience, Inc., USA) and its concentration was calculated with standard curve of ampicillin in pH 3 or 5 buffer with TPP. The ampicillin loading efficiency (LE, %) was determined by the following equation;

$$\mathrm{LE}(\%) = [(C_{start} - C_{super}) / C_{start}] \times 100$$

where C_{start} and C_{super} indicate the starting amount of ampicillin and its remaining amount in the supernatant, respectively. The ampicillin load per 1 mg chitosan precursor or NPs (AL, μg/mg precursor or NPs) was calculated by the following equations;

$$\mathrm{AL}_{\mathrm{pre}} = (C_{start} - C_{super}) / W_{pre}$$

$$\mathrm{AL}_{\mathrm{NP}} = (C_{start} - C_{super}) / W_{NP}$$

where W_{pre} and W_{NPs} indicate the weight of chitosan precursor or NPs fabricated, measured after freeze-drying.

6.6.5 NPs Surface Attachment

Titanium foils (thickness of 50 μm, Nilaco Corp.) and Ti6Al4V discs (25 mmφ × 2.5 mm, Japan Metal Service Corp.) were employed as model metal substrates. Ti6Al4V discs were polished with SiC papers up to #800, a diamond suspension up to 3 μm, and a colloidal silica suspension with H2O2 for a mirror-finish surface. Then, the discs were ultrasonically rinsed with acetone three times, followed by air-dry. Titanium foils were cut into 10 mm squares or 5 × 10 mm depending on the following measurement. Prior to NP coating, these specimens were cleaned by oxygen plasma (HDT-400, JEOL Ltd., Japan), followed by silanization with APTMS (1% v/v) in dehydrated toluene under inert nitrogen conditions. Then, chitosan NPs resuspended with Milli-Q water were spin-coated on the amine-terminated surface. The amount of coated NPs was decided based on the weight difference of each specimen before/after spin-coating.

6.6.6 Ampicillin Release Kinetics

Milli-Q water and phosphate-buffered saline (PBS) were employed for in-vitro ampicillin release from NPs. The NPs were added into 20 mL of each solution and kept under mild orbital shaking (~240 rpm) for up to 7 days. Aliquots (100 µL) of the NP solution were retrieved at fixed time intervals. Aliquots were centrifuged at 10 000 g for 10 min to remove any interfering molecules from the solution, and UV-Vis was measured at 240 nm.

6.6.7 Antimicrobial Studies

Antimicrobial studies were performed on *E. coli* and *S. aurues* (EZ-PEC^{TM}, microbiologics, USA) with 1x10^5 -1x10^6 CFU/ml were used for the antimicorbial studies to determine the MIC of the fabricated chitosan NPs. All the antimicrobial studies were conducted in line with the JIS Z 2801 and JIS L 1902/ISO 20743 protocol for the fabricated NPs.

6.6.8 Electrochemical Impedance Spectroscopy

Measurements were performed in 5 mL of PBS media with 2 mg/ml chitosan NPs (HMW & LMW). A typical three- electrode system [a platinum wire, Ag/AgCl (3 M NaCl), and uncoated or polymer-coated ZM21 as a working electrode] was used. A working area of 0.264 cm^2 had a contact with the electrolyte. An experimental chamber was placed in the incubator (25 °C) for 24 hours. Electrochemical impedance spectroscopy (EIS) data were obtained using a potentiostat equipped with a frequency response analyzer (VersaSTAT3, Princeton Applied Research, USA) at 2, 6, 24, and 48 h of incubation at the open circuit potential (OCP) with AC amplitude of 5 mV in a frequency range of 10−2–105 Hz [422, 423].

6.7 Results and Discussion

The ionotropic gelation method was used to form the NPs using chitosan as the positively charged polyelectrolytes and sodium tripolyphosphate as the negatively charged polyelectrolytes. The dynamic nature of the fabricated NPs was addressed using glutaraldehyde as the covalent crosslinker. Crosslinking the chitosan NPs with glutaraldehyde resulted in a fluorescently active Schiff base formation.

6.7.1 Characterization of NPs

FTIR measurement of the chitosan precursor and NPs was carried out in the ATR mode in the range 4000-700 cm^{-1}, as shown in **Fig. 6.11**. In the spectra of the chitosan precursor, two distinct peaks were observed at 2973 and 2984 cm^{-1} due to the CH stretching of chitosan monomeric units. In the chitosan NPs, there was a red shift to 3027 and 3042 cm^{-1} of CH stretching due to a reduction in the vibrational energies due to hydrogen bond formation [424]. The chitosan precursor peak at 2298 cm^{-1} was obtained due to the CH stretching of the methyl group in the chitosan backbone [425]. In contrast, there was a red shift to 2346 cm^{-1} in the chitosan NPs post-TPP and glutaraldehyde crosslinking due to extensive inter- and intra-crosslinking in the NPs attributed to the asymmetric stretching [426]. FTIR peak due to the carbonyl group was present at 1714 cm^{-1} (chitosan precursor), post crosslinking peak due to the cyano- group appeared at 1670 and 1655 cm^{-1} in the Chitosan NPs [401, 427]. FTIR peak due to the C=C functional group was present in both chitosan precursor (1528 cm^{-1}) and NPs (1538 cm^{-1}), as shown in the FTIR graph [401]. FTIR peak due to the glucosamine backbone was present in both the precursor (991 cm^{-1}) and NPs (1065 cm^{-1}) [428]. Banu *et al.* fabricated bisacodyl-loaded chitosan NPs and studied protein interaction using BSA as the model protein. FTIR spectra of the NPs revealed a CH stretching peak at 2973 cm^{-1}, C=C stretching at 1538 cm^{-1}, and a peak due to the glucosamine backbone at 1065 cm^{-1} [429]. Zhang *et al.* fabricated chitosan-based films for wound dressing applications and characterized them using the FTIR measurement. The group also observed the CH stretching peak at 2877 cm^{-1} and a peak at 1022 cm^{-1} in the chitosan films [430]. Other research groups also reported a peak at 1091 cm^{-1} due to the glucosamine backbone of the chitosan molecule and a peak at 2873 cm^{-1} due to the CH stretching of the chitosan backbone [431]. In another study, chitosan NPs were fabricated for the drug loading applications characterized by the FTIR and SEM analysis. FTIR spectra revealed a peak due to CH_2 symmetric stretching at 2934 cm^{-1} and a peak at 1565 cm^{-1} due to $CONH_2$ in the chitosan NPs due to crosslinking due to TPP molecules. Further peak at 1011 cm^{-1} was observed due to the glucosamine groups in the chitosan backbone [432].

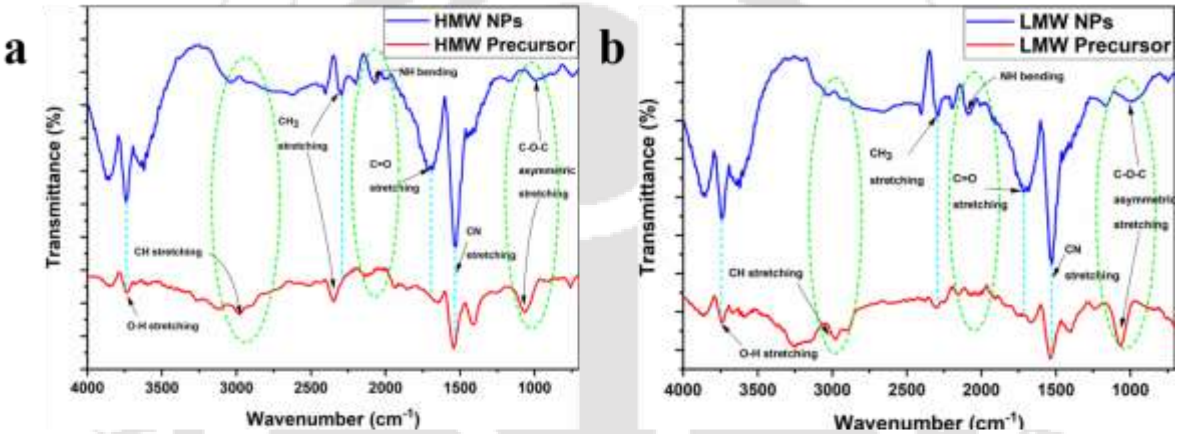

Figure 6.11: FTIR spectra of precursors and fabricated nanoparticles (NPs). (a) high molecular weight (HMW) precursor and NPs, and (b) low molecular weight (LMW) precursor and NPs.

SEM analysis of the fabricated NPs was carried out to determine the size and shape of the NPs. This freshly fabricated NPs solution was drop cast on the carbon tape, followed by drying in the laminar airflow and storing the samples in the desiccator before the analysis. LMW and HMW NPs were utilized to form the NPs using the ionotropic gelation method coupled with glutaraldehyde-based crosslinking chemistry. NPs were characterized for shape and size using the SEM technique based on the glutaraldehyde concentration used for the crosslinking to shift the dynamic equilibrium state of the NPs to the durable and robust fabricated NPs. Based on the SEM images, it was clear that all the fabricated NPs were spherical. Though the air-dry method was employed immediately after the synthesis to cast the samples onto the carbon tape, it might have led to the shrinking and aggregation of the neighboring particles, resulting in particles with larger diameters. Critical point drying should have been employed for the sample's preparation as the slightly larger particle size from SEM data than the DLS diameter indicated some degree of agglomeration and artifact formation during the sample preparation process. NPs without the crosslinker showed a particle dia. of 270±2.8 nm (HMW NPs) and 332.5±48.3 nm (LMW NPs), followed by the 2mM crosslinker concentration, with 470.3±57.3 nm (HMW NPs) and 424.5±52.9 nm (LMW NPs). Freely available glutaraldehyde might have interfered with the NPs, while the SEM sample preparation was comparable to the sample size with and without a crosslinker. For the HMW NPs, the particle size with the variable concentration of the glutaraldehyde was 463.49±58.4 nm (4mM), 430.1±18 nm (6mM), and 351.6±22 nm (8mM). In the case of the LWM NPs, there might be slight interference from the unbound crosslinker, as evident from the following data: 247.6±40 nm (4mM), 424.3±39.4 nm (6mM), and 246.7±24.6 nm (8mM) as shown in **Fig. 6.12**. Banu *et al*. fabricated chitosan NPs that were spherical in shape and uniform in nature [429]. Another research group also investigated the chitosan NPs formation using SEM and were spherical with slightly tapered ends, though the particles were significant [432]. Zheng *et al.* also characterized the NPs of chitosan variants and observed uniform spherical-shaped NPs without any visible aggregation [433]. Particles observed under SEM post-sample drying do not reflect their accurate size in the solution conditions. Tian *et al.* also observed spherical chitosan NPs in SEM, but the samples tended to agglomerate due to the sample preparation conditions [434]. Hu *et al.* fabricated peptide-loaded chitosan NPs to promote dentin remineralization and characterized the morphology using SEM. Uniform spherical particles with a 100-200 nm diameter were visible in the SEM micrograph. However, the same samples were found to be 300 nm in size using the TEM analysis, with some large agglomerates formed during the sample preparation [435].

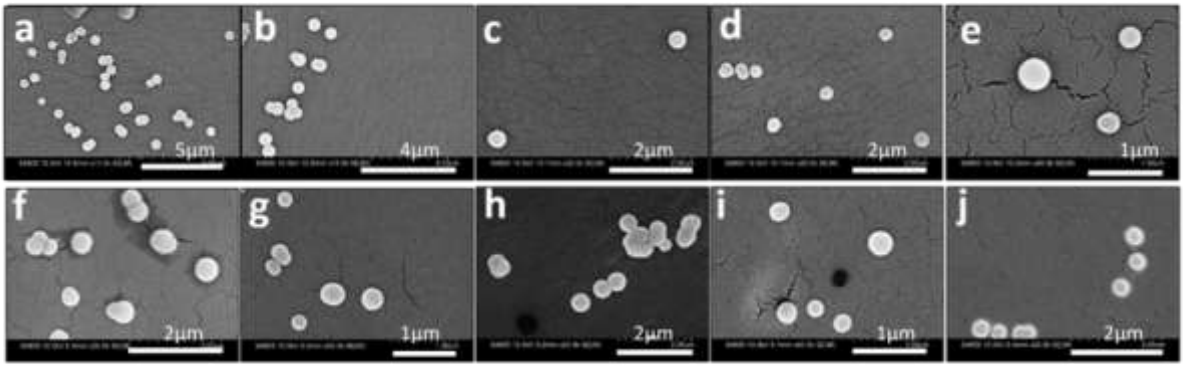

Figure 6.12: SEM observation of the HMW NPs (a-e) and LMW NPs (f-j) with two mM (a, f), 4 mM (b, g), 6 mM (c, h), and 8 mM (d, i) and 0 mM (e, j) glutaraldehyde.

In DLS measurement of the samples, chitosan precursor, without any external effect, remained in a linear form or a loosely entangled strand. The larger the chain length, the higher the chances of self-entanglement, which is why the LMW precursor has a higher hydrodynamic diameter (~662 nm) than the HMW precursor (~412 nm). LMW NPs were ~210 nm, and HMW NPs were 327 nm in size post NPs synthesis, as shown in **Fig. 6.13(b)**. The structural stability of the fabricated NPs was also studied by keeping the samples at RT conditions, showing the change in the hydrodynamic diameter in the permissible range. DLS measurement also indicates the stability of the as-fabricated NPs up to 72 hours after preparation. Zheng *et al.* also characterized the formed NPs using the DLS measurement. NPs composite showed a hydrodynamic diameter of 196.72 nm and BSA-coated NPs of 231.3 nm [433]. Other research groups performed DLS measurements to determine the size of the chitosan NPs, which was 240-260 nm in range post-drug loading [434]. Other researchers also quantified the chitosan NPs using the DLS measurement, and particles were found to be 276±7.07 nm in hydrodynamic diameter [435]. Moreover, glutaraldehyde crosslinking resulted in the formation of the fluorescent Schiff bases determined by the fluorometer data shown in **Figure 6.13(a)**. Zheng *et al.* investigated the stability of the NPs in the simulated gastric and intestinal fluid using the UV-Vis measurement in the transmittance mode. NPs showed no significant disintegration in the gastric fluids, showing resistance and passing through the stomach fluid. However, NPs showed drastic disintegration in the intestinal fluid within 8 hr, which was stabilized post 72 hr treatment with remarkable enteric stability and compatible with oral administration [433]. FTIR analysis after SAM-treated and NP-coated Ti6Al4V discs, confirming the immobilization of NPs on Ti6Al4V disc surfaces by the relative increase in peak strength around 1600 cm-1 assigned to N-H stretching as shown in **Fig. 6.14**.

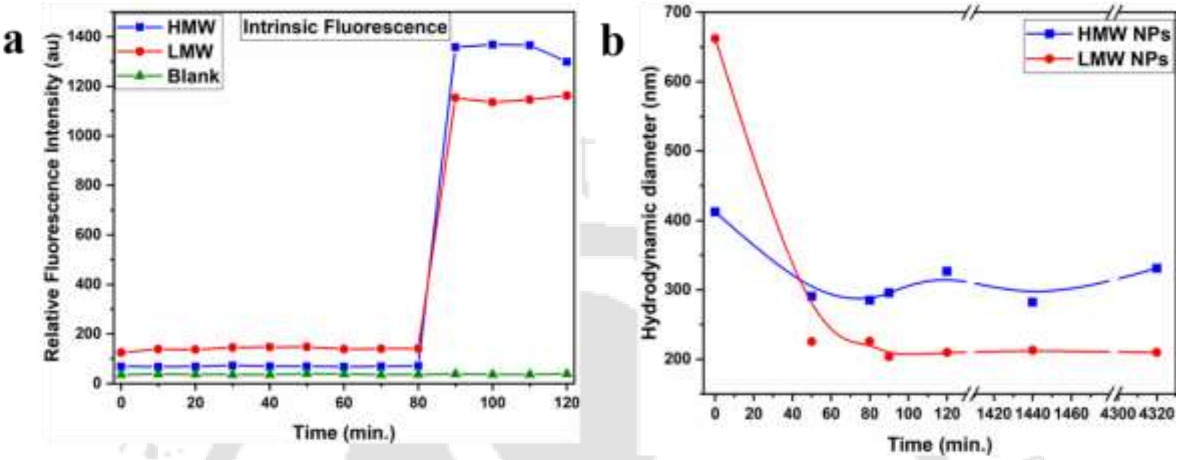

Figure 6.13: Fluorescence intensity (a) and the hydrodynamic diameter (b) of the reaction mixture during the nanoparticles (NPs) synthesis at pH 5 with glutaraldehyde concentration of 2 mM. HMW and LMW indicate the high molecular weight and low molecular weight chitosan precursors, respectively. The hydrodynamic diameter was measured using the DLS method.

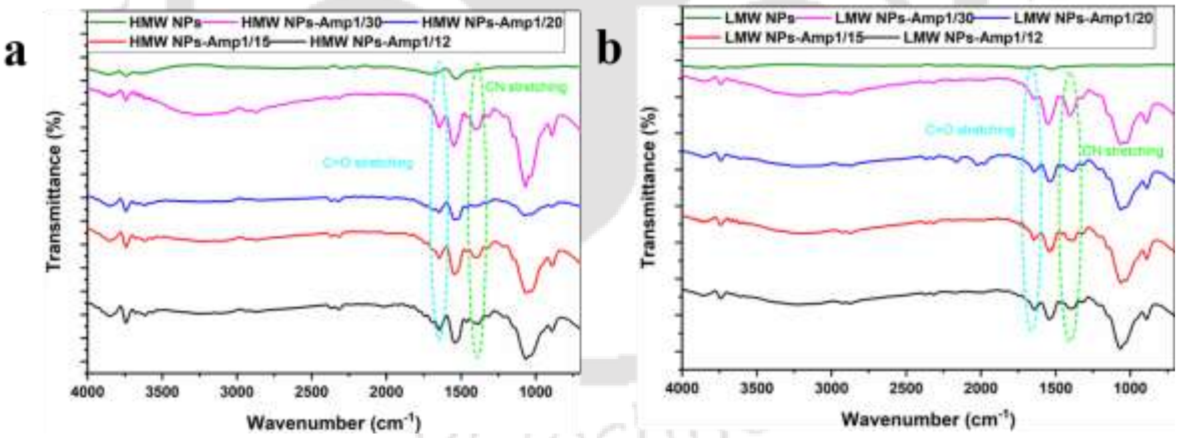

Figure 6.14: FTIR spectra of the ampicillin-loaded nanoparticles (NPs) derived from high molecular weight (HMW), (a) and low molecular weight (LMW), (b) precursors at different ampicillin: chitosan precursor ratios.

6.7.2 Ampicillin loading

Ampicillin loading capacity and efficiency were also determined at variable glutaraldehyde concentration at 1:30 ratio (ampicillin: chitosan) and pH 5. There was a linear increase in the ampicillin loading with the increase in the crosslinker concentration for the HMW NPs, as shown in **Fig. 6.15**. On the other hand, loading efficiency was almost independent of the crosslinker concentration, as tabulated in **Table 6.1**. HMW NPs showed the highest loading of 41 µg/mg for the 8mM crosslinker concentration. Other research groups investigated the loading efficiency of the salicylic acid in chitosan-based loading vehicles. It was observed that bare chitosan showed 96.13% while the chitosan NPs showed 87.13 % loading efficiency [432]. Zheng *et al.* used BSA as the model drug to assess the drug loading capacity of the synthesized NPs. The molar ratio of two chitosan variants, namely carboxymethyl chitosan and hydroxypropyl trimethylammonium chloride chitosan, were used with 1:4 to 3:4 ratios, which resulted in a decrease of encapsulation efficiency from 65.32±1.52 % to 37.83±2.37% and the loading capacity diminished to 23.42±0.55% from 45.21±0.81%. Reduction in the surface potential and electrostatic forces might have resulted in the compromised encapsulation efficiency and loading capacity [433]. In a drug loading study conducted by Hu *et al.*, both encapsulation efficiency and loading capacity increased in the initial phase, followed by reduction, and maxima were attained for the encapsulation efficiency (69.63±2.22%) and loading capacity (13.21±0.73%) with a mass ratio of 4:1 for the chitosan: loaded peptide [435].

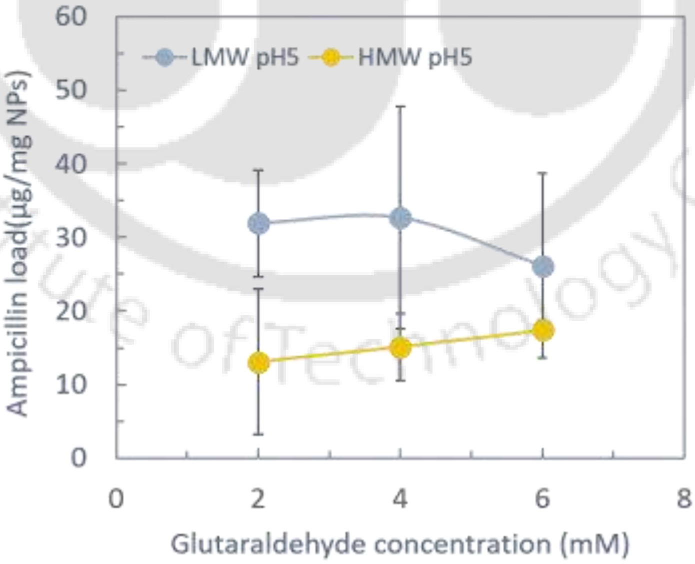

Figure 6.15: Ampicillin load per 1 mg of NPs. NPs were fabricated at 2mM glutaraldehyde and ampicillin: chitosan ratio of 1:30 (=0.033)

Table 6.1: Amount of ampicillin load per 1 mg of NPs at pH5 and ampicillin: chitosan ratio of 1:30 (mean ±SD, µg/mg).

	Glutaraldehyde concentration			
Precursor type	2 mM	4 mM	6 mM	8 mM
LMW	31.9±7.3	32.7±15.1	26.1±12.5	27.8
HMW	13.0±9.9	15.1±4.6	17.4±1.3	41.0

6.7.3 Ampicillin Release kinetics

Ampicillin release kinetics was initially conducted at neutral pH (MilliQ water). It showed the ampicillin burst release within 1 h, followed by the slow release up to 6 hours without reaching the plateau phase for all the drug-loading vehicles, i.e., NPs, as shown in **Fig. 6.16(a-b)**. The total amount of ampicillin released from the chitosan NPs and the release percentages are presented. Burst release occurred during the first hour, followed by slow release. Slopes of L2A and H2A, L8A, and H8A are not significantly different, but intercepts indicate no significant difference in the slow release behavior after 1h.

Interestingly, the LMW NPs show a slower release of ampicillin compared to the HMW NPs, though their ampicillin loading is higher than that of the HMW NPs. This can be related to the difference in the size of the precursor chitosan moieties. In a study conducted by Esmaeel *et al.*, berberine release kinetics was studied from the chitosan/pectin NPs. Cumulative release of the berberine was measured up to 240 min, and it was observed that there was linear release of the berberine without any significant lag phase up to 100 min followed by a stationary phase signifying no net release of the drug post 100 minutes [431].

A research group investigated the release profile of the salicylic acid. It was observed that the NPs showed sudden burst release in the initial phase (up to 5hr), and the remaining drug molecule was released in a sustained manner till 48 hrs. Contrary to our findings in the current work, authors observed higher drug release in the PBS buffer (51.5-69.4%) while less in the water/ethanol mixture (34.9-50.4%). However, the drug release is dependent on the nature of the drug moiety and loading vehicle as well as the drug-loading vehicle interactions [432]. In vitro release of the model drug, BSA, was investigated from the chitosan variant NPs in PBS conditions by another research group. Rapid burst release was detected in the 0-4 hr due to desorption of the BSA from the surface of the NPs; upto 68.21±2% of the drug was released within 12 hr of the incubation in the PBS buffer [433]. Drug release from the loading vehicles occurs via surface erosion desorption, diffusion or disintegration and degradation of the vehicle, and release of the drug moieties. Tian et al. investigated the pH and time-dependent release of the beta acids from the chitosan NPs in a simulated tumor microenvironment (pH 6.6), simulated body fluids (pH 7.4), and gastric fluid microenvironment (pH 1.5) at physiological conditions. The biphasic release was observed, with the first burst release followed by the slow, gradual release for the pH conditions [434]. In-vitro drug release kinetic was investigated by Hu *et al*., who found that in the first 4 hour, drug moiety released rapidly, attaining a cumulative release of 57.67±3.06%, followed by a slower sustained release post 12 hr with 80 % of the drug load released after 36 hour [435].

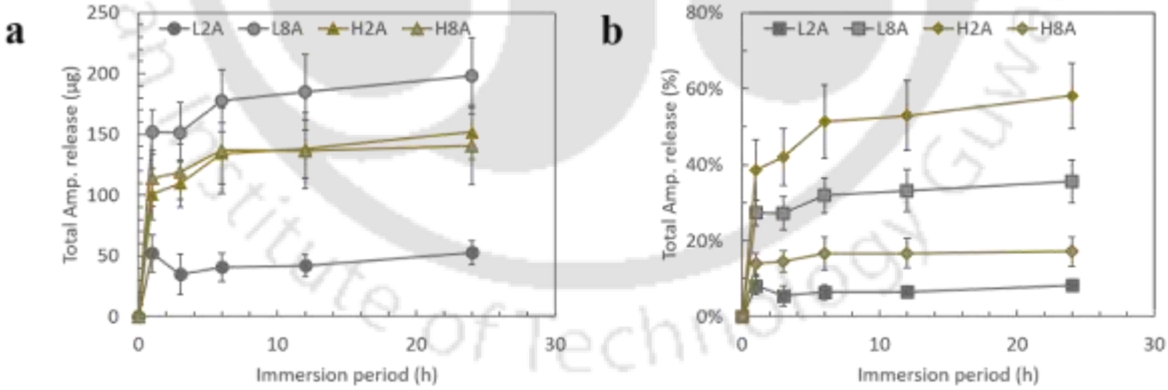

Figure 6.16: The total ampicillin release was plotted against the immersion periods. (a) The total amount of ampicillin released, and (b) the ratio of released ampicillin against the ampicillin load. L2A, L8A, H2A, and H8A indicate the NPs fabricated from LMW and HMW chitosan precursors with 2 or 8 mM glutaraldehyde addition and ampicillin: chitosan ratio of 1:30 (=0.033) at pH 5 condition.

6.10.4 Antimicrobial Studies

<u>6.10.4.1 MIC determination</u>

Antibacterial activities of fabricated NPs were examined using clinically relevant bacteria *Escherichia coli* (gram-negative) and *Staphylococcus aureus* (gram-positive), and the results were shown in **Table 6.2**. LMW NPs have higher antibacterial activities (i.e., smaller MIC) than corresponding HMW NPs for *E. coli* and *S. aureus*. NPs prepared with 2 mM glutaraldehyde crosslinker concentration had better antibacterial activities than 8 mM. Ampicillin-loaded NPs have smaller MICs than NPs without ampicillin for both bacteria. Ampicillin-loaded LMW NPs obtained the best antibacterial activity with 2 mM glutaraldehyde at 691 µg/mL for *E. coli* and 67.3 µg/mL for *S. aureus*. The antimicrobial efficacy of the beta acids loaded chitosan NPs was evaluated by Tian *et al.* against the clinically relevant bacterial strains, i.e., *S.aureus* and *E.coli*. Zone of inhibition was measured for the beta acid-loaded NPs; it was found to be 7.23-14.7 mm (*S.aureus*) and 7.17-12.37 mm (*E.coli*). Antimicrobial efficacy increased with the amount of beta acid encapsulated in the NPs[434]. Maedeh *et al.* fabricated chitosan NPs to study the expression of Fosfomycin-resistant genes in the *Proteus mirabilis* using the chitosan NPs. Antimicrobial studies of the chitosan NPs were performed against *P.mirablis* using the micro broth dilution method, and MIC was found to be 500 µg/ml in the studies[367]. In another study, quaternized chitosan NPs were fabricated and were tested for the MIC and Maximum Bactericidal Concentration (MBC) studies against 6 clinically relevant pathogenic strains namely, *S.aureus*, *E.coli*, *P.vulgaris*, *K.pneumoniae*, *S.epidermidis*, *P.aeruginosa* and both MIC and MBC results were quite similar with 250 µg/ml against all strains except for the *P.aeruginosa* (500 µg/ml) [436].

Table 6.2: Minimum inhibitory concentration (MIC) of fabricated NPs against Escherichia coli and Staphylococcus aureus (mg/mL)

	LMW				HMW			
Ampicillin	(+)		(-)		(+)		(-)	
Glutaraldehyde conc.	2 mM	8 mM	2 mM	8 mM	2 mM	8 mM	2 mM	8 mM
E. coli	0.691	0.939	0.816	1.303	0.979	2.315	1.858	3.166
S. aureus	0.0673	0.198	0.594	1.137	0.0660	0.0681	0.910	1.818

* Inoculation condition of bacteria was 0.5-2.3 × 10^6 CFU/mL.

6.10.4.2 Antimicrobial activity of antimicrobial surface coatings:

The antibacterial activity of Ti6Al4V coated by fabricated NPs was tested using *S. aureus* and *E. coli, as* shown in **Table 6.3**. Surfaces coated with HMW NPs with ampicillin and LMW NPs with/without ampicillin exhibited excellent bactericidal activities, as no bacteria survival was observed after 24h of contact. Ti6Al4V coated with HMW NPs without ampicillin and SAMs-immobilized ones have almost similar levels of bacterial growth to that of non-treated ones. These results demonstrate the success of our research concept to give antibacterial activity onto the Ti6Al4V surface via the coating of antibiotic-loaded chitosan NPs. The antimicrobial nature of the chitosan is attributed to the cationic amino groups in the chitosan structure. NPs-based antimicrobial strategy imparts efficient uptake of drugs or macromolecules at lower concentrations, enhanced stability, and lower cytotoxicity. Primo *et al.* investigated the MIC of the various antibiotics-loaded chitosan NPs against the three multidrug-resistant (MDR) *Mycobacterium tuberculosis* and showed the best MIC for the N-acetylcysteine-chitosan NPs (<0.977 µg/ml) [437].

Table 6.3: Estimated CFU/sample after 24h of contact with *S. aureus.*

	Ti6Al4V	**Ti6Al4V-SAMs**	**LMW**		**HMW**	
			Ampicillin (-)	Ampicillin (+)	Ampicillin (-)	Ampicillin (+)
Ave.	1.13×10^{8}	7.18×10^{7}	<1	<1	8.60×10^{7}	<1
s.d.	1.56×10^{7}	5.08×10^{6}	-	-	7.43×10^{6}	-

Ave.: average, s.d.: standard deviation
*LMW and HMW NPs were prepared at 8 mM of glutaraldehyde concentration.
**The bacteria were inoculated at ca. 3.0×10^{6} CFU/sample.

6.7.5 Electrochemical Studies

Electrochemical impedance spectroscopy (EIS) was explored to investigate the nature of the coating on the surfaces in phosphate-buffered saline after 2h of immersion at 25ºC (Fig. 8). The obtained spectra were analyzed with an equivalent circuit shown in **Fig. 6.17(c)**, as results were shown in **Table 6.4**. Amine SAMs modification imparted electric charge on the titanium surface, as confirmed by the elevation of the capacitance and reduction in the resistance of the surface layer. Chemisorption (electrical adsorption) of the NPs was confirmed as the heightened resistance and lowered capacitance of the surface layer (including SAM and NPs). The higher resistance of spin-coated NPs than that of the solution-adsorbed NPs is due to the higher concentration of the NPs in the surface layer on spin-coated samples. EIS is quite a good approach for analyzing interfacial properties to get an insight into the interactions occurring at the surface-NPs interface. In the impedance plot, the high-frequency region depicts a semicircle preceded by a Warburg line in the low-frequency region, signifying the diffusion phase of the process. Warburg line was used to quantify the diffusion and the attachment process at the titanium surface. Song *et al.* fabricated an immunosensor based on the functionalized chitosan nanocomposite. Resistance of the glassy carbon electrode (GCE) decreased after the deposition of the gold layer due to the conductive properties of the deposition. R_{et} further decreased after deposition of the Pb but decreased post-fabrication of the chitosan-based nanocomposite on the GCE[438]. Hazhir *et al.* also utilized EIS based approach for the electrochemical sensing of the analyte by the change in the surface current. The electron transfer capability of variously modified electrodes was investigated by EIS. The charge transfer resistance (R_{ct}) was as follows in the descending order: glassy carbon-iron oxide ($336\ \Omega$) > glassy carbon [GC] ($126\ \Omega$) > reduced graphene oxide/GC ($55\ \Omega$) > iron oxide/reduced graphene/GC ($37.6\ \Omega$) and post addition of the analyte [439].

Indian Institute of Technology Guwahati

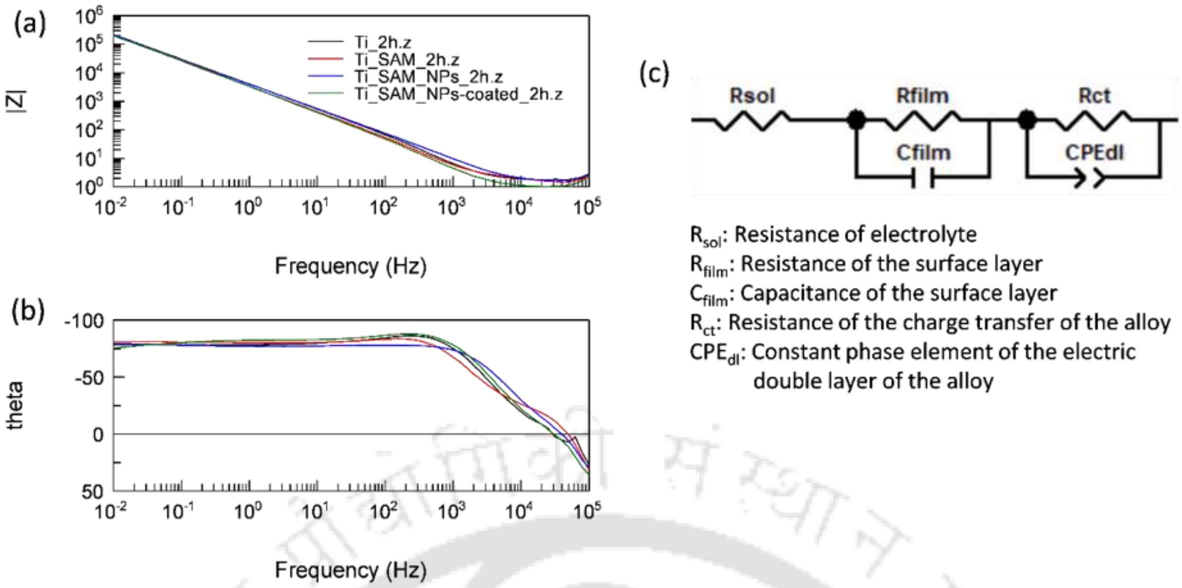

Figure 6.17: EIS spectra (a,b) of NPs-coated Ti foil and an equivalent circuit model (c) used for analysis.

Table 6.4: Parameters of EIS analysis with an equivalent circuit model

Sample	**R_{sol} [Ω.cm^{-2}]**	**R_{film} [Ω.cm^{-2}]**	**C_{film} [x10^{-5}F.cm^{-2}]**	**R_{ct} [x10^{6}Ω.cm^{-2}]**	**CPE_{dl}-T [x10^{-5}F.s^{P-1}.cm^{-2}]**	**CPE_{dl}-P**
Ti	1.19±0.69	1439±747	9.06±1.70	1.06±0.42	5.87±0.67	0.974
Ti+SAMs	1.56±0.12	212±22	29.75±5.82	3.71±2.39	6.41±0.63	0.915
Ti+SAMs+NPs	1.01±0.77	614±666	14.1±13.36	65.79±88.67	3.70±2.28	0.925
Ti+SAMs+NPs-coated	1.21±0.29	1026±15	13.69±7.42	2.80±2.79	4.35±2.55	0956

6.8 Conclusion

Chitosan NPs (HMW and LMW) were successfully fabricated using an ionotropic gelation method coupled with glutaraldehyde crosslinking. The fabricated NPs showed a spherical morphology, with hydrodynamic diameters of 290-360 nm for HMW NPs and 200-270 nm for LMW NPs. They were stable for up to 72 hours at room temperature. Glutaraldehyde crosslinking resulted in the formation of fluorescently active Schiff bases, with intrinsic fluorescence increasing with the molar concentration of glutaraldehyde introduced for crosslinking. Higher crosslinker molarity increased ampicillin encapsulation efficiency. Antimicrobial chitosan NPs were successfully attached to the surfaces of titanium and

Indian Institute of Technology Guwahati

Ti6Al4V, as confirmed by FTIR spectra. In-vitro release kinetics were performed under MQ and PBS buffer conditions, with HMW NPs showing the highest release for both pH levels. The antimicrobial activity was best against S. aureus with low molarity of the crosslinker, possibly due to better diffusion or easy disintegration/degradation of the chitosan NPs. LMW NPs with/without ampicillin showed better results. Chitosan NPs were covalently attached to the surface of Ti6Al4V discs using silane chemistry against S. aureus. Ampicillin-loaded HMW and LMW NPs showed negligible bacterial CFU, while bare HMW NPs showed a significant bacterial CFU due to slower disintegration/degradation and higher covalent crosslinking. Glutaraldehyde crosslinked NPs were biocompatible, but HMW NPs with 8mM glutaraldehyde molarity showed slightly compromised biocompatibility.

Chapter 7

Conclusion and Future Scope

This chapter focuses on the overall conclusion of the thesis including all the chapters along with the future scope.

7.1 Conclusion

Biomaterial surfaces such as silica, titanium, and Ti6Al4V were functionalized with silane-based SAMs to tune the surface properties. Silane-based SAMs of octyl-, amine-, hybrid-, carboxyl-, hexadecyl- and octadecyl- were fabricated along with the mixed SAMs of amine-octyl and hexadecyl-octyl SAMs that underwent further modification to carboxyl SAMs. Mixed SAMs incorporated the features of the silane precursors as apparent from the intermediate surface energy of the mixed SAMs, and an increase in the octyl SAMs moiety resulted in a rise in the hydrophobicity. So, the AO-, AC-, HO-, and HC- series of the mixed SAMs were explored for various parameters for surface tunability. It was observed that the equal proportions of the precursor silanes resulted in intermittent hydrophobicity and surface energy. Carboxyl SAMs with varied acidified $KMnO_4$ and incubation time showed the lowest surface energy for the 0 min sample (26.7±0.5 mJ/m^2), which increased with the incubation time for all the conc of the acidified $KMnO_4$. 5% conc incubated samples took the least saturation time, while 2%, 3%, and 4% conc incubated samples took twice the time to attain the saturation phase. Response time was also poor for the 1% conc, almost twice that for the 2%, 3% and 4% conc., while 1% conc. took 5 times the response time. It was also observed that the decrease in the CH_2 peak area is inversely proportional to the rise in the peak area due to the carboxyl group. The thickness of the various silanes was quantified and showed the highest thickness for the octadecyl SAMs surfaces and the least for the amine SAMs surfaces.

Protein adsorption studies were conducted to evaluate the trend in the secondary structure change. BSA and FBS adsorption was carried out on the AO-, AC-, HO-, and HC- series samples to investigate the change in the secondary structure. AO series showed an increase in the β-sheet and a decrease in the β-turn conformation upon increasing octyl proportionality. On the other hand, there was a decremental trend in the α-helicity and an increase in the β-sheet conformation with the increase in the carboxyl proportionality. FTIR deconvolution exhibited a decrease in the β-sheet conformation and an increase in the α-helicity for the HO series; α-helicity showed an increase with the increase in the hybrid proportionality in the HC series. FBS adsorption on the AO- and AC- series samples showed a decrease in the α- helicity but an increase in the β-turn conformation for the AO- series and β-sheet conformation for the AC-series samples. There is a slight increase in the β-sheet conformation for HO- and HC- series and a decrease in the α-helicity with increased octyl proportionality in the HO series samples and a decrease in the β-turn conformation with increased carboxyl proportionality for the HC-series. Carboxyl SAMs surfaces showed a decrease in the β-sheet structure with increased incubation time compared to octyl SAMs for 1% and 2% acidified $KMnO_4$ incubated samples. 3% incubated surfaces showed an increase in the β-sheet with an initial lag phase, while α-helicity increased, but the β-turn conformation decreased for the 5% incubated surfaces. BSA exhibited a decrease of α-helicity with the increase in the conc for the octadecyl and hexadecyl SAMs surfaces; samples adsorbed with lower BSA conc exhibited unfolding behaviour as reflected by the change in the protein conformation. α-helicity increased while the β-turn conformation decreased with the increase of the adsorbed FN conc on the hexadecyl SAMs functionalized surfaces. Mixed$_{(16\text{-}8)}$ and carboxyl$_{(16\text{-}8)}$ SAMs functionalized surfaces showed a decrease in the α-helicity and an increase in the β-turn conformation of the adsorbed BSA secondary structure.

Table 7.1: Table summarizing various surface and biological paramters

SAMs	Water Contact Angle (θ)	BSA secondary structure			Cell Adhesion parameters		
		α-helix (%)	β-sheet (%)	β-turn (%)	Surface coverage (%)	Average cell area (μm^2)	Circularity
Amine	64.6±1.4°	51.13±2.13	27.8±1.66	18.28±1.3	43.9±1.8	1502±108	0.49±0.02
Octyl	107.7±1°	51.28±1.26	35.15±1.95	10.45±1.57	22.63±0.11	753.5±70	0.61±0.04
Carboxyl	39.3±1°	53.28±3.5	39.74±1.95	5.0±2	30.4±0.26	1370±155	0.51±0.04
Hybrid	87.3±0.5°	35.6±3.3	40.35±1.24	21.46±4.2	70.2±1.6	822.7±98	0.44±0.02
Hexadecyl	114.9±2°	27.87±1.48	39.59±2.2	29.5±2.48	45.6±2.4	643.9±47	0.50±0.05

Cell adhesion studies were performed to investigate the effect of silane-based SAMs functionalization on the overall biological properties of the surfaces. Primary modification of the amine and octyl SAMs was carried out, and variations in the proportionalities of both moieties were undertaken to evaluate the best fabrication parameters. Amine and octyl were secondarily modified into hybrid and carboxyl SAMs. Amine and hybrid SAMs exhibited remarkable cell proliferation with a circularity of ~0.4, whereas carboxyl gave intermittent circularity of 0.5, and the least was ~0.6 for the octyl SAMs. Amine and hybrid SAMs with a >50% surface coverage for the 12 hour duration and high average cell area were the most desirable silane functionalities for biomaterial fabrication. Further, another silane moiety with hydrophobicity was tried for the functionalization, hexadecyl SAMs with twice the chain length of octyl SAMs. Poor biological features of the octyl and hexadecyl SAMs were attempted to be addressed by using the ECM pre-adsorption strategy. FBS pre-adsorption was tried with a circularity of ~0.4 for the octyl SAMs, indicating better cell spreading. However, the surface coverage increased to only 23.4% without FBS supplementation, compared to the bare

Ti6Al4V surfaces, a 1.5fold increase in the cell adhesion activity. Hexadecyl was subjected to single and mixed protein pre-adsorption to determine the cell adhesion activity. The best surface coverage was ~37% for Col-I, followed by BSA (~30%) and the least for the FN (~15%); a mixed system of BSA/col-I showed coverage of ~34%, introduction of the FN reduced the surface coverage but enhanced the cell proliferation of the surfaces, best being ~0.45 for the FN/Col-I system with highest concentration. Overall, BSA, Col-I, and FBS pre-adsorption addressed the hydrophobicity issue of the silanes and enhanced their overall cell adhesion properties. Various surface and biological paramters of different silane functionalized surfaces were summarized in **Table 7.1**.

Besides investigating the change in the various cell adhesion parameters, antimicrobial coatings of benign AgNPs and chitosan-based antimicrobial and drug-loading vehicles were explored. Chitosan NPs (HMW and LMW) were successfully fabricated using an ionotropic gelation method coupled with glutaraldehyde crosslinking. The fabricated NPs showed a spherical morphology, with hydrodynamic diameters of 290-360 nm for HMW NPs and 200-270 nm for LMW NPs. They were stable for up to 72 hours at room temperature. Glutaraldehyde crosslinking resulted in the formation of fluorescently active Schiff bases, with intrinsic fluorescence directly proportional to the molar concentration of glutaraldehyde introduced for crosslinking with higher crosslinker molarity increased ampicillin encapsulation efficiency. Antimicrobial chitosan NPs were successfully attached to the surfaces of titanium and Ti6Al4V, as confirmed by FTIR spectra, and *in-vitro* release kinetics were performed under MQ and PBS buffer conditions, with HMW NPs showing the highest release for both pH conditions. The antimicrobial activity was best against *S. aureus* with low molarity of the crosslinker, possibly due to better diffusion or easy disintegration/degradation of the chitosan NPs, while LMW NPs with/without ampicillin showed better results. Chitosan NPs were covalently attached to the surface of Ti6Al4V discs using silane chemistry against *S. aureus*, and ampicillin-loaded HMW and LMW NPs showed negligible bacterial CFU. In contrast, bare HMW NPs showed a significant bacterial CFU due to slower disintegration/degradation and higher covalent crosslinking. Glutaraldehyde crosslinked NPs were biocompatible, but HMW NPs with 8mM glutaraldehyde molarity showed slightly compromised biocompatibility.

7.2 Future Scope

Multi-modal drug loading inside the fabricated chitosan NPs

Chitosan-based antimicrobial coatings can target the hip prosthesis stem with two antibacterial activities: an initial phase with high efficacy and the latter phase with prolonged suppression. A combination of chitosan NPs with different molecular weights can be employed for prolonged activity. For the initial phase, antibiotics can be loaded into NPs by evaluating materials/surface biocompatibility and antibacterial activity after long-term exposure to a physiological environment, as shown in **Fig. 7.1**.

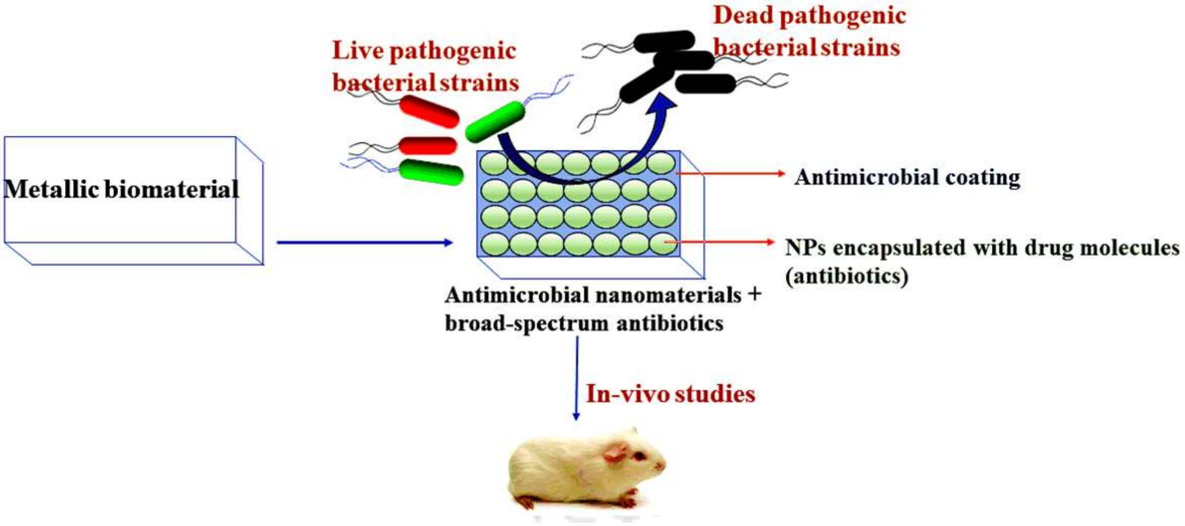

Figure 7.1: Chitosan NPs based multi-modal drug vehicle

Chitosan-based hydrogels/sponges fabrication

Patients undergoing implantation require high antibiotic dosages to prevent the spread of chance bacteria exposed to the incised site. Rather than administering high dosages of antibiotics orally in a non-specific manner, it will be quite efficient to supply the antibiotics locally by making the surface of the implant material antimicrobial in nature so antibiotic-loaded hydrogels can be fabricated to address the chance of bacterial invasion on the soft tissues. For this purpose, chitosan-based hydrogels/sponges loaded with conventional antibiotics that mimic the inner bone marrow-like structure can be tried, as shown in **Fig. 7.2**.

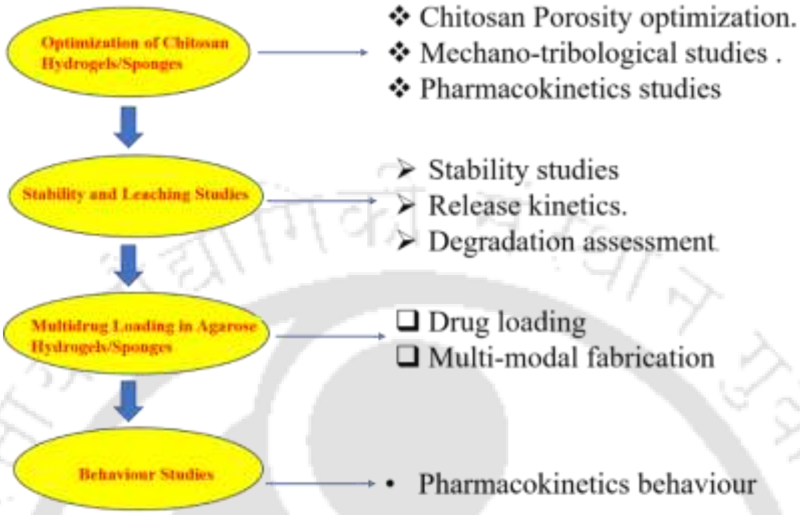

Figure 7.2: Chitosan hydrogels/sponges as antimicrobial coatings.

Indian Institute of Technology Guwahati

REFERENCES:

1. Rahmati, B., et al., *Development of tantalum oxide (Ta-O) thin film coating on biomedical Ti-6Al-4V alloy to enhance mechanical properties and biocompatibility.* Ceramics International, 2016. **42**(1): p. 466-480.
2. Hu, C., et al., *Bioinspired surface modification of orthopedic implants for bone tissue engineering.* 2019. **219**: p. 119366.
3. Jemat, A., et al., *Surface modifications and their effects on titanium dental implants.* 2015. **2015**.
4. Zhao, X., et al., *3D patterned substrates for bioartificial blood vessels–The effect of hydrogels on aligned cells on a biomaterial surface.* 2015. **26**: p. 159-168.
5. Dangas, G.D., et al., *Prosthetic heart valve thrombosis.* 2016. **68**(24): p. 2670-2689.
6. Zhang, J., et al., *Intravascular ultrasound versus angiography-guided drug-eluting stent implantation: the ULTIMATE trial.* 2018. **72**(24): p. 3126-3137.
7. Cui, Z., B. Yang, and R.-K.J.E. Li, *Application of biomaterials in cardiac repair and regeneration.* 2016. **2**(1): p. 141-148.
8. Chen, Q., G.A.J.M.S. Thouas, and E.R. Reports, *Metallic implant biomaterials.* 2015. **87**: p. 1-57.
9. Tan, F., et al., *Recent advances in the implant-based drug delivery in otorhinolaryngology.* Acta Biomater, 2020. **108**: p. 46-55.
10. Xu, C., et al., *Triggerable Degradation of Polyurethanes for Tissue Engineering Applications.* ACS Appl Mater Interfaces, 2015. **7**(36): p. 20377-88.
11. dos Santos, V., R.N. Brandalise, and M. Savaris, *Biomaterials: Characteristics and properties*, in *Engineering of Biomaterials*. 2017, Springer. p. 5-15.
12. Hadjesfandiari, N., et al., *Development of antifouling and bactericidal coatings for platelet storage bags using dopamine chemistry.* 2018. **7**(5): p. 1700839.
13. Pacelli, S., et al., *Tailoring biomaterial surface properties to modulate host-implant interactions: implication in cardiovascular and bone therapy.* 2016. **4**(9): p. 1586-1599.
14. Augustine, R., et al., *Electrospun poly(vinylidene fluoride-trifluoroethylene)/zinc oxide nanocomposite tissue engineering scaffolds with enhanced cell adhesion and blood vessel formation.* Nano Research, 2017. **10**(10): p. 3358-3376.
15. He, J., et al., *Microstructure and tribological properties of in-situ synthesized TiC reinforced reactive plasma sprayed Co-based coatings.* Materials Chemistry and Physics, 2020. **248**: p. 122913.
16. Kruchinin, V.N., et al., *Optical Properties of TiO2 Films Deposited by Reactive Electron Beam Sputtering.* Journal of Electronic Materials, 2017. **46**(10): p. 6089-6095.
17. Bagheri, H., et al., *Facile fabrication of uniform hierarchical structured (UHS) nanocomposite surface with high water repellency and self-cleaning properties.* Applied Surface Science, 2018. **436**: p. 1134-1146.
18. Li, J., et al., *Hydrodynamic control of titania nanotube formation on Ti-6Al-4V alloys enhances osteogenic differentiation of human mesenchymal stromal cells.* Materials Science and Engineering: C, 2020. **109**: p. 110562.
19. Hasan, A., S.K. Pattanayek, and L.M. Pandey, *Effect of Functional Groups of Self-Assembled Monolayers on Protein Adsorption and Initial Cell Adhesion.* ACS Biomaterials Science & Engineering, 2018. **4**(9): p. 3224-3233.
20. Graziani, G., et al., *Fabrication and characterization of biomimetic hydroxyapatite thin films for bone implants by direct ablation of a biogenic source.* Materials Science and Engineering: C, 2019. **99**: p. 853-862.
21. Zhang, X., et al., *Laser cladding of manganese oxide doped aluminum oxide granules on titanium alloy for biomedical applications.* Applied Surface Science, 2020. **520**: p. 146304.
22. Cheung, D.L. and K.H.A. Lau, *Atomistic Study of Zwitterionic Peptoid Antifouling Brushes.* Langmuir, 2019. **35**(5): p. 1483-1494.

23. Constantino, J.C.P., et al., *Development of functional TiO2 coatings deposited on cementitious materials.* Construction and Building Materials, 2020. **250**: p. 118732.
24. Bundesmann, C. and T. Amelal, *Secondary particle properties for the ion beam sputtering of TiO2 in a reactive oxygen atmosphere.* Applied Surface Science, 2019. **485**: p. 391-401.
25. Correa, D.R.N., et al., *Development of Ti-15Zr-Mo alloys for applying as implantable biomedical devices.* Journal of Alloys and Compounds, 2018. **749**: p. 163-171.
26. Bagherifard, S., et al., *Nanoscale surface modification of AISI 316L stainless steel by severe shot peening.* Materials & Design, 2016. **102**: p. 68-77.
27. Nnamchi, P.S., *First principles studies on structural, elastic and electronic properties of new Ti Mo Nb Zr alloys for biomedical applications.* Materials & Design, 2016. **108**: p. 60-67.
28. Alemón, B., et al., *Tribocorrosion behavior and ions release of CoCrMo alloy coated with a TiAlVCN/CNx multilayer in simulated body fluid plus bovine serum albumin.* Tribology International, 2015. **81**: p. 159-168.
29. Gilbert, J.L., et al., *Direct in vivo inflammatory cell-induced corrosion of CoCrMo alloy orthopedic implant surfaces.* J Biomed Mater Res A, 2015. **103**(1): p. 211-23.
30. Ren, Y., et al., *Rapid coating of AZ31 magnesium alloy with calcium deficient hydroxyapatite using microwave energy.* Mater Sci Eng C Mater Biol Appl, 2015. **49**: p. 364-372.
31. Jain, A. and V. Bajpai, *Mechanical micro-texturing and characterization on Ti6Al4V for the improvement of surface properties.* Surface and Coatings Technology, 2019. **380**.
32. Lucas, E.J., et al., *Comparison of the microbiological milieu of patients randomized to either hydrophilic or conventional PVC catheters for clean intermittent catheterization.* 2016. **12**(3): p. 172. e1-172. e8.
33. Shahemi, N., et al., *Long-term wear failure analysis of uhmwpe acetabular cup in total hip replacement.* 2018. **87**: p. 1-9.
34. López-Saucedo, F., et al., *Antimicrobial silver-loaded polypropylene sutures modified by radiation-grafting.* 2018. **100**: p. 290-297.
35. Ko, J., et al., *Hydrophilic surface modification of poly (methyl methacrylate)-based ocular prostheses using poly (ethylene glycol) grafting.* 2017. **158**: p. 287-294.
36. Kondyurina, I., et al., *Urinary catheter with polyurethane coating modified by ion implantation.* 2015. **342**: p. 39-46.
37. Mondal, D., et al., *Polycaprolactone-based biomaterials for tissue engineering and drug delivery: Current scenario and challenges.* 2016. **65**(5): p. 255-265.
38. Narayanan, G., et al., *Poly (lactic acid)-based biomaterials for orthopaedic regenerative engineering.* 2016. **107**: p. 247-276.
39. Adamzyk, C., et al., *Bone tissue engineering using polyetherketoneketone scaffolds combined with autologous mesenchymal stem cells in a sheep calvarial defect model.* J Craniomaxillofac Surg, 2016. **44**(8): p. 985-94.
40. Davenport Huyer, L., et al., *Highly elastic and moldable polyester biomaterial for cardiac tissue engineering applications.* 2016. **2**(5): p. 780-788.
41. Behera, R.R., et al., *Laser cladding with HA and functionally graded TiO2-HA precursors on Ti–6Al–4V alloy for enhancing bioactivity and cyto-compatibility.* Surface and Coatings Technology, 2018. **352**: p. 420-436.
42. Behera, R.R., et al., *Mechano-tribological properties and in vitro bioactivity of biphasic calcium phosphate coating on Ti-6Al-4V.* J Mech Behav Biomed Mater, 2018. **86**: p. 143-157.
43. Ginebra, M.-P., et al., *Bioceramics and bone healing.* 2018. **3**(5): p. 173-183.
44. Bose, S., D. Banerjee, and A. Bandyopadhyay, *Introduction to biomaterials and devices for bone disorders*, in *Materials for Bone Disorders*. 2017, Elsevier. p. 1-27.
45. Behera, S.S., et al., *Chitosan/TiO2 composite membrane improves proliferation and survival of L929 fibroblast cells: Application in wound dressing and skin regeneration.* Int J Biol Macromol, 2017. **98**: p. 329-340.

46. Borkowski, L., et al., *Effect of a carbonated HAP/beta-glucan composite bone substitute on healing of drilled bone voids in the proximal tibial metaphysis of rabbits.* Mater Sci Eng C Mater Biol Appl, 2015. **53**: p. 60-7.
47. Harb, S.V., et al., *PMMA-silica nanocomposite coating: Effective corrosion protection and biocompatibility for a Ti6Al4V alloy.* Mater Sci Eng C Mater Biol Appl, 2020. **110**: p. 110713.
48. Schierano, G., et al., *An alumina toughened zirconia composite for dental implant application: in vivo animal results.* 2015. **2015**.
49. Yang, H., et al., *In vitro and in vivo studies on zinc-hydroxyapatite composites as novel biodegradable metal matrix composite for orthopedic applications.* 2018. **71**: p. 200-214.
50. Nnamchi, P.S., et al., *Mechanical and electrochemical characterisation of new Ti-Mo-Nb-Zr alloys for biomedical applications.* J Mech Behav Biomed Mater, 2016. **60**: p. 68-77.
51. Santos, P.F., et al., *Microstructures, mechanical properties and cytotoxicity of low cost beta Ti-Mn alloys for biomedical applications.* Acta Biomater, 2015. **26**: p. 366-76.
52. Xie, F., et al., *Selective laser sintered porous Ti–(4–10)Mo alloys for biomedical applications: Structural characteristics, mechanical properties and corrosion behaviour.* Corrosion Science, 2015. **95**: p. 117-124.
53. Costa, B.C., et al., *Vanadium ionic species from degradation of Ti-6Al-4V metallic implants: In vitro cytotoxicity and speciation evaluation.* Mater Sci Eng C Mater Biol Appl, 2019. **96**: p. 730-739.
54. Neacsu, P., et al., *In vitro performance assessment of new beta Ti-Mo-Nb alloy compositions.* Mater Sci Eng C Mater Biol Appl, 2015. **47**: p. 105-13.
55. Toptan, F., et al., *Corrosion and tribocorrosion behavior of Ti-B4C composite intended for orthopaedic implants.* J Mech Behav Biomed Mater, 2016. **61**: p. 152-163.
56. Jamrozik, M.K., et al., *Technological capabilities of surface layers formation on implant made of Ti-6Al-4V ELI alloy.* Acta of Bioengineering and Biomechanics, 2015. **17**(1): p. 31-37.
57. Kumar, D., et al., *Tribological performance of laser peened Ti–6Al–4V.* Wear, 2015. **322-323**: p. 203-217.
58. Samanta, A., et al., *Nano- and micro-tribological behaviours of plasma nitrided Ti6Al4V alloys.* J Mech Behav Biomed Mater, 2018. **77**: p. 267-294.
59. Wang, G., et al., *Surface thermal oxidation on titanium implants to enhance osteogenic activity and in vivo osseointegration.* 2016. **6**: p. 31769.
60. Khanlou, H.M., et al., *Prediction and characterization of surface roughness using sandblasting and acid etching process on new non-toxic titanium biomaterial: adaptive-network-based fuzzy inference System.* 2015. **26**(7): p. 1751-1761.
61. Nouri, A. and C. Wen, *Introduction to surface coating and modification for metallic biomaterials*, in *Surface Coating and Modification of Metallic Biomaterials*. 2015, Elsevier. p. 3-60.
62. Hasan, A., V. Saxena, and L.M. Pandey, *Surface Functionalization of Ti6Al4V via Self-assembled Monolayers for Improved Protein Adsorption and Fibroblast Adhesion.* Langmuir, 2018.
63. Van Hooreweder, B., et al., *Improving the fatigue performance of porous metallic biomaterials produced by Selective Laser Melting.* Acta Biomater, 2017. **47**: p. 193-202.
64. Bobbert, F.S.L., et al., *Additively manufactured metallic porous biomaterials based on minimal surfaces: A unique combination of topological, mechanical, and mass transport properties.* Acta Biomater, 2017. **53**: p. 572-584.
65. Biesiekierski, A., et al., *Investigations into Ti-(Nb,Ta)-Fe alloys for biomedical applications.* Acta Biomater, 2016. **32**: p. 336-347.
66. Cifuentes, S.C., et al., *In vitro degradation of biodegradable polylactic acid/magnesium composites: Relevance of Mg particle shape.* Acta Biomater, 2016. **32**: p. 348-357.
67. Tang, H. and Y. Gao, *Preparation and characterization of hydroxyapatite containing coating on AZ31 magnesium alloy by micro-arc oxidation.* Journal of Alloys and Compounds, 2016. **688**: p. 699-708.

68. Bian, D., et al., *Fatigue behaviors of HP-Mg, Mg-Ca and Mg-Zn-Ca biodegradable metals in air and simulated body fluid.* Acta Biomater, 2016. **41**: p. 351-60.
69. Jang, Y., et al., *Understanding corrosion behavior of Mg-Zn-Ca alloys from subcutaneous mouse model: effect of Zn element concentration and plasma electrolytic oxidation.* Mater Sci Eng C Mater Biol Appl, 2015. **48**: p. 28-40.
70. Khoshakhlagh, P., et al., *Development and characterization of a bioglass/chitosan composite as an injectable bone substitute.* Carbohydr Polym, 2017. **157**: p. 1261-1271.
71. Ren, K., et al., *Electrospun PCL/gelatin composite nanofiber structures for effective guided bone regeneration membranes.* Mater Sci Eng C Mater Biol Appl, 2017. **78**: p. 324-332.
72. Barrioni, B.R., et al., *Synthesis and characterization of biodegradable polyurethane films based on HDI with hydrolyzable crosslinked bonds and a homogeneous structure for biomedical applications.* Mater Sci Eng C Mater Biol Appl, 2015. **52**: p. 22-30.
73. Hasan, A. and L.M. Pandey, *Polymers, surface-modified polymers, and self assembled monolayers as surface-modifying agents for biomaterials.* Polymer-Plastics Technology and Engineering, 2015. **54**(13): p. 1358-1378.
74. Vergnol, G., et al., *In vitro and in vivo evaluation of a polylactic acid-bioactive glass composite for bone fixation devices.* J Biomed Mater Res B Appl Biomater, 2016. **104**(1): p. 180-91.
75. Gao, X., et al., *Polydopamine-Templated Hydroxyapatite Reinforced Polycaprolactone Composite Nanofibers with Enhanced Cytocompatibility and Osteogenesis for Bone Tissue Engineering.* ACS Appl Mater Interfaces, 2016. **8**(5): p. 3499-515.
76. Manavitehrani, I., et al., *Reinforced Poly(Propylene Carbonate) Composite with Enhanced and Tunable Characteristics, an Alternative for Poly(lactic Acid).* ACS Appl Mater Interfaces, 2015. **7**(40): p. 22421-30.
77. Hench, L.L.J.J.o.M.S.M.i.M., *The future of bioactive ceramics.* 2015. **26**(2): p. 86.
78. Piconi, C. *Bioinert ceramics: State-of-the-art*. in *Key Engineering Materials*. 2017. Trans Tech Publ.
79. Vallet-Regí, M. and A.J. Salinas, *Ceramics as bone repair materials*, in *Bone repair biomaterials*. 2019, Elsevier. p. 141-178.
80. Monsees, T.K., et al., *Biodegradable ceramics consisting of hydroxyapatite for orthopaedic implants.* 2017. **7**(11): p. 184.
81. Alkharrat, A.R., et al., *Fracture behavior of all-ceramic, implant-supported, and tooth–implant-supported fixed dental prostheses.* 2018. **22**(4): p. 1663-1673.
82. Chen, Y.-W., et al., *Zirconia in biomedical applications.* 2016. **13**(10): p. 945-963.
83. Elsayed, A., et al., *Comparison of fracture strength and failure mode of different ceramic implant abutments.* 2017. **117**(4): p. 499-506.
84. Baino, F.J.M.L., *Porous glass-ceramic orbital implants: A feasibility study.* 2018. **212**: p. 12-15.
85. Kammermeier, A., et al., *In vitro performance of one-and two-piece zirconia implant systems for anterior application.* 2016. **53**: p. 94-101.
86. Ünal, M., O. Akkuş, and R.E. Marcus, *Fundamentals of musculoskeletal biomechanics*, in *Musculoskeletal research and basic science*. 2016, Springer. p. 15-36.
87. Ali, W., et al., *Effect of fluoride coating on degradation behaviour of unidirectional Mg/PLA biodegradable composite for load-bearing bone implant application.* 2019. **124**: p. 105464.
88. Vallittu, P.K.J.C.O.H.R., *Fiber-Reinforced Composites for Implant Applications.* 2018. **5**(3): p. 194-201.
89. Janićijević, Ž., et al., *Poly (DL-Lactide-co-ε-Caprolactone)/Poly (Acrylic Acid) Composite Implant for Controlled Delivery of Cationic Drugs.* 2019. **19**(2): p. 1800322.
90. Yan, H., et al., *A novel and homogeneous scaffold material: preparation and evaluation of alginate/bacterial cellulose nanocrystals/collagen composite hydrogel for tissue engineering.* 2018. **75**(3): p. 985-1000.

91. Bohnenberger, T. and U.J.T.s.f. Schmid, *Layer-by-layer approach for deposition of pure carbon nanotubes and composite films for use as electrodes in electrochemical devices.* 2014. **565**: p. 116-121.
92. Majoni, S. and A.J.T.A. Chaparadza, *Thermal degradation kinetic study of polystyrene/organophosphate composite.* 2018. **662**: p. 8-15.
93. Da, L., et al., *Composite elastomeric polyurethane scaffolds incorporating small intestinal submucosa for soft tissue engineering.* Acta Biomater, 2017. **59**: p. 45-57.
94. Hart, L.R., et al., *3D Printing of Biocompatible Supramolecular Polymers and their Composites.* ACS Appl Mater Interfaces, 2016. **8**(5): p. 3115-22.
95. Hasan, A., et al., *Nano-biocomposite scaffolds of chitosan, carboxymethyl cellulose and silver nanoparticle modified cellulose nanowhiskers for bone tissue engineering applications.* International Journal of Biological Macromolecules, 2018. **111**: p. 923-934.
96. Hasan, A., et al., *Fabrication and characterization of chitosan, polyvinylpyrrolidone, and cellulose nanowhiskers nanocomposite films for wound healing drug delivery application.* Journal of Biomedical Materials Research Part A, 2017. **105**(9): p. 2391-2404.
97. Hotchkiss, K.M., et al., *Titanium surface characteristics, including topography and wettability, alter macrophage activation.* Acta Biomater, 2016. **31**: p. 425-434.
98. Shao, D., et al., *Macrophage polarization by plasma sprayed ceria coatings on titanium-based implants: Cerium valence state matters.* Applied Surface Science, 2020. **504**: p. 144070.
99. Geesala, R., et al., *Porous polymer scaffold for on-site delivery of stem cells--Protects from oxidative stress and potentiates wound tissue repair.* Biomaterials, 2016. **77**: p. 1-13.
100. Rahimizadeh, A., et al., *Porous architected biomaterial for a tibial-knee implant with minimum bone resorption and bone-implant interface micromotion.* 2018. **78**: p. 465-479.
101. Cai, X.Y., et al., *Biomimetic anchors applied to the host-guest antifouling functionalization of titanium substrates.* J Colloid Interface Sci, 2016. **475**: p. 8-16.
102. Hasan, A., G. Waibhaw, and L.M.J.L. Pandey, *Conformational and organizational insights into serum proteins during competitive adsorption on self-assembled monolayers.* 2018. **34**(28): p. 8178-8194.
103. Hasan, A. and L.M. Pandey, *Surface modification of Ti6Al4V by forming hybrid self-assembled monolayers and its effect on collagen-I adsorption, osteoblast adhesion and integrin expression.* Applied Surface Science, 2020. **505**: p. 144611.
104. Chakraborty, R., et al., *Synthesis of calcium hydrogen phosphate and hydroxyapatite coating on SS316 substrate through pulsed electrodeposition.* Mater Sci Eng C Mater Biol Appl, 2016. **69**: p. 875-83.
105. Parmar, V., et al., *Oxidation facilitated antimicrobial ability of laser micro-textured titanium alloy against gram-positive Staphylococcus aureus for biomedical applications.* Journal of Laser Applications, 2018. **30**(3).
106. Bock, R.M., et al., *Surface modulation of silicon nitride ceramics for orthopaedic applications.* Acta Biomater, 2015. **26**: p. 318-30.
107. Fazel Anvari-Yazdi, A., et al., *Cytotoxicity assessment of adipose-derived mesenchymal stem cells on synthesized biodegradable Mg-Zn-Ca alloys.* Mater Sci Eng C Mater Biol Appl, 2016. **69**: p. 584-97.
108. Behera, R.R., et al., *Deposition of biphasic calcium phosphate film on laser surface textured Ti–6Al–4V and its effect on different biological properties for orthopedic applications.* Journal of Alloys and Compounds, 2020. **842**: p. 155683.
109. Behera, R.R., et al., *Effect of TiO2 addition on adhesion and biological behavior of BCP-TiO2 composite films deposited by magnetron sputtering.* Materials Science and Engineering: C, 2020. **114**: p. 111033.
110. Pradhan, D., et al., *Investigating the structure and biocompatibility of niobium and titanium oxides as coatings for orthopedic metallic implants.* Mater Sci Eng C Mater Biol Appl, 2016. **58**: p. 918-26.

111. Goncalves, A.I., et al., *Exploring the Potential of Starch/Polycaprolactone Aligned Magnetic Responsive Scaffolds for Tendon Regeneration.* Adv Healthc Mater, 2016. **5**(2): p. 213-22.

112. Cheng, S., et al., *Self-Adjusting, Polymeric Multilayered Roll that can Keep the Shapes of the Blood Vessel Scaffolds during Biodegradation.* Adv Mater, 2017. **29**(28).

113. Buyuksungur, S., et al., *3D printed poly(epsilon-caprolactone) scaffolds modified with hydroxyapatite and poly(propylene fumarate) and their effects on the healing of rabbit femur defects.* Biomater Sci, 2017. **5**(10): p. 2144-2158.

114. Ashley-Koch, A., Q. Yang, and R.S.J.A.j.o.e. Olney, *Sickle hemoglobin (Hb S) allele and sickle cell disease: a HuGE review.* 2000. **151**(9): p. 839-845.

115. Pelton, J.T. and L.R.J.A.b. McLean, *Spectroscopic methods for analysis of protein secondary structure.* 2000. **277**(2): p. 167-176.

116. Wedemeyer, W.J., et al., *Disulfide bonds and protein folding.* 2000. **39**(15): p. 4207-4216.

117. Huber, R., *Conformational flexibility and its functional significance in some protein molecules*, in *Biological Functions of Proteinases*. 1979, Springer. p. 1-16.

118. D'Imprima, E., et al., *Protein denaturation at the air-water interface and how to prevent it.* Elife, 2019. **8**: p. e42747.

119. Xu, L.-C. and C.A. Siedlecki, *Effects of surface wettability and contact time on protein adhesion to biomaterial surfaces.* Biomaterials, 2007. **28**(22): p. 3273-3283.

120. Lee, C.H., A. Singla, and Y. Lee, *Biomedical applications of collagen.* International journal of pharmaceutics, 2001. **221**(1-2): p. 1-22.

121. Mithieux, S.M. and A.S. Weiss, *Elastin*, in *Advances in protein chemistry*. 2005, Elsevier. p. 437-461.

122. Pankov, R. and K.M. Yamada, *Fibronectin at a glance.* Journal of cell science, 2002. **115**(20): p. 3861-3863.

123. Mosesson, M., *Fibrinogen and fibrin structure and functions.* Journal of Thrombosis and Haemostasis, 2005. **3**(8): p. 1894-1904.

124. Weisel, J.W., *Fibrinogen and fibrin*, in *Advances in protein chemistry*. 2005, Elsevier. p. 247-299.

125. Gray, J.J., *The interaction of proteins with solid surfaces.* Current opinion in structural biology, 2004. **14**(1): p. 110-115.

126. Schmidt, D.R., H. Waldeck, and W.J. Kao, *Protein adsorption to biomaterials*, in *Biological interactions on materials surfaces*. 2009, Springer. p. 1-18.

127. Ulmschneider, M.B. and M.S. Sansom, *Amino acid distributions in integral membrane protein structures.* Biochimica et Biophysica Acta (BBA)-Biomembranes, 2001. **1512**(1): p. 1-14.

128. Dawes, H., et al., *Protein instability of wines: Influence of protein isoelectric point.* American Journal of Enology and Viticulture, 1994. **45**(3): p. 319-326.

129. Rabe, M., D. Verdes, and S. Seeger, *Understanding protein adsorption phenomena at solid surfaces.* Advances in colloid and interface science, 2011. **162**(1-2): p. 87-106.

130. Roach, P., D. Farrar, and C.C. Perry, *Interpretation of protein adsorption: surface-induced conformational changes.* Journal of the American Chemical Society, 2005. **127**(22): p. 8168-8173.

131. Lee, M.H., et al., *Effect of biomaterial surface properties on fibronectin–α5β1 integrin interaction and cellular attachment.* Biomaterials, 2006. **27**(9): p. 1907-1916.

132. Wang, Y.-X., et al., *Effects of the chemical structure and the surface properties of polymeric biomaterials on their biocompatibility.* Pharmaceutical research, 2004. **21**(8): p. 1362-1373.

133. Hallab, N.J., et al., *Evaluation of metallic and polymeric biomaterial surface energy and surface roughness characteristics for directed cell adhesion.* Tissue engineering, 2001. **7**(1): p. 55-71.

134. Karplus, M. and J. Kuriyan, *Molecular dynamics and protein function.* Proceedings of the National Academy of Sciences, 2005. **102**(19): p. 6679-6685.

135. Ansari, A., et al., *The role of solvent viscosity in the dynamics of protein conformational changes.* Science, 1992. **256**(5065): p. 1796-1798.

136. Ramsden, J.J., *Experimental methods for investigating protein adsorption kinetics at surfaces.* Quarterly reviews of biophysics, 1994. **27**(1): p. 41-105.
137. Satulovsky, J., M. Carignano, and I. Szleifer, *Kinetic and thermodynamic control of protein adsorption.* Proceedings of the National Academy of Sciences, 2000. **97**(16): p. 9037-9041.
138. Lee, R.G. and S.W. Kim, *Adsorption of proteins onto hydrophobic polymer surfaces: adsorption isotherms and kinetics.* Journal of biomedical materials research, 1974. **8**(5): p. 251-259.
139. Russell, S.M. and G. Carta, *Multicomponent protein adsorption in supported cationic polyacrylamide hydrogels.* AIChE journal, 2005. **51**(9): p. 2469-2480.
140. Hirsh, S.L., et al., *The Vroman effect: competitive protein exchange with dynamic multilayer protein aggregates.* Colloids and Surfaces B: Biointerfaces, 2013. **103**: p. 395-404.
141. Noh, H. and E.A. Vogler, *Volumetric interpretation of protein adsorption: competition from mixtures and the Vroman effect.* Biomaterials, 2007. **28**(3): p. 405-422.
142. van der Veen, M., M.C. Stuart, and W. Norde, *Spreading of proteins and its effect on adsorption and desorption kinetics.* Colloids and Surfaces B: Biointerfaces, 2007. **54**(2): p. 136-142.
143. Fang, F., J. Satulovsky, and I. Szleifer, *Kinetics of protein adsorption and desorption on surfaces with grafted polymers.* Biophysical journal, 2005. **89**(3): p. 1516-1533.
144. Herranz-Diez, C., et al., *Mechanical and physicochemical characterization along with biological interactions of a new Ti25Nb21Hf alloy for bone tissue engineering.* J Biomater Appl, 2015. **30**(2): p. 171-81.
145. Hasan, A., V. Saxena, and L.M.J.L. Pandey, *Surface functionalization of Ti6Al4V via self-assembled monolayers for improved protein adsorption and fibroblast adhesion.* 2018. **34**(11): p. 3494-3506.
146. Khoshnood, N., A. Zamanian, and A. Massoudi, *Effect of silane-coupling modification on bioactivity and in vitro properties of anodized titania nanotube arrays.* Materials Letters, 2016. **185**: p. 374-+.
147. Zhang, H., et al., *Macrophage polarization, inflammatory signaling, and NF-kappaB activation in response to chemically modified titanium surfaces.* Colloids Surf B Biointerfaces, 2018. **166**: p. 269-276.
148. Rodriguez-Contreras, A., et al., *Modification of titanium surfaces by adding antibiotic-loaded PHB spheres and PEG for biomedical applications.* J Mater Sci Mater Med, 2016. **27**(8): p. 124.
149. Chen, Q., et al., *Modification of titanium surfaces via surface-initiated atom transfer radical polymerization to graft PEG-RGD polymer brushes to inhibit bacterial adhesion and promote osteoblast cell attachment.* Journal of Wuhan University of Technology-Mater. Sci. Ed., 2017. **32**(5): p. 1225-1231.
150. Chouirfa, H., et al., *Review of titanium surface modification techniques and coatings for antibacterial applications.* Acta Biomater, 2019. **83**: p. 37-54.
151. Pawlik, A., et al., *Surface modification of nanoporous anodic titanium dioxide layers for drug delivery systems and enhanced SAOS-2 cell response.* Colloids Surf B Biointerfaces, 2018. **171**: p. 58-66.
152. Hasan, A. and L.M. Pandey, *Surface modification of Ti6Al4V by forming hybrid self-assembled monolayers and its effect on collagen-I adsorption, osteoblast adhesion and integrin expression.* Applied Surface Science, 2019.
153. Staehlke, S., et al., *Terminal chemical functions of polyamidoamine dendrimer surfaces and its impact on bone cell growth.* Mater Sci Eng C Mater Biol Appl, 2019. **101**: p. 190-203.
154. Santos, F.S.F.d., et al., *PEEK Physical Surface Modification: Evaluation Of Particles Leaching Process.* 2019. **22**(2).
155. Fernández-Yagüe, M., et al., *Enhanced osteoconductivity on electrically charged titanium implants treated by physicochemical surface modifications methods.* 2019. **18**: p. 1-10.
156. Mas-Moruno, C., B. Su, and M.J.J.A.h.m. Dalby, *Multifunctional coatings and nanotopographies: Toward cell instructive and antibacterial implants.* 2019. **8**(1): p. 1801103.

157. Zhou, L., et al., *Biofunctionalization of microgroove titanium surfaces with an antimicrobial peptide to enhance their bactericidal activity and cytocompatibility.* Colloids Surf B Biointerfaces, 2015. **128**: p. 552-560.

158. Araujo-Gomes, N., et al., *Characterization of serum proteins attached to distinct sol-gel hybrid surfaces.* J Biomed Mater Res B Appl Biomater, 2018. **106**(4): p. 1477-1485.

159. Trino, L.D., et al., *Zinc oxide surface functionalization and related effects on corrosion resistance of titanium implants.* Ceramics International, 2018. **44**(4): p. 4000-4008.

160. Muller, W.E.G., et al., *Biologizing titanium alloy implant material with morphogenetically active polyphosphate.* Rsc Advances, 2015. **5**(92): p. 75465-75473.

161. Beline, T., et al., *Production of a biofunctional titanium surface using plasma electrolytic oxidation and glow-discharge plasma for biomedical applications.* Biointerphases, 2016. **11**(1): p. 011013.

162. Yang, C.H., et al., *Oxygen plasma immersion ion implantation treatment enhances the human bone marrow mesenchymal stem cells responses to titanium surface for dental implant application.* Clin Oral Implants Res, 2015. **26**(2): p. 166-75.

163. Patelli, A., et al., *Nanoroughness, Surface Chemistry, and Drug Delivery Control by Atmospheric Plasma Jet on Implantable Devices.* ACS Appl Mater Interfaces, 2018. **10**(46): p. 39512-39523.

164. Huang, X., et al., *Cytocompatibility of Titanium Microsphere-Based Surfaces.* ACS Biomaterials Science & Engineering, 2017. **3**(12): p. 3254-3260.

165. Qin, J., et al., *Micro- and nano-structured 3D printed titanium implants with a hydroxyapatite coating for improved osseointegration.* J Mater Chem B, 2018. **6**(19): p. 3136-3144.

166. Lu, R., et al., *Effects of hydrogenated TiO2 nanotube arrays on protein adsorption and compatibility with osteoblast-like cells.* Int J Nanomedicine, 2018. **13**: p. 2037-2049.

167. Mu, P., et al., *High-Throughput Screening of Rat Mesenchymal Stem Cell Behavior on Gradient TiO2 Nanotubes.* ACS Biomaterials Science & Engineering, 2018. **4**(8): p. 2804-2814.

168. Ulasevich, S.A., et al., *Photocatalytic Deposition of Hydroxyapatite onto a Titanium Dioxide Nanotubular Layer with Fine Tuning of Layer Nanoarchitecture.* Langmuir, 2016. **32**(16): p. 4016-21.

169. Zhu, L., et al., *Fabrication of the Silicate Containing CaTiO₃ Film with Hydrophilic and Smooth Surface on Titanium to Improve Osteoconductivity.* Materials Transactions, 2019. **60**(9): p. 1807-1813.

170. Li, S., et al., *Evaluation of highly carbonated hydroxyapatite bioceramic implant coatings with hierarchical micro-/nanorod topography optimized for osseointegration.* Int J Nanomedicine, 2018. **13**: p. 3643-3659.

171. Yuan, Z., et al., *Investigation of osteogenic responses of Fe-incorporated micro/nano-hierarchical structures on titanium surfaces.* J Mater Chem B, 2018. **6**(9): p. 1359-1372.

172. Delgado, A.H. and A.M. Young, *Modelling ATR-FTIR Spectra of Dental Bonding Systems to Investigate Composition and Polymerisation Kinetics.* 2021. **14**(4): p. 760.

173. Lorenzetti, M., et al., *Surface properties of nanocrystalline TiO2 coatings in relation to the in vitro plasma protein adsorption.* Biomed Mater, 2015. **10**(4): p. 045012.

174. Iwasa, F., K. Baba, and T. Ogawa, *Enhanced intracellular signaling pathway in osteoblasts on ultraviolet lighttreated hydrophilic titanium.* Biomedical Research, 2016. **37**(1): p. 1-11

175. Huang, Q., et al., *The development of Cu-incorporated micro/nano-topographical bio-ceramic coatings for enhanced osteoblast response.* Applied Surface Science, 2019. **465**: p. 575-583.

176. Cei, S., et al., *Protein adsorption on a laser-modified titanium implant surface.* Implant Dent, 2015. **24**(2): p. 134-41.

177. Zheng, G., et al., *Topographical cues of direct metal laser sintering titanium surfaces facilitate osteogenic differentiation of bone marrow mesenchymal stem cells through epigenetic regulation.* Cell Prolif, 2018. **51**(4): p. e12460.

178. Khandaker, M., et al., *Effect of Collagen-Polycaprolactone Nanofibers Matrix Coating on the In Vitro Cytocompatibility and In Vivo Bone Responses of Titanium.* J Med Biol Eng, 2018. **38**(2): p. 197-210.
179. Fukuhara, Y., et al., *Phospholipid polymer electrodeposited on titanium inhibits platelet adhesion.* J Biomed Mater Res B Appl Biomater, 2016. **104**(3): p. 554-60.
180. Vyas, V., et al., *Biofunctionalization of commercially pure titanium with chitosan/hydroxyapatite biocomposite via silanization: evaluation of biological performances.* Journal of Adhesion Science and Technology, 2017. **31**(16): p. 1768-1781.
181. Hasan, A., G. Waibhaw, and L.M. Pandey, *Conformational and Organizational Insights into Serum Proteins during Competitive Adsorption on Self-Assembled Monolayers.* Langmuir, 2018. **34**(28): p. 8178-8194.
182. Ettelt, V., et al., *Streptavidin-coated surfaces suppress bacterial colonization by inhibiting non-specific protein adsorption.* J Biomed Mater Res A, 2018. **106**(3): p. 758-768.
183. Wu, C., et al., *A facile technique for fabricating poly (2-methacryloyloxyethyl phosphorylcholine) coatings on titanium alloys.* Journal of Coatings Technology and Research, 2017. **14**(5): p. 1127-1135.
184. Xu, K., et al., *Metal-phenolic networks as a promising platform for pH-controlled release of bioactive divalent metal ions.* Applied Surface Science, 2020. **511**.
185. Dayan, A., et al., *RGD-modified dihydrolipoamide dehydrogenase as a molecular bridge for enhancing the adhesion of bone forming cells to titanium dioxide implant surfaces.* J Biomed Mater Res A, 2019. **107**(3): p. 545-551.
186. Jia, S., et al., *Enhanced Hydrophilicity and Protein Adsorption of Titanium Surface by Sodium Bicarbonate Solution.* Journal of Nanomaterials, 2015. **2015**: p. 1-12.
187. Martinez-Ibanez, M., et al., *Enhancement of plasma protein adsorption and osteogenesis of hMSCs by functionalized siloxane coatings for titanium implants.* J Biomed Mater Res B Appl Biomater, 2018. **106**(3): p. 1138-1147.
188. Loreto, S., et al., *Hydration and Confinement Effects on Horse Heart Myoglobin Adsorption in Mesoporous TiO2.* The Journal of Physical Chemistry C, 2018. **122**(41): p. 23393-23404.
189. Huangfu, C., et al., *Mechanistic Study of Protein Adsorption on Mesoporous TiO2 in Aqueous Buffer Solutions.* Langmuir, 2019. **35**(34): p. 11037-11047.
190. Lin, D.J., L.J. Fuh, and W.C. Chen, *Nano-morphology, crystallinity and surface potential of anatase on micro-arc oxidized titanium affect its protein adsorption, cell proliferation and cell differentiation.* Mater Sci Eng C Mater Biol Appl, 2020. **107**: p. 110204.
191. Dias-Netipanyj, M.F., et al., *Effect of crystalline phases of titania nanotube arrays on adipose derived stem cell adhesion and proliferation.* Mater Sci Eng C Mater Biol Appl, 2019. **103**: p. 109850.
192. Gong, Z., et al., *Effects of diameters and crystals of titanium dioxide nanotube arrays on blood compatibility and endothelial cell behaviors.* Colloids Surf B Biointerfaces, 2019. **184**: p. 110521.
193. Sawada, R., et al., *Evaluation of Photocatalytic and Protein Adsorption Properties of Anodized Titanium Plate Immersed in Simulated Body Fluid.* Int J Biomater, 2019. **2019**: p. 7826373.
194. Zhang, X., et al., *Cellular response to nano-structured Zr and ZrO2 alloyed layers on Ti-6Al-4V.* Mater Sci Eng C Mater Biol Appl, 2018. **90**: p. 523-530.
195. Majumdar, P., et al., *Influence of boron addition to Ti-13Zr-13Nb alloy on MG63 osteoblast cell viability and protein adsorption.* Mater Sci Eng C Mater Biol Appl, 2015. **46**: p. 62-8.
196. Sperling, C., et al., *Neutrophil extracellular trap formation upon exposure of hydrophobic materials to human whole blood causes thrombogenic reactions.* Biomater Sci, 2017. **5**(10): p. 1998-2008.
197. Li, L., et al., *Effects of Zn and Ag Ratio on Cell Adhesion and Antibacterial Properties of Zn/Ag Coimplanted TiN.* ACS Biomaterials Science & Engineering, 2019. **5**(7): p. 3303-3310.

198. Zhang, X., et al., *Synergistic effects of lanthanum and strontium to enhance the osteogenic activity of TiO2 nanotube biological interface.* Ceramics International, 2020. **46**(9): p. 13969-13979.
199. Choi, S.H., et al., *Effect of wet storage on the bioactivity of ultraviolet light- and non-thermal atmospheric pressure plasma-treated titanium and zirconia implant surfaces.* Mater Sci Eng C Mater Biol Appl, 2019. **105**: p. 110049.
200. Dini, C., et al., *UV-photofunctionalization of a biomimetic coating for dental implants application.* Mater Sci Eng C Mater Biol Appl, 2020. **110**: p. 110657.
201. Aslı, G., A. Elif Burcu, and S. Mustafa Kemal, *A novel electrochemical immunosensor based on ITO modified by carboxyl-ended silane agent for ultrasensitive detection of MAGE-1 in human serum.* Analytical Biochemistry, 2017. **537**: p. 84-92.
202. Martínez-Hernández, M., V.I. García-Pérez, and A. Almaguer-Flores, *Potential of salivary proteins to reduce oral bacterial colonization on titanium implant surfaces.* Materials Letters, 2019. **252**: p. 120-122.
203. Toffoli, A., et al., *Thermal treatment to increase titanium wettability induces selective proteins adsorption from blood serum thus affecting osteoblasts adhesion.* Mater Sci Eng C Mater Biol Appl, 2020. **107**: p. 110250.
204. Zhang, C., et al., *Silver nanowires on acid-alkali-treated titanium surface: Bacterial attachment and osteogenic activity.* Ceramics International, 2019. **45**(18): p. 24528-24537.
205. Weidt, A., S.G. Mayr, and M. Zink, *Influence of Topological Cues on Fibronectin Adsorption and Contact Guidance of Fibroblasts on Microgrooved Titanium.* ACS Applied Bio Materials, 2019. **2**(3): p. 1066-1077.
206. Zhao, F.H., et al., *Conformation changes of albumin and lysozyme on electrospun TiO2 nanofibers and its effects on MSC behaviors.* Colloids Surf B Biointerfaces, 2020. **185**: p. 110604.
207. Bassous, N.J., C.L. Jones, and T.J. Webster, *3-D printed Ti-6Al-4V scaffolds for supporting osteoblast and restricting bacterial functions without using drugs: Predictive equations and experiments.* Acta Biomater, 2019. **96**: p. 662-673.
208. Jia, Z., et al., *Constructing Multilayer Silk Protein/Nanosilver Biofunctionalized Hierarchically Structured 3D Printed Ti6Al4 V Scaffold for Repair of Infective Bone Defects.* ACS Biomaterials Science & Engineering, 2018. **5**(1): p. 244-261.
209. Jiang, N., et al., *Exploring the mechanism behind improved osteointegration of phosphorylated titanium implants with hierarchically structured topography.* Colloids Surf B Biointerfaces, 2019. **184**: p. 110520.
210. Jiang, N., et al., *Promoting Osseointegration of Ti Implants through Micro/Nanoscaled Hierarchical Ti Phosphate/Ti Oxide Hybrid Coating.* ACS Nano, 2018. **12**(8): p. 7883-7891.
211. Park, B.-W., et al., *A Novel Hybrid-Structured Titanium Surface Promotes Adhesion of Human Dermal Fibroblasts and Osteogenesis of Human Mesenchymal Stem Cells while ReducingS. epidermidisBiofilm Accumulation.* Advanced Engineering Materials, 2016. **18**(4): p. 518-531.
212. Anbazhagan, E., et al., *Divalent ion encapsulated nano titania on Ti metal as a bioactive surface with enhanced protein adsorption.* Colloids Surf B Biointerfaces, 2016. **143**: p. 213-223.
213. Romero-Gavilan, F., et al., *The effect of strontium incorporation into sol-gel biomaterials on their protein adsorption and cell interactions.* Colloids Surf B Biointerfaces, 2019. **174**: p. 9-16.
214. Isoshima, K., et al., *The change of surface charge by lithium ion coating enhances protein adsorption on titanium.* J Mech Behav Biomed Mater, 2019. **100**: p. 103393.
215. Sit, I., Z. Xu, and V.H. Grassian, *Plasma protein adsorption on TiO2 nanoparticles: Impact of surface adsorption on temperature-dependent structural changes.* Polyhedron, 2019. **171**: p. 147-154.
216. Xu, Z. and V.H. Grassian, *Bovine Serum Albumin Adsorption on TiO2 Nanoparticle Surfaces: Effects of pH and Coadsorption of Phosphate on Protein–Surface Interactions and Protein Structure.* The Journal of Physical Chemistry C, 2017. **121**(39): p. 21763-21771.

217. Felgueiras, H.P., et al., *Competitive Adsorption of Plasma Proteins Using a Quartz Crystal Microbalance.* ACS Appl Mater Interfaces, 2016. **8**(21): p. 13207-17.
218. Sabino, R.M., et al., *Interaction of blood plasma proteins with superhemophobic titania nanotube surfaces.* Nanomedicine, 2019. **21**: p. 102046.
219. Stobener, D.D., et al., *Dynamic Protein Adsorption onto Dendritic Polyglycerol Sulfate Self-Assembled Monolayers.* Langmuir, 2018. **34**(35): p. 10302-10308.
220. Huang, C.J. and L.C. Wang, *Bio-inspired multifunctional catecholic assembly for photo-programmable biointerface.* Colloids Surf B Biointerfaces, 2015. **134**: p. 247-53.
221. Nishida, M., et al., *Titanium alloy modified with anti-biofouling zwitterionic polymer to facilitate formation of bio-mineral layer.* Colloids Surf B Biointerfaces, 2017. **152**: p. 302-310.
222. Li, Q., et al., *Novel mussel-inspired Ti-6Al-4V surfaces with biocompatibility, blood ultra-drag reduction and superior durability.* Mater Sci Eng C Mater Biol Appl, 2017. **76**: p. 1041-1047.
223. Hoyos-Nogues, M., et al., *All-in-one trifunctional strategy: A cell adhesive, bacteriostatic and bactericidal coating for titanium implants.* Colloids Surf B Biointerfaces, 2018. **169**: p. 30-40.
224. Fan, Y., et al., *Influence of chirality on catalytic generation of nitric oxide and platelet behavior on selenocystine immobilized TiO2 films.* Colloids Surf B Biointerfaces, 2016. **145**: p. 122-129.
225. Fabre, H., et al., *Impact of hydrophilic and hydrophobic functionalization of flat TiO2/Ti surfaces on proteins adsorption.* Applied Surface Science, 2018. **432**: p. 15-21.
226. Felgueiras, H.P. and V. Migonney, *Cell Spreading and Morphology Variations as a Result of Protein Adsorption and Bioactive Coating on Ti6Al4V Surfaces.* Irbm, 2016. **37**(3): p. 165-171.
227. Rodriguez, G.M., et al., *Functionalisation of Ti6Al4V and hydroxyapatite surfaces with combined peptides based on KKLPDA and EEEEEEEE peptides.* Colloids Surf B Biointerfaces, 2017. **160**: p. 154-160.
228. Wu, S., X. Liu, and C. Gao, *Role of adsorbed proteins on hydroxyapatite-coated titanium in osteoblast adhesion and osteogenic differentiation.* Science Bulletin, 2015. **60**(7): p. 691-700.
229. Laura Maria Duran Gleriani, P., et al., *Antimicrobial peptides grafted onto the surface of N-acetylcysteine-chitosan nanoparticles can revitalize drugs against clinical isolates of Mycobacterium tuberculosis.* Carbohydrate Polymers, 2024. **323**: p. 121449.
230. Branemark, R., et al., *Osseointegration in skeletal reconstruction and rehabilitation: a review.* Journal of rehabilitation research and development, 2001. **38**(2): p. 175-182.
231. Canullo, L., et al., *Platform switching and marginal bone-level alterations: the results of a randomized-controlled trial.* Clinical oral implants research, 2010. **21**(1): p. 115-121.
232. Hsu, R.W.-W., et al., *Electrochemical corrosion properties of Ti–6Al–4V implant alloy in the biological environment.* Materials Science and Engineering: A, 2004. **380**(1-2): p. 100-109.
233. Kamachimudali, U., T. Sridhar, and B. Raj, *Corrosion of bio implants.* Sadhana, 2003. **28**(3-4): p. 601-637.
234. Foerster, A., et al., *Stainless steel surface functionalization for immobilization of antibody fragments for cardiovascular applications.* J Biomed Mater Res A, 2016. **104**(4): p. 821-32.
235. Godoy-Gallardo, M., et al., *Anhydride-functional silane immobilized onto titanium surfaces induces osteoblast cell differentiation and reduces bacterial adhesion and biofilm formation.* Mater Sci Eng C Mater Biol Appl, 2016. **59**: p. 524-532.
236. Ekambaram, B.K., et al., *Introduction of Laser Interference Lithography to Make Nanopatterned Surfaces for Fundamental Studies on Stem Cell Response.* Acs Biomaterials Science & Engineering, 2018. **4**(5): p. 1820-1832.
237. Liu, Z., et al., *Construction of poly (vinyl alcohol)/poly (lactide-glycolide acid)/vancomycin nanoparticles on titanium for enhancing the surface self-antibacterial activity and cytocompatibility.* Colloids Surf B Biointerfaces, 2017. **151**: p. 165-177.
238. Chen, R., et al., *Antimicrobial peptide melimine coating for titanium and its in vivo antibacterial activity in rodent subcutaneous infection models.* Biomaterials, 2016. **85**: p. 142-51.

239. Nie, B., et al., *Covalent Immobilization of Enoxacin onto Titanium Implant Surfaces for Inhibiting Multiple Bacterial Species Infection and In Vivo Methicillin-Resistant Staphylococcus aureus Infection Prophylaxis.* Antimicrob Agents Chemother, 2017. **61**(1).
240. Godoy-Gallardo, M., et al., *Antibacterial properties of hLf1-11 peptide onto titanium surfaces: a comparison study between silanization and surface initiated polymerization.* Biomacromolecules, 2015. **16**(2): p. 483-96.
241. Lv, H., et al., *Layer-by-layer self-assembly of minocycline-loaded chitosan/alginate multilayer on titanium substrates to inhibit biofilm formation.* J Dent, 2014. **42**(11): p. 1464-72.
242. Chen, J., et al., *Antimicrobial Titanium Surface via Click-Immobilization of Peptide and Its in Vitro/Vivo Activity.* ACS Biomaterials Science & Engineering, 2018. **5**(2): p. 1034-1044.
243. O'Cearbhaill, E.J.S.T.M., *Shedding light on implant-associated infection.* 2019. **11**(511): p. eaaz3709.
244. Mitra, D., E.-T. Kang, and K.G. Neoh, *Applications and challenges of smart antibacterial coatings*, in *Advances in Smart Coatings and Thin Films for Future Industrial and Biomedical Engineering Applications*. 2020, Elsevier. p. 537-556.
245. Ghosh, S. and J. Haldar, *Cationic polymer–based antibacterial smart coatings*, in *Advances in Smart Coatings and Thin Films for Future Industrial and Biomedical Engineering Applications*. 2020, Elsevier. p. 557-582.
246. Wojcieszak, D., et al., *Influence of Cu-Ti thin film surface properties on antimicrobial activity and viability of living cells.* Materials Science and Engineering C, 2015. **56**: p. 48-56.
247. Chu, Y.Y., et al., *Promising antimicrobial capability of thin film metallic glasses.* Materials Science and Engineering C, 2014. **36**(1): p. 221-225.
248. Lalitha, K., et al., *Intrinsic Hydrophobic Antibacterial Thin Film from Renewable Resources: Application in the Development of Anti-Biofilm Urinary Catheters.* ACS Sustainable Chemistry and Engineering, 2017. **5**(1): p. 436-449.
249. Wei, X., et al., *Polymer antimicrobial coatings with embedded fine Cu and Cu salt particles.* Applied Microbiology and Biotechnology, 2014. **98**(14): p. 6265-6274.
250. Cao, S., et al., *Preparation and antimicrobial assay of ceramic brackets coated with TiO2 thin films.* Korean Journal of Orthodontics, 2016. **46**(3): p. 146-154.
251. Cao, B., et al., *Preparation of an orthodontic bracket coated with an nitrogen-doped TiO2-xNy thin film and examination of its antimicrobial performance.* Dental Materials Journal, 2013. **32**(2): p. 311-316.
252. Chung, C.J., et al., *An antimicrobial TiO2 coating for reducing hospital-acquired infection.* Journal of Biomedical Materials Research - Part B Applied Biomaterials, 2008. **85**(1): p. 220-224.
253. Vallejo, W., et al., *Zn(II)-tetracarboxy-phthalocyanine-Sensitized TiO2Thin Films as Antimicrobial Agents under Visible Irradiation: A Combined DFT and Experimental Study.* ACS Omega, 2021. **6**(21): p. 13637-13646.
254. Dunnill, C.W., et al., *Sulfur-and nitrogen-doped titania biomaterials via APCVD.* Chemical Vapor Deposition, 2010. **16**(1-3): p. 50-54.
255. Promdet, P., et al., *High Defect Nanoscale ZnO Films with Polar Facets for Enhanced Photocatalytic Performance.* ACS Applied Nano Materials, 2019. **2**(5): p. 2881-2889.
256. Ali, D., et al., *Synthesis, characterization and antibacterial performance of transparent c-axis oriented Al doped ZnO thin films.* Surfaces and Interfaces, 2021. **27**.
257. Dellasega, D., et al., *Nanostructured high valence silver oxide produced by pulsed laser deposition.* Applied Surface Science, 2009. **255**(10): p. 5248-5251.
258. Mandracci, P., et al., *Reduction of bacterial adhesion on dental composite resins by silicon-oxygen thin film coatings.* Biomedical Materials (Bristol), 2015. **10**(1).
259. Wojcieszak, D., et al., *Structural and surface properties of semitransparent and antibacterial (Cu,Ti,Nb)Ox coating.* Applied Surface Science, 2016. **380**: p. 159-164.

260. Kedia, S., et al., *Potential tribological and antibacterial benefits of pulsed laser-deposited zirconia thin film on Ti6Al4V bio-alloy.* Applied Physics A: Materials Science and Processing, 2022. **128**(8).
261. Anghel, A.G., et al., *MAPLE fabricated Fe3O4@Cinnamomum verum antimicrobial surfaces for improved gastrostomy tubes.* Molecules, 2014. **19**(7): p. 8981-8994.
262. Lyutakov, O., et al., *One-step preparation of antimicrobial silver nanoparticles in polymer matrix.* Journal of Nanoparticle Research, 2015. **17**(3).
263. Bhardwaj, A. and L.M.J.M.L. Pandey, *Design of antibiofilm surfaces by immobilization of biogenic silver nanoparticles on amine self-assembled monolayers.* 2022. **311**: p. 131574.
264. Inoue, A., H. Sugimoto, and M. Fujii, *Silver nanoparticles stabilized with a silicon nanocrystal shell and their antimicrobial activity.* RSC Advances, 2019. **9**(27): p. 15171-15176.
265. Myllymaa, K., et al., *Formation and retention of staphylococcal biofilms on DLC and its hybrids compared to metals used as biomaterials.* Colloids and Surfaces B: Biointerfaces, 2013. **101**: p. 290-297.
266. Iconaru, S.L., et al., *Nitrogen and bromide co-doped hydroxyapatite thin films with antimicrobial properties.* Coatings, 2021. **11**(12).
267. Balaure, P.C., et al., *Biocompatible hybrid silica nanobiocomposites for the efficient delivery of anti-staphylococcal drugs.* International Journal of Pharmaceutics, 2016. **510**(2): p. 532-542.
268. Jones, D.S., et al., *Poly(ε-caprolactone) and poly(ε-caprolactone)-polyvinylpyrrolidone-iodine blends as ureteral biomaterials: Characterisation of mechanical and surface properties, degradation and resistance to encrustation in vitro.* Biomaterials, 2002. **23**(23): p. 4449-4458.
269. Nagaraja, A., et al., *Synthesis, Characterization, and Fabrication of Hydrophilic Antimicrobial Polymer Thin Film Coatings.* Macromolecular Research, 2019. **27**(3): p. 301-309.
270. Shen, N., et al., *Photograftable Zwitterionic Coatings Prevent Staphylococcus aureus and Staphylococcus epidermidis Adhesion to PDMS Surfaces.* ACS Applied Bio Materials, 2021. **4**(2): p. 1283-1293.
271. Martin, T.P., et al., *Initiated chemical vapor deposition of antimicrobial polymer coatings.* Biomaterials, 2007. **28**(6): p. 909-915.
272. Richert, L., et al., *Layer by Layer Buildup of Polysaccharide Films: Physical Chemistry and Cellular Adhesion Aspects.* Langmuir, 2004. **20**(2): p. 448-458.
273. Foster, L.J.R. and J. Butt, *Chitosan films are NOT antimicrobial.* Biotechnology Letters, 2011. **33**(2): p. 417-421.
274. Nogueira, F., I.C. Gonçalves, and M.C.L. Martins, *Effect of gastric environment on Helicobacter pylori adhesion to a mucoadhesive polymer.* Acta Biomaterialia, 2013. **9**(2): p. 5208-5215.
275. Alias, R., et al., *Mechanical, antibacterial, and biocompatibility mechanism of PVD grown silver–tantalum-oxide-based nanostructured thin film on stainless steel 316L for surgical applications.* Materials Science and Engineering C, 2020. **107**.
276. Ferreri, I., et al., *Silver activation on thin films of Ag-ZrCN coatings for antimicrobial activity.* Materials Science and Engineering C, 2015. **55**: p. 547-555.
277. Dhall, A., et al., *Bimodal Nanocomposite Platform with Antibiofilm and Self-Powering Functionalities for Biomedical Applications.* ACS Applied Materials and Interfaces, 2021. **13**(34): p. 40379-40391.
278. Cassin, M.E., et al., *The design of antimicrobial LL37-modified collagen-hyaluronic acid detachable multilayers.* Acta Biomaterialia, 2016. **40**: p. 119-129.
279. Demircan, D., S. Ilk, and B. Zhang, *Cellulose-Organic Montmorillonite Nanocomposites as Biomacromolecular Quorum-Sensing Inhibitor.* Biomacromolecules, 2017. **18**(10): p. 3439-3446.
280. Wojciechowski, K., et al., *Antimicrobial films of poly(2-aminoethyl methacrylate) and its copolymers doped with TiO2 and CaCO3.* Colloids and Surfaces B: Biointerfaces, 2020. **185**.

281. Reis, R., et al., *Amine Enrichment of Thin-Film Composite Membranes via Low Pressure Plasma Polymerization for Antimicrobial Adhesion.* ACS Applied Materials and Interfaces, 2015. **7**(27): p. 14644-14653.
282. Cámara-Torres, M., et al., *3D additive manufactured composite scaffolds with antibiotic-loaded lamellar fillers for bone infection prevention and tissue regeneration.* 2021. **6**(4): p. 1073-1082.
283. Surmeneva, M., et al., *Decreased bacterial colonization of additively manufactured Ti6Al4V metallic scaffolds with immobilized silver and calcium phosphate nanoparticles.* Applied Surface Science, 2019.
284. Polo, L., et al., *Antimicrobial activity of commercial calcium phosphate based materials functionalized with vanillin.* 2018. **81**: p. 293-303.
285. Ibrahim, D.M., et al., *Bioactive and elastic nanocomposites with antimicrobial properties for bone tissue regeneration.* 2020. **3**(5): p. 3313-3325.
286. Chen, D., et al., *Anti-biofouling therapeutic nanoparticles with removable shell and highly efficient internalization by cancer cells.* Biomaterials science, 2019. **7**(1): p. 336-346.
287. Chen, J., et al., *Antimicrobial Titanium Surface via Click-Immobilization of Peptide and Its in Vitro/Vivo Activity.* ACS Biomater Sci Eng, 2019. **5**(2): p. 1034-1044.
288. Aslan, S., et al., *Carbon nanotube-based antimicrobial biomaterials formed via layer-by-layer assembly with polypeptides.* Journal of Colloid and Interface Science, 2012. **388**(1): p. 268-273.
289. Ahmed, F., et al., *Antimicrobial applications of electroactive PVK-SWNT nanocomposites.* Environmental Science and Technology, 2012. **46**(3): p. 1804-1810.
290. Ito, K., et al., *Sustainable antimicrobial effect of silver sulfadiazine-loaded nanosheets on infection in a mouse model of partial-thickness burn injury.* Acta Biomaterialia, 2015. **24**: p. 87-95.
291. Huang, Y.H., et al., *Evenly distributed thin-film Ag coating on stainless plate by tricomponent Ag/silicate/PU with antimicrobial and biocompatible properties.* ACS Applied Materials and Interfaces, 2014. **6**(22): p. 20324-20333.
292. Pulit-Prociak, J., et al., *Analysis of the physicochemical properties of antimicrobial compositions with zinc oxide nanoparticles.* Science and Technology of Advanced Materials, 2019. **20**(1): p. 1150-1163.
293. Tamayo, L., et al., *Porous Nanogold/Polyurethane Scaffolds with Improved Antibiofilm, Mechanical, and Thermal Properties and with Reduced Effects on Cell Viability: A Suitable Material for Soft Tissue Applications.* ACS Applied Materials and Interfaces, 2018. **10**(16): p. 13361-13372.
294. Abdallah, M.N., et al., *Comparative adsorption profiles of basal lamina proteome and gingival cells onto dental and titanium surfaces.* Acta Biomater, 2018. **73**: p. 547-558.
295. Zheng, T., et al., *Molecular investigations of tripeptide adsorption onto TiO2 surfaces: Synergetic effects of surface nanostructure, hydroxylation and bioactive ions.* Applied Surface Science, 2020. **512**.
296. Liamas, E., et al., *Tribocorrosion behaviour of pure titanium in bovine serum albumin solution: A multiscale study.* J Mech Behav Biomed Mater, 2019. **102**: p. 103511.
297. Masdek, N.R.N., et al., *Effect of Protein Concentration on Corrosion of Ti-6Al-4V and 316L SS Alloys.* ISIJ International, 2018. **58**(8): p. 1519-1523.
298. Delgado, A.H. and A.M.J.M. Young, *Modelling ATR-FTIR spectra of dental bonding systems to investigate composition and polymerisation kinetics.* 2021. **14**(4): p. 760.
299. Pandey, L.M. and S.K.J.A.S.S. Pattanayek, *Hybrid surface from self-assembled layer and its effect on protein adsorption.* 2011. **257**(10): p. 4731-4737.
300. Pandey, L.M. and S.K.J.A.s.s. Pattanayek, *Properties of competitively adsorbed BSA and fibrinogen from their mixture on mixed and hybrid surfaces.* 2013. **264**: p. 832-837.
301. Hasan, A., et al., *Effect of functional groups of self-assembled monolayers on protein adsorption and initial cell adhesion.* 2018. **4**(9): p. 3224-3233.

302. Liu, Q., et al., *The role of surface functional groups in calcium phosphate nucleation on titanium foil: a self-assembled monolayer technique.* 2002. **23**(15): p. 3103-3111.

303. Tack, L., et al., *Immobilization of specific proteins to titanium surface using self-assembled monolayer technique.* 2015. **31**(10): p. 1169-1179.

304. Jongseok, K., et al., *A stiff and flat membrane operated DC contact type RF MEMS switch with low actuation voltage.* Sensors and Actuators A: Physical, 2009. **153**(1): p. 114-119.

305. Howarter, J.A. and J.P. Youngblood, *Optimization of Silica Silanization by 3-Aminopropyltriethoxysilane.* Langmuir, 2006. **22**(26): p. 11142-11147.

306. Callow, M.E., R.L.J.I.b. Fletcher, and biodegradation, *The influence of low surface energy materials on bioadhesion—a review.* 1994. **34**(3-4): p. 333-348.

307. Kennedy, S.B., et al., *Combinatorial screen of the effect of surface energy on fibronectin-mediated osteoblast adhesion, spreading and proliferation.* 2006. **27**(20): p. 3817-3824.

308. Zhao, G., et al., *Requirement for both micron-and submicron scale structure for synergistic responses of osteoblasts to substrate surface energy and topography.* 2007. **28**(18): p. 2821-2829.

309. Scotchford, C.A., et al., *Growth of human osteoblast-like cells on alkanethiol on gold self-assembled monolayers: The effect of surface chemistry.* 1998. **41**(3): p. 431-442.

310. Lim, J.Y., et al., *Surface energy effects on osteoblast spatial growth and mineralization.* 2008. **29**(12): p. 1776-1784.

311. Zhao, G., et al., *Requirement for both micron- and submicron scale structure for synergistic responses of osteoblasts to substrate surface energy and topography.* Biomaterials, 2007. **28**(18): p. 2821-2829.

312. Arima, Y. and H. Iwata, *Effect of wettability and surface functional groups on protein adsorption and cell adhesion using well-defined mixed self-assembled monolayers.* Biomaterials, 2007. **28**(20): p. 3074-82.

313. Tan, G., et al., *Preparation and characterization of APTES films on modification titanium by SAMs.* 2011. **519**(15): p. 4997-5001.

314. Pandey, L.M. and S.K. Pattanayek, *Properties of competitively adsorbed BSA and fibrinogen from their mixture on mixed and hybrid surfaces.* Applied Surface Science, 2013. **264**: p. 832-837.

315. Naik, V.V., et al., *Multiple transmission-reflection IR spectroscopy shows that surface hydroxyls play only a minor role in alkylsilane monolayer formation on silica.* 2013. **4**(16): p. 2745-2751.

316. Stoch, A., et al., *FTIR monitoring of the growth of the carbonate containing apatite layers from simulated and natural body fluids.* 1999. **511**: p. 287-294.

317. Toworfe, G., et al., *Nucleation and growth of calcium phosphate on amine-, carboxyl-and hydroxyl-silane self-assembled monolayers.* 2006. **27**(4): p. 631-642.

318. Gündoğdu, A., E.B. Aydın, and M.K.J.A.b. Sezgintürk, *A novel electrochemical immunosensor based on ITO modified by carboxyl-ended silane agent for ultrasensitive detection of MAGE-1 in human serum.* 2017. **537**: p. 84-92.

319. Ciceo-Lucacel, R., et al., *Behavior of molybdenum lowly doped SiO2–CaO–P2O5 composite interfacing a simulated biologic medium with serum albumin.* 2021. **1240**: p. 130564.

320. Mahmood, A., et al., *Degradation behavior of mixed and isolated aromatic ring containing VOCs: Langmuir-Hinshelwood kinetics, photodegradation, in-situ FTIR and DFT studies.* 2021. **9**(2): p. 105069.

321. Zhai, Q., et al., *Trimethoxysilane Coupling Agents: Hydrolysis Kinetics by FTNIR PLS Model, Synthesis and Characterization of Fluorinated Silicone Resin.* 2023. **15**(9): p. 3945-3957.

322. Zhai, Q., et al., *Hydrolysis kinetics of silane coupling agents studied by near-infrared spectroscopy plus partial least squares model.* 2019.

323. Schartner, J., et al., *Universal method for protein immobilization on chemically functionalized germanium investigated by ATR-FTIR difference spectroscopy.* 2013. **135**(10): p. 4079-4087.

324. Suys, O., A. Derenne, and E.J.I.j.o.m.s. Goormaghtigh, *ATR-FTIR biosensors for antibody detection and analysis.* 2022. **23**(19): p. 11895.

325. Parry, D. and J.J.A.s. Harris, *Attenuated total reflection FT-IR spectroscopy to measure interfacial reaction kinetics at silica surfaces.* 1988. **42**(6): p. 997-1004.

326. Naik, V.V., et al., *Multiple Transmission-Reflection IR Spectroscopy Shows that Surface Hydroxyls Play Only a Minor Role in Alkylsilane Monolayer Formation on Silica.* The Journal of Physical Chemistry Letters, 2013. **4**(16): p. 2745-2751.

327. Barros, L.P., et al., *On-line ATR-MIR for real-time quantification of chemistry kinetics along the barrel in extrusion-based processes.* 2021. **103**: p. 107350.

328. Carrer, V., et al., *Lanolin-based synthetic membranes as percutaneous absorption models for transdermal drug delivery.* 2018. **10**(3): p. 73.

329. Chavez-Diaz, M.P., et al., *Effect of the Heat-Treated Ti6Al4V Alloy on the Fibroblastic Cell Response.* Materials (Basel), 2017. **11**(1).

330. Blanquer, A., et al., *Cytocompatibility assessment of Ti-Zr-Pd-Si-(Nb) alloys with low Young's modulus, increased hardness, and enhanced osteoblast differentiation for biomedical applications.* J Biomed Mater Res B Appl Biomater, 2018. **106**(2): p. 834-842.

331. Gnilitskyi, I., et al., *Cell and tissue response to nanotextured Ti6Al4V and Zr implants using high-speed femtosecond laser-induced periodic surface structures.* Nanomedicine, 2019. **21**: p. 102036.

332. Jager, M., et al., *Intrasurgical Protein Layer on Titanium Arthroplasty Explants: From the Big Twelve to the Implant Proteome.* Proteomics Clin Appl, 2019. **13**(2): p. e1800168.

333. Bins-Ely, L., et al., *On the increase of the chemical reactivity of cp titanium and Ti6Al4V at low electrical current in a protein-rich medium.* Biomedical Physics & Engineering Express, 2018. **5**(1).

334. Nadia, A., O. Sasha, and A.-K. Mehdi, *Functionalization of a gold surface with fibronectin (FN) covalently bound to mixed alkanethiol self-assembled monolayers (SAMs): The influence of SAM composition on its physicochemical properties and FN surface secondary structure.* Thin Solid Films, 2012. **522**: p. 381-389.

335. Agata, P., et al., *Hybrid chitosan/β-1,3-glucan matrix of bone scaffold enhances osteoblast adhesion, spreading and proliferation via promotion of serum protein adsorption.* Biomedical Materials, 2016. **11**(4): p. 045001.

336. Pandey, L.M. and S.K. Pattanayek, *Hybrid surface from self-assembled layer and its effect on protein adsorption.* Applied Surface Science, 2011. **257**(10): p. 4731-4737.

337. Jacopo, B., et al., *Effect on albumin and fibronectin adsorption of silver doping via ionic exchange of a silica-based bioactive glass.* Ceramics International, 2023. **49**(9, Part A): p. 13728-13741.

338. Ciceo-Lucacel, R., et al., *Behavior of molybdenum lowly doped SiO2–CaO–P2O5 composite interfacing a simulated biologic medium with serum albumin.* Journal of Molecular Structure, 2021. **1240**: p. 130564.

339. Cristina, C.B., et al., *The correlation between the adsorption of adhesive proteins and cell behaviour on hydroxyl-methyl mixed self-assembled monolayers.* Biomaterials, 2009. **30**(3): p. 307-316.

340. Mingcong, S., D. Jun, and G. Changyou, *The correlation between fibronectin adsorption and attachment of vascular cells on heparinized polycaprolactone membrane.* Journal of Colloid and Interface Science, 2015. **448**: p. 231-237.

341. Morais, J.M., F. Papadimitrakopoulos, and D.J. Burgess, *Biomaterials/tissue interactions: possible solutions to overcome foreign body response.* AAPS J, 2010. **12**(2): p. 188-96.

342. Elias, C.N., *Factors affecting the success of dental implants*, in *Implant Dentistry-A Rapidly Evolving Practice*. 2011, IntechOpen.

343. Branemark, R., et al., *Osseointegration in skeletal reconstruction and rehabilitation: a review.* J Rehabil Res Dev, 2001. **38**(2): p. 175-81.

344. Canullo, L., et al., *Platform switching and marginal bone-level alterations: the results of a randomized-controlled trial.* Clin Oral Implants Res, 2010. **21**(1): p. 115-21.

345. Shiau, D.K., et al., *Enhancing the blood response and antibacterial adhesion of titanium surface through oxygen plasma immersion ion implantation treatment.* Surface & Coatings Technology, 2019. **365**: p. 173-178.

346. Romero-Gavilán, F., et al., *The effect of strontium incorporation into sol-gel biomaterials on their protein adsorption and cell interactions.* Colloids and Surfaces B: Biointerfaces, 2019. **174**: p. 9-16.

347. Zlotnik, S., et al., *Functionalized-ferroelectric-coating-driven enhanced biomineralization and protein-conformation on metallic implants.* J Mater Chem B, 2019. **7**(13): p. 2177-2189.

348. Jewell, C.M. and J.H. Collier, *Biomaterial interactions with the immune system.* Biomater Sci, 2019. **7**(3): p. 713-714.

349. Low, S.P., et al., *Evaluation of mammalian cell adhesion on surface-modified porous silicon.* Biomaterials, 2006. **27**(26): p. 4538-46.

350. Mitsuhiro, H., et al., *Effect of sterilization and water rinsing on cell adhesion to titanium surfaces.* Applied Surface Science, 2014. **311**: p. 498-502.

351. Rezek, B., et al., *Assembly of osteoblastic cell micro-arrays on diamond guided by protein pre-adsorption.* Diamond and Related Materials, 2010. **19**(2): p. 153-157.

352. Rahmati, M. and M.J.M.T.C. Mozafari, *Protein adsorption on polymers.* 2018. **17**: p. 527-540.

353. Schmidt, D.R., et al., *Protein adsorption to biomaterials.* 2009: p. 1-18.

354. Latour, R.A.J.E.o.b. and b. engineering, *Biomaterials: protein-surface interactions.* 2005. **1**: p. 270-284.

355. Adhikari, N. and D.B. Pandey, *Treatment planning challenges for prosthesis prostate cancer patients in radiation therapy.* South Asian journal of cancer, 2017. **6**(1): p. 37.

356. Bertrand, J., et al., *Ceramic prosthesis surfaces induce an inflammatory cell response and fibrotic tissue changes.* Bone Joint J, 2018. **100**(7): p. 882-890.

357. Gohil, S., et al., *Polymers and composites for orthopedic applications*, in *Materials for Bone Disorders*. 2017, Elsevier. p. 349-403.

358. Peng, J. and Q. Cheng, *High-performance nanocomposites inspired by nature.* Advanced Materials, 2017. **29**(45): p. 1702959.

359. Tonsomboon, K. and M.L. Oyen, *Composite electrospun gelatin fiber-alginate gel scaffolds for mechanically robust tissue engineered cornea.* Journal of the mechanical behavior of biomedical materials, 2013. **21**: p. 185-194.

360. Sutter, R., S. Rüegg, and S. Tschudin-Sutter, *Seizures as adverse events of antibiotic drugs A systematic review.* Neurology, 2015: p. 10.1212/WNL. 0000000000002023.

361. Kulkarni, V., et al., *Methicillin, Vancomycin and Multidrug-Resistance Among Staphylococcus Aureus.* National Journal of Integrated Research in Medicine, 2018. **8**(3): p. 68-74.

362. Manor, Y., et al., *Characteristics of Early Versus Late Implant Failure: A Retrospective Study.* Journal of Oral and Maxillofacial Surgery, 2009. **67**(12): p. 2649-2652.

363. Gristina, A.G., *Implant failure and the immuno-incompetent fibro-inflammatory zone.* Clinical orthopaedics and related research, 1994(298): p. 106-118.

364. Zhan, W., et al., *Bioinspired Blood Compatible Surface Having Combined Fibrinolytic and Vascular Endothelium-Like Properties via a Sequential Coimmobilization Strategy.* Advanced Functional Materials, 2015. **25**(32): p. 5206-5213.

365. Knetsch, M.L. and L.H. Koole, *New strategies in the development of antimicrobial coatings: the example of increasing usage of silver and silver nanoparticles.* Polymers, 2011. **3**(1): p. 340-366.

366. Lau, K.H.A., et al., *Surface-grafted polysarcosine as a peptoid antifouling polymer brush.* Langmuir, 2012. **28**(46): p. 16099-16107.

367. Alinaghiyan, M., E.S. Mirsamadi, and M.K. Rahimi, *The expression of the fosfomycin (fos) resistant gene in chitosan nanoparticle-treated Proteus mirabilis isolated from urine samples.* Gene Reports, 2024. **34**: p. 101863.
368. Sharma, T.K., et al., *Green synthesis and antimicrobial potential of silver nanoparticles.* International Journal of Green Nanotechnology, 2012. **4**(1): p. 1-16.
369. Kaur, R., et al., *Synthesis and surface engineering of magnetic nanoparticles for environmental cleanup and pesticide residue analysis: a review.* Journal of separation science, 2014. **37**(14): p. 1805-1825.
370. Khan, M.F., et al., *Flower-shaped ZnO nanoparticles synthesized by a novel approach at near-room temperatures with antibacterial and antifungal properties.* International journal of nanomedicine, 2014. **9**: p. 853.
371. Jiang, H., et al., *Zwitterionic gold nanorods: low toxicity and high photothermal efficacy for cancer therapy.* Biomaterials science, 2017. **5**(4): p. 686-697.
372. Zhuang, Y., et al., *Tracing drug release process with dual-modal hyperbranched polymer-gold nanoparticle complexes.* Science China Chemistry, 2016. **59**(12): p. 1600-1608.
373. Dutta, B., et al., *PEG coated vesicles from mixtures of Pluronic P123 and l-α-phosphatidylcholine: structure, rheology and curcumin encapsulation.* Physical Chemistry Chemical Physics, 2017. **19**(39): p. 26821-26832.
374. Oyen, M., *Mechanical characterisation of hydrogel materials.* International Materials Reviews, 2014. **59**(1): p. 44-59.
375. Kim, J.S., et al., *Antimicrobial effects of silver nanoparticles.* Nanomedicine: Nanotechnology, Biology and Medicine, 2007. **3**(1): p. 95-101.
376. Lee, S.J., et al., *One-step fabrication of AgNPs embedded hybrid dual nanofibrous oral wound dressings.* Journal of biomedical nanotechnology, 2016. **12**(11): p. 2041-2050.
377. Richter, A.P., et al., *An environmentally benign antimicrobial nanoparticle based on a silver-infused lignin core.* Nature nanotechnology, 2015. **10**(9): p. 817.
378. Iravani, S., et al., *Synthesis of silver nanoparticles: chemical, physical and biological methods.* Research in pharmaceutical sciences, 2014. **9**(6): p. 385.
379. Kumar, R., et al., *Rapid Green synthesis of silver nanoparticles (AgNPs) using (Prunus persica) plants extract: Exploring its antimicrobial and catalytic activities.* Journal of Nanomedicine and Nanotechnology, 2017. **8**(452).
380. Kim, D.-Y., et al., *Green synthesis of silver nanoparticles using Laminaria japonica extract: characterization and seedling growth assessment.* Journal of cleaner production, 2018. **172**: p. 2910-2918.
381. Jeong, Y., D.W. Lim, and J. Choi, *Assessment of Size-Dependent Antimicrobial and Cytotoxic Properties of Silver Nanoparticles.* Advances in Materials Science and Engineering, 2014. **2014**: p. 6.
382. Lu, Z., et al., *Size-dependent antibacterial activities of silver nanoparticles against oral anaerobic pathogenic bacteria.* Journal of Materials Science: Materials in Medicine, 2013. **24**(6): p. 1465-1471.
383. Yun’an Qing, L.C., et al., *Potential antibacterial mechanism of silver nanoparticles and the optimization of orthopedic implants by advanced modification technologies.* International journal of nanomedicine, 2018. **13**: p. 3311.
384. Crozier, A., M.N. Clifford, and H. Ashihara, *Plant secondary metabolites: occurrence, structure and role in the human diet.* 2008: John Wiley & Sons.
385. Fanti, J.R., et al., *Biogenic silver nanoparticles inducing Leishmania amazonensis promastigote and amastigote death in vitro.* Acta tropica, 2018. **178**: p. 46-54.
386. Darroudi, M., et al., *Effect of accelerator in green synthesis of silver nanoparticles.* International journal of molecular sciences, 2010. **11**(10): p. 3898-3905.

387. Zhang, P.-Y., et al., *Combined treatment with the antibiotics kanamycin and streptomycin promotes the conjugation of Escherichia coli.* FEMS microbiology letters, 2013. **348**(2): p. 149-156.

388. Joseph, V., et al., *Simple carbazole based deep-blue emitters: The effect of spacer, linkage and end-capping cyano group on the photophysical and electroluminescent properties.* Dyes and Pigments, 2018. **151**: p. 310-320.

389. Nayak, S., S. Talukdar, and S.C. Kundu, *Potential of 2D crosslinked sericin membranes with improved biostability for skin tissue engineering.* Cell and tissue research, 2012. **347**(3): p. 783-794.

390. Mude, N., et al., *Synthesis of silver nanoparticles using callus extract of Carica papaya—a first report.* Journal of Plant Biochemistry and Biotechnology, 2009. **18**(1): p. 83-86.

391. Suman, T., et al., *Biosynthesis, characterization and cytotoxic effect of plant mediated silver nanoparticles using Morinda citrifolia root extract.* Colloids and surfaces B: Biointerfaces, 2013. **106**: p. 74-78.

392. Philip, D., *Green synthesis of gold and silver nanoparticles using Hibiscus rosa sinensis.* Physica E: Low-dimensional Systems and Nanostructures, 2010. **42**(5): p. 1417-1424.

393. Saravanakumar, K., et al., *Synthesis, characterization, and cytotoxicity of starch-encapsulated biogenic silver nanoparticle and its improved anti-bacterial activity.* International Journal of Biological Macromolecules, 2021. **182**: p. 1409-1418.

394. Van Ingen, R., R. Fastenau, and E. Mittemeijer, *Laser ablation deposition of Cu-Ni and Ag-Ni films: Nonconservation of alloy composition and film microstructure.* Journal of applied physics, 1994. **76**(3): p. 1871-1883.

395. Harisha, K.S., et al., *Characterization and antibacterial properties of biogenic spherical silver nanoparticles.* Materials Today: Proceedings, 2021. **42**: p. 405-409.

396. Chappard, D., et al., *Metaplastic woven bone in bone metastases: A Fourier-transform infrared analysis and imaging of bone quality (FTIR).* Morphologie, 2018. **102**(337): p. 69-77.

397. Rheder, D.T., et al., *Synthesis of biogenic silver nanoparticles using Althaea officinalis as reducing agent: evaluation of toxicity and ecotoxicity.* Scientific reports, 2018. **8**.

398. Sowmya, C., et al., *Exploration of Phyllanthus acidus mediated silver nanoparticles and its activity against infectious bacterial pathogen.* Chemistry Central Journal, 2018. **12**(1): p. 42.

399. Hasan, A. and L.M. Pandey, *Kinetic studies of attachment and re-orientation of octyltriethoxysilane for formation of self-assembled monolayer on a silica substrate.* Materials Science and Engineering: C, 2016. **68**: p. 423-429.

400. Dhayalan, M., M.I.J. Denison, and K. Krishnan, *In vitro antioxidant, antimicrobial, cytotoxic potential of gold and silver nanoparticles prepared using Embelia ribes.* Natural product research, 2017. **31**(4): p. 465-468.

401. Wei, W., et al., *Preparation and application of novel microspheres possessing autofluorescent properties.* Advanced Functional Materials, 2007. **17**(16): p. 3153-3158.

402. Barabadi, H., et al., *Green synthesis, characterization, antibacterial and biofilm inhibitory activity of silver nanoparticles compared to commercial silver nanoparticles.* Inorganic Chemistry Communications, 2021. **129**: p. 108647.

403. Bhat, M., et al., *Biogenic synthesis, characterization and antimicrobial activity of Ixora brachypoda (DC) leaf extract mediated silver nanoparticles.* Journal of King Saud University - Science, 2021. **33**(2): p. 101296.

404. Kora, A.J. and J. Arunachalam, *Green fabrication of silver nanoparticles by gum Tragacanth (Astragalus gummifer): a dual functional reductant and stabilizer.* Journal of Nanomaterials, 2012. **2012**: p. 69.

405. Arora, A.K., et al., *Raman spectroscopy of optical phonon confinement in nanostructured materials.* Journal of Raman Spectroscopy: An International Journal for Original Work in all Aspects of Raman Spectroscopy, Including Higher Order Processes, and also Brillouin and Rayleigh Scattering, 2007. **38**(6): p. 604-617.

406. Donato, M.G., et al., *Optical force decoration of 3D microstructures with plasmonic particles.* Optics Letters, 2018. **43**(20): p. 5170-5173.
407. Scibilia, S., et al., *Self-assembly of silver nanoparticles and bacteriophage.* Sensing and bio-sensing research, 2016. **7**: p. 146-152.
408. Das, S., A. Bhardwaj, and L.M. Pandey, *Functionalized Biogenic Nanoparticles for Use in Emerging Biomedical Applications: A Review.* Current Nanomaterials, 2021. **6**(2).
409. Jeyanthi, V., et al., *Effect of naturally isolated hydroquinone in disturbing the cell membrane integrity of Pseudomonas aeruginosa MTCC 741 and Staphylococcus aureus MTCC 740.* Heliyon, 2021. **7**(5): p. e07021.
410. Mohan, A., et al., *Oxidative stress induced antimicrobial efficacy of chitosan and silver nanoparticles coated Gutta-percha for endodontic applications.* Materials Today Chemistry, 2020. **17**: p. 100299.
411. Huang, X., et al., *Biomaterial scaffolds in maxillofacial bone tissue engineering: A review of recent advances.* Bioact Mater, 2024. **33**: p. 129-156.
412. Liang, J., et al., *Biomaterial-based scaffolds in promotion of cartilage regeneration: Recent advances and emerging applications.* J Orthop Translat, 2023. **41**: p. 54-62.
413. Mohd Salleh, N.K., et al., *Strategies to improve the antimicrobial properties of metal-oxide based photocatalytic coating: A review.* Progress in Organic Coatings, 2024. **187**: p. 108183.
414. Ding, L., et al., *Surface Attachment of Natural Antimicrobial Coatings onto Conventional Polypropylene Nonwoven Fabric and Its Antimicrobial Performance Assessment.* J Food Prot, 2018. **81**(2): p. 172-177.
415. Wang, Z., et al., *Fabrication of antimicrobial cationic hydrogels driven by physically and chemically crosslinking for wound healing.* Int J Biol Macromol, 2024. **259**(Pt 1): p. 129213.
416. Kyvik, A.R., et al., *Antibiofilm surfaces based on the immobilization of a novel recombinant antimicrobial multidomain protein using self-assembled monolayers.* Materials Advances, 2023. **4**(10): p. 2354-2364.
417. Morella-Aucejo, A., et al., *Remarkable enhancement of cinnamaldehyde antimicrobial activity encapsulated in capped mesoporous nanoparticles: A new "nanokiller" approach in the era of antimicrobial resistance.* Biomater Adv, 2024. **160**: p. 213840.
418. Renata Katsuko Takayama, K., et al., *Chapter 6 - Metallic nanoparticles as a potential antimicrobial for catheters and prostheses.* 2019: p. 153-196.
419. Swarupa, S. and P. Thareja, *Techniques, applications and prospects of polysaccharide and protein based biopolymer coatings: A review.* Int J Biol Macromol, 2024. **266**(Pt 2): p. 131104.
420. Chen, L., et al., *Organized assembly of chitosan into mechanically strong bio-composite by introducing a recombinant insect structural protein OfCPH-1.* Carbohydr Polym, 2024. **334**: p. 122044.
421. Shoueir, K.R., et al., *Chitosan based-nanoparticles and nanocapsules: Overview, physicochemical features, applications of a nanofibrous scaffold, and bioprinting.* Int J Biol Macromol, 2021. **167**: p. 1176-1197.
422. Agnieszka, W., et al., *Influence of biodegradable polymer coatings on corrosion, cytocompatibility and cell functionality of Mg-2.0Zn-0.98Mn magnesium alloy.* Colloids and Surfaces B: Biointerfaces, 2016. **144**: p. 284-292.
423. Agnieszka, W., Y. Akiko, and Ś. Wojciech, *Influence of SaOS-2 cells on corrosion behavior of cast Mg-2.0Zn0.98Mn magnesium alloy.* Colloids and Surfaces B: Biointerfaces, 2017. **150**: p. 288-296.
424. Ramesh, S., et al., *FTIR studies of PVC/PMMA blend based polymer electrolytes.* Spectrochim Acta A Mol Biomol Spectrosc, 2007. **66**(4-5): p. 1237-42.
425. Radu, E.R., et al., *Preparation and Characterization of Chitosan/LDH Composite Membranes for Drug Delivery Application.* Membranes (Basel), 2023. **13**(2): p. 179.

426. Nan-Hai, L. and S. Shi-Gang, *In situ FTIR spectroscopic studies of the electrooxidation of C4 alcohol on a platinum electrode in acid solutions Part I. Reaction mechanism of 1-butanol oxidation.* Journal of Electroanalytical Chemistry, 1997. **436**(1-2): p. 65-72.

427. Rudzki, A., et al., *Thermal analysis and FTIR study of 4-hexadecyloxybenzoic acid (16OB).* Journal of Thermal Analysis and Calorimetry, 2023. **148**(20): p. 10663-10677.

428. Jin, Z., et al., *Rapid Identification for the Pterocarpus Bracelet by Three-Step Infrared Spectrum Method.* Molecules, 2022. **27**(15): p. 4793.

429. Banu, A., et al., *Synthesis and characterization of bisacodyl loaded chitosan nanoparticles (BSL@CS NPs), multispectroscopic study of their interaction with bovine serum albumin (BSA).* Journal of Molecular Liquids, 2023. **387**: p. 122488.

430. Zhang, Q., et al., *Incorporation of Ag NPs/palygorskite into chitosan/glycyrrhizic acid films as a potential antibacterial wound dressing.* Results in Materials, 2023. **18**: p. 100396.

431. Babaeenezhad, E., et al., *Cytotoxic and epigenetic effects of berberine-loaded chitosan/pectin nanoparticles on AGS gastric cancer cells: Role of the miR-185-5p/KLF7 axis, DNMTs, and global DNA methylation.* Int J Biol Macromol, 2024. **260**(Pt 2): p. 129618.

432. Lotfy, V.F. and A.H. Basta, *Performance effectiveness of nano-lignin in production of gel with nano-chitosan for controlling release of salicylic acid.* Int J Biol Macromol, 2024. **265**(Pt 2): p. 131098.

433. Jin, Z., G. Hu, and K. Zhao, *Mannose-anchored quaternized chitosan/thiolated carboxymethyl chitosan composite NPs as mucoadhesive carrier for drug delivery.* Carbohydr Polym, 2022. **283**: p. 119174.

434. Tian, B., et al., *Synthesis of beta-acids loaded chitosan-sodium tripolyphosphate nanoparticle towards controlled release, antibacterial and anticancer activity.* Int J Biol Macromol, 2024. **257**(Pt 2): p. 128719.

435. Hu, D., et al., *Novel biomimetic peptide-loaded chitosan nanoparticles improve dentin bonding via promoting dentin remineralization and inhibiting endogenous matrix metalloproteinases.* Dent Mater, 2024. **40**(2): p. 160-172.

436. Li, B., et al., *Preparation and characterization of antibacterial, antioxidant, and biocompatible p-coumaric acid modified quaternized chitosan nanoparticles.* Int J Biol Macromol, 2023. **242**(Pt 4): p. 125087.

437. Primo, L., et al., *Antimicrobial peptides grafted onto the surface of N-acetylcysteine-chitosan nanoparticles can revitalize drugs against clinical isolates of Mycobacterium tuberculosis.* Carbohydr Polym, 2024. **323**: p. 121449.

438. Song, Z., et al., *Dual amplification strategy for the fabrication of highly sensitive amperometric immunosensor based on nanocomposite functionalized interface.* Sensors and Actuators B: Chemical, 2010. **145**(2): p. 817-825.

439. Teymourian, H., A. Salimi, and S. Khezrian, *Fe3O4 magnetic nanoparticles/reduced graphene oxide nanosheets as a novel electrochemical and bioeletrochemical sensing platform.* Biosens Bioelectron, 2013. **49**: p. 1-8.

Research output from thesis:

1. **Aman Bhardwaj**, and Lalit M. Pandey*. "Design of antibiofilm surfaces by immobilization of biogenic silver nanoparticles on amine self-assembled monolayers." Materials Letters 311 (2022): 131574. 10.1016/j.matlet.2021.131574
2. **Bhardwaj, A**., Pandey, L.M*. In: Pandey, L.M., Hasan, A. (eds) "Biomaterials: Types and Applications". Nanoscale Engineering of Biomaterials: Properties and Applications. Springer, Singapore. (2022), 89-114. 10.1007/978-981-16-3667-7_4

Under preparation

3. **Aman Bhardwaj** and Lalit M. Pandey. "Experimental insights into carboxyl SAMs formation reaction kinetics and protein adsorption studies."
4. **Aman Bhardwaj** and Lalit M. Pandey. "Silane functionalization of Ti6Al4V surfaces protein adsorption and cell adhesion studies."
5. **Aman Bhardwaj**, Akiko YAMAMOTO and Lalit M. Pandey. "Chitosan nanoparticles mediated antimicrobial agents and drug-loading vehicles for antimicrobial coatings on the amine-SAMs functionalization titanium and alloy surface."

Other publications:

6. Apurba Das, Susmita Rabha, Varun Saxena, **Aman Bhardwaj**, Lalit M. Pandey, K. A. Emmanuel, and Pamu Dobbidi*. "The role of electrical property in determining the response of 20H-80S composite thin films fabricated for biological applications." Journal of Materials Science 57, no. 28 (2022): 13586-13602. 10.1007/s10853-022-07455-7
7. Apurba Das, Varun Saxena, **Aman Bhardwaj**, Susmita Rabha, Lalit M. Pandey, and Pamu Dobbidi*. "Microstructural, interfacial, biological and electrical activity in sputtered Hydroxyapatite-Barium strontium titanate bilayered thin films." Surfaces and Interfaces 31 (2022): 102063. 10.1016/j.surfin.2022.102063
8. Apurba Das, **Aman Bhardwaj**, Susmita Rabha, Lalit M. Pandey, and Pamu Dobbidi*. "Physical, chemical, and biological investigations of composites for biomedical applications." Journal of the American Ceramic Society 105, no. 3 (2022): 1790-1808. 10.1111/jace.17952
9. Apurba Das, Emon Barua, Suman Kumar Mushahary, **Aman Bhardwaj**, Varun Saxena, Lalit Pandey, Ashish Deoghare, and Pamu Dobbidi*. "A comparative study of microstructural, biological, and mechanical properties in 20H-80B and 20H-80S composite scaffolds." Materials Letters 304 (2021): 130668. 10.1016/j.matlet.2021.130668
10. Apurba Das, Pamu Dobbidi*, **Aman Bhardwaj**, Varun Saxena, and Lalit M. Pandey. "Microstructural, electrical and biological activity in $Ca_{10}(PO_4)_6(OH)_2$-$Ba_{0.5}Sr_{0.5}TiO_3$ ceramic

composites designed for tissue engineering applications," Scientific Reports 11, no. 1 (2021): 22304. 10.1038/s41598-021-01748-8

11. Samvidha Das, **Aman Bhardwaj**, and Lalit M. Pandey*. "Functionalized biogenic nanoparticles for use in emerging biomedical applications: a review." Current Nanomaterials 6, no. 2 (2021): 119-139. 10.2174/2468187310999201222112144
12. Fopase, R., **Bhardwaj, A**., Yadav, V.S., Pandey, L.M.*. In: Chandra, P., Pandey, L. (eds) Engineered Drug Delivery Systems: Insights of Biointerface. Biointerface Engineering: Prospects in Medical Diagnostics and Drug Delivery. Springer, Singapore. (2020) 1-30. 10.1007/978-981-15-4790-4_1

Conferences and seminars attended:

1. **Aman Bhardwaj** and Lalit Mohan Pandey, (poster presentation) International Conference on Frontiers in Chemical Sciences (FICS - 2018), IIT Guwahati, India, 2018
2. **Aman Bhardwaj**, workshop on " ImageJ, advance excel & OriginPro software" at Research Conclave 2018
3. **Aman Bhardwaj**, "Recent Advances on Bio-inspired Nanomaterials for Environmental Applications", UK-India Education and Research Initiative (UKIERI), IIT Guwahati, India, 2018
4. **Aman Bhardwaj** and Lalit Mohan Pandey,(poster presentation), 1st Departmental Retreat, IIT Guwahati, India, 2019
5. **Aman Bhardwaj**, SPIE MATLAB Workshop, IIT Guwahati, India, 2019
6. **Aman Bhardwaj** and Lalit Mohan Pandey, Conference on "Emerging Trends in Applied Materials Science and Surface Engineering" 16-17 Jan 2020
7. **Aman Bhardwaj**, workshop cum symposium on "Bio- Nanomaterials For Environmental Applications", UK-India Education and Research Initiative (UKIERI), IIT Guwahati, India, 2020
8. **Aman Bhardwaj** and Lalit M. Pandey, North-East Research Conclave: Sustainable Science and Technology (NERC-2022). IIT Guwahati, India, 2022